Infrared Spectro-Interferometry of Massive Stars: Disks, Winds, Outflows, and Stellar Multiplicity

Dissertation

zur

Erlangung des Doktorgrades (Doctor rerum naturalium)

der

Mathematisch-Naturwissenschaftlichen Fakultät

der

Rheinischen Friedrich-Wilhelms-Universität, Bonn

vorgelegt von

Stefan Kraus

aus

Aschaffenburg, Deutschland

June 2007

Angefertigt mit Genehmigung
der Mathematisch-Naturwissenschaftlichen Fakultät
der Rheinischen Friedrich-Wilhelms-Universität Bonn

Referenten: **Prof. Dr. Gerd Weigelt**[1]
Prof. Dr. Ulrich Klein[2]

[1] Max-Planck-Institut für Radioastronomie, Bonn
[2] Argelander-Institut für Astronomie, Bonn

Gewidmet

meinen Eltern

Dedicated

to my parents

Infrared Spectro-Interferometry of Massive Stars: Disks, Winds, Outflows, and Stellar Multiplicity

Dissertation presented

by

Stefan Kraus

Infrared Spectro-Interferometry of Massive Stars: Disks, Winds, Outflows, and Stellar Multiplicity

by Stefan Kraus

ABSTRACT

Interferometry is the ultimate technology for overcoming the limitations which diffraction and the atmosphere-induced seeing impose on the resolution achievable with ground-based telescopes. The latest generation of long-baseline interferometric instruments (in particular VLTI/AMBER and VLTI/MIDI), combines the high spatial resolution (typically a few milliarcseconds) with spectroscopic capabilities, allowing one to characterize the geometry of a continuum-emitting region over a wide spectral range or to spatially resolve the emitting region of Doppler-broadened spectral lines in many velocity channels.

One branch of astrophysics which might particularly benefit from these advances in technology is the study of massive (O–B type) stars. In order to characterize these stars and their companions and to study accretion and outflow processes in their vicinity with unprecedented angular resolution, we have performed interferometric studies on four key objects, representing the still most enigmatic evolutionary phases of massive stars; namely the pre-main-sequence (MWC 147, NGC 7538 IRS1, θ^1Ori C) and the post-main-sequence phase (η Carinae).

MWC 147: As indicated by its strong infrared excess, this young Herbig Be star (B6-type) is still associated with residual material from its formation; maybe arranged in a circumstellar disk. In order to investigate the geometry of the material, we combined, for the first time, long-baseline spectro-interferometric observations at near- (NIR) and mid-infrared (MIR) wavelengths (using VLTI/AMBER, VLTI/MIDI, and archival PTI data). Fitting analytic models to the obtained interferometric data revealed a significant elongation of the continuum-emitting region. For a physical interpretation, we modeled the geometry of the dust distribution using 2-D radiative transfer simulations of Keplerian disks with and without a puffed-up inner rim, simultaneously fitting the wavelength-dependent visibilities and the SED, which we complemented with archival *Spitzer*/IRS spectra. Surprisingly, we found that passive disk models, which can reproduce the SED well, are in strong conflict with the interferometric data. However, when including emission from an optically thick inner gaseous disk, good quantitative agreement was found for all observables, suggesting that MWC 147 harbours a still actively accreting disk.

NGC 7538 IRS1/2: NGC 7538 IRS1 is a high-mass (O7-type) protostar with a CO outflow, an associated ultracompact H II region, and a linear methanol maser structure, which might trace a Keplerian-rotating circumstellar disk. We investigated the NIR morphology of the source with unprecedented resolution using NIR bispectrum speckle interferometry obtained at the BTA 6 m and the MMT 6.5 m telescopes. Our high-dynamic range images show fan-shaped outflow structures, in which we detected 18 stars and several blobs of diffuse emission. Complementary archival *Spitzer*/IRAC images were used

to relate the detected structures with the outflow at larger scales. We found a misalignment of various outflow axes and interpreted this in the context of a disk precession model, also using molecular hydrodynamic simulations. As a possible triggering mechanism, we identified non-coplanar tidal interaction of an (yet undiscovered) close companion with the circumbinary disk. Finally, our observations resolved the nearby massive protostar NGC 7538 IRS2 as a close binary with a separation of 195 mas, finding indications for shock interaction between the outflows from IRS1 and IRS2.

θ^1 Ori C/D: Located in the Orion Trapezium Cluster, θ^1 Ori C is one of the youngest and nearest high-mass (O5–O7) stars. The star is also known to be a close binary system. We traced the orbital motion from 1997.8 to 2004.8 using visual and NIR bispectrum speckle interferometry at the BTA 6 m telescope. In 2005.9, we obtained first IOTA long-baseline interferometry on the θ^1 Ori C system, allowing us to derive preliminary solutions for the dynamical orbit and the dynamical mass. Taking the measured flux ratio and the derived location in the HR-diagram into account, we estimated the spectral types and masses of θ^1 Ori C1 and C2 to be O5.5 ($M = 34.0\ M_\odot$) and O9.5 ($M = 15.5\ M_\odot$), respectively. Thus, the companion C2 appears to be much more massive than previously thought, suggesting strong wind-wind interaction during the periastron passage, which we predict for epoch 2007.5 with a small physical separation of only ~ 1.5 AU. From the IOTA data on θ^1 Ori C, we reconstructed the first optical aperture synthesis image of a young star. We also obtained IOTA data for θ^1 Ori D, which appears resolved, perhaps indicating the presence of a close, faint companion.

η Carinae: Using VLTI/AMBER, we performed the first NIR spectro-interferometry of the Luminous Blue Variable (LBV) η Car, simultaneously obtaining high spatial and spectral resolutions ($\lambda/\Delta\lambda = 1\,500$ and $12\,000$). The measured wavelength-dependent visibilities, differential phases, and closure phases were used to constrain the geometry of the continuum-emitting region, as well as the Brγ 2.166 μm and He I 2.059 μm line-emitting region. We compared the measured visibilities with predictions of the radiative transfer model of Hillier et al. (2001), finding good agreement. For the interpretation of the non-zero differential and closure phases measured within the Brγ line, we present a simple geometric model of an inclined, latitude-dependent wind zone. Thus, our observations support theoretical models of anisotropic winds from fast-rotating, luminous hot stars with enhanced high-velocity mass loss near the polar regions. In the He I 2.059 μm line, we measured non-zero phases as well, indicating asymmetries in the brightness distribution, which we discuss in the context of wind-wind interaction between η Car and its hypothetical hot binary companion. Using simulations, we examined the possibility to directly detect this companion in future observations.

Besides these astrophysical results of my dissertation, I present work related to methodological and technical aspects of infrared interferometry. The principles of a data reduction software developed for IOTA/IONIC3 and a pipeline for VLTI/AMBER are discussed. Furthermore, I summarize comparative studies which aim to evaluate the performance of different image reconstruction algorithms in order to explore the prospects and limitations of optical aperture synthesis imaging.

Contents

List of Figures

List of Tables

1 Introduction

1.1 Motivation and Outline of this Thesis

In the last few decades, the tremendous advances in instrumentation have resulted in a significant improvement of our understanding of the formation process and the evolution of stars. This is particularly true for low-mass stars, where detailed observational investigations could establish a new paradigm for the star formation process. For several reasons, the life-cycle of massive (O–B type) stars is not as well understood. Some of the challenges which these stars pose on observations are that high-mass stars are very distant, scarce in number, have very short evolutionary time scales, and form and evolve in dense clusters with strong dynamical interaction, stellar winds, and outflows. Therefore, high-angular resolution studies are required to achieve further progress in understanding the evolutionary sequence of these stars.

Comparing the fractional number of low- ($\sim$ 93.9% for $M < 1\ M_{\odot}$, Kroupa 2002), intermediate- ($\sim$ 5.7% for $1\ M_{\odot} < M < 8\ M_{\odot}$) and high-mass stars ($\sim$ 0.4% for $M > 8\ M_{\odot}$) reveals that massive stars make up only a small fraction of the total galactic stellar population. Nevertheless, these stars have a tremendous impact on their environment throughout their entire life-cycle. Shortly after their birth, they start to disperse the natal molecular cloud with strong stellar winds and outflows and photoevaporate the protoplanetary disks around nearby low-mass stars. After a short (Bernasconi & Maeder 1996) hydrogen-burning phase, they pass very short-lived evolutionary phases as *Luminous Blue Variable* (LBV) and *Wolf-Rayet* stars, both dominated by extreme mass-loss, before the most massive stars end their evolution as supernovae, enriching the interstellar medium (ISM) with metals and triggering the next generation of stars by compression through supernova shock waves.

In the course of my PhD thesis, I have applied infrared interferometric techniques to study intermediate and high-mass stars at evolutionary stages reaching from the protostellar to the LBV phase, covering a wide mass range from $\sim 7\ M_{\odot}$ to $100\ M_{\odot}$. By using the latest generation of infrared interferometric instruments, we aim not only to study the continuum emission from these objects at a single wavelength, but also to combine the high-angular resolution with spectroscopic capabilities. This can be used either to spatially resolve the continuum-emitting region over a broad wavelength range (such as applied in our studies on MWC 147 and θ^1 Ori C), or to perform interferometry in spatially and spectrally resolved spectral lines, which allows us to study the kinematics of gas emerging in stellar winds or wind-shock

regions (as in our study on η Carinae). Whenever possible, we combine the information obtained at high angular resolution with conventional imaging as provided by the *Spitzer* Space Telescope and by observations at radio wavelengths (as in our study on NGC 7538 IRS1), or with conventional spectra.

Because infrared long-baseline interferometry only recently went beyond the stage of experimental technology, it is missing established general user software for data processing, interpretation, and modeling. Therefore, a large fraction of my PhD work involved developing, implementing, and testing data reduction routines for state-of-the-art infrared interferometers like VLTI/AMBER and IOTA, as well as software related to model fitting, radiative transfer modeling, and the reconstruction of aperture synthesis images.

This thesis is structured as follows: First, as part of this introduction, I sketch our current knowledge about the life-cycle of massive stars **(Sect. 1.2)**, simultanously placing the studied objects in a broader context. Then I briefly review the fundamental challenges we face when dealing with high-angular resolution imaging at visual and infrared wavelengths, and the technologies which have been developed to face them **(Sect. 1.3)**. In **Sect. 2**, I introduce the basic principles of long-baseline interferometry and its observables. In the two following sections, I describe the two near-infrared (NIR) instruments used for my thesis work, namely IOTA/IONIC3 **(Sect. 3)** and VLTI/AMBER **(Sect. 4)**, and outline some of my work related to data reduction procedures for these instruments. Data from two other instruments, namely the mid-infrared (MIR) instrument VLTI/MIDI and the NIR interferometer PTI, were also used for one of my PhD projects. As I could use existing data reduction software on these data sets, these instruments are not presented in a separate chapter, but only introduced in the context of the corresponding science project (Sect. 6). **Sect. 5** presents a brief summary of our studies related to aperture synthesis imaging.

The following four Chapters present the astrophysical aspects of my PhD work and are based on four articles published, submitted, or close to submission to A&A. They are structured as individual units and cover the following topics:

Sect. 6: VLTI/MIDI and VLTI/AMBER observations of the Herbig Be star MWC 147 and radiative transfer modeling of its active accretion disk.

Sect. 7: Bispectrum speckle imaging of the high-mass protostars NGC 7538 IRS1 and IRS2 and modeling of its possibly precessing outflow.

Sect. 8: Bispectrum speckle and IOTA/IONIC3 interferometry of the Orion Trapezium stars θ^1Ori C and θ^1Ori D and determination of a preliminary orbital solution for the θ^1Ori C system.

Sect. 9: VLTI/AMBER spectro-interferometry and modeling of the aspherical stellar wind and the potential wind-wind interaction region around the LBV η Carinae.

1.2 The Life-Cycle of Massive Stars

It is believed that massive stars form through the collapse of cold, dense cores. These cores set the stage for high-mass star formation and might be observed as *infrared dark clouds* (IRDCs). IRDCs are massive (a few hundred to a few thousand $M_{\odot}$), cold (10–20 K), star-less aggregations of gas and dust, which appear in absorption against the mid-infrared (MIR) galactic background (Menten et al. 2005). IRDCs seem to collapse to *hot cores* (labeled as Class 0 in Figure 1.1), which are internally heated (50–250 K) and rather compact (< 0.1 pc, Rathborne et al. 2006). Further on in the evolution, molecular outflows and maser emission appear. From the large number of maser species found in high-mass star-forming regions, Class II methanol masers (6.7 GHz) were identified as especially reliable tracers of the earliest stages of high-mass star formation (Pestalozzi et al. 2005; Ellingsen 2006). Shortly after its birth, the formed protostar already starts to ionize its environment, creating hyper- (HCH II) or ultra-compact (UCH II) regions (Hoare 2005, Class I). The natal molecular cloud is dispersed by strong (sometimes collimated) outflows and stellar winds. Once the density and extinction of the envelope are sufficiently reduced, the star emerges from its parental cloud as a mid- or near-infrared source. By the time, an O star appears at optical wavelengths, it has already burned a noticable fraction of its central hydrogen content and has developed towards the main-sequence (Bernasconi & Maeder 1996).

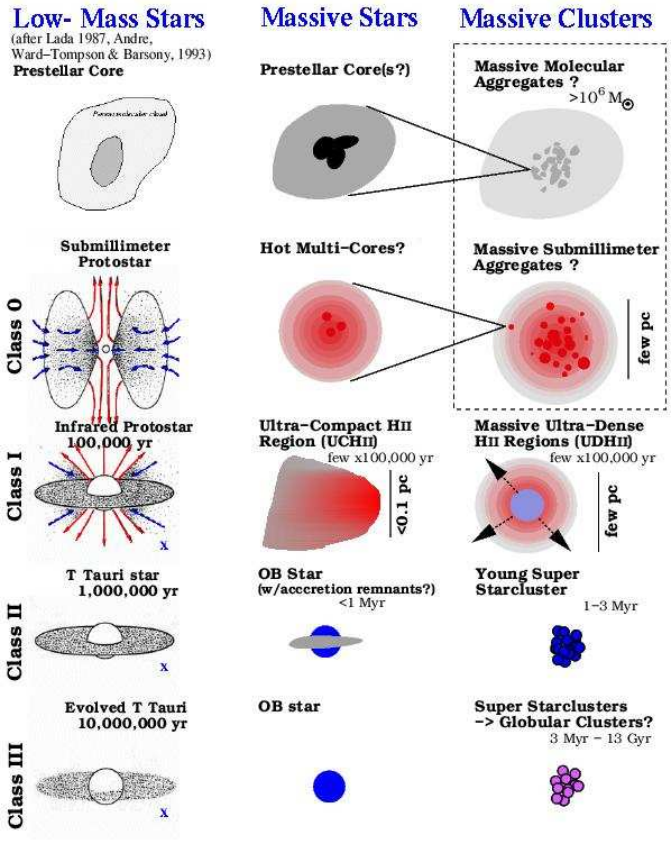

Figure 1.1: Schematic evolutionary sequence of the stages in the low- and high-mass star formation process (Image credit: `http://physics.uwyo.edu/~chip/`).

Another effect of the dramatic influence of the intense ultraviolet (UV) radiation field on its vicinity was discovered in the Orion Trapezium Cluster, where the winds and UV-flux of the most massive

Trapezium star, θ^1Ori C, disperses and ionizes the protoplanetary disks around nearby low- and intermediate mass stars. The line-emission of these *proplyds* was first observed rather early (Laques & Vidal 1979), although their precise structure and properties were not revealed before very sensitive Hubble Space Telescope observations could be performed in the late 90's (O'dell 1998).

Another characteristic of high-mass star formation is that it tends to occur in dense clusters, as sketched in the right-hand column of Figure 1.1. This has not only the consequence that strong gravitational interaction between the OB stars leads to stellar ejection or merging (Zinnecker 2004), but also seems to be reflected in the stellar multiplicity rate, which is much higher for high-mass than for low-mass stars (Preibisch et al. 1999; Köhler et al. 2006).

After the central hydrogen-burning phase, which typically lasts just a few million years, the most massive stars enter another short-lived phase as Luminous Blue Variables (LBVs, Conti 1984). This phase is dominated by strong mass loss via stellar winds. Perhaps the most studied, but still mysterious example for this evolutionary stage is η Carinae. With its $\sim$ 100 $M_\odot$, it is also one of the most massive stars known in the galaxy. For η Carinae, the LBV-typical, near-Eddington-limit mass-loss also manifests in the surrounding complex Homunculus reflection nebula, which was likely ejected during an outburst around 1840. Further enhancing the mass loss, the most massive stars become completely obscured by their optically thick wind and enter the *Wolf-Rayet* phase before they ultimatively explode as supernovae.

Despite the general picture presented above, some fundamental aspects of the life-cycle of massive stars are still poorly understood. This concerns, in particular, the pre-main-sequence (PMS) stage. For low- to intermediate-mass stars, it now seems well-established that the formation of these stars happens through accretion of envelope material through an accretion disk. The accretion disk geometry allows the transport of large amounts of material towards the stars, while a smaller fraction of the material, carrying most of the angular momentum, is transported outwards (Lynden-Bell & Pringle 1974). In fact, for the young B6-type star MWC 147, which we observed with long-baseline interferometry, we found strong indications for the presence of an actively accreting circumstellar disk (see Chapter 6).

For stars with even higher masses ($\gtrsim$10 $M_\odot$), early spherical symmetric calculations suggested that the accretion scenario might halt due to strong radiation pressure. Therefore, it was proposed that high-mass stars might not form by accretion, but by stellar merging instead (Bonnell et al. 1998). Recent theoretical work has loosened the originally derived radiation pressure limit by considering more complex disk and infall geometries (e.g. Yorke & Sonnhalter 2002). However, even these studies have found a barrier around 40 $M_\odot$, at which the radiation pressure stops or even reverses the accretion process. Possible solutions to this problem are currently discussed in literature (e.g. Krumholz et al. 2005), but the results are still inconclusive.

Observationally, the accretion disk hypothesis for massive stars is mainly supported by the detection of large rotating, disk-like structures in mm-radio lines (e.g. Cesaroni et al. 2005) and by very extended

disk-like structures imaged in the infrared continuum (e.g. Chini et al. 2006). Further evidence for disk-like Keplerian rotating disks around massive stars comes from modeling the line profiles of hydrogen recombination lines (Bik & Thi 2004). The appearance of masers in linear or arc-like alignment was also often discussed as a possible tracer of circumstellar disks, as the spatial alignment is sometimes accompanied by a well-defined velocity gradient indicating ordered motion (Norris et al. 1998; Minier et al. 2000). One source where the maser-disk hypothesis has been deeply tested is the methanol maser feature A in NGC7538-IRS1 (Pestalozzi et al. 2004). It was found that the observed velocity gradient can be fitted very accurately assuming a Keplerian rotating circumstellar disk 750 AU in radius around a 30 $M_{\odot}$ star. As an alternative explanation for the appearance of linear-aligned maser features, it was suggested that these masers might form within shocks or outflows (Walsh et al. 1998; De Buizer 2003; Dodson et al. 2004), which are then traced on larger scales by CO line emission or within shock-tracer lines like H_2, [Fe II], or [S II].

As stars with masses above 100 $M_{\odot}$ clearly seem to exist, further observational evidence is clearly needed to unambigously identify the different phases of the complex formation process of massive stars.

1.3 Interferometry and the Quest for Spatial Resolution

Progress in astronomy has often been driven by revolutions in instrumentation. One of the most fundamental optical properties, which limits the performance of any telescope and the amount of details we can image on celestrial objects, is *Fraunhofer diffraction*. For a telescope with circular aperture (diameter D), perfect optical properties, and without the perturbing influence of the terrestrial atmosphere, the theoretical limit in spatial resolution is given by the Rayleigh criterion

$$\Theta = 1.22\lambda D^{-1}. \tag{1.1}$$

Here, Θ gives the angular separation of two point sources for which the first diffraction minimum coincides with the maximum of the other (for a particular wavelength λ). While Θ might be a realistic measure for the achievable resolution of space telescope facilities like the Hubble Space Telescope (HST) or the *Spitzer* Space Telescope, ground-based telescopes additionally have to face the problem of atmospheric turbulence.

1.3.1 The turbulent Earth atmosphere

The Earth atmosphere can be considered as a large number of turbulence cells of different temperatures and densities. As the diffractive index depends on the temperature, these cells scatter the incident stellar light in a random pattern, which causes the image of a point source to break up into a *speckle* pattern (see Fig. 1.2). Long-exposure imaging, as performed in conventional astrophotography (with detector integration times of a few seconds and longer), records a time-averaged speckle pattern, the so-called *seeing disk*. Due to the random nature of the intensity and phase variations, induced by the Earth's atmosphere, the brightness of the seeing disk is approximately Gaussian distributed. The atmospheric conditions are characterized by the spatial coherence length r_0 (Fried parameter), which is the characteristic scale over which the incoming wave front suffers no distortions, and the coherence time t_0, over which temporal changes in the atmosphere can be neglected, and the atmosphere can be considered as

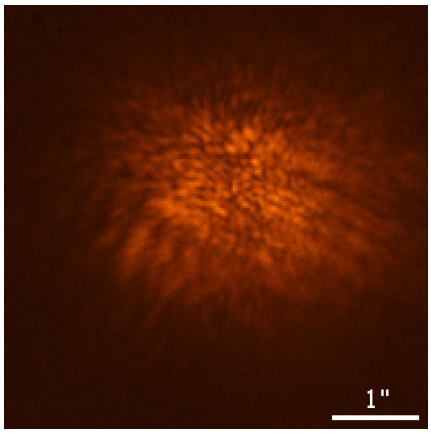

Figure 1.2: Speckle pattern caused by the turbulent structure of the terrestrial atmosphere. This K-band speckle interferogram was taken by our group in 1999 at the BTA 6 m telescope on the 76 mas binary HIP4849 (Image Credit: `http://www.mpifr-bonn.mpg.de/div/ir-interferometry/`).

"frozen". From r_0, the FWHM of the seeing disk $\epsilon = 0.98\lambda/r_0$ can also be computed for a particular wavelength λ (Sarazin & Roddier 1990). For visual wavelengths (e.g. $\lambda_V = 550$ nm), typical values are $t_0 = 10$ ms and $r_0 = 10$ cm (Buscher 1988), corresponding to a size of the seeing disk of $\sim 1''.1$. Towards longer wavelengths, the restrictions relax slightly, as r_0 increases as $r_0 \propto \lambda^{6/5}$ (for Kolmogorov turbulence, Sarazin & Roddier 1990).

1.3.2 Speckle interferometry and adaptive optics imaging

Great efforts have been taken to overcome the limitations imposed by the atmospheric influence. In 1970, a first success was achieved by Labeyrie with the speckle interferometry method. This technique uses short exposure times (i.e. comparable to t_0) to "freeze" the atmospheric turbulence. Therefore, each speckle interferogram represents a convolution of the object brightness distribution with the current transfer function of the "frozen" atmospheric screen. The method proposed by Labeyrie does not retrieve the phase information of the image, but computes the autocorrelation of the speckle interferograms. Therefore, this method is not applicable to objects with very complex brightness distributions, but can be used, for instance, to measure the separation and position angle (PA) of binary stars, although even in these cases a 180° degeneracy remains.

To extract real images from speckle data, other methods have been developed. A method proposed by Knox & Thompson (1974) cancels the atmospheric influence by dividing the average cross-spectrum of the target speckle interferograms with those of a reference star. Then the phases can be recursively reconstructed. The bispectrum speckle interferometry method (Weigelt & Wirnitzer 1983; Lohmann et al. 1983; Hofmann & Weigelt 1986), which evolved historically from speckle masking (Weigelt 1977), also reobtains the phases recursively. By using the average bispectrum (see Sect. 2.2.2), this method makes use of the property that on triangles in Fourier space (which are defined by two spatial frequency vectors; therefore *bi*spectrum), phase errors cancel out. Furthermore, for each triangle the phase information can be retrieved on various paths, which provide reduced residual errors on the reconstructed phase signal after averaging.

Although speckle interferometry can provide diffraction-limited imaging at visual and NIR wavelengths, it is limited in sensitivity (typically V$\approx 14^m$ and K$\approx 12^m$) due to its short integration times. Recently, adaptive optics (AO) systems were developed which also allow long integration times (typically a few minutes), exploiting the full sensitivity provided by the large aperture of the current generation of telescopes. These systems operate routinely at NIR wavelengths and correct the atmospheric wave front distortions using deformable mirrors (e.g. NAOS-CONICA on the VLT).

1.3.3 Long-baseline interferometry

As speckle imaging and AO systems are already pushing towards the theoretical diffraction-limit of a single-dish telescope, a conceptual turn has to be taken to gain further resolution in optical astronomy. The most basic principles of optical (i.e. visual and infrared) interferometry were already formulated in 1868 by Armand Fizeau, who proposed to place a mask with two holes in front of a telescope aperture. He suggested measuring the diameter of stars by finding the hole separation at which the formed interference pattern (the *fringe*) vanished. This technique was used four years later by Edouard Stéphan to obtain an upper limit for the diameter of some stars and was successfully applied by Albert Abraham Michelson to measure for the first time the diameter of the Galilean moons (Michelson 1891). In 1919, Michelson enhanced the resolution of the 100-inch Hooker telescope by mounting 20-foot beams on top, resulting in the first measurement of a stellar diameter (Michelson & Pease 1921). Another milestone was reached in 1974 when Antoine Labeyrie succeeded in combining the light of two separate telescopes, spaced 12 m apart. At this stage, the radio astronomy community had already developed important concepts for long baseline radio interferometry which could be adopted to optical wavelengths. Some important contributions were the development of Earth rotation aperture synthesis (e.g. Ryle & Hewish 1960) and the concept of the closure phase (Rogers et al. 1974), allowing to obtain accurate phase information even in presence of strong atmospheric perturbations. The first optical aperture synthesis images were presented by Buscher et al. (1990) and Baldwin et al. (1996), and imaged the surface of Betelgeuse and the binary star Capella, respectively.

In the following Sections, I will introduce the basic principles of long-baseline interferometry (Sect. 2) and adopt these to the IOTA/IONIC3 (Sect. 3) and VLTI/AMBER (Sect. 4) instrument. Then I present some of our studies related to aperture synthesis imaging (Sect. 5).

2 Principles of Long-Baseline Interferometry

2.1 Basics of Interferometry

One solution to the time-independent Helmholtz equation (and thus also the Maxwell equations) is the monochromatic, stationary planar wave $\Psi_s(\vec{x})$ (Bergmann & Schaefer 1993). The propagation of this wave through source-free vacuum can be expressed by

$$\Psi(\vec{x},t) = \Psi_s(\vec{x})e^{-\imath(ckt+\phi)}, \tag{2.1}$$

where $k = 2\pi\nu/c = 2\pi/\lambda$ is the *wave number* and ϕ the *phase* of the wave. As usual, c denotes the speed of light in vacuum, ν the frequency, and λ the wavelength.

For long-baseline interferometry, the same electromagnetic wave Ψ is sampled with several apertures. While propagating throughout the optical system, the wave experiences optical path differences, which we take into account by including a delay term τ_i for each spatially filtered wave front. Additionally there are rapidly changing phase modulations induced by the atmosphere, which we denote with ζ_i (this piston might be wavelength dependent). Therefore, for the wave that reaches the detector from aperture i, we yield

$$\psi_i(\vec{x},t) = \sqrt{P_i(\vec{x})}\Psi_i(\vec{x},t)e^{-\imath ck(\tau_i+\zeta_i)}, \tag{2.2}$$

where $P_i(\vec{x})$ denotes the pupil function (including transmission).

The *intensity* I_i of the light from this telescope is then given by the absolute square of the complex wavefunction ψ_i. Due to the finite sampling time, we compute the time-averaged intensity with

$$I_i(\vec{x},t) = \langle|\psi_i(\vec{x},t)|^2\rangle \tag{2.3}$$

$$= P_i(\vec{x})\langle|\Psi_i(\vec{x},t)|^2\rangle \tag{2.4}$$

If light from N apertures is superposed, the measured signal is given by

$$
\begin{aligned}
I(\vec{x},t) &= \left\langle \left| \sum_{i=1}^{N} \psi_i \right|^2 \right\rangle && (2.5)\\
&= \left\langle \sum_{i,j=1}^{N} \psi_i \psi_j^* \right\rangle && (2.6)\\
&= \sum_{i=1}^{N} \langle |\psi_i|^2 \rangle + \sum_{1 \leqslant i < j \leqslant N} 2\Re \langle \psi_i \psi_j^* \rangle && (2.7)\\
&= \sum_{i=1}^{N} I_i + \sum_{i<j} 2\Re \langle \psi_i \psi_j^* \rangle && (2.8)\\
&= \sum_{i=1}^{N} I_i + \sum_{i<j} 2\sqrt{P_i P_j}\Re \left[\left\langle \Psi_i e^{-\imath ck(\tau_i+\zeta_i)} \left(\Psi_j e^{-\imath ck(\tau_j+\zeta_j)} \right)^* \right\rangle \right] && (2.9)\\
&= \sum_{i=1}^{N} I_i + \sum_{i<j} 2\sqrt{I_i I_j}\Re \left[\frac{\langle \Psi_i \Psi_j^* \rangle}{\sqrt{\langle |\Psi_i|^2 \rangle \langle |\Psi_j^*|^2 \rangle}} e^{-\imath [ck(\tau_i+\zeta_i) - ck(\tau_j+\zeta_j)]} \right] && (2.10)
\end{aligned}
$$

where ψ^* is the complex conjugate of ψ. The real (imaginary) part of a complex function is denoted with $\Re()$ and $\Im()$. We define the complex visibility $\mathbb{V}_{ij}$, which is identical with the complex degree of coherence, with

$$\mathbb{V}_{ij} := \frac{\langle \Psi_i \Psi_j^* \rangle}{|\Psi_i||\Psi_j^*|} \tag{2.11}$$

which, for the interferogram given above yields:

$$
\begin{aligned}
I(\vec{x},t) &= \sum_{i=1}^{N} I_i + \sum_{i<j} 2\sqrt{I_i I_j}\Re \left[\mathbb{V}_{ij} e^{-\imath ck(\tau_i - \tau_j + \zeta_i - \zeta_j)} \right] && (2.12)\\
&:= I^{\mathrm{DC}}(\vec{x}) + \sum_{i<j} 2\Re \left[\mathbb{I}_{ij}^{\mathrm{AC}}(\vec{x}, \tau_i, \tau_j) \right] && (2.13)
\end{aligned}
$$

While the first term in equation 2.13 corresponds to a constant, underlying continuum (I^{DC}, this term has to be removed at the data reduction stage), the interference pattern is given by the second term (real part of $\mathbb{I}^{\mathrm{AC}}$). For a single planar wave (corresponding to an unresolved point-source), $|\mathbb{V}_{ij}| \equiv 1$ everywhere. A more general case will be considered in Section 2.5.

The fringe pattern γ_{ij} at the detector shows a cosine modulation, with an amplitude given by the visibility $V_{ij} = |\mathbb{V}_{ij}|$:

$$I(\vec{x},t) = \sum_{i=1}^{N} I_i + \sum_{i<j} 2\sqrt{I_i I_j} V_{ij} \cos[-ck(\tau_i - \tau_j + \zeta_i - \zeta_j) - (\phi_i - \phi_j)] \tag{2.14}$$

$$:= \sum_{i=1}^{N} I_i + \sum_{i<j} 2\gamma_{ij}\sqrt{I_i I_j} \tag{2.15}$$

2.2 Interferometric Observables

2.2.1 Visibility

The most fundamental observable in interferometry is the *fringe contrast*, given by the amplitude of the complex visibility (see definition in 2.11). While the phase of $\mathbb{V}_{ij}$ is strongly affected by atmospheric perturbations, the atmospheric (and instrumental) effects on the fringe amplitude vary rather smoothly and can be corrected using measurements on calibrator stars. Therefore, it is common to use the (phase-independent) absolute square of the complex visibility as observable:

$$V_{ij}^2 := |\mathbb{V}_{ij}|^2 . \tag{2.16}$$

This quantity can be extracted from the interferogram power spectrum, although the removal of underlying background and bias terms has to be done with caution.

2.2.2 Closure phase and bispectrum

Besides the fringe amplitude (i.e. V^2, as defined in equation 2.16), the phase of the complex visibility carries additional information about the source brightness distribution. The Fourier phase ϕ of the complex visibility is given by

$$-\phi = \arg(\mathbb{V}) = \tan^{-1}\left(\frac{\Im(\mathbb{V})}{\Re(\mathbb{V})}\right). \tag{2.17}$$

However, when extracting this quantity from an interferogram which was obtained with a ground-based interferometer, the phase signal will be completely corrupted by the piston introduced by the turbulent atmosphere. This atmospheric phase screen can be described by the ζ's in equation 2.2 and following. One possibility for overcoming this phase corruption is currently being investigated using the technique of phase referencing, such as with the PRIMA fringe tracker (Delplancke et al. 2003) for the VLTI.

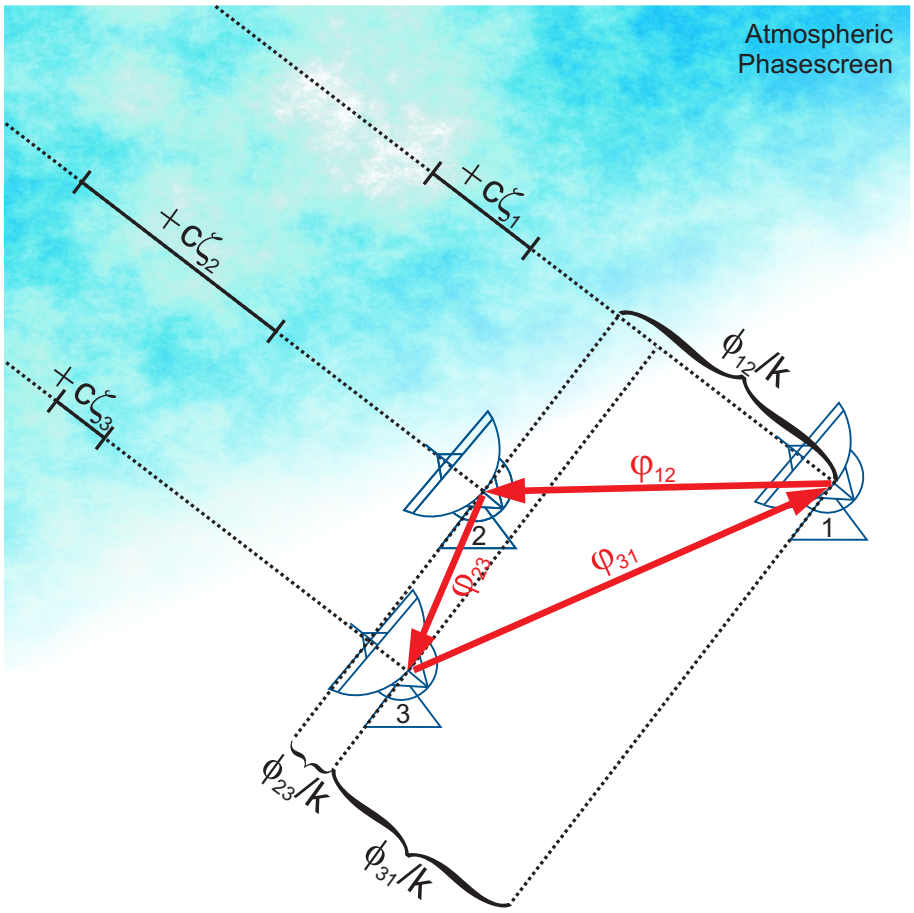

Figure 2.1: Definition of the vector directions in the CP triangle.

However, in 1958 Jennison noted that some of the phase information can also be retrieved with non-phase-referenced interferometers. The underlying idea is illustrated in Figure 2.1 and makes use of the fact that for observations with three or more apertures, the atmospheric disturbance terms ζ cancel out when adding the phase terms in a closed triangle telescope configuration. If we consider the case for $N = 3$ and denote the telescopes with 1, 2, and 3, then we obtain the following interferogram phases:

$$\varphi_{12} := -\arg(I_{12}^{\mathrm{AC}}) = \phi_{12} - ck(\zeta_1 - \zeta_2 + \tau_1 - \tau_2) \tag{2.18}$$

$$\varphi_{23} := -\arg(I_{23}^{\mathrm{AC}}) = \phi_{23} - ck(\zeta_2 - \zeta_3 + \tau_2 - \tau_3) \tag{2.19}$$

$$\varphi_{31} := -\arg(I_{31}^{\mathrm{AC}}) = \phi_{31} - ck(\zeta_3 - \zeta_1 + \tau_3 - \tau_1), \tag{2.20}$$

where $\phi_{ij} := \phi_i - \phi_j$.

Adding these φ_{ij} yields the remarkable result that the phase Φ (also known as *Closure Phase*) is invariant to the atmospheric phase perturbation terms:

$$\Phi = \varphi_{12} + \varphi_{23} + \varphi_{31} \tag{2.21}$$
$$= \phi_{12} + \phi_{23} + \phi_{31}. \tag{2.22}$$

Due to this property, closure phases (CPs) are also self-calibrating; i.e., no calibrator measurements are needed to monitor changes in the atmospheric conditions (as required for V^2 measurements). For an array of N telescopes ($N > 2$), in total $(N-1)(N-2)/2$ CPs may be defined (Readhead et al. 1988). For $N > 3$, some *Amplitude Closure Relations* can additionally be obtained (Rogers et al. 1974).

As was pointed out later, the CP is mathematically equivalent to the phase of the *bispectrum* (Lohmann et al. 1983). If we denote with $\tilde{\mathbb{I}}$ the Fourier transform of $\mathbb{I}$, the bispectrum $\mathbb{B}$ can be defined as

$$\mathbb{B} := \langle \tilde{\mathbb{I}}_{12}^{\mathrm{AC}} \tilde{\mathbb{I}}_{23}^{\mathrm{AC}} \tilde{\mathbb{I}}_{13}^{\mathrm{AC}*} \rangle \tag{2.23}$$
$$= \left|\tilde{\mathbb{I}}_{12}^{\mathrm{AC}}\right| \left|\tilde{\mathbb{I}}_{23}^{\mathrm{AC}}\right| \left|\tilde{\mathbb{I}}_{13}^{\mathrm{AC}*}\right| \cdot \tag{2.24}$$
$$\cdot e^{-\imath[\phi_{12}+ck(\tau_1+\zeta_1)-ck(\tau_2+\zeta_2)]} \cdot e^{-\imath[\phi_{23}+ck(\tau_2+\zeta_2)-ck(\tau_3+\zeta_3)]} \cdot e^{\imath[\phi_{13}+ck(\tau_1+\zeta_1)-ck(\tau_3+\zeta_3)]}$$
$$= \left|\tilde{\mathbb{I}}_{12}^{\mathrm{AC}}\right| \left|\tilde{\mathbb{I}}_{23}^{\mathrm{AC}}\right| \left|\tilde{\mathbb{I}}_{13}^{\mathrm{AC}*}\right| \cdot e^{-\imath[\phi_{12}+ck(\tau_1+\zeta_1)-ck(\tau_2+\zeta_2)+\phi_{23}+ck(\tau_2+\zeta_2)-ck(\tau_3+\zeta_3)-\phi_{13}-(ck\tau_1+\zeta_1)+(ck\tau_3+\zeta_3)]}$$
$$= \left|\tilde{\mathbb{I}}_{12}^{\mathrm{AC}}\right| \left|\tilde{\mathbb{I}}_{23}^{\mathrm{AC}}\right| \left|\tilde{\mathbb{I}}_{13}^{\mathrm{AC}*}\right| \cdot e^{-\imath[\phi_{12}+\phi_{23}-\phi_{13}]}. \tag{2.25}$$

Thus, we find that the argument of $\mathbb{B}$ is identical to the CP, as defined in equation 2.22:

$$\arg(\mathbb{B}) = \phi_{12} + \phi_{23} + \phi_{31} \tag{2.26}$$
$$\equiv \Phi. \tag{2.27}$$

2.2.3 Differential observables

From spectrally dispersed interferograms, differential observables can be extracted in addition to the before-mentioned absolute observables. In analogy to the V^2 estimator, the *differential visibility* measures the relative change of the visibility in adjacent spectral channels. Perhaps even more powerful is the *differential phase*, which resembles the wavelength-dependence of the individual Fourier phases. Similar to the CP, differential observables are self-calibrating; i.e., they do not require a calibrator measurement to compensate for atmospheric effects.

2.3 Array Geometry and Optical Path Delays

The waves from the individual telescopes must experience the same time delay before they can be recombined. Therefore, it is important to identify the effects which delay the wavefronts with respect to each other. Once identified, these delays can be compensated by using delay lines, allowing us to observe the fringe pattern at zero optical path delay (OPD).

One cause of delay might be due to path differences in the optical trains (*internal delays*). Another important contributor is the *geometric path delay* τ_{geom}, which results from the geometric arrangement of the apertures (see Fig. 2.2). As this geometric delay changes constantly while the observed star moves across the sky, it has to be compensated with high frequency during the observation. τ_{geom} can be computed from the relative ground coordinates of the telescope stations. When observing a star towards direction $\vec{r}$ ($\vec{B}$ is the baseline vector), then τ_{geom} for this particular baseline is given by $\sin(\vec{B}\vec{r})/c$. The *projected baseline* B_p, which also defines the effective resolution of the observation, is given by

$$B_p = \cos(\vec{B}\vec{r}) = |\vec{B}| \cos z, \tag{2.28}$$

where z denotes the zenith angle of the observations.

2.4 Fringe Signal Coding

Long-baseline interferometers collect the same wave with different apertures and then recombine it in a *beam combiner*. In order to ensure that the sampled light combines coherently, two distinct strategies can be used (Malbet et al. 1999; Schöller et al. 2000). While the *coaxial* combination scheme superposes the wave at the same position on the detector, but modulates the time when the waves arrive there (yielding *temporal self-coherence*), the *multiaxial* combination scheme records the interferogram at one time, but spread in space (*spatial self-coherence*).

2.4.1 Coaxial beam combination

In the coaxial combination scheme, the beams are first aligned and then combined in the pupil plane. The signals from the beam combiners are then focused at a detector, which might consist of a single pixel, although it is advantageous to record the two phase-shifted output signals from the beam splitter, which requires two pixels per beam combiner.

To scan the fringe signal, the delay between the beams has to be temporally modulated. This is done by modifying the OPD τ systematically by introducing an additional delay of known amplitude. Technically, this can be realized, for instance, using Piezo scanners, which introduce a sawtooth-shaped delay on $N-1$ of the N baselines (at one baseline the delay may stay fixed).

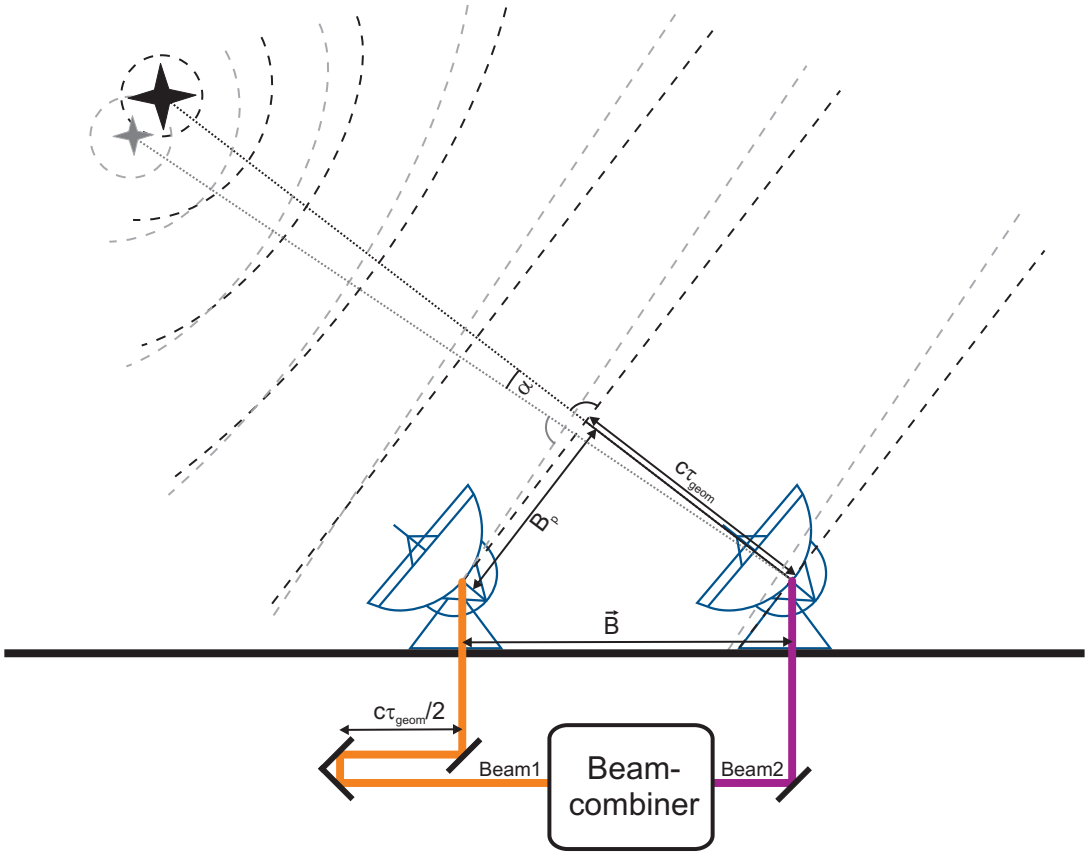

Figure 2.2: Basic components of a Michelson stellar interferometer. The wavefront requires different light travel times to reach the telescopes, introducing the geometric delay τ_{geom}, which depends on the position of the star on the sky.

This concept is similar to the one applied in the Michelson-Morley interferometer. For stellar interferometers, coaxial beam combination is used at the IOTA, VLTI/VINCI, VLTI/MIDI, and some other interferometers.

2.4.2 Multiaxial beam combination

In multiaxial beam combination, the fringe signal can be recorded at one time (in one exposure), but is spread in the image plane over many pixels on the detector plane. The spatial fringe coding is achieved by placing the exit pupils at certain distances to each other and then to superpose the beams using, for instance, a lens, introducing geometric path differences. For $N > 2$ telescopes, confusion between the formed fringes can be avoided by placing the corresponding exit pupils at varying distances to each other. This results in different frequencies in the carrying waves, which allows one to separate the

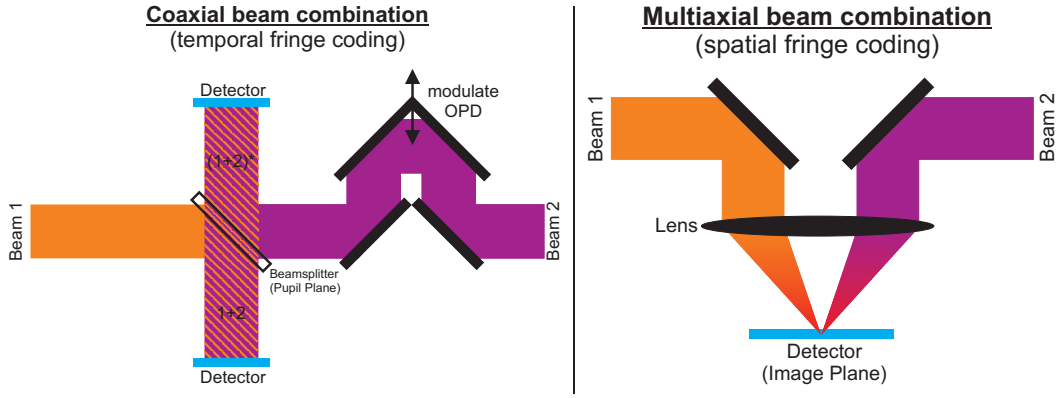

Figure 2.3: Basic principles used in the current generation of optical interferometric beam combiners: *Left:* Coaxial beam combination. *Right:* Multiaxial beam combination.

interferograms from the different baselines during data reduction.

An intuitive example for multiaxial beam combination is Young's double slit experiment or Michelson's 20-foot steller interferometer. Nowadays, this method is realized at GI2T or VLTI/AMBER.

2.5 The van-Cittert-Zernike Theorem

The van-Cittert-Zernike theorem (Thompson et al. 1986) relates the complex visibility (as defined in equation 2.13) with the source brightness distribution $I(x,y)$ and provides, therefore, the basic theory for any modeling of interferometric data. The coordinates x and y shall be measured parallel to the right ascension (RA) and declination axis (DEC), respectively. Then, the van-Cittert-Zernike theorem relates $\mathbb{V}$ with the Fourier transform of the irradiance distribution $\tilde{I}(x,y)$, i.e.

$$\mathbb{V}(u,v) = \tilde{I}(x,y) = \int_{-\infty}^{\infty}\int_{-\infty}^{\infty} I(x,y)e^{-\imath k(ux+vy)}\,dxdy. \tag{2.29}$$

The new coordinates u and v are measured in frequency space (e.g. in cycles per mas) and give the East and North component of the sky projected ground baseline vector $\vec{B}$. For a point source (unresolved) $V = 1$, whereas for uniformly bright background emission filling the whole FOV (overresolved source) $V = 0$.

2.5.1 Basic analytic visibility profiles

Based on the van-Cittert-Zernike Theorem, it is straight-forward to compute the visibility profile for arbitrary brightness distributions. Since for some of our studies the brightness distribution of the studied objects is rather complicated (e.g. on MWC 147, η Car) or follows an exotic center-to-limb variation

(CLV), these cases require a direct application of equation 2.29. However, it can be useful to find analytic descriptions for the visibility profiles of simple geometries like binary stars (applied for θ^1Ori C), uniformly bright disks, or Gaussian CLVs (for η Car). As the derivation of these analytic descriptions is rather straightforward and already demonstrated in literature (e.g. Millan-Gabet et al. 2001; Kraus 2003), we give the descriptions for the following, commonly used brightness profiles without derivation:

Uniform Disk (UD): The visibility function for a disk with diameter Θ and of uniform brightness I, depends on the projected baseline as

$$V_{\mathrm{UD}}(\Theta) = 2\frac{J_1(k\Theta B_p)}{k\Theta B_p}, \tag{2.30}$$

where J_1 denotes the Bessel function of first kind and first order.

Gaussian Brightness Distribution: If we consider a Gaussian brightness distribution of full width half maximum (FWHM) diameter Θ, the visibility profile is given by

$$V_{\mathrm{Gauss}}(\Theta) = \exp\left[-\frac{(k\Theta B_p)^2}{4\ln 2}\right]. \tag{2.31}$$

Binary source: Let us consider a brightness distribution which contains two components, each having an arbitrary intensity (I_1 and I_2) and visibility profile ($\mathbb{V}_1$ and $\mathbb{V}_2$). Then the complex visibility depends on the component separation vector $\vec{s}$ as

$$\mathbb{V}_{\mathrm{Binary}}(\vec{s}) = \frac{I_1\mathbb{V}_1 + I_2\mathbb{V}_2 e^{-ik\vec{B}\vec{s}}}{I_1 + I_2}. \tag{2.32}$$

3 The IOTA/IONIC3 Interferometer

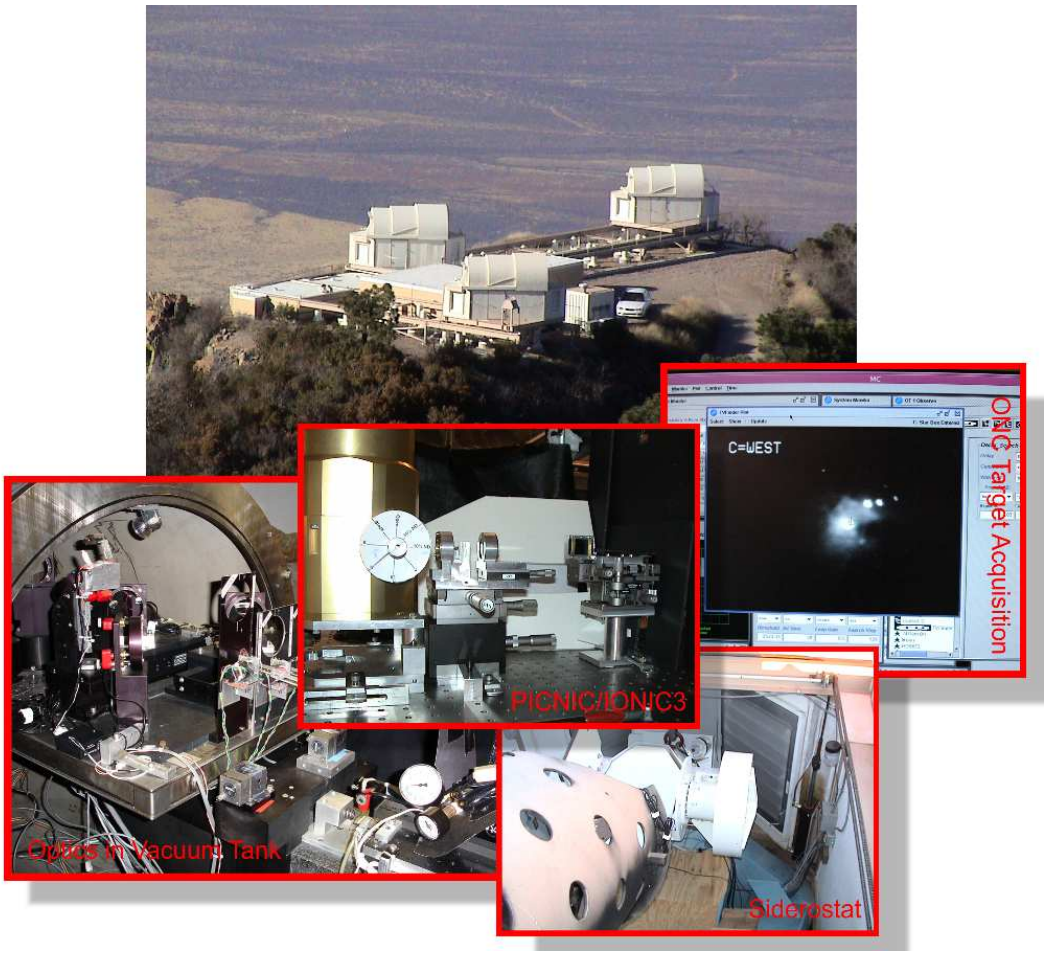

Figure 3.1: The IOTA with the IONIC3 instrument.

3.1 Overview and Context

The *Infrared Optical Telescope Array* (IOTA) was used for observations for one of my PhD projects; namely, on θ^1Ori C and D (Sect. 8). Due to the low brightness, the data reduction process for these sources was rather challenging and could not be performed with the data reduction algorithms which I had implemented earlier in the context of my Master thesis work on IOTA (Kraus 2003). Therefore, it was necessary to implement new algorithms, which are very briefly described and illustrated in this chapter.

3.2 Instrument Design and Signal Coding

The IOTA is a three telescope interferometer located at the Fred Whipple Observatory atop Mount Hopkins, Arizona. It was jointly constructed by the Smithsonian Astrophysical Observatory, Harvard University, the University of Massachusetts, the University of Wyoming, and the MIT/Lincoln Laboratory (Traub et al. 2003). IOTAs telescopes can be moved on an L-shaped track and are mounted on stations 5 and 7 m apart. With track lengths of 15 m (southeast direction) and 35 m (northeast direction), baselines up to 38 m can be formed. The collecting optics consist of f/2.5 45 cm Cassegrain primary mirrors, which are fed by siderostats. The atmospherically induced motion of the image is compensated by tip-tilt servo systems mounted behind the telescopes.

Passing various mirrors and path-compensating delay lines, the beams are deflected into the laboratory, where the infrared component of the beam is coupled into fibers. The fibers feed the spatially filtered signal into the IONIC3 integrated optics beam combiner (Berger et al. 2003), which combines the beams coaxially (see Sect. 2.4.1) and pairwise with a ratio of 50:50. For each baseline, the beam combination produces two complementary outputs, which are shifted in phase by π with respect to each other, and which are recorded on a PICNIC camera (Pedretti et al. 2004). Although the information recorded by these two channels is in principle redundant, it can be used to remove residual photometric fluctuations simply by subtracting the signals from the two channels.

Piezo scanners installed at two of the telescopes modulate the OPD to temporally scan the interference fringe pattern (for the AB and AC baseline the OPD stroke is 50 μm, resulting in a stroke of 100 μm for the BC baseline). Thus, for each τ we record six signals I_j ($1 \leqslant j \leqslant 6$). In the following, we denote the output of the beam combiner which combines telescopes A and B with I_1, I_2, the beam combiner output from A and C with I_3, I_4, and the one from B and C with I_5, I_6.

Because we observed with IOTA using an H-broadband filter, the assumption of a monochromatic wave, which was used in the derivation of the interferometric equation in Sect. 2.1, cannot be used to describe IOTA interferograms. Therefore, we integrate the interferometric equation over the spectral window of an rectangular-shaped filter (central wavelength λ_c and bandwidth $\Delta\lambda$) and yield that the

cosine fringe signal (see equation 2.15) is convolved with the function $\mathrm{sinc}[\pi\Delta\lambda(t+\tau_i-\tau_j+\zeta_i-\zeta_j)-(\phi_i-\phi_j)]$ (with $\mathrm{sinc}(x)=\sin(x)/x$; for a derivation see Kraus 2003). The width of this envelope function is inversely proportional to $\Delta\lambda$, and it is symmetrically centered around the so-called *white light fringe*. In Figure 3.3 we show a typical H-band IOTA interferogram.

Following each object observation (during which several datasets were recorded, typically consisting of 200 scans), four calibration files were acquired. One of these files measures the camera background signal with the light from all telescopes shuttered out (this is required for subtraction of the thermal background). For the other three files, the light of two telescopes is shuttered out alternately. This allows us to determine the coefficients of the transfer matrix (κ matrix, Coude Du Foresto et al. 1997). The κ matrix quantifies the light contributions of a certain telescope to both beam combiner outputs of the three baselines (j=1...6):

$$I_j = \kappa_{jA}F_A + \kappa_{jB}F_B + \kappa_{jC}F_C \tag{3.1}$$

3.3 Constructing the interferograms

To achieve a high accuracy in the visibility, the recorded interferograms must be corrected for photometric fluctuations (Coude Du Foresto et al. 1997), which requires to record the photometry simultaneously to the interferometric signal. Two-telescope beam combiners (like FLUOR, VINCI, or MIDI in SCI-PHOT mode) or multiaxial beam combiners (like AMBER) obtain this photometric information by separating a certain fraction of the light before the beam combination and recording the photometry in separate channels.

However, if three or more telescopes are combined pairwise, the photometric information can also be extracted from the interferometric signal without additional channels. An important advantage of this procedure is the reduced complexity of the optical design and the increased flux in the interferometric channels. To my knowledge, this procedure was first suggested by Ned Carleton for IOTA-3T. I thank John Monnier for discussion on this topic, who applied a similar procedure also to asymmetric beam combiners (Monnier 2001).

With all shutters open, we obtain the interferometric signals

$$I_1 = \kappa_{1A}F_A + \kappa_{1B}F_B + \kappa_{1C}F_C + 2\gamma^+_{AB}\sqrt{\kappa_{1A}\kappa_{1B}F_AF_B} \tag{3.2}$$
$$I_2 = \kappa_{2A}F_A + \kappa_{2B}F_B + \kappa_{2C}F_C + 2\gamma^-_{AB}\sqrt{\kappa_{2A}\kappa_{2B}F_AF_B} \tag{3.3}$$
$$I_3 = \kappa_{3A}F_A + \kappa_{3B}F_B + \kappa_{3C}F_C + 2\gamma^+_{AC}\sqrt{\kappa_{3A}\kappa_{3C}F_AF_C} \tag{3.4}$$
$$I_4 = \kappa_{4A}F_A + \kappa_{4B}F_B + \kappa_{4C}F_C + 2\gamma^-_{AC}\sqrt{\kappa_{4A}\kappa_{4C}F_AF_C} \tag{3.5}$$
$$I_5 = \kappa_{5A}F_A + \kappa_{5B}F_B + \kappa_{5C}F_C + 2\gamma^+_{BC}\sqrt{\kappa_{5B}\kappa_{5C}F_BF_C} \tag{3.6}$$

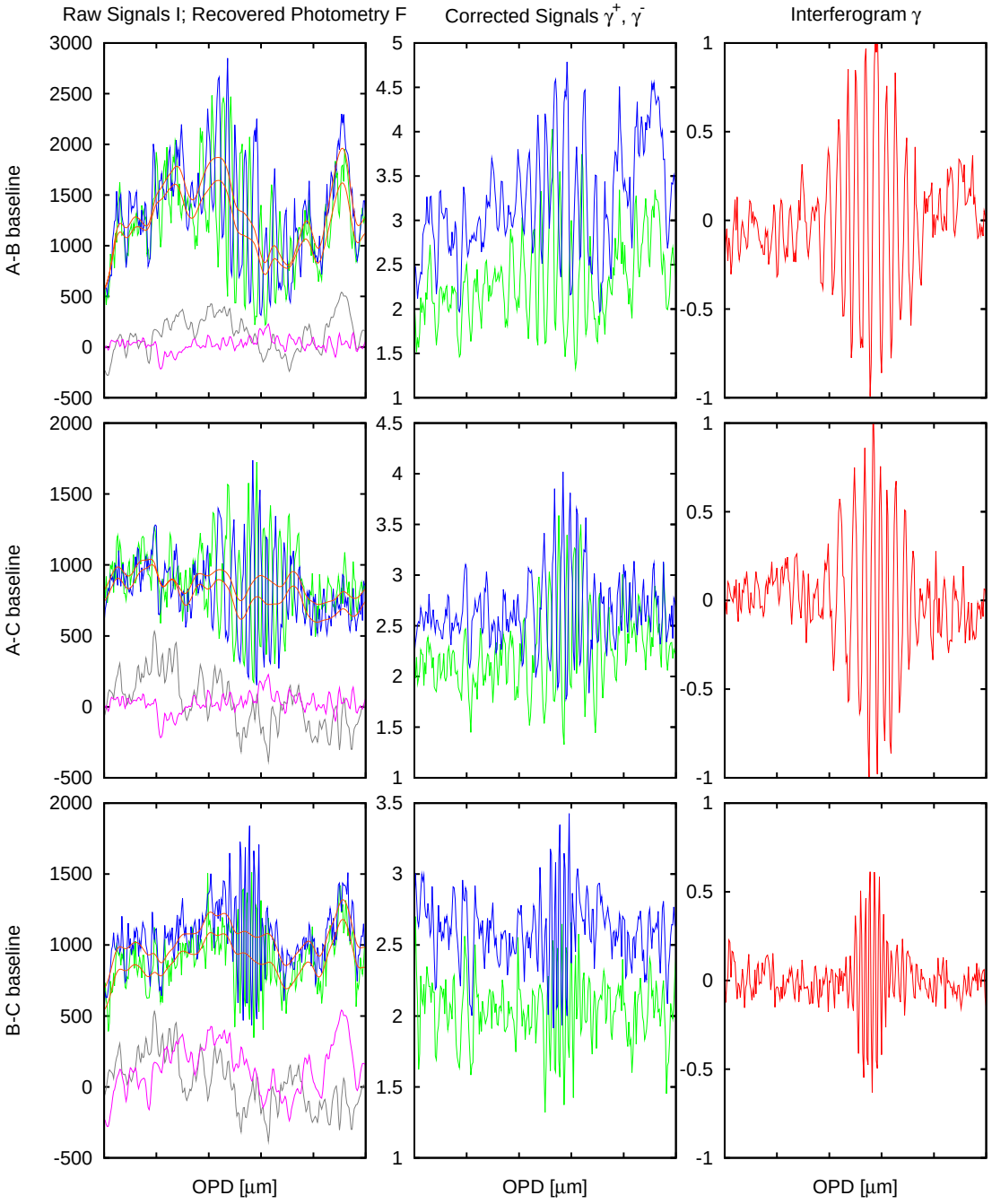

Figure 3.2: Illustration of the signal processing applied to IOTA interferograms: From the intensities recorded on the IOTA/PICNIC detector (green and blue curve in left-handed column), the photometric information is retrieved using equation 3.11 (magenta and grey curve, shown with arbitrary offset). The photometry-correct curves (equations 3.13 to 3.17) are shown in the column in the middle. The final interferograms (right-handed column) are obtained using equations 3.18 to 3.20. The data shown was recorded on the calibrator star HD34137 (H=4.4, for more details see caption of Figure 3.3).

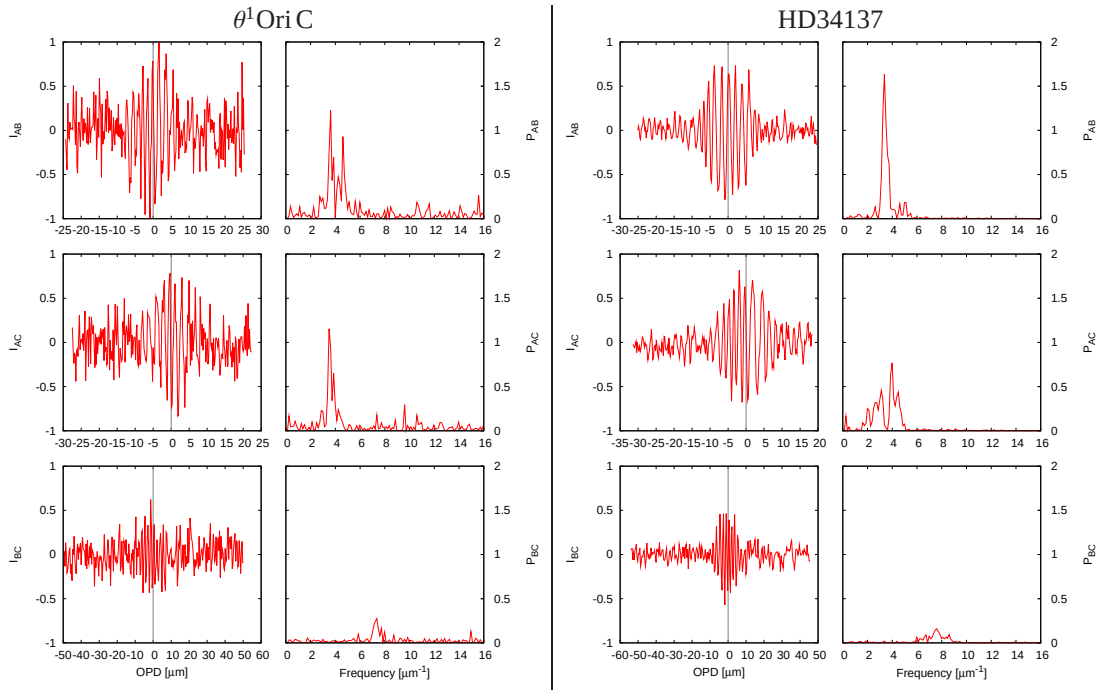

Figure 3.3: IOTA fringes on the science target θ^1Ori C (H=4.4) and the calibrator star HD34137 (H=4.4), both recorded on 2005-12-06 (datasets #72 and #140).

$$I_6 \quad = \quad \kappa_{6A}F_A + \kappa_{6B}F_B + \kappa_{6C}F_C + 2\gamma^-_{BC}\sqrt{\kappa_{6B}\kappa_{6C}F_BF_C} \tag{3.7}$$

where $\gamma^+_x(\tau)$ and $\gamma^-_x(\tau)$ are the interference patterns of interest (compare with equation 2.15).

For a perfect detector, the κ's corresponding to the telescopes which do not contribute light to a certain output (e.g. κ_{1C} for I_1 in equation 3.2) are identical to zero. However, infrared detectors (as HAWAII or NICMOS) are known to exhibit detector biases; i.e., they have the property that the pixels on the detector are not completely independent. Let us consider the case that the signals on two pixels X and Y (located in different corners on the detector) are read, with pixel X shuttered out, simply recording the detector background. Illuminating pixel Y will result in a bias on the background signal measured on X (the more flux on pixel Y, the stronger the negative bias on pixel X). Assuming that the bias on X depends linearly on the flux on Y, this bias can be taken into account in a natural way with the presented method. The κ's corresponding to these bias terms have the opposite sign than the κ's for the contributing telescopes.

With some arithmetics, the coherence terms (γ_x) can be cancelled out by adding the outputs from each beam-combiner pair-wise:

$$\begin{pmatrix} I_1/\sqrt{\kappa_{1A}\kappa_{1B}} + I_2/\sqrt{\kappa_{2A}\kappa_{2B}} \\ I_3/\sqrt{\kappa_{3A}\kappa_{3C}} + I_4/\sqrt{\kappa_{4A}\kappa_{4C}} \\ I_5/\sqrt{\kappa_{5B}\kappa_{5C}} + I_6/\sqrt{\kappa_{6B}\kappa_{6C}} \end{pmatrix} = \mathbf{M} \cdot \begin{pmatrix} F_A \\ F_B \\ F_C \end{pmatrix} \tag{3.8}$$

$$\mathbf{I} = \mathbf{M} \cdot \mathbf{F} \tag{3.9}$$

with

$$\mathbf{M} = \begin{pmatrix} \sqrt{\frac{\kappa_{1A}}{\kappa_{1B}}} + \sqrt{\frac{\kappa_{2A}}{\kappa_{2B}}} & \sqrt{\frac{\kappa_{1B}}{\kappa_{1A}}} + \sqrt{\frac{\kappa_{2B}}{\kappa_{2A}}} & \frac{\kappa_{1C}}{\sqrt{\kappa_{1A}\kappa_{1B}}} + \frac{\kappa_{2C}}{\sqrt{\kappa_{2A}\kappa_{2B}}} \\ \sqrt{\frac{\kappa_{3A}}{\kappa_{3C}}} + \sqrt{\frac{\kappa_{4A}}{\kappa_{4C}}} & \frac{\kappa_{3B}}{\sqrt{\kappa_{3A}\kappa_{3C}}} + \frac{\kappa_{4B}}{\sqrt{\kappa_{4A}\kappa_{4C}}} & \sqrt{\frac{\kappa_{3C}}{\kappa_{3A}}} + \sqrt{\frac{\kappa_{4C}}{\kappa_{4A}}} \\ \frac{\kappa_{5A}}{\sqrt{\kappa_{5B}\kappa_{5C}}} + \frac{\kappa_{6A}}{\sqrt{\kappa_{6B}\kappa_{6C}}} & \sqrt{\frac{\kappa_{5B}}{\kappa_{5C}}} + \sqrt{\frac{\kappa_{6B}}{\kappa_{6C}}} & \sqrt{\frac{\kappa_{5C}}{\kappa_{5B}}} + \sqrt{\frac{\kappa_{6C}}{\kappa_{6B}}} \end{pmatrix}. \tag{3.10}$$

The diagonal terms in $\mathbf{M}$ (upper right to lower left) correspond to the detector bias terms; i.e., for a perfect detector, these terms are identical zero. The photometry can be obtained by performing a matrix inversion:

$$\mathbf{F} = \mathbf{M}^{-1} \cdot \mathbf{I} \begin{pmatrix} F_A \\ F_B \\ F_C \end{pmatrix} = \mathbf{M}^{-1} \cdot \begin{pmatrix} I_1/\sqrt{\kappa_{1A}\kappa_{1B}} + I_2/\sqrt{\kappa_{2A}\kappa_{2B}} \\ I_3/\sqrt{\kappa_{3A}\kappa_{3C}} + I_4/\sqrt{\kappa_{4A}\kappa_{4C}} \\ I_5/\sqrt{\kappa_{5B}\kappa_{5C}} + I_6/\sqrt{\kappa_{6B}\kappa_{6C}} \end{pmatrix} \tag{3.11}$$

Using the obtained photometric information, the interferograms can be corrected for photometric fluctuations:

$$\gamma^+_{AB} = \frac{I_1 - \kappa_{1A}F_A - \kappa_{1B}F_B - \kappa_{1B}F_C}{2\sqrt{\kappa_{1A}\kappa_{1B}F_AF_B}} \tag{3.12}$$

$$\gamma^-_{AB} = \frac{I_2 - \kappa_{2A}F_A - \kappa_{2B}F_B - \kappa_{2B}F_C}{2\sqrt{\kappa_{2A}\kappa_{2B}F_AF_B}} \tag{3.13}$$

$$\gamma^+_{AC} = \frac{I_3 - \kappa_{3A}F_A - \kappa_{3B}F_B - \kappa_{3C}F_C}{2\sqrt{\kappa_{3A}\kappa_{3C}F_AF_C}} \tag{3.14}$$

$$\gamma^-_{AC} = \frac{I_4 - \kappa_{4A}F_A - \kappa_{4B}F_B - \kappa_{4C}F_C}{2\sqrt{\kappa_{4A}\kappa_{4C}F_AF_C}} \tag{3.15}$$

$$\gamma^+_{BC} = \frac{I_5 - \kappa_{5A}F_A - \kappa_{5B}F_B - \kappa_{5C}F_C}{2\sqrt{\kappa_{5B}\kappa_{5C}F_BF_C}} \tag{3.16}$$

$$\gamma^-_{BC} = \frac{I_6 - \kappa_{6A}F_A - \kappa_{6B}F_B - \kappa_{6C}F_C}{2\sqrt{\kappa_{6B}\kappa_{6C}F_BF_C}} \tag{3.17}$$

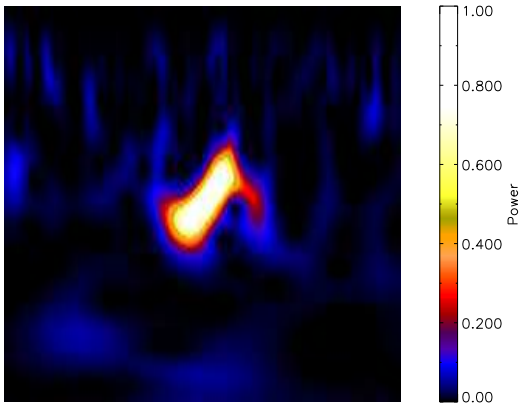

Figure 3.4: The wavelet spectral density power spectra shown in the bottom panels are calculated from the corresponding raw interferograms. On the ordinate of the CWT plots, the scale quantity is given, which is equivalent to the period and inversely proportional to the frequency of the corresponding rescaled wavelet. The contours demonstrate how our departitioning algorithm removes regions not connected to the area with the highest peak and separates the fringe peak from the piston and resonances for the visibility estimation.

Remaining photometric fluctuations can be removed by subtracting the two channels, yielding the final interferograms for the three baselines:

$$\gamma_{AB} = \frac{\gamma^+_{AB} - \gamma^-_{AB}}{2} \tag{3.18}$$

$$\gamma_{AC} = \frac{\gamma^+_{AC} - \gamma^-_{AC}}{2} \tag{3.19}$$

$$\gamma_{BC} = \frac{\gamma^+_{BC} - \gamma^-_{BC}}{2}. \tag{3.20}$$

3.3.1 Extracting the visibility using the Continous Wavelet Transform

The methods which have been proposed to extract the visibility from OPD-modulated interferograms, such as those recorded by IOTA, can be mainly subdivided into those which measure the fringe amplitude in the time-domain (i.e. by fitting an analytic function to $\gamma(\tau)$) or in the frequency domain (i.e. by measuring the fringe power in the power spectrum $\mathcal{P} = |\tilde{\gamma}(\tau)|^2$). An important advantage of the frequency-domain approach is that the power-spectra of an arbitrary number of interferograms can be averaged, even if the fringe packet moves due to the influence of atmospheric piston. In the averaged power-spectrum, the fringe power can be easily obtained by integrating the power over the fringe peak to estimate the fringe amplitude (squared visibility, V^2).

Recently, another approach to obtain the visibility was identified, making use of the continuous wavelet transform (Ségransan et al. 2003; Kraus 2003; Kervella et al. 2004c; Kraus et al. 2005b). In contrast to the Fourier Transform (FT, which measures the signal against periodic, non-localized cosine waves), the CWT decomposes the signal into a localized *mother wavelet* function $\psi(\tau)$ (Torrence & Compo 1998). For the decomposition, a mother wavelet is used which roughly resembles the analytic fringe function, such as the Morlet wavelet (which is given by a cosine wave modulated with a Gaussian

envelope, k_0 is the wavenumber)

$$\psi(\eta) = \pi^{-1/4} e^{ik_0\eta - \eta^2/2}. \tag{3.21}$$

Then the CWT $\mathbb{W}(\tau, s)$ and the wavelet spectral density power spectrum $\mathcal{P}_W(\tau, s)$ are defined as

$$\mathbb{W}(\tau, s) := \frac{1}{\sqrt{s}} \int_{-\infty}^{\infty} I_{\rm red}(t) \psi^* \left(\frac{\tau - t}{s} \right) dt \tag{3.22}$$

$$\mathcal{P}_W(\tau, s) := |\mathbb{W}(\tau, s)|^2, \tag{3.23}$$

where the *scale* s is equivalent to the period and inversely proportional to the frequency of the corresponding rescaled mother wavelet. For the computation of the CWT, we used the algorithm described by Torrence & Compo[1].

In contrast to the power spectrum fitting approach, the CWT has the advantage that the information about the position of the fringe in the OPD is conserved, which can be used to effectively separate the fringe from underlying non-localized signals (e.g. noise). In our original implementation of the CWT algorithm (Kraus 2003; Kraus et al. 2005b), we used the integral over the fringe peak in $\mathcal{P}_W(\tau, s)$ as visibility estimator, which was very efficient in removing contributions from disturbing resonances in the IOTA interferograms of very bright objects such as Capella (H=-1.6). However, when we started working on interferograms for the significantly fainter objects θ^1Ori C and D (H=4.6 and H=5.9), we found this original algorithm unsuitable, as the fringe signal in the CWT of an individual interferogram is too noisy.

Therefore, we had to implement a modified CWT algorithm, which combines the advantages of the CWT with the major advantages of the power spectrum fitting algorithm; namely that the fringe signal can be constructively built up by averaging. We apply a method similar to the procedure presented by Kervella et al. (2004c). First, the fringe peak is localized in the CWT. In order to minimize noise contributions, a small window around the fringe peak position is cut out. Then, we integrate along the OPD axis, yielding a power spectrum. After recentering the fringe peak position for each scan (to compensate frequency changes induced by atmospheric piston), we average the power spectra for all scans within a dataset. In the resulting averaged power spectrum, we fit and remove the background contributions and integrate over the fringe power to obtain an estimate for V^2.

In order to use only high-quality interferograms for the visibility computation, we apply the following selection criteria:

- We reject the leading ten scans from each dataset, as these scans are degenerated by electronic noise.

[1] The algorithm by Torrence & Compo allows to compute the wavelet transform efficiently using Fast Fourier Transforms (FFTs), as described on the website http://atoc.colorado.edu/research/wavelets/wavelet3.html

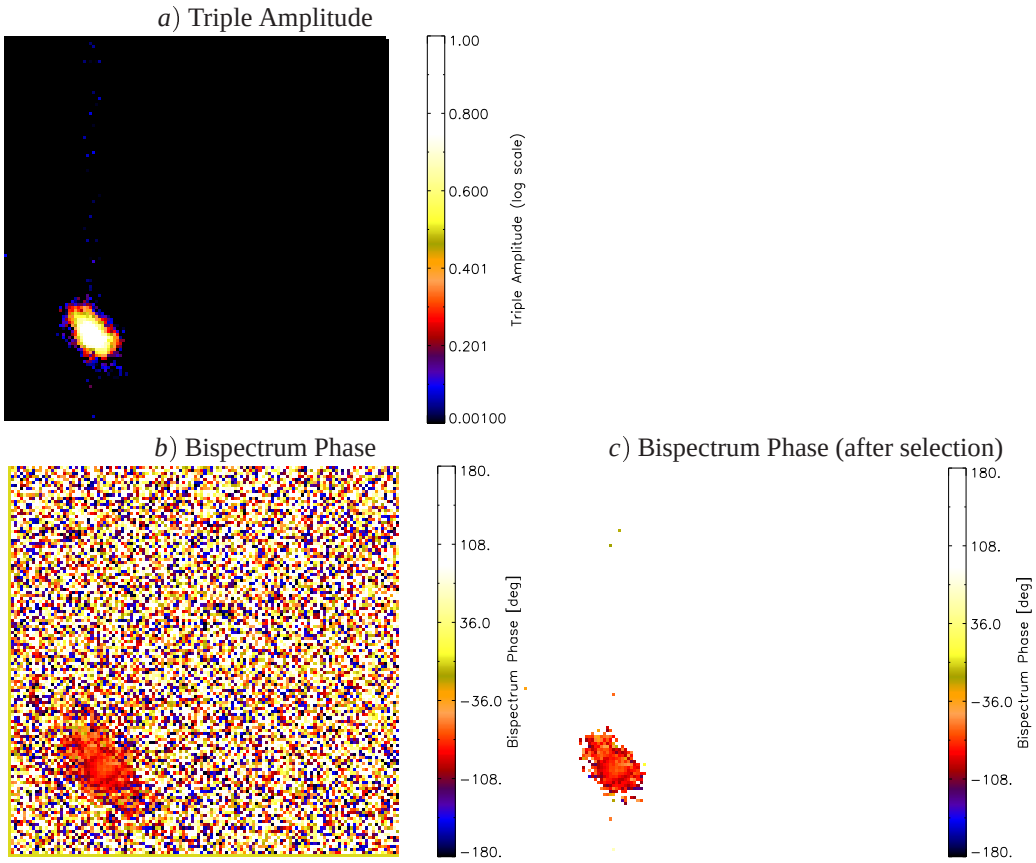

Figure 3.5: Illustration of the bispectrum algorithm used to extract CPs from the IOTA scans. The plot shows the averaged bispectrum for the HD34137 calibrator datasets mentioned in Figure 3.3. For a description of the algorithm, we refer to the text.

- We reject scans which seem not to contain any fringe signal. For the signal detection we use the AMES fringe tracker software.
- We reject scans which are strongly affected by atmospheric piston. These scans are identified by measuring the extension of the fringe packet in the CWT of each scan both along the scale and the OPD axis.

3.3.2 Extracting the closure phase

Another refinement in our software concerns the CP estimation. In contrast to our earlier approach, where we used the FT to determine the phase for each interferogram separately (Kraus 2003; Kraus et al. 2005b), we found that for low-SNR data the best results can be obtained by averaging the bispectra

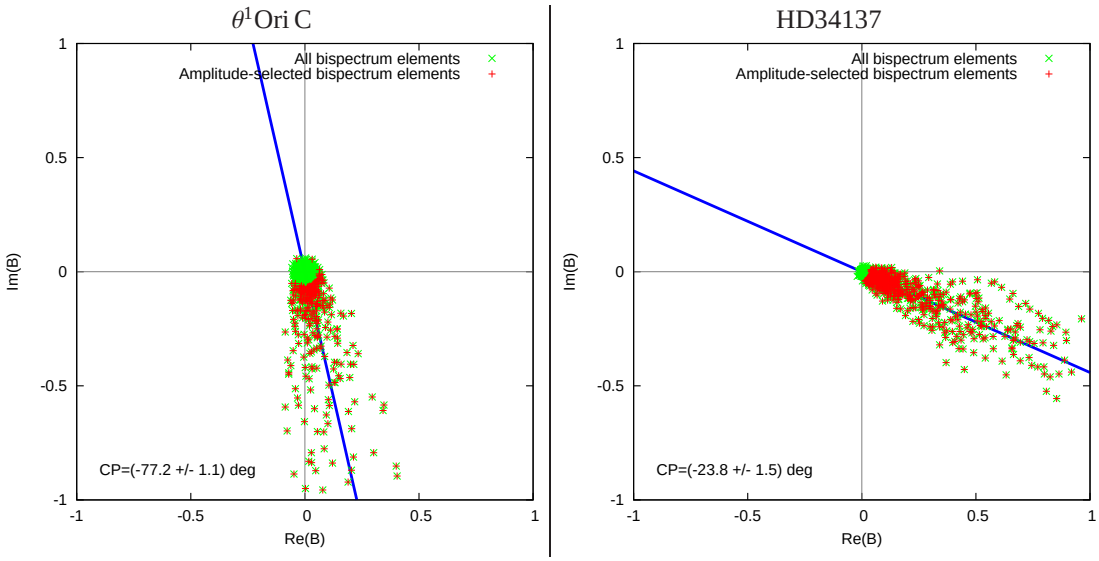

Figure 3.6: After applying the selection process illustrated in Figure 3.5, we average the phases of individual bispectrum elements in the complex plane, yielding the final averaged CP (same datasets as in Figure 3.3).

from all scans. The bispectrum (equation 2.24) is given by the triple product of the FT of the scans at the three baselines (Hofmann & Weigelt 1993). Figure 3.5 shows the average triple amplitude and bispectrum phase of a representative IOTA dataset comprised of 200 scans. Using the triple amplitude (Figure 3.5*a*), we identify the bispectrum elements with the highest SNR, for which we select the best bispectrum phase measurements (*b* before selection, *c* after selection). Finally, the bispectrum phases of the triple-amplitude selected bispectrum elements are averaged in the complex plane to obtain the average CP.

4 The VLTI/AMBER Interferometer

Figure 4.1: Mosaic of the VLT/VLTI infrastructure (4 UTs, to the right) with the AMBER instrument, which is located in the optical laboratory. In the upper left corner, one of reflectors of the VLTI delay lines is shown (Image Credits: ESO & AMBER consortium).

4.1 Optical Design and Signal Coding

4.1.1 The VLT interferometer and its infrastructure

AMBER (Astronomical Multi-BEam combineR, see Figure 4.1, Petrov et al. 2003a, 2006a,b) is the first-generation near-infrared (*J*-, *H*-, *K*-band) beam-combiner instrument of the *Very Large Telescope Interferometer*. The VLTI array (see Figure 4.2) comprises four 8.2 m unit telescopes (UTs, arranged in a half-moon shaped configuration including baseline lengths from 47 to 130 m) and four 1.8 m auxiliary telescopes (ATs, which can be mounted on 30 differents stations, forming baselines between 8 and 202 m).

The UTs are equipped with MACAO adaptive optics systems (Ivanescu et al. 2004), which optimize the Strehl ratio. Each beam is redirected into a VLTI delay line, where the OPD difference between the telescopes is compensated (providing an accuracy of 0.05 μm over a length of 120 m). Finally, the beams enter the optical laboratory, where the atmospherically-induced motion of the beam is compensated by the IRIS instrument (Gitton et al. 2004, operating in the *H*- or *K*-band). Although this beam stabilization increases the flux on AMBER, it cannot compensate the phase-fluctuations which are imposed by the atmosphere. The FINITO fringe tracker (Gai et al. 2004), which is currently under commissioning, will remove these random phase shifts in the near future, allowing AMBER to use integration times much longer than the atmospheric coherence time.

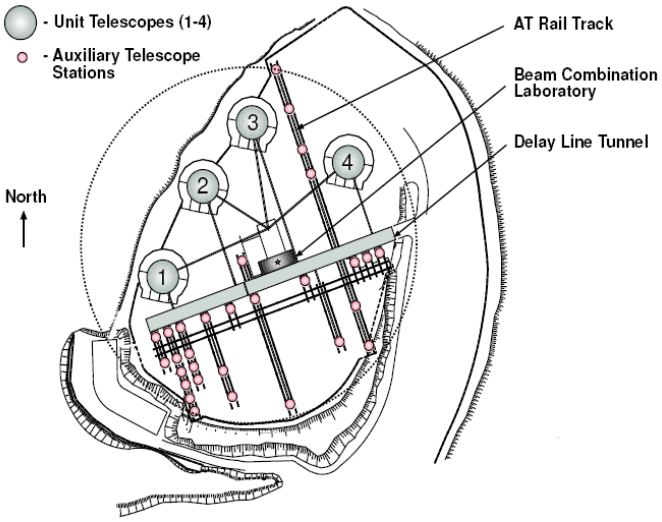

Figure 4.2: Besides the four UTs, the VLTI infrastructure offers four ATs (Image Credit: Glindemann et al. 2003).

4.1.2 The AMBER instrument

The AMBER instrument was built by an international consortium comprising French, Italian, and German institutes, and installed on Cerro Paranal in Spring 2004. As the sketch in Figure 4.3 shows, the light from up to three VLTI telescopes is first spatially filtered using single-mode fibers (corresponding to a field-of-view diameter of 65 mas for the UTs and 280 mas for the ATs on the sky). After the spatial filtering, a beam splitter separates a small fraction of the light from each beam and redirects it into photometric channels, whereas the main part of the light is combined using the multiaxial beam combination scheme (see Sect. 2.4.2). The three exit pupils are placed in separations of 1:2:3, which leads to different fringe frequencies in the formed interferogram, making the fringes from the three baselines clearly distinguishable (although they still slightly overlap in Fourier space). Then, both the interferometric and the photometric beams are spectrally dispersed using a spectrograph. Three different dispersive elements can be chosen, resulting in three different spectral modes:

Low-resolution (LR) mode: Using a PRISM, the interferograms are spectrally dispersed with a resolution of $R=\lambda/\Delta\lambda=75$. The LR mode provides the highest sensitivity, and allows to cover the

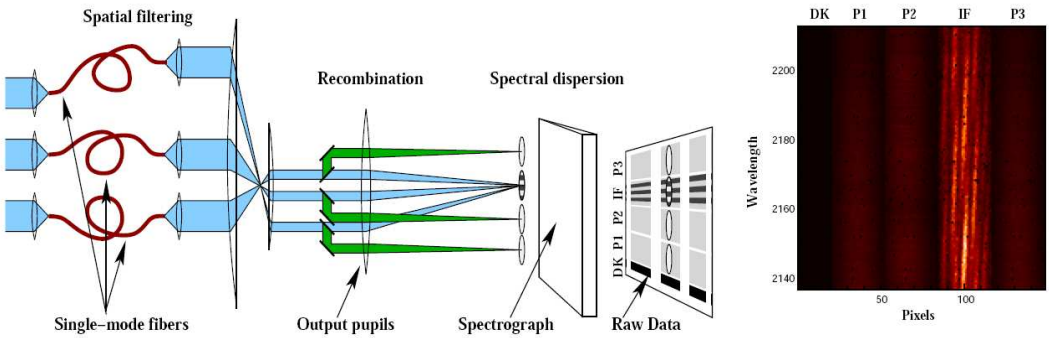

Figure 4.3: Sketch of the AMBER instrument design: The three beams, which enter AMBER are spatially filtered using single-mode fibers, recombined on the detector plane and then spectrally dispersed using a spectrograph (Image Credit: Tatulli et al. 2006).

widest spectral range (*J*-, *H*-, *K*-band in one exposure).

Medium-resolution (MR) mode: Using a GRISM with R=1 500, this mode offers a compromise between moderate sensitivity and sufficient spectral resolution to separate spectral features and to resolve Doppler-broadened spectral lines typically over a few spectral channels.

High-resolution (HR) mode: With R=12 000 (using a GRISM), this mode allows detailed kinematic studies in spectral lines, which are resolved over typically a few dozens of spectral channels.

On the AMBER detector, not only the interferometric (IF) and three photometric channels (P1, P2, P3; each measuring 32 pixel in spatial direction and an arbitrary number of pixels in spectral direction), are recorded, but also a narrow dark strip (DK; 20 pixel in spatial direction). The DK records the detector noise and thermal background. Therefore, only a small fraction of the 512×512 pixels on the HAWAII detector contains scientific information. To reduce the detector readout time, the AMBER detector electronics and software allows one to read-out individual sub-windows, which are placed along the before-mentioned stripes (arranged on the detector in the following order: from left to right DK, P1, P2, IF, P3). These sub-frames are then stored in FITS data cubes for further processing.

4.2 AMBER Data Reduction Pipeline

AMBER interferograms allow one to extract a large number of observables, including the spatially-filtered object spectrum, visibilities, differential visibilities (DV), differential phases (DP), and CPs. To extract these observables, the AMBER consortium has developed the software library *amdlib*, which employes the *Pixel-to-Visibility-Matrix* (P2VM) algorithm. This algorithm, somewhat similar to the ABCD method (Colavita 1999), fits the three fringe systems in the interferogram in image space (Tatulli

et al. 2006). For each spectral channel, the complex visibilities and squared visibilities are computed and then stored in the OI-FITS data format. Consortium members have also developed an interactive user-interface based on the real-time interpreter language *yorick*, called *ammyorick*, which can be used to remove the influence of wavelength-dependent piston, yielding differential observables (Millour et al. 2006). Besides the science files (containing the interferograms and the recorded photometry), ten calibration files (P2VM files), a sky file, a bad pixel mask (BPM), and a flat-field mask are needed as input for this software.

In the course of my PhD, I have developed complementary software, which uses these existing software packages (namely *amdlib* to extract complex visibilities and *ammyorick* to obtain the differential observables) and processes and manages the data in a pipeline. Besides a high efficiency in reducing large amounts of data, this approach allows us to study the influence of the various free data reduction parameters on the final averaged observables. Such parameter studies are important to identify the optimal parameter sets for data reduction, and also to trace down data reduction artefacts. The AMBER data reduction pipeline also performs the averaging and calibration of the derived observables and produces summary plots. The pipeline (consisting of C programs, which are embedded in C bourne shell scripts) is complemented by tools which allow, for instance, to generate mosaic plots from the raw data (such as shown in this chapter), or to bin several spectral channels of the raw interferograms.

In the following sections, I discuss some procedures and present some studies related to AMBER data reduction, namely on data selection (Sect. 4.4) and on the dependence of the results on the BPM (Sect. 4.6). For all studies shown here, we used amdlib 2.4/ammyorick 0.56 for data reduction of LR data, and amdlib 2.19/ammyorick 0.59 for MR data. These software packages are available from the website `http://amber.obs.ujf-grenoble.fr`.

4.3 Determining Wavelength Shifts

As the photometric and interferometric channels of AMBER pass different optical components, the spectral channels are often shifted with respect to each other by a few pixels (see Figure 4.4, left column). In case the flux in adjacent spectral channels changes significantly (as in the wings of spectral lines or in atmospheric telluric features), such shifts could introduce strong artefacts in the derived visibilities and phases. Therefore, these shifts have to be determined accurately. Although at Paranal a software is estimating these shifts automatically, we found that a careful refinement can significantly improve the obtained results. Furthermore, during the early operation of AMBER, the before-mentioned software was not operational, so that we wrote independent software which extracts the spectra from the AMBER raw data, and computes the autocorrelation of the extracted spectra in order to determine the optimal shift value (see Figure 4.4, right column).

a) LR data on MWC 147

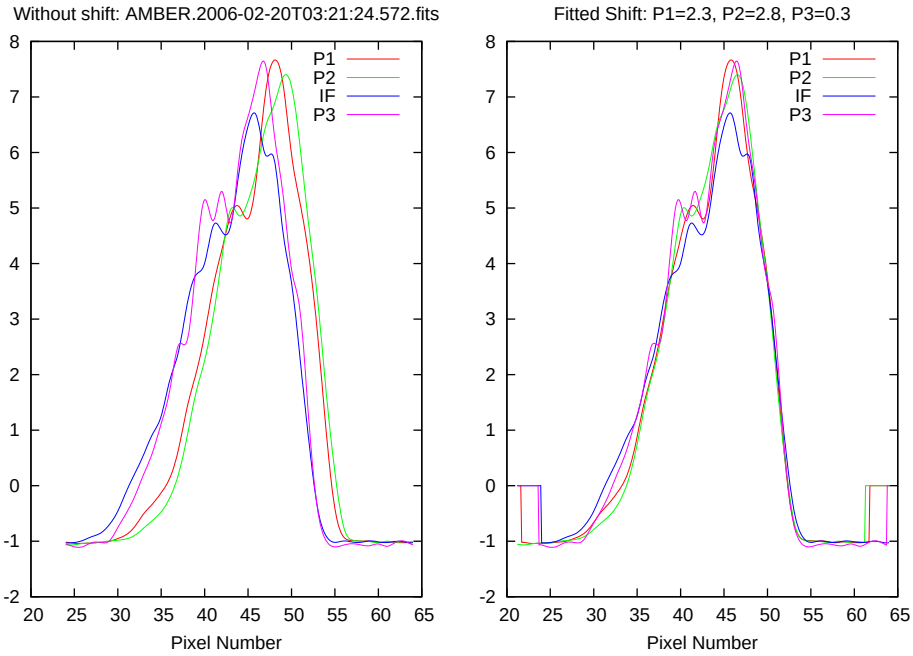

b) MR data on η Carinae (He I line)

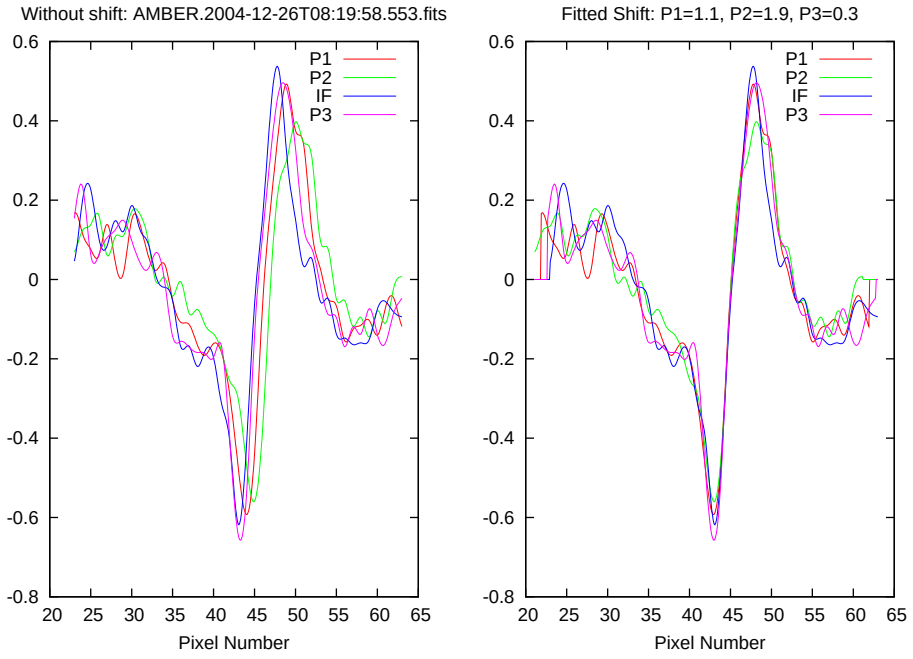

Figure 4.4: *Left:* The spectra from the photometric and interferometric channels of AMBER are typically shifted by a few spectral channels. *Right:* Computing the autocorrelation of the spectra, we determine the optimal recentered position. In order to reach sub-pixel accuracy, we perform a spline-interpolation of the extracted spectra.

4.4 Data Selection

In Spring 2004, the first on-sky observations with AMBER have shown that the quality of the AMBER interferograms is limited by the influence of high-frequency jitter, which is imposed on the telescope beams by some components in the VLTI infrastructure. This jitter degenerates the fringe contrast and systematically biases the derived interferometric observables. As the technical and engineering work, which aims to eliminate this disturbing effect, is ongoing, the problem has currently to be faced at the data reduction stage. For example, one can carefully select those interferograms which are least affected by the influence of the jitter. We perform a four-stage data selection procedure, which incorporates the following steps:

1.) The leading ten frames of each data set are typically degenerated by electronic noise. Therefore, these frames are rejected.

2.) Frame selection based on the photometry, where we set thresholds *a)* on the flux collected by each telescope, and *b)* on the flux balance between the beams contributing to a certain baseline.

3.) Frame selection based on fringe SNR.

4.) Frame selection based on piston.

In the following sections, we describe the selection steps 2.) to 4.) in more detail and illustrate them using real science raw data from our projects on MWC 147 (LR data, $K = 5.7$, K-band) and on η Carinae (MR data, $K = 0.2$, Brγ line). We refer to chapters Chapters 6 and 9 for more details on these data sets and on the extracted observables.

4.4.1 Photometric selection

In order to obtain a clear interference pattern on a baseline formed by telescopes i and j, a sufficient number of photons from both telescopes (corresponding to intensities I_i, I_j) must enter the fibers and reach the detector. Furthermore, equation 2.15 shows that high-quality interferograms also require that the flux ratio between the telescopes is rather balanced, i.e. that the beams from both telescopes have to be roughly equally bright.

If for a certain interferogram one of these conditions is not satisfied, we reject this interferogram from the further processing. Rejecting this scan (which cannot contain real fringes) seems advisable, since *detector fringes*[1] (which are spurious time-variable fringe patterns appearing randomly on the AMBER detector) could confuse the *amdlib* fringe fitting results.

[1] see also the discussion by Gianluca Li Causi at the website http://www.mporzio.astro.it/~licausi/ADC/

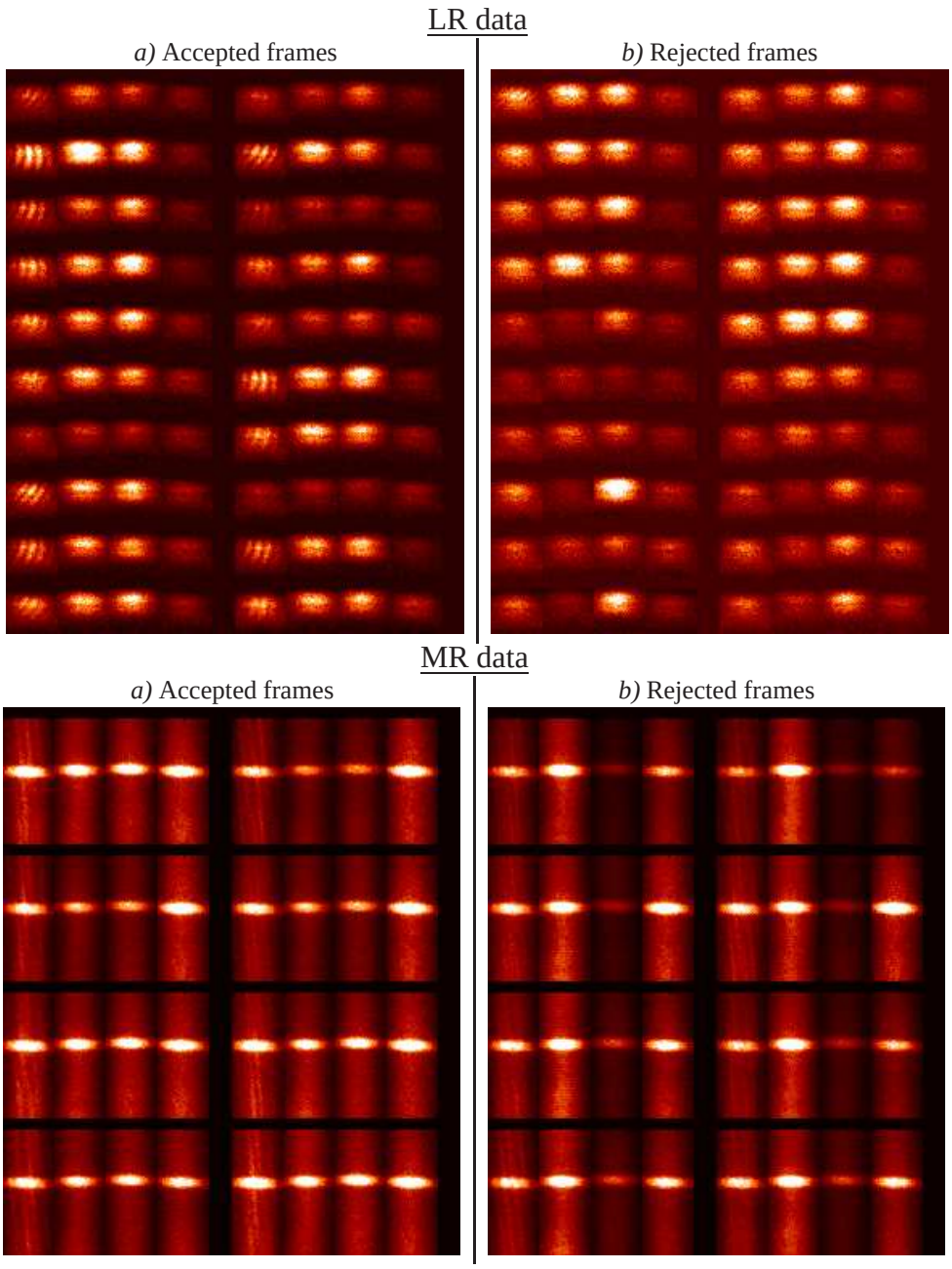

Figure 4.5: Mosaic of AMBER raw data (File `AMBER.2006-02-20T03:21:24.572.fits`), sorted by the photometric contrast (best frames top left, worst frames bottom right, here selected for baseline BL12). Each AMBER raw data set comprises an image of the interferometric channel (IF, left), and three photometric channels (2nd from left: P1 (corresponding to the baseline B12, combining telescope #1 and #2), 3rd from left: P2 (B23), 4th from left: P3 (B31). Whereas *a)* shows frames which passed the chosen photometric criteria, *b)* shows the frames which were rejected from further processing.

For LR-interferograms of MWC 147, we defined the following criteria (where the intensities are integrated over all spectral and spatial channels and background-subtracted using a sky file; the background flux I_{bg} is measured in the DK):

$$I_1/I_{\mathrm{bg}} \geqslant 1.5 \tag{4.1}$$

$$I_2/I_{\mathrm{bg}} \geqslant 1.5 \tag{4.2}$$

$$I_1/I_2 \leqslant 10 \tag{4.3}$$

$$I_2/I_1 \leqslant 10 \tag{4.4}$$

4.4.2 Fringe SNR selection

In the P2VM algorithm, a fringe contrast quality criterium can be defined (see equation 20 in Tatulli et al. 2006). Therefore, it seems a reasonable approach to use this fringe SNR as a criterium to select those interferograms which are least degenerated by jitter. However, one has to keep in mind that any criterium which judges the quality of the fringe pattern itself could lead to systematic biases in the derived fringe contrast (visibility). Especially, if the correlated flux (i.e. either the brightness or the intrinsic visibility) between the target and the calibrator star is different, a fringe SNR selection could lead to biases in the absolute calibration. Therefore, we do not select the best interferograms for the target and the calibrator based on a fixed fringe SNR threshold, but keep a fixed fraction (typically 30%) of all recorded interferograms. Ideally, above a certain fractional threshold, one reaches a convergence-like behaviour in the derived visibility, as can be seen in Figure 4.7.

We select the frames for each baseline separately and determine the best frames not with respect to single data files, but relative to the whole data set (taking all files on a particular object and in a particular instrument mode into account).

4.4.3 Piston selection

Wavelength-dependent piston causes the fringe pattern to "tilt" with respect to the wavelength-axis. If the piston reaches the order of the coherence length, this effect can significantly degenerate the fringe contrast and thus bias the derived absolute visibility as well as the wavelength-dependent differential visibility. Of course, the importance of this effect correlates with the width of the recorded spectral window, i.e. for observations in the HR and MR mode the influence of piston can generally be neglected, while it must be clearly taken into account for LR mode observations.

In a first approach we select those frames for which the piston (as determined by *amdlib*), is less than 0.5 times the coherence length $\lambda^2/\Delta\lambda$. We found that this significantly improves the data reduction results for LR data. Future investigations could also attempt to model the bias induced by piston and

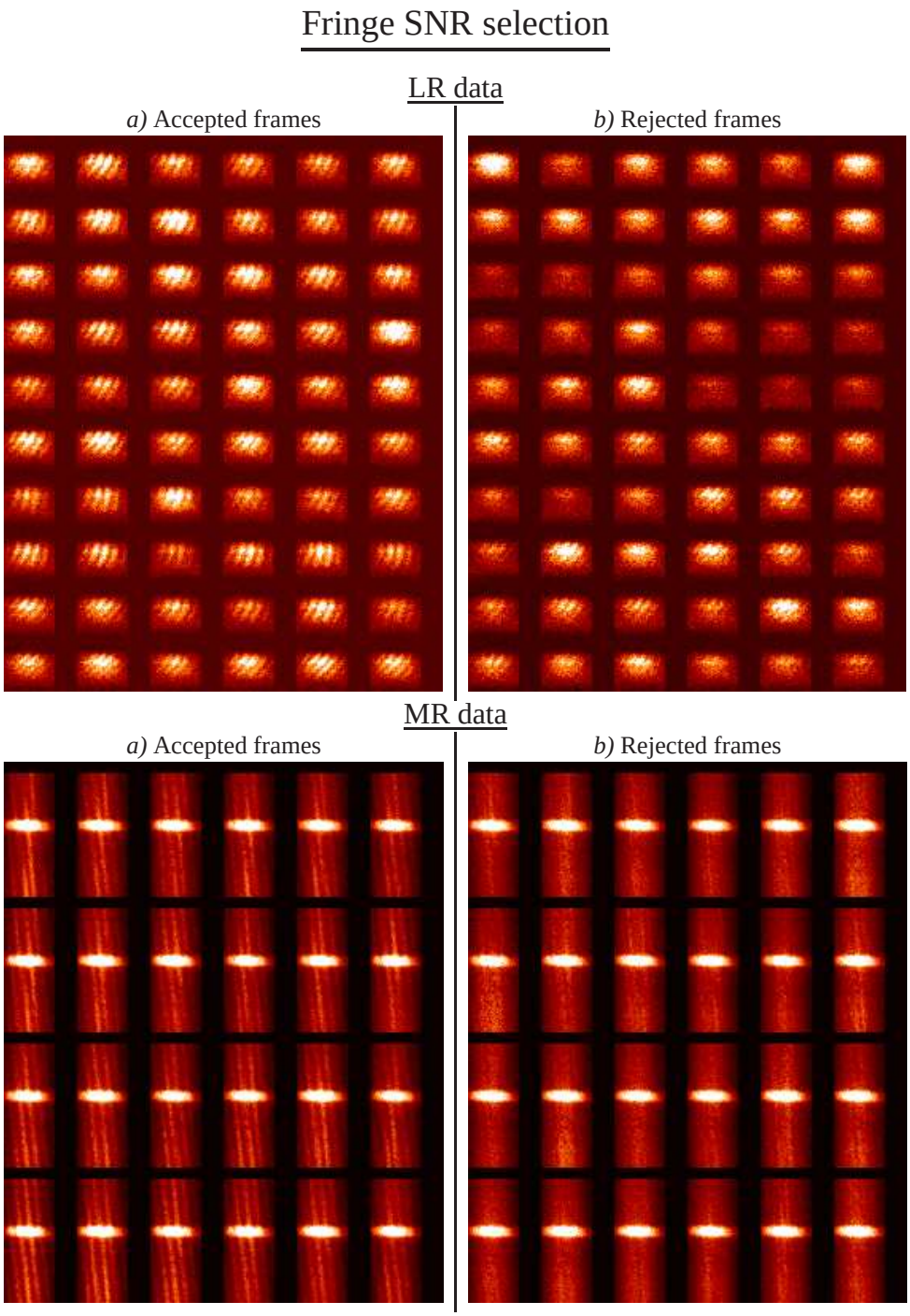

Figure 4.6: Similar as Figure 4.5, but showing some of the AMBER raw frames selected/rejected by the fringe SNR criterium.

a) V^2 vs. SNR

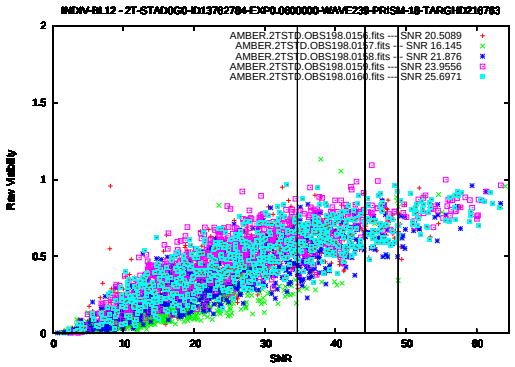

b) V^2 distribution

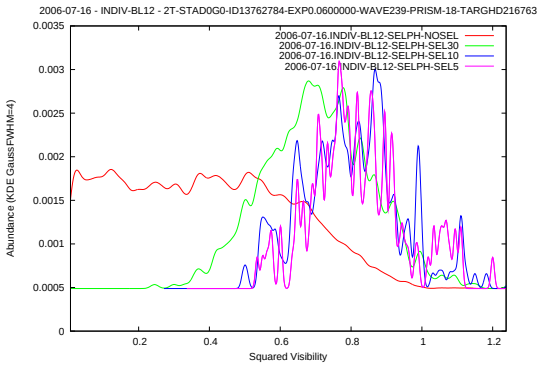

Figure 4.7: *a)* The squared raw visibility is plotted against the fringe SNR criterium for five data sets taken during the AT commissioning run on 2006-07-16 on the star HD 216763. Fringes with low SNR show a systematically lower visibility, as expected if these interferograms are degenerated by jitter. The vertical lines depict the selection thresholds for the best 30%, 10%, and 5% of all interferograms (from left to right). Under good conditions, above a certain selection threshold, one reaches a convergence-like behaviour. *b)* This histogram shows the distribution of the derived V^2 values. With increasing selection, the distribution of V^2 values becomes more Gaussian-like, defining a clear mean value. This can be seen, for instance, by comparing the red curve (corresponding to no selection) with the magenta curve (corresponding to 5% selection).

correct it to some extend in the course of data processing.

4.5 Data Averaging and Calibration

Following the data selection, we use *amdlib* to extract visibilities and CPs from the pre-selected AMBER raw data files. The *amdlib* software bins an arbitrary number of interferograms to extract these observables (Tatulli et al. 2006) and stores the results in OI-FITS files. Then we apply weighted averaging in order to obtain mean visibilities and CPs including statistical errors for each spectral channel. The CPs are averaged in the complex plane, similar to the method described in Section 3.3.2.

The same procedure is applied to the target and to the calibrator measurement. Finally, before dividing the target visibilities through the calibrator visibilities, we correct for the calibrator UD diameter (using equation 2.30).

4.6 Investigating the Dependence of AMBER Results on the Bad Pixel Mask

In the course of our work on AMBER data reduction, we noticed that the use of certain BPMs might introduce significant artefacts in the derived observables. The first artefacts we noticed appeared within

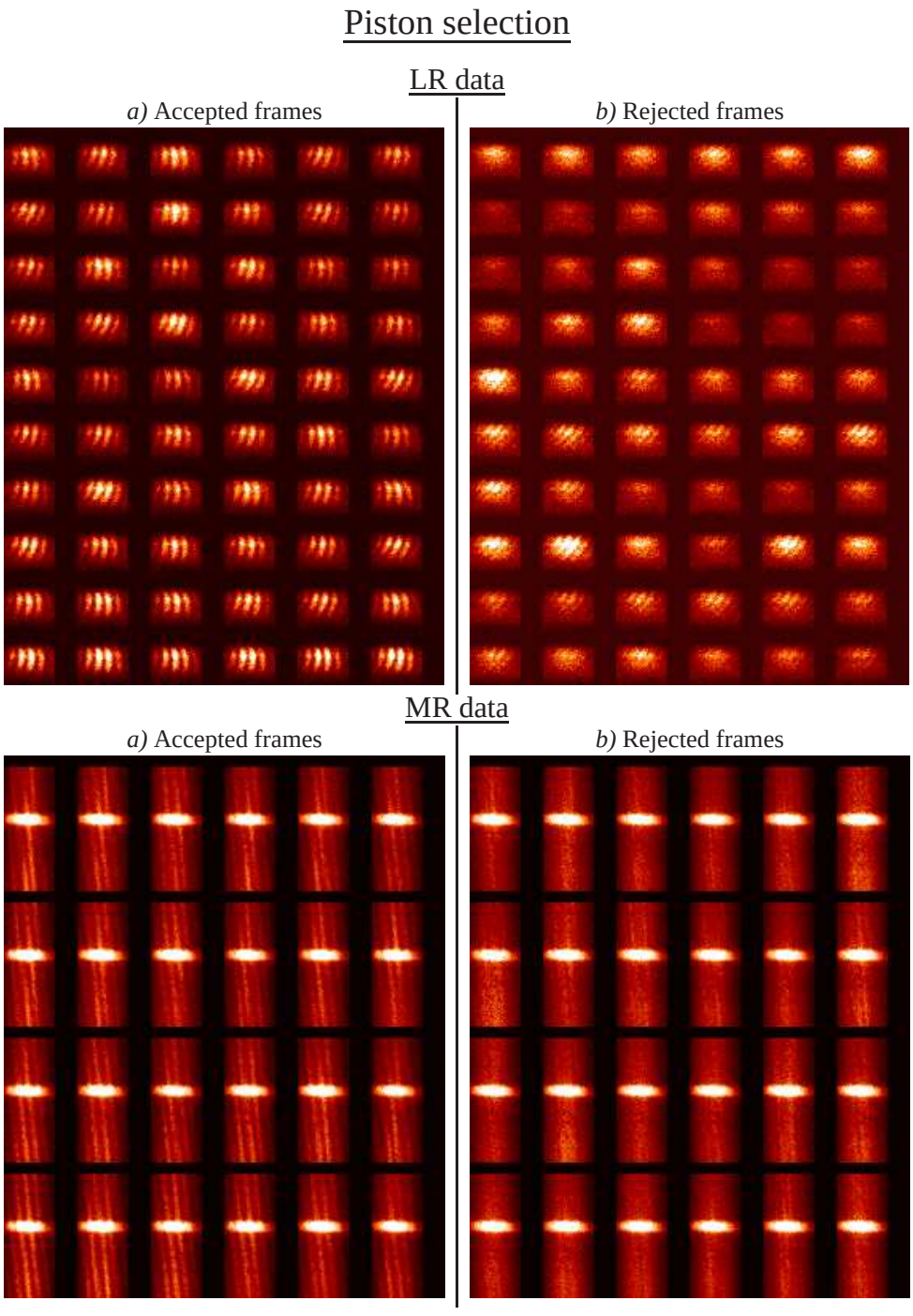

Figure 4.8: Similar as Figure 4.5, but showing some of the AMBER raw frames selected/rejected by the piston SNR criterium.

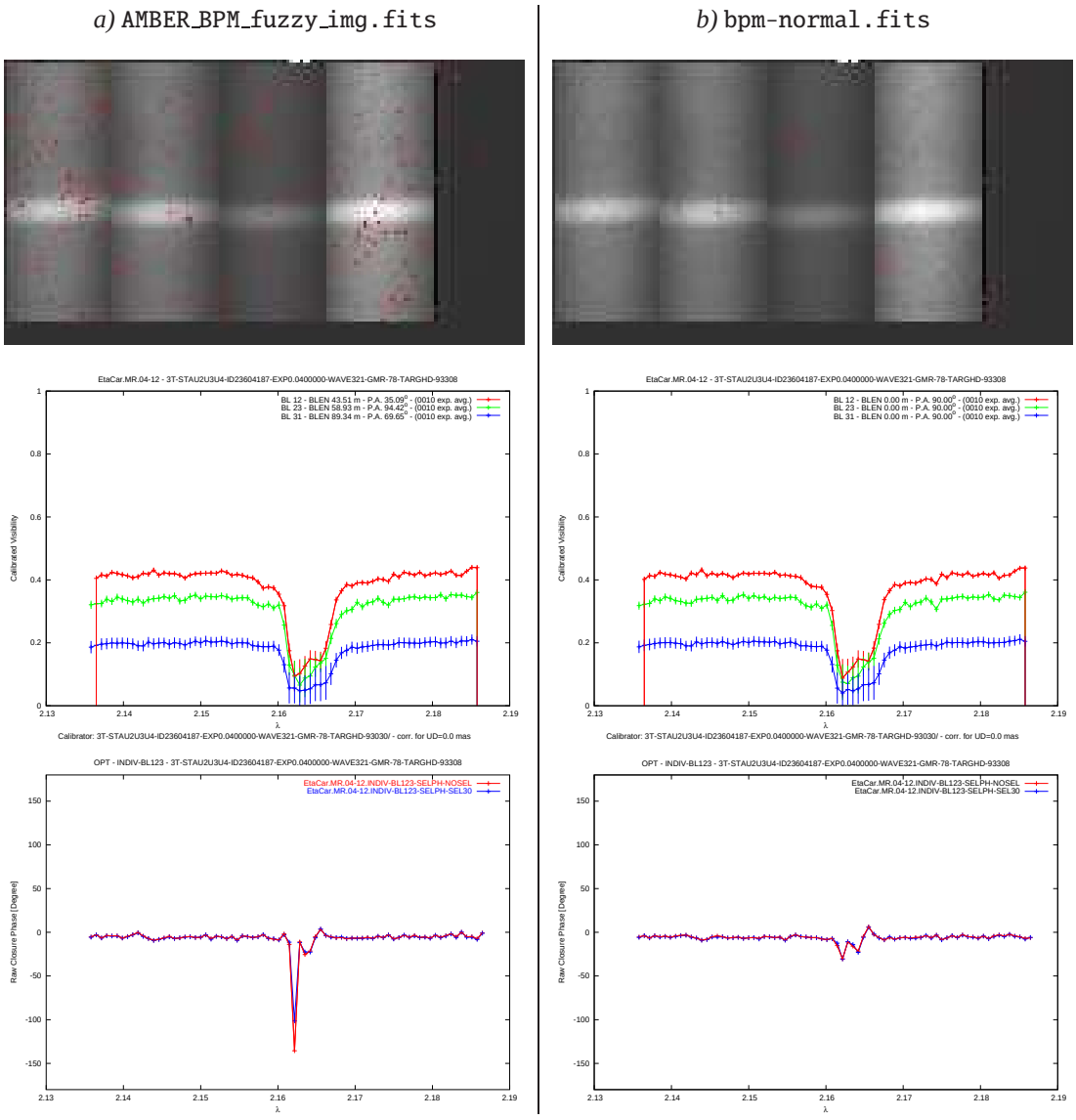

Figure 4.9: *Upper row:* The current default BPM (`AMBER_BPM_fuzzy_img.fits`, left column) and the new BPM (`bpm-normal.fits`, right column) superposed as red spots on the η Carinae MR data set, averaged over all frames (from left to right: IF, P1, P2, P3, DK; same data set as shown in Figures 4.5 to 4.8). *Middle and Lower row:* Visibilities and CPs derived from the same data set. Within the Brγ line, a strong CP signal appears. For the CP we show one processing without any selection (red curve) and with a selection of the 30% best frames (blue curve).

the CP signal derived from AMBER-GTO medium resolution data, acquired on η Carinae during the night 2004-12-26. Using the data reduction pipeline, we derived an average CP signal of $\approx -140^\circ$ within the blue-shifted wing of the Brγ line. With a data selection of 30% (based on the fringe SNR), this value dropped to $\approx -100^\circ$ (see Figure 4.9a).

To investigate the influence of the BPM on the obtained results, our software engineer Matthias Heiniger generated three new BPMs from detector calibration data taken during the AMBER commissioning run #2 (for a description of our criteria for bad pixel identification, we refer to Kraus et al. 2005a). Using these new BPMs (one of which, namely `bpm-normal.fits`, is shown in Figure 4.9), we re-reduced the η Carinae data and compared the results to the results obtained using the current default BPM-file `AMBER_BPM_fuzzy_img.fits`. Whereas the derived visibility seems to depend only marginally on the BPM file used (variance < 0.03 for the calibrated visibility), we obtained a significantly different result for the CP within the Brγ line ($\Phi < 40^\circ$). This value is more consistent with the CP signal derived from AMBER-data taken during the GTO run in February ($\Phi < 40^\circ$) with a similar instrumental setup and baseline configuration (see Chapter 9).

Therefore we recommend to use `bpm-normal.fits` as a new default BPM. In addition, it seems advisable to check for the consistency of the obtained data reduction results using several BPMs and to update the BPM on a regular basis, e.g. every six months.

5 Image Reconstruction Algorithms

Summarizing results which appeared in an AJ article and two SPIE articles:
Kraus, S., Schloerb, F. P., Traub, W. A., et al., AJ 130, 246 (2005)
Hofmann, K.-H., Kraus, S., Lopez, B., et al., Proc. of SPIE 6268, 88 (2006)
Lawson, P. R., Cotton, W., Hummel, C. A., et al., Proc. of SPIE 6268, 59 (2006)

5.1 Overview and Context

Extracting scientific results from interferometric observables is, in general, not a trivial task. Most commonly, the interpretation of optical interferometric data consists of fitting analytic profiles (such as those presented in Sect. 2.5) to the measured visibilities and CPs. However, this model fitting approach requires a-priori knowledge about the source structure, and might therefore be not applicable (if insufficient is known about the source), or lead to biased results (if we have a wrong idea about the source structure). Therefore, it is highly desirable to obtain model-independent aperture synthesis images. Such imaging capabilities will also be of special importance for the upcoming generation of groundbased (such as VLTI/MATISSE or VLTI/VSI) and space interferometers (such as DARWIN or TPF-I).

In principle, the van-Cittert-Zernike theorem (equation 2.29) can be inverted (by applying an inverse Fourier transform) to re-obtain the source brightness distribution on the sky. However, this approach would require a complete sampling of the *uv*-plane, in contrast to the very limited coverage achievable with the current optical interferometric arrays. Furthermore, from the ground only CPs can be measured due to the atmospherically induced phase variations, which makes aperture synthesis imaging of phase-instable interferometers a highly non-linear problem. Thus, sophisticated algorithms are required to retrieve the lost phase information.

The radio astronomy community has developed various strategies, which seem suitable for this task, including the conventional *Hybrid Mapping* (CHM; Cornwell & Wilkinson 1981) and the *Difference Mapping* (DFM; Pearson et al. 1994) algorithm. In both algorithms, the individual phases are recovered

from the measured CP by self-calibration (Pearson & Readhead 1984). The necessary deconvolutions can be performed with the CLEAN algorithm (Högbom 1974). However, there are indications that these algorithms, which were developed and optimized for interferometric imaging at radio wavelength (i.e. using relatively large arrays such as the VLA with $N = 27$ and suffering typically only from marginal phase-instabilities) do not optimally meet the requirements for imaging with optical interferometers, which typically employ $N = 3$ telescopes and suffer from a complete loss of the Fourier phases.

Therefore it is important to develop image reconstruction algorithms, which are optimized for the conditions provided by optical interferometry and to test and refine these algorithms using simulated and observational data.

Hofmann & Weigelt had presented in 1993 an algorithm, which was originally developed to reconstruct images from bispectrum speckle data, but which seems also very promising for application to long-baseline interferometric data. When starting my PhD work, Karl-Heinz Hofmann provided Fortran code fragments of this algorithm, which I incorporated into a new C software. In close collaboration with Karl-Heinz Hofmann, both the Fortran and C software was refined and used for independent studies on simulated datasets (MATISSE: Sect. 5.3; IAU Imaging Beauty Contest 2006: Sect. 5.4) and observational interferometric data (Capella: Sect. 5.2; θ^1 Ori C: Sect. 8). All image reconstruction shown here were obtained with my C software implementation.

5.2 Reconstruction of Simple Binary Structure

In the context of my Master thesis work (Kraus 2003), I have implemented the CHM and DFM algorithms and applied them to IOTA measurements on the bright binary star Capella. We applied the BBM algorithm to the same dataset in order to compare the quality of the resulting images.

The data set was taken within five nights of IOTA/IONIC3 observations (2002 November 12–16) in two array configurations (2002 Nov 12–14: A35, B15, C0; 2002 Nov 15–16: A15, B15, C0) on the bright (H=-1.6), $\sim$ 44 mas separation binary Capella. The Capella system ($d = 12.94 \pm 0.15$ pc) consists of a G8 III and a G1 III giant, which makes the stellar surfaces ($\Theta_{Aa} = 8.9 \pm 0.6$ mas, $\Theta_{Ab} = 5.8 \pm 0.8$ mas) of the binary components marginally resolvable.

Due to the period of $P = 104.022$ days (Hummel et al. 1994), the PA of the binary pair changed by $\sim 14^\circ$ over the five successive nights covered by our observations. In order to combine the data from the five nights (yielding a better *uv*-coverage) for our comparative study of the CHM, DFM, and BBM image reconstruction algorithms, we applied a rotation-compensating coordinate transformation (Kraus et al. 2005b). The resulting *uv*-coverage is shown in Figure 5.1*a*. When applying our image reconstruction software, we obtained with identical initial conditions the aperture synthesis images shown in Figure 5.1*b*. All three algorithms successfully reobtained the binary structure of the brightness distribution, although the intensity ratio I_{Aa}/I_{Ab} measured within the maps (CHM: 1.9; DFM: 1.6; BBM: 1.8) slightly deviates from the intensity ratio obtained by model fitting (1.49 ± 0.10). For the stellar diameter, we measured within the unconvolved BBM map $\Theta_{Aa}^{\rm map} = 8.3 \pm 1.6$ mas and $\Theta_{Ab}^{\rm map} = 6.8 \pm 1.2$ mas, which is in good agreement with the fitting results given above (for the other maps we did not extract the stellar diameters, as these algorithms do provide only convolved maps). The noise features and artefacts are similarly strong in all maps ($\sim$ 5%). Therefore we conclude that for this dataset the three algorithms performed equally well.

In order to test the performance on a even poorer *uv*-coverage, we subdivided the data set into three subsets (2002 Nov 12-13, 2002 Nov 14, 2002 Nov 15-16). Since we observed during the first two epochs with the telescope configuration including the longest baseline (and hereby missing lower frequencies), the convergence of the maps had to be supported by limiting the reconstruction area. We attempted to reconstruct images with all three algorithms, but succedded only with the BBM algorithm to reconstruct maps from this very poor *uv*-coverage. The resulting maps (Figure 5.2) make the orbital motion of the Capella giants over the five successive nights clearly perceivable. Also the intensity of the stars (from left to right: $I_{Aa}/I_{Ab} \approx 1.6, 1.7, 1.6$) could be estimated reliably.

a) ***uv*-coverage**

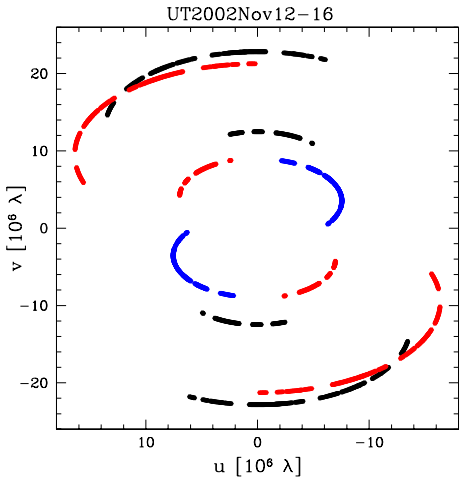

b) **Reconstructed Images**

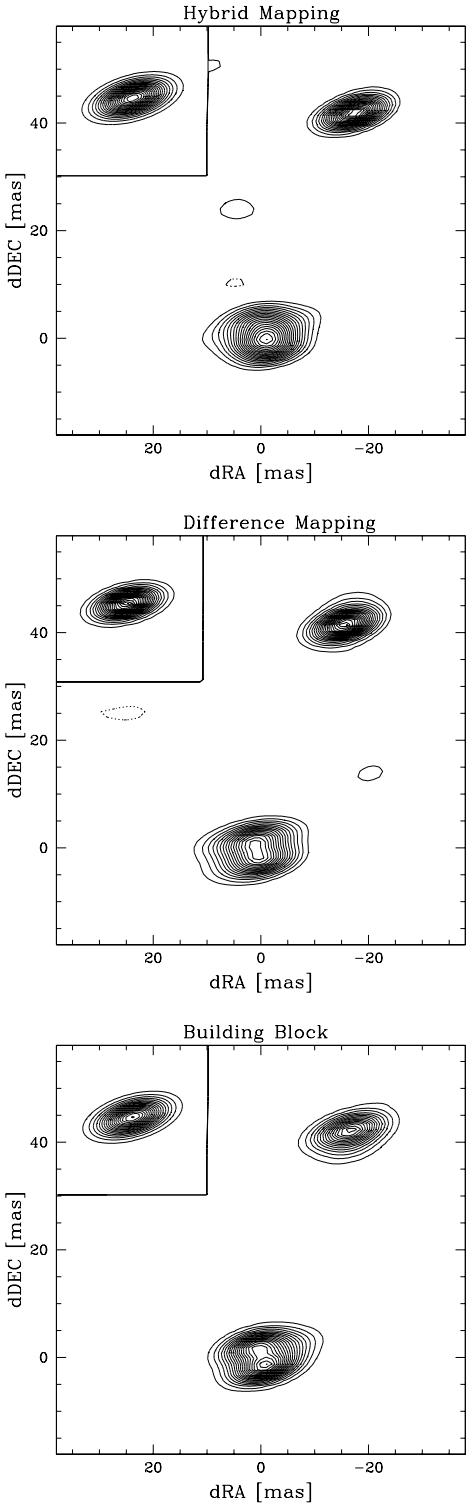

Figure 5.1: Aperture synthesis maps of Capella generated with IOTA data from 2002 Nov 12-16. Maps generated with the CHM (top), DFM (middle), and BBM (bottom) algorithm are shown. Each map shows the surface brightness plotted with 5% interval contours (scaled to the peak intensity) and the beam (5.4 × 2.6 mas) depicted in the upper-left corner. To compensate for the motion of the stars over the observed interval ($\sim 14^{\circ}$), the *uv*-plane was moved synchronously to the orbital motion. The maps are oriented north up, east left.

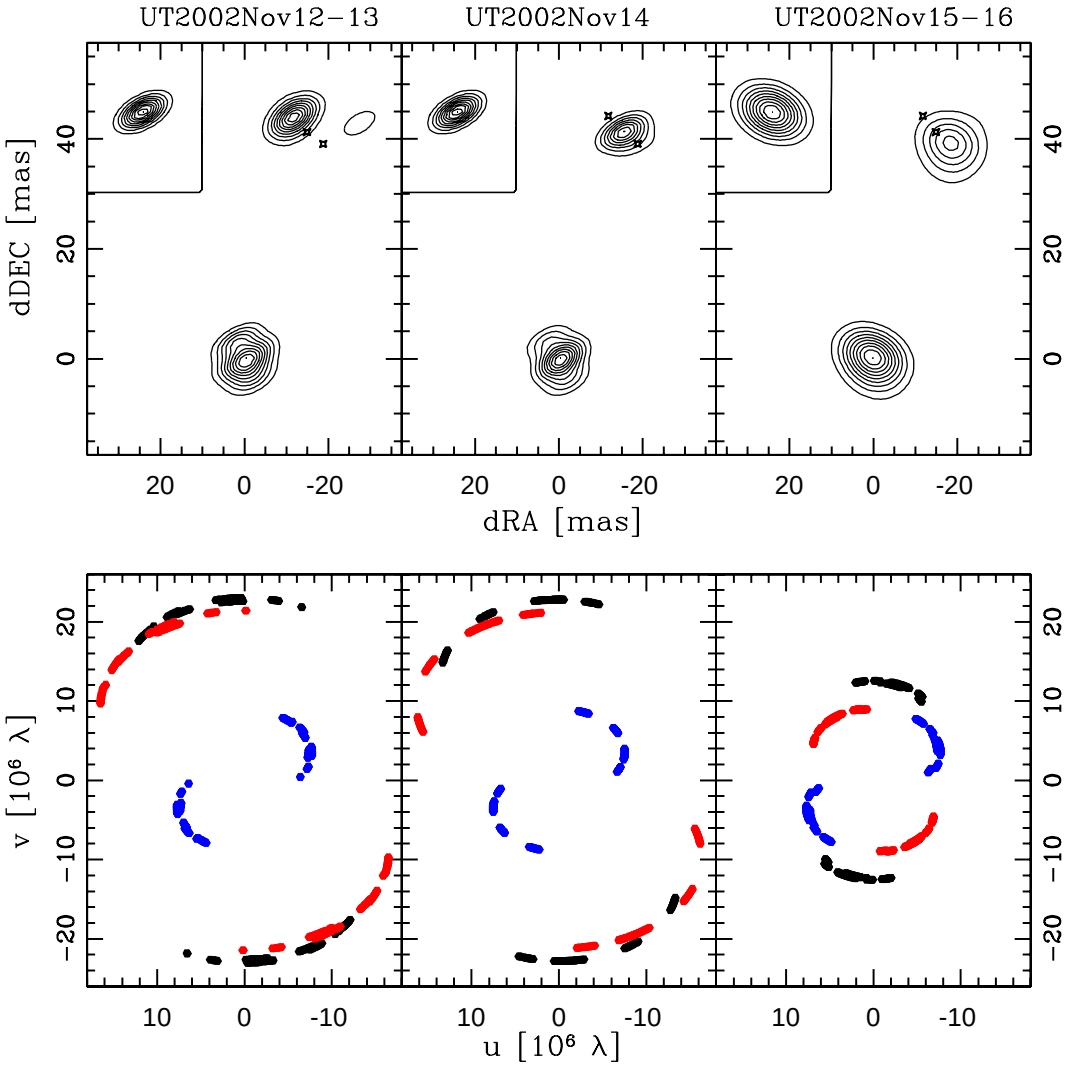

Figure 5.2: Image reconstructions from subsets of our complete data set revealing the orbital motion of the stars between three epochs. To compensate the marginal orbital motion within the subsets, the *uv*-plane was rotated synchronously to the reference position of the components at the intermediary modified julian dates MJD=91.437, 93.907 and 94.262 (MJD=JD−2452500). The crosses within the maps indicate the "centers of light" of the stars within the other images. Whereas the positions fit the expectations accurately ($\leqslant$ 1 mas), the intensity ratio between the two stars was not always obtained properly due to the poor sampling (the coverage is shown below each map). The contours show 10% intervals scaled to the peak.

5.3 Reconstruction of Complex Structure

In a second image reconstruction experiment, which was performed in the context of a study for the VLTI second-generation instrument MATISSE (Lopez et al. 2006; Lagarde et al. 2006), we reconstructed aperture synthesis images from simulated data. The simulations were designed to demonstrate that the 4-beam combiner MATISSE will allow interferometric imaging within realistic observation time constraints.

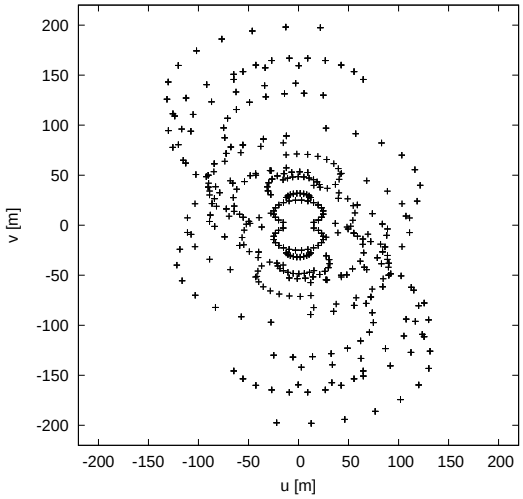

Figure 5.3: *uv*-coverage of the data set simulated in the course of the MATISSE image reconstruction study (3 nights with 4 ATs). For each *uv*-point, visibitilies and closure phases for only one spectral channel (at 10.5 μm) were simulated.

The input data was provided by our collaborators at the MPIA in Heidelberg (in particular Frank Przygodda and Sebastian Wolf). As input image, a protostellar disk around a T Tauri star ($M = 0.5\ M_{\odot}$) was simulated. Using the radiative transfer code MC3D (Wolf 2003), our collaborators generated a 10.5 μm image of such a disk as seen under an inclination of 60°, assuming a distance of 140 pc and an inner disk radius of 4 AU. Visibilities and CPs were computed, assuming observations on 3 nights with 4 ATs (9 hours of observation each night, one measurement per hour, telescopes mounted on the stations B5-G1-J3-D0, B5-B1-K0-D1, G2-A0-J2-J6; see Figure 5.3).

From these data sets, we generated aperture synthesis images using the CHM and the BBM algorithm. To test the algorithms also in presence of noise and to distinguish limitations on the image quality due to the *uv*-coverage from limitations due to the SNR, we reconstructed images from data with and without noise.

Comparing the reconstructed images with the input image (see Figure 5.4), we find that in the absence of noise, both algorithms succeed in reconstructing the basic structure, although the CHM image shows significantly stronger artefacts. When introducing 5% noise, our implementation of the CHM algorithm can barely recover the ring-like morphology, whereas the disk is still clearly perceptible in the BBM image.

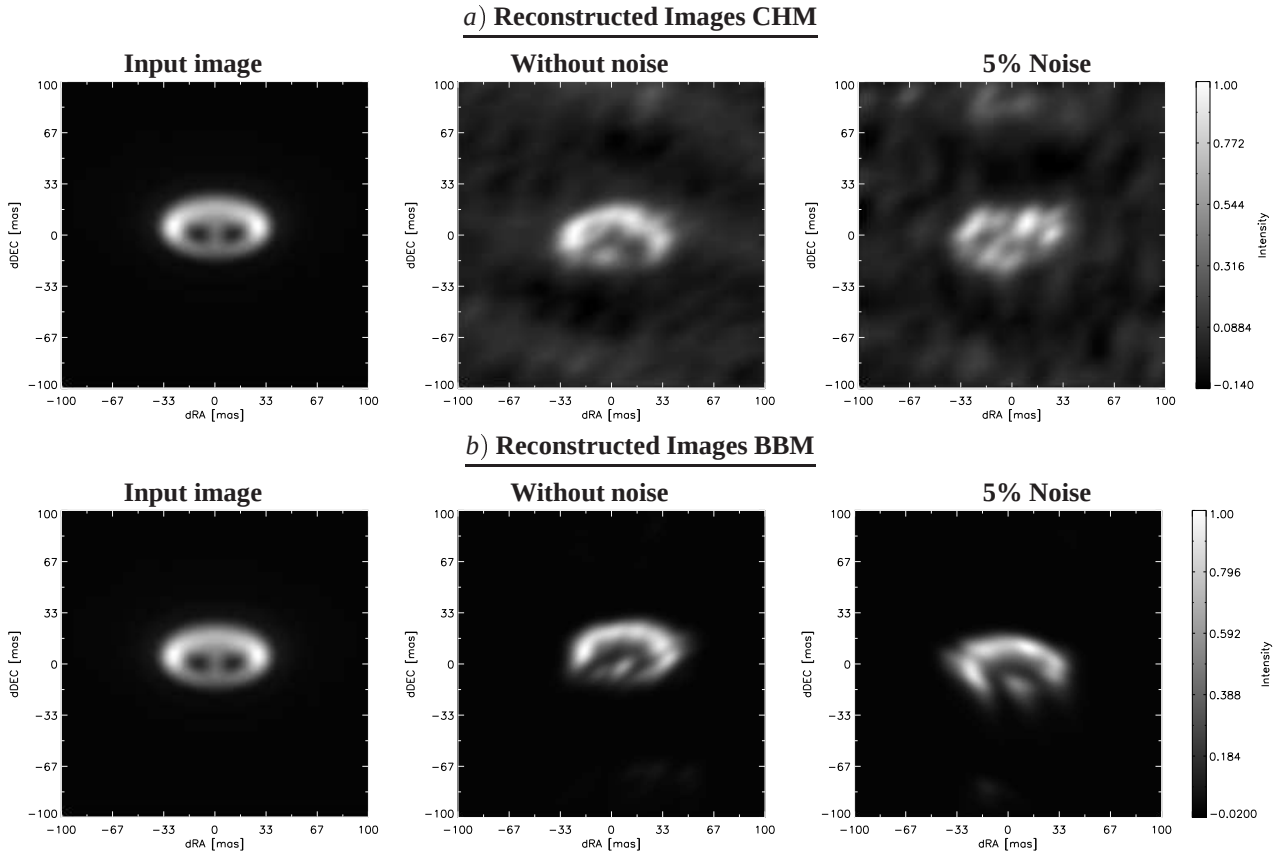

Figure 5.4: In the context of our image reconstruction study for the MATISSE instrument, we reconstructed images from a data set corresponding to just 3 nights of observations with 4 telescopes (see Figure 5.3 for the corresponding *uv*-coverage). Besides a data set without noise (middle column), we used a data set to which 5% noise was added (right column). The left column shows the input image, depicting a low-mass protostellar disk. Both the CHM algorithm (upper row) and the BBM algorithm (lower row) were used for this experiment.

5.4 Reconstruction of Complex, Extended Structure: The IAU Imaging Beauty Contest 2006

In order to stimulate the development and refinement of image reconstruction algorithms, members of the IAU Working Group on Optical/IR Interferometry have initiated a contest, in which the performance of image reconstruction algorithms is evaluated in a blind test. Up to now, two of these "Interferometry Imaging Beauty Contests" have been organized, namely in 2004 (Lawson et al. 2004) and 2006 (Lawson et al. 2006).

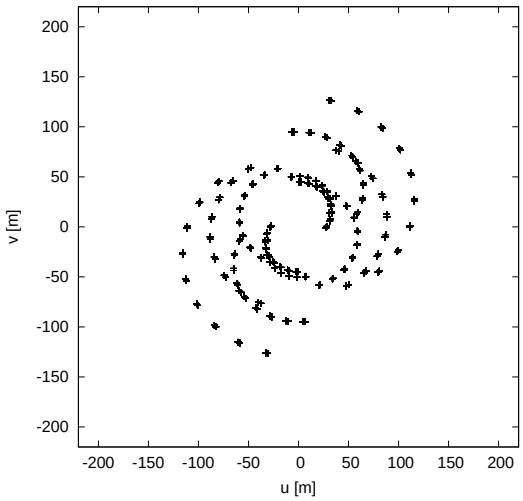

Figure 5.5: *uv*-coverage of the data set of the IAU Imaging Beauty Contest 2006. For each *uv*-point, *J*-, *H*-, and *K*-band visibilities and CPs were provided.

In the 2006 contest, five groups participated using the following algorithms: BSMEM (Fabien Baron, John Young), MACIM (Markov Chain Imager; Michael Ireland), MIRA (Eric Thiebaut), Recursive Phase Reconstruction (Sridharan Rengaswarmy), and BBM (Building Block Mapping; Stefan Kraus, Karl-Heinz Hofmann, Gerd Weigelt). The contest data set consisted of simulated visibilities and CPs, generated by Christian Hummel using a model image of an optically thin circumstellar disk (provided by Olivier Chesneau). The data set, which was delivered to the contestants without information about the physical nature or structure of the source, was rather challenging due to the simulated poor *uv*-coverage (corresponding to four nights of observations with VLTI/AMBER in the LR-JHK mode on the UTs, see Figure 5.5) and also due to the simulated low (all $V^2 \leqslant 8\%$) and noisy visibility data.

The organizers judged the quality of the images submitted by the various groups by convolving them to the same resolution. Following a normalization of the intensity, the RMS between the model and the reconstructed image was computed taking all intensities inside a rectangular area into account (boxes marked in Figure 5.6). As can be seen in Figure 5.6, four of the five algorithm successfully reconstructed the basic source geometry inspite of the challenging conditions. Based on the RMS measure, the quality of the entries was ranked as follows: BSMEM (RMS=90.5), MIRA (RMS=97.2), BBM (RMS=109.1), MACIM (RMS=114.7), and Recursive Phase Reconstruction (RMS=885.73).

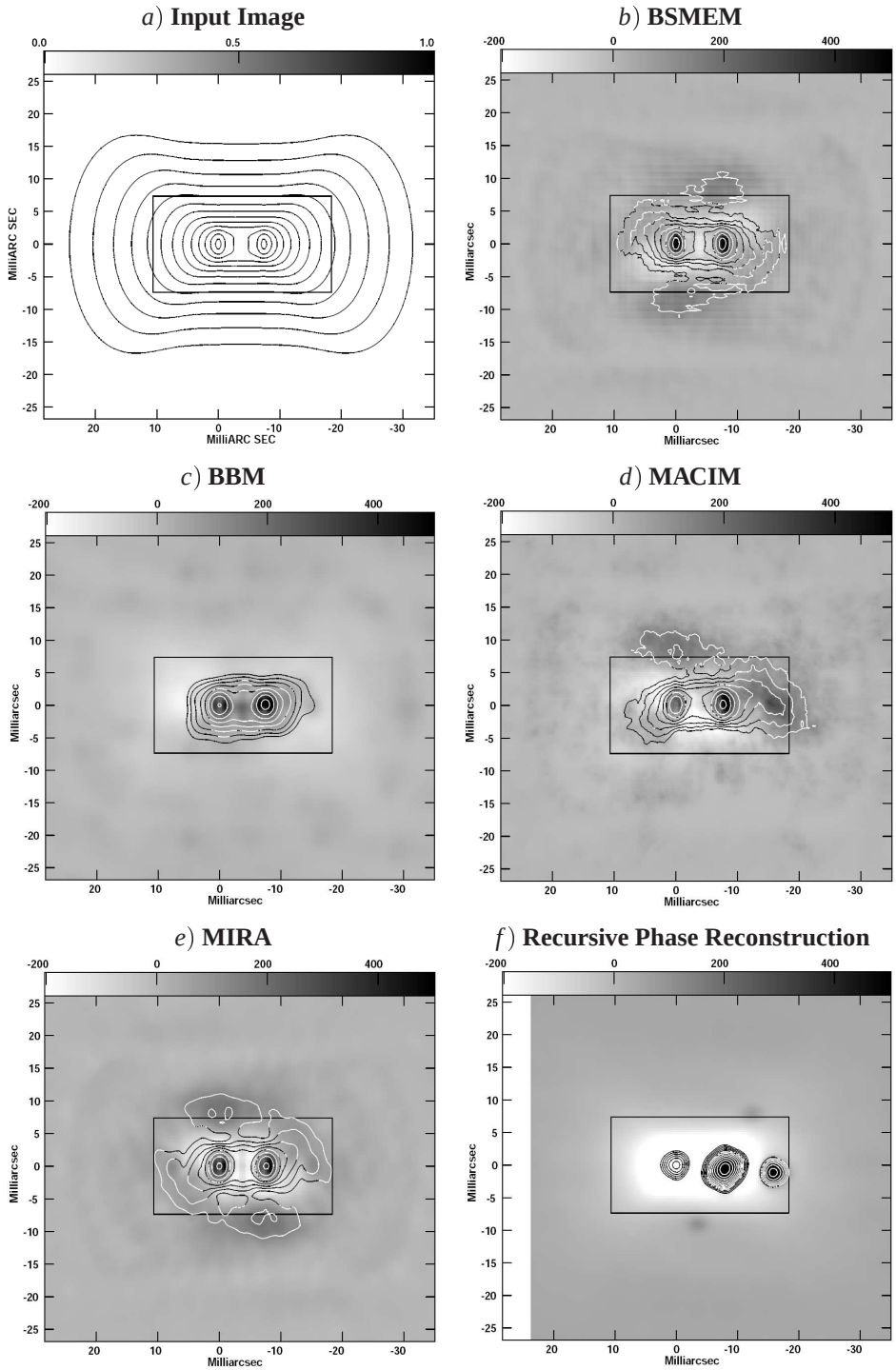

Figure 5.6: For the IAU imaging beauty contest 2006, a image of a optically thin disk had to be reconstructed (Figure *a*). Figures *b* to *f* depict the entry images by the contestants. Whereas the contours show the brightness distribution, the greyscale shows the residuals relative to the original image (Image Credit: Lawson et al. 2006).

5.5 Conclusions

From the studies presented in this chapter, we conclude that model-independent aperture synthesis imaging is coming in reach of optical interferometry:

- Our comparative study using observational data of Capella (Section 5.2), has demonstrated that simple source geometries, such as binary stars, allow the reconstruction of real images already with very sparse *uv*-coverage. In this case, the quality of the reconstruction did not depend strongly on the algorithm used (CHM, DFM, BBM), although for very poor coverage (corresponding to observations on only one 3-telescope configuration) we succeeded only using the BBM algorithm and assuming a restricted reconstruction area.

- Our work on simulated data in the context of the MATISSE study showed that with a reasonable amount of observing time (3 nights with 4 ATs), also complex, astrophysical highly relevant objects such as protoplanetary disks, can be mapped with optical interferometers. Especially in the presence of noise (5%), the maps obtained with the BBM algorithm showed a significantly higher quality than the CHM results.

- For the IAU Interferometry Imaging Beauty Contest 2006, we have contributed aperture synthesis reconstructions obtained with the BBM algorithm. The contest has demonstrated that already several sophisticated algorithms are available, which can deal even with very challenging data sets, corresponding to only 4 nights with 3 UTs, and resembling objects with extended structure. Comparing our image with the aperture synthesis images contributed by other groups, the quality of our reconstruction was ranked as #3 out of 5.

6 Radiative Transfer Modeling of the Active Accretion Disk around MWC 147

Based on an article to be submitted to ApJ.
Kraus, S., Preibisch, Th., Ohnaka, K.

6.1 Overview and Context

For Herbig AeBe stars, several indications for their pre-main-sequence evolutionary stage have been found. Perhaps most characteristic is their strong near- to far-infrared excess emission, which is generally interpreted as the presence of substantial quantities of gas and dust; the residual material from their formation. These stars were also found to possess line emission, e.g. from hydrogen or helium, maybe tracing ongoing accretion from the circumstellar disk onto the star via magnetospheric accretion columns.

While it is well established that circumstellar dust is responsible for the IR excess emission characteristic for an HAeBe star, the three-dimensional distribution of this material is still being debated. By modeling the spectral energy distribution (SED), various authors attempted to constrain the distribution of the circumstellar matter; assuming as different geometries as optically thick accretion disks (e.g. Hillenbrand et al. 1992), optically thin spherical envelopes (Miroshnichenko et al. 1997), envelopes with bipolar outflow cavities (Hartmann et al. 1993), or combinations of disk and halo geometries (Vinković et al. 2006). However, as demonstrated by Men'shchikov & Henning (1997) and others, these SED model fits are highly ambiguous, and only the combination of SED modeling with high-resolution imaging can provide crucial constraints on the real geometry of the circumstellar matter.

In recent years, first near-infrared (NIR) interferometric studies on Herbig AeBe stars could make important contributions for a better understanding of the structure of the circumstellar material around these stars. For instance, a survey performed by Millan-Gabet et al. (2001) with the IOTA interferometer provided the surprising result that the NIR emission is best described by ring-like or spherical geometries

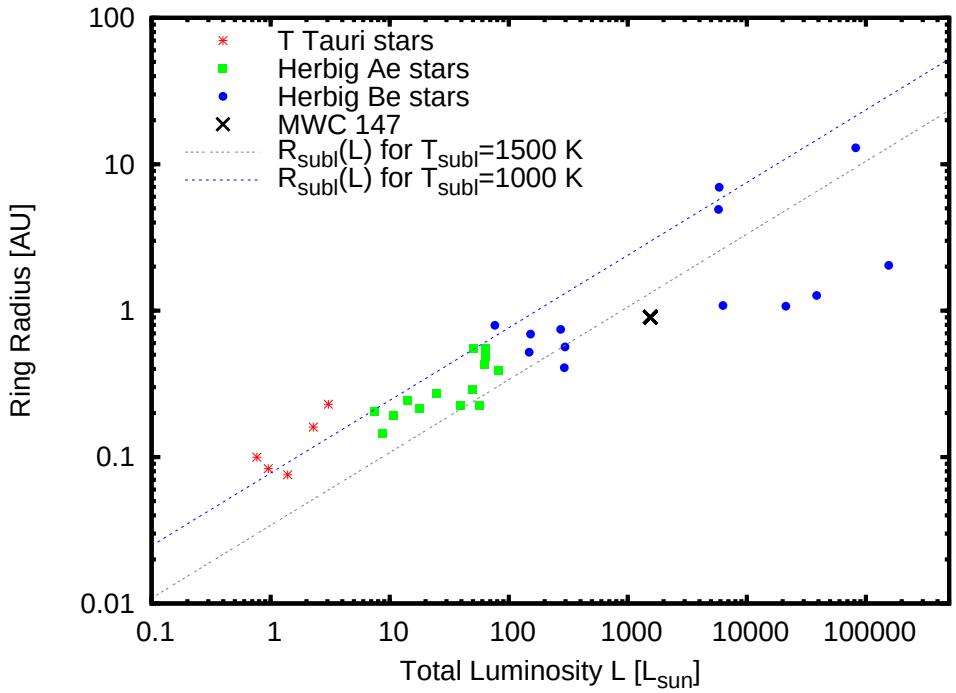

Figure 6.1: Size-Luminosity relation for Herbig AeBe stars (Figure adopted from Millan-Gabet et al. 2007), containing continuum long-baseline interferometric observations from various interferometers. While the measured sizes for most T Tauri and Herbig Ae stars seem to follow the dust sublimation radius $R_{\rm subl}$ corresponding to sublimation temperatures between 1000 and 1500 K (dotted line), some Herbig Be stars (including MWC 147, marked as cross) show significantly smaller diameters. Monnier & Millan-Gabet (2002) interpreted this trend with the presence of optically-thick gas shielding the dust at the inner rim and causing the measured sizes to shrink.

rather than with the "classical" optically thick, geometrically thin accretion disk models (e.g. Lynden-Bell & Pringle 1974; Hillenbrand et al. 1992; Chiang & Goldreich 1997). This observational result also stimulated theoretical work, especially for passive irradiated circumstellar disks; e.g. by Natta et al. (2001), Dullemond et al. (2001), and Isella & Natta (2005). These models reproduce the ring-like morphology by introducing pronounced, hot dust emission at the inner rim of the circumstellar disk.

Monnier & Millan-Gabet (2002) found a correlation between the NIR size and the stellar luminosity, suggesting that the NIR continuum emission mainly traces hot dust at the inner sublimation radius, missing any shielding by optically thick gas inside of the sublimation radius. However, for the most luminous Herbig Be stars, deviations from the simple $R \propto L^{1/2}$ size-luminosity relation were found (see Fig. 6.1) with measured sizes smaller than expected from the stellar luminosity. Monnier & Millan-Gabet speculated that for these hot stars, the inner rim might be located closer to the star due to the presence of an inner gaseous disk, which shields the dust disk from the stellar radiation.

In order to resolve this puzzle, we studied the particularly luminous Herbig Be star MWC 147. The

spectral type of B6 (corresponding to a stellar mass of $\sim$ 6.6 $M_{\odot}$) places MWC 147 at the upper end of the mass-range covered by the Herbig Be class. By combining, for the first time, near- and mid-infrared long-baseline interferometric observations on one Herbig AeBe star, we probe different dust temperatures and regions within the putative accretion disk. We have obtained spectro-interferometric observations of MWC 147 with the VLTI instruments MIDI (*N*-band) and AMBER (*K*-band) and complement our data sets with archival PTI NIR broadband interferometry. The emission from MWC 147 is clearly resolved and has a characteristic physical size of $\sim$ 1.3 AU and $\sim$ 9 AU (Gauss FWHM for $d = 800$ pc) at wavelengths of 2.2 μm and 11 μm, respectively. The spectrally dispersed AMBER and MIDI interferograms both reveal a strong increase of the characteristic size towards longer wavelengths, much steeper than predicted by analytic disk models assuming power-law radial temperature distributions.

To derive constraints on the geometrical distribution of the dust, we compare our interferometric measurements to 2-D, frequency-dependent radiation transfer simulations of circumstellar disks and envelopes. These models take the SED from the optical to the far-infrared into account and are also constrained by complementary archival spectra from IRS onboard the *Spitzer* Space Telescope. We consider Keplerian disk models with and without a puffed-up inner rim. The shape of the rim is refined iteratively by our radiative transfer code, taking the density-dependence of the sublimation temperature into account. We also consider accretion luminosity from a gaseous disk inside the dust sublimation zone as a potential contributor to the continuum emission.

We find that radiative transfer models of passive irradiated disks, which match the SED very well, predict visibilities that are considerably lower than measured. As this corresponds to an overestimation of the angular size by factors of 4 (at 2.2 μm) and 2 (at 11 μm), respectively, such models can be ruled out. Including the radiation from an inner gaseous accretion disk leads to good agreement between the model predictions and the observed SED, NIR visibilities, and MIR visibilities.

This project was conducted in close collaboration with Thomas Preibisch, who also wrote the initial ESO proposals, in which frame the VLTI data was collected. For the radiative transfer modeling, I applied the Monte Carlo radiative transfer code *mcsim_mpi* written by Keiichi Ohnaka. He also gave assistance on using the code and introducing accretion luminosity. Besides implementing various new disk and envelope geometries, I adopted the code to iteratively refine the shape and location of the inner dust rim. The software was also embedded in a software framework, which allows us to manage a large number of simulations and which analyses the resulting SEDs and images and fits them to spectro-interferometric data. Thomas Preibisch gave important feedback in the course of the modeling process and also commented the A&A paper draft.

6.2 Introduction

The distribution of the circumstellar material around Herbig Ae/Be (HAeBe) stars, i.e. intermediate-mass, pre-main sequence stars, is still a matter of debate. Until recently, the spatial scales of the inner circumstellar environment (a few AU, corresponding to $\lesssim 0.1''$) were not accessible to optical and infrared imaging observations, and conclusions drawn on the spatial distribution of the circumstellar material were, in most cases, entirely based on the modeling of the spectral energy distribution (SED). However, fits to the observed SEDs are highly ambiguous. For example, the SEDs of some HAeBes could be equally well explained with very different models such as geometrically thin disks and spherical envelopes (Hillenbrand et al. 1992; Miroshnichenko et al. 1997). More complex models like disks surrounded by a spherical envelope (Natta & Kruegel 1995; Natta et al. 2001; Miroshnichenko et al. 1999), flared outer disks, puffed-up inner disk rims (Dullemond et al. 2001), and disk plus inner halo models (Vinković et al. 2006) have also been used to successfully fit the observed SEDs of HAeBes. To make further progress on this topic, observations with spatial resolution at the level $\lesssim$ 10 milli-arcseconds (mas) are needed to explore the inner circumstellar regions of these objects in detail. Such observations can only be performed with long-baseline interferometry.

In recent years, NIR interferometry made important contributions towards a better understanding of the structure of the circumstellar material around HAeBe stars. Malbet et al. (1998) and Akeson et al. (2000) partially resolved the circumstellar environment of several YSOs with the Palomar Testbed Interferometer (PTI). Later, a survey performed by Millan-Gabet et al. (2001, ApJ 546, 358) with the Infrared Optical Telescope Array (IOTA) showed that the NIR continuum emission is best described by ring-like or spherical geometries. Other NIR interferometric studies on YSOs were carried out using the Keck interferometer (e.g. Eisner et al. 2004) and the Very Large Telescope Interferometer (VLTI, Malbet et al. 2006a).

Due to their limited *uv*-coverage, most existing studies could not investigate the geometry of individual sources in detail and derived only characteristic sizes of the emission via the comparison of the data to simple analytic models. The correlation between the characteristic NIR size and the stellar luminosity is consistent with the idea that the NIR continuum emission mainly traces hot ($T_{\rm subl} \approx 1\,500$ K) dust close to the inner dust sublimation radius $R_{\rm subl}$ (Monnier & Millan-Gabet 2002). While a rather simple $R \propto L^{1/2}$ scaling law between stellar luminosity L and NIR size R appears to hold throughout the low- to medium luminosity part of the observed stellar sample, the very luminous early B-type stars exhibit some deviations from this size-luminosity relation; in some cases the derived NIR sizes are smaller than predicted. Monnier & Millan-Gabet (2002) speculated that this might be due to the presence of an inner gaseous disk which shields the dust disk from the stellar radiation, allowing the inner rim of the dust disk to exist closer to the star. This shielding effect would be most efficient for hot stars since they emit strong UV radiation, which would be particularly efficiently scattered by an optically thick gaseous

Table 6.1: Stellar parameters for MWC 147 from Hernández et al. (2004), assuming $R_V = 3.1$.

Parameter		Value
Spectral Type		B6
Effective Temperature	$T_{\rm eff}$	14,125 K
Luminosity	L	1,550 $L_\odot$
Mass	M	6.6 $M_\odot$
Age	t	0.32 Myr
Distance	d	800 pc
Extinction	A_V	1.2 mag
Stellar Radius	$R_\star$	6.63 $R_\odot$

inner disk.

At mid-infrared (MIR) wavelengths, MIDI observations of HAeBe stars by Leinert et al. (2004) revealed characteristic dimensions of the emitting regions at 10 μm, which ranged from 1 AU to 10 AU. Again, due to the poor uv-coverage, only very limited information about the geometry of the dust distribution could be derived. A more detailed interferometric study of one Herbig Ae star, HR 5999, was performed recently by our group (Preibisch et al. 2006), based on a set of ten MIDI measurements at different projected baseline lengths and position angles. Detailed modeling with 2-D, frequency-dependent radiation transfer simulations provided a good fit of the MIDI data with a model of a geometrically thick disk, which is truncated at $\sim$ 2.7 AU and seen under an inclination angle of $\sim 60^\circ$. Other recent MIR studies tried to determine the geometry of FU Orionis objects (Ábrahám et al. 2006; Quanz et al. 2006).

MWC 147 (alias HD 259431, BD+10 1172, HBC 529, V700 Mon) is a well-studied Herbig Be star in Monoceros. There is some uncertainty concerning the distance and the physical parameters of this star. From the analysis of the Hipparcos parallax data by van den Ancker et al. (1998), a lower limit on the distance of > 130 pc was derived, while a reanalysis suggested a distance of 290^{+200}_{-84} pc (Bertout et al. 1999). This distance estimate, however, is in conflict with the apparent location of MWC 147 in the NGC 2247 dark cloud, which is part of the cloud complex in the Monoceros OB1 association at a distance of $\sim 800 - 900$ pc (Oliver et al. 1996, A&A 315, 578). In this paper, we assume a distance of 800 pc for MWC 147 (consistent with most other recent studies of MWC 147) and use the main stellar parameters as listed in Table 6.1, which were taken from the study of Hernández et al. (2004).

Numerous observational results strongly suggest the presence of a circumstellar disk around MWC 147. The object shows a strong infrared excess of about 6 mag at MIR wavelengths, clearly demonstrating the presence of circumstellar material. Hillenbrand et al. (1992) fitted the SED of MWC 147 with a model assuming a massive, actively accreting disk ($\dot{M}_{\rm acc} = 1.01 \times 10^{-5} M_\odot {\rm yr}^{-1}$). Mid-infrared (10 μm and 18 μm) observations revealed an elongated diffuse emission component around MWC 147 along

PA $\sim$60°, extending out to $\sim$6″ and contributing $\sim$ 34% to the total flux (Polomski et al. 2002). Mannings (1994) determined the 1.1 mm flux of MWC 147 and estimated the mass in the circumstellar disk/envelope to be $< 0.09 M_{\odot}$. The study of the far UV spectrum of MWC 147 by Bouret et al. (2003) also suggested the presence of a flared circumstellar disk. Polomski et al. (2002) imaged MWC 147 in the MIR and concluded that the star is surrounded by a moderately flared disk and probably also an extended envelope. Measurements by Jain et al. (1990) showed a significant amount of linear polarization ($\sim$1% along PA $\sim$ 106°) but no wavelength-dependence of the polarization. The high observed rotational velocity of $v \sin i = 90$ km s^{-1} (Boehm & Catala 1995) suggests a high inclination of the rotation axis of MWC 147 with respect to the line-of-sight; this implies that the orientation of the circumstellar disk should be closer to edge-on than to face-on.

Evidence for a strong stellar wind from MWC 147 comes from the observed P Cygni profiles in several emission lines (Bouret et al. 2003). A quantitative modeling of FUSE spectra revealed multiple absorption components with different temperatures, consistent with a flared disk interpretation (Bouret et al. 2003). Based on the intensity ratio of infrared hydrogen lines, Nisini et al. (1995) estimated a mass loss rate of $2.0 \pm 0.4 \times 10^{-7} M_{\odot}$yr^{-1}, which is slightly higher than the mass loss rates determined from radio observations ($0.68 \times 10^{-7} M_{\odot}$yr^{-1}, Skinner et al. 1993).

First interferometric measurements on MWC 147 were presented by Millan-Gabet et al. (2001), providing an upper limit on the *H*-band size. Akeson et al. (2000) observed MWC 147 with the Palomar Testbed Interferometer (PTI) and resolved its emission in the *K*-band at baselines around 100 m. They derived a best-fit uniform disk diameter of 2.28 mas (0.7 AU) in the *K*-band.

The star has a visual companion at a projected separation of 3.1″ ($\approx$ 2 500 AU, Baines et al. 2006). While Vieira & Cunha (1994) classified MWC 147 as a spectroscopic binary with a period of about one year, this claim could not be confirmed in more recent observations (Corporon & Lagrange 1999).

6.3 Observations and Data Reduction

6.3.1 PTI

The Palomar Testbed Interferometer (Colavita et al. 1999) is a NIR long-baseline interferometer operated by the Jet Propulsion Laboratory (JPL). Its three 40 cm-telescopes can be combined pairwise to measure the visibility amplitude. The FOV corresponding to the diffraction-limited beam of the PTI telescopes is about 1.″4, while the interferometric FOV is about 25-30 mas (Monnier et al. 2006).

MWC 147 was observed on the NS (Akeson et al. 2000) and NS & NW baselines (Wilkin & Akeson 2003). Yet unpublished data for the SW baseline was retrieved from the PTI archive. To obtain a uniformly calibrated dataset, we processed the new dataset together with the previously published data

Table 6.2: Calibrator stars information for the interferometric observations presented in Table 9.1.

Star	V	K	N [Jy]	Spectral Type	$d_{\mathrm{UD},K}$ [mas]	$d_{\mathrm{UD},N}$ [mas]
HD 42807	6.44	4.85	0.5	G2V	0.45 ± 0.03^a	
HD 43042	5.20	4.13	1.0	F6V	0.59 ± 0.10^b	
HD 43587	5.71	4.21	1.0	F9V	0.48 ± 0.30^c	
HD 45415	5.55	3.02	3.3	G9III	1.06 ± 0.02^a	
HD 46709	5.91	2.62	4.4	K5III	1.66 ± 0.02^a	
HD 50692	5.76	4.29	0.8	G0V	0.56 ± 0.10^b	
HD 25604	4.35	2.03	7.2	K0III		1.88 ± 0.05^a
HD 31421	4.09	1.41	13.6	K2IIIb		2.58 ± 0.15^a
HD 49161	4.78	1.58	7.2	K4III		2.88 ± 0.17^a

Notes – The V-band magnitudes were taken from SIMBAD, the K-band magnitudes from the 2MASS point source catalog, and the N-band (12 μm) flux density from the IRAS point source catalog V2.0

[a] UD diameter taken from the CHARM2 catalog (Richichi et al. 2005).

[b] UD diameter taken from the CHARM catalog (Richichi & Percheron 2002).

[c] UD diameter adopted from Pasinetti Fracassini et al. (2001), using the Hipparcos parallax of 51.76 mas measured for HD 43587.

using the V2Calib V1.4 software[1]. The individual PTI measurments were binned so that each bin contains datasets covering less than 15° variation along PA. As the measurements on the PTI-NS baseline also cover a relatively wide range of PAs ($\sim$ 23°), we divided those measurements into two halves (depending on PA) before averaging.

Taking the projection of the telescope baselines onto the sky into account, the length of the baselines range from 78.6 m to 105.1 m (see Table 9.1), corresponding to angular resolutions of 7.″1 and 5.″3 mas (=5.7 AU, 4.3 AU) at 2.24 μm.

6.3.2 VLTI/AMBER

AMBER (Petrov et al. 2003b, 2006a) is the NIR beam-combiner of the ESO Very Large Telescope Interferometer and allows one to combine the light from up to three telescopes simultaneously, providing not only three simultaneous visibility amplitudes, but also the closure phase relation. With our observations on MWC 147, we obtained spectrally dispersed interferograms in the low resolution (LR) mode ($R = \lambda/\Delta\lambda = 35$), which resolves the K-band into 11 spectral channels. The observations were conducted within ESO open time (OT) programme 076.C-0138 (P.I. Th. Preibisch) using the 8.4 m unit telescopes UT1-UT3-UT4. Due to problems with the fiber injection during that night, the flux reaching

[1]The V2Calib software is available from the website http://msc.caltech.edu/software/V2calib/

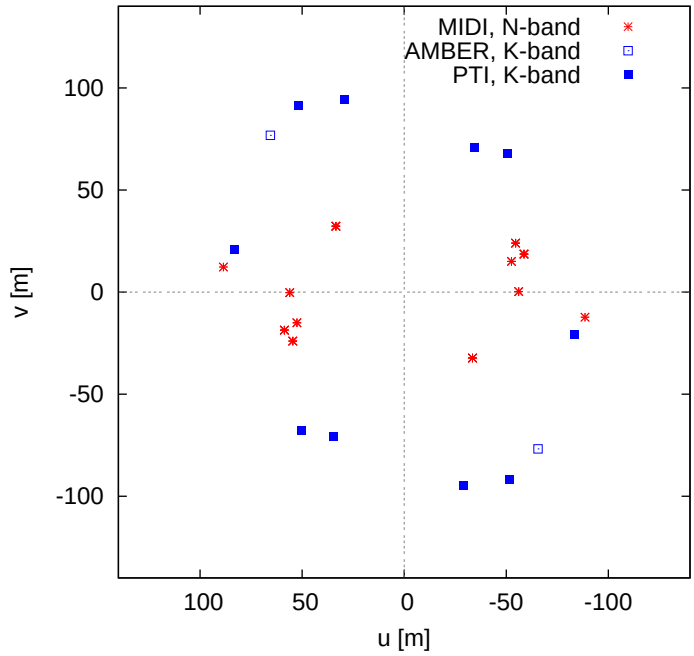

Figure 6.2: *uv*-plane coverage of the VLTI/MIDI, VLTI/AMBER, and archival PTI data.

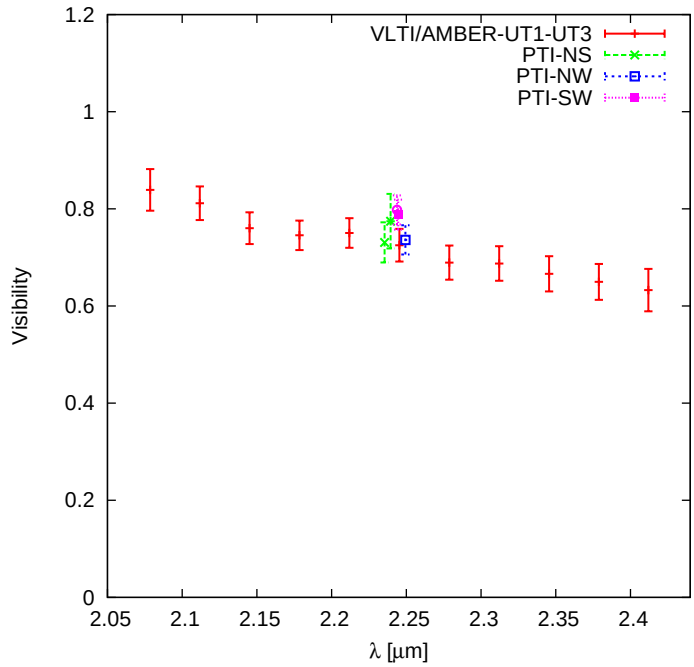

Figure 6.3: Wavelength-dependence of the visibility measured with VLTI/AMBER and the visibilities measured with PTI using broad-band filters.

the AMBER beam combiner from UT4 was about a factor of 3 lower than from the other telescopes. Therefore, clear fringes were detectable only on one of the three baselines (UT1-UT3), and no closure phase signal could be measured. The length and orientation of the projected baseline for this AMBER measurement (101 m, PA 40°) is similar to the measurement at the PTI-NS baseline, but adds the information about the spectral dependence of the visibility along the *K*-band. Since AMBER uses fibers as spatial filters to convert phase variations into amplitude modulations, the FOV is given by the diameter of the fibers on the sky ($\sim$ 60 mas).

The AMBER data were reduced with version 2.4 of the *amdlib* software (Tatulli et al. 2006). Due to the absence of a fringe tracker, a large fraction of the interferograms is of rather low contrast (see discussion in Petrov et al. 2006a). Therefore, we remove those frames from our dataset for which *(a)* the light injection from the contributing telescopes was unsatisfying; i.e., the intensity ratio between the photometric channels was larger than 4, *(b)* the atmospheric piston was larger than $1/4$ of the coherence length $\lambda \cdot R$, or *(c)* the fringe contrast was decreased due to instrumental jitter (the 20% best interferograms were selected based on the Fringe SNR criteria, as defined in Tatulli et al. 2006). In Fig. 6.3 the calibrated *K*-band visibilities derived from the AMBER and PTI measurements are shown as a function of wavelength.

6.3.3 VLTI/MIDI

The MIDI instrument allows one to coherently combine the light of two VLTI telescopes and operates at MIR wavelengths (*N*-band, 8-13 μm). The recorded spectrally dispersed interferograms are produced by modulating the optical path delay (OPD) around the point of zero OPD. From these scans, not only the spatially filtered flux (FOV 2″), but also the visibility amplitude can be derived for each wavelength bin separately. For a more detailed description of the MIDI instrument and observation procedure, we refer to Przygodda et al. (2003) and Leinert et al. (2004).

The MIDI observations presented in this paper were carried out for the OT programme 074.C-0181 (P.I. Th. Preibisch), using the NaCl prism as dispersive element (providing a spectral resolution of $R = 30$) and the HIGH-SENS instrument mode. In total, seven observations were carried out on three different baseline configurations, including the telescope pairs UT2-UT4, UT2-UT3, UT3-UT4. The lengths of the projected baselines range from 46.5 to 89.4 m, yielding an effective angular resolution between 54 and 28 mas at a wavelength of 10 μm (corresponding to 43 and 23 AU).

To extract visibilities from the MIDI data, we used the data reduction software package MIA+EWS[2] (Release 1.3). This package contains two data reduction programs which are based on independent algorithms; namely, a coherent (EWS) and an incoherent approach (MIA). The reduction results obtained with both algorithms agree very well (within 3% for the calibrated visibility) with the datasets

[2]The MIA+EWS software package is avaiable from the website http://www.mpia-hd.mpg.de/MIDISOFT/

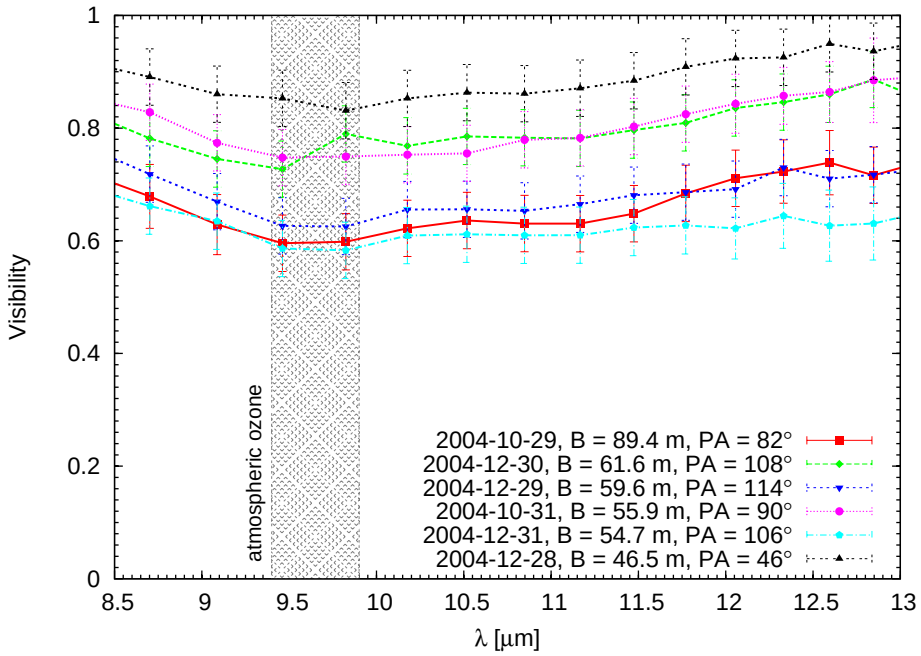

Figure 6.4: Visibilities measured with MIDI as a function of wavelength.

from 2004-10-30, 2004-11-01, 2004-12-30, 2004-12-31, 2004-12-29, and 2005-01-01, indicating a good quality of these datasets. However, by inspecting the acquisition image for the dataset from 2005-02-28, we found that the beam overlap was poor for this measurement and, thus, rejected it from our further analysis. The inspection of the acquisition images also indicated that the visual companion at a separation of 3.″1 was not in the MIDI FOV and therefore does not affect the measured visibilities. The wavelength-dependent calibrated visibilities of the remaining six datasets are shown in Fig. 6.4.

For all interferometers used within our study, the visibility measurements were corrected for atmospheric and instrumental effects using calibrator stars observed during the same night. The calibrator stars as well as their assumed angular diameters are listed in Table 8.1. Fig. 9.4 shows the *uv*-plane coverage obtained with the presented observations.

6.3.4 Complementary Spitzer/IRS spectra

In order to constrain the SED for our radiative transfer modeling as tightly as possible, we obtained MIR spectra from the *Spitzer* Space Telescope Archive. These spectra were recorded on 2004-10-26 within GTO programme ID 3470 (P.I. J. Bouwman) using the Infrared Spectrograph IRS (Houck et al. 2004). The dataset is comprised of four exposures, two taken in the Short-High mode (SH, wavelength range

from 9.9 to 19.6 μm) and two taken in the Long-High mode (LH, 18.7 to 37.2 μm). Both modes provide a spectral resolution of $R \approx 600$. With slit sizes of $4\farcs7 \times 11\farcs3$ (SH mode) and $11\farcs1 \times 22\farcs3$ (LH mode), IRS integrates flux from areas much larger than those collected in the spatially filtered MIDI spectrum. The spectra were pre-processed by the S13.2.0 pipeline version at the Spitzer Science Center (SSC) and then extracted with the SMART software, Version 5.5.7 (Higdon et al. 2004).

Table 6.3: Observation log for interferometric observations on MWC 147. For more detailed information about the calibrator stars, we refer to Table 8.1.

Instrument	Date (UT)	HA	Band/ Spectral Mode	Baseline	Projected Baseline Length [m]	Projected Baseline PA [°]	Calibrators	Ref.
			Near-Infrared					
IOTA/FLOUR	1998		H	38m	~ 22	~ 25	see Ref. 1	1
IOTA/FLOUR	1998		K'	38m	~ 21	~ 15	see Ref. 1	1
PTI	1999, 2000, 2003	< 0	K	NS	105.1	29	HD 42807, HD 43042,	2,3
		$\geqslant 0$		NS	98.9	17	HD 43587, HD 46709, HD 50692	
PTI	2004		K	NW	85.7	76	HD 43042, HD 46709 HD 50692	3
PTI	2003, 2004	< 0	K	SW	78.6	-26	HD 42807, HD 46709	
		$\geqslant 0$		SW	84.4	-37	HD 50692	
VLTI/AMBER	2006-02-20	03:14	K/LR	UT1-UT3	101.0	40	HD 45415	
			Mid-Infrared					
VLTI/MIDI	2004-10-30	08:49	N/PRISM	UT2-UT4	89.4	82	HD 31421, HD 49161	
VLTI/MIDI	2004-11-01	05:23	N/PRISM	UT2-UT4	55.9	90	HD 25604, HD 49161, HD 31421	
VLTI/MIDI	2004-12-30	02:33	N/PRISM	UT3-UT4	59.6	114	HD 49161	
VLTI/MIDI	2004-12-31	04:26	N/PRISM	UT3-UT4	61.6	108	HD 49161	
VLTI/MIDI	2005-01-01	05:43	N/PRISM	UT3-UT4	54.7	106	HD 31421, HD 49161	
VLTI/MIDI	2004-12-29	06:42	N/PRISM	UT2-UT3	46.5	46	HD 49161	
VLTI/MIDI (rej.)	2005-02-28	00:04	N/PRISM	UT2-UT3	39.3	44	HD 49161	

References – [1] Millan-Gabet et al. 2001, and re-processing of data presented in [2] Akeson et al. 2000 and [3] Wilkin & Akeson 2003

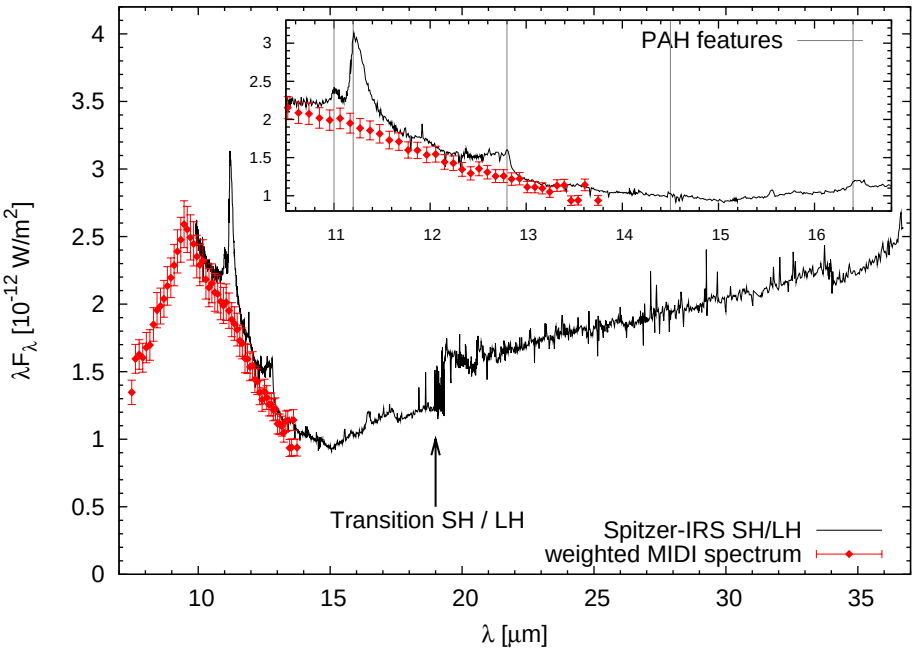

Figure 6.5: Comparison of the measured MIDI spectrum and the spectrum extracted from archival *Spitzer* IRS data.

6.4 Results

6.4.1 MIR spectrum

In the overlapping wavelength regime between 10 and 13 μm, the MIDI and *Spitzer*-IRS spectra show good quantitative agreement, both in the absolute level of the continuum flux and in the spectral slope (see Fig. 6.5). However, the IRS spectrum exhibits some line features which do not appear in the MIDI spectrum. As these emission lines are most pronounced at wavelengths of 11.0, 11.2, 12.8, 14.5, and 16.4 μm, we attribute these features to the presence of Polycyclic Aromatic Hydrocarbons (PAHs, Allamandola et al. 1985; van Dishoeck 2004). For the strong and rather broad emission feature at 11.2 μm, contributions from the 11.3 μm crystalline silicate feature are also possible.

PAHs were found towards a large variety of objects, including T Tauri stars and HAeBe stars (Acke & van den Ancker 2004). Meeus et al. (2001) found that the PAH bands are, on average, stronger in sources with strong far-infrared/millimeter excess. Since a strong far-infrared excess emission is often attributed to a flared disk geometry, this might indicate that the PAH emission mainly arises from the outer regions of a flared disk. This scenario is also supported by our data, as the PAH spectral features are only seen in the *Spitzer*-IRS spectrum, but not in the MIDI spectrum with its much smaller field-of-view of only $\sim 2''$. This effect agrees qualitatively with observations of other sources which attributed large fractions

of the PAH emission either to surrounding reflection nebulae (e.g. van Boekel et al. 2004b, Rho et al. 2006) or to the outer regions of HAeBe disks (Habart et al. 2004, 2006). This difference in the beam size is probably also causing the bump which appears in the IRS spectrum at the transition between the two gratings (see Fig. 6.5).

6.4.2 Geometric model fits

As a direct image reconstruction is not yet feasible with the current generation of infrared interferometers, the measured observables (e.g. visibilities) are used to constrain the parameters of a model for the object morphology. In most studies presented until now, either purely geometric profiles (in particular uniform disk (UD) and Gaussian profiles) or physically motivated geometries, such as ring profiles or analytic accretion disk models with a temperature power law are employed. Ring models are justified by the theoretical expectation that most of the NIR emission originates from a rather small region around the dust sublimation radius (e.g., Millan-Gabet et al. 2001; Monnier & Millan-Gabet 2002). A common problem with such simple geometric models is that the observed emission does not originate exclusively from the circumstellar material: a certain fraction comes directly from the central star and contributes as a spatially (nearly) unresolved component, and the existence of extended background emission, which is fully resolved, is also possible. For the model fits one therefore has to specify which fraction of the total flux $F_{\rm tot}$ at any wavelength has to attributed to the different spatial components. The stellar flux contribution $f_{\rm star/tot}(\lambda) = F_{\rm star}/F_{\rm tot}$ is often estimated from the SED, while the extended component $f_{\rm ext/tot}(\lambda) = F_{\rm ext}/F_{\rm tot}$ is usually assumed to be identical zero. These assumptions are, however, associated with a considerable uncertainty.

To allow comparison with earlier NIR interferometric studies on MWC 147, we keep the flux ratios from Millan-Gabet et al. (2001), namely $f_{\rm star/tot}(2.1\,\mu{\rm m}) = 0.16$, and $f_{\rm ext/tot}(2.1\,\mu{\rm m}) = 0.0$ for the analytic fits. The same flux ratio was assumed by Wilkin & Akeson (2003), while Akeson et al. (2000) used $f_{\rm star/tot}(2.1\,\mu{\rm m}) = 0.10$. At mid-infarad wavelengths, the stellar contribution is likely to be negligible for a B6-type star; i.e., $f_{\rm star/tot}(10\,\mu{\rm m}) \sim 0$. In Sect. 6.6.6.3 we will discuss the reliability of these values based on the results of our radiative transfer modeling.

6.4.2.1 Wavelength-dependent characteristic sizes

To obtain a first estimate for the object size, we fit the most common analytic profiles to our interferometric data; namely, the Gaussian, UD, and ring profiles. For mathematical descriptions of these profiles, we refer to Kraus et al. (2005b, UD profile) and Millan-Gabet et al. (2001, Gaussian & ring profile). For consistency with Monnier et al. (2005) and others, for the ring profile we assume a uniform bright ring with average diameter Θ and a fixed width of 20%. As the apparent object size is expected to change with wavelength, we fitted these profiles to subsets of our data, covering the wavelength ranges

of 2.0-2.4 μm, 8.2-9.9 μm, 10.5-11.8 μm, and 12.0-13.1 μm. The visibilities measured in these subbands are fitted to the visibility profiles using a Levenberg-Marquardt least-square fitting algorithm, taking the chromatic change in resolution within the bandwidth into account.

The fits were performed for the case of circular symmetry (e.g. a disk seen face-on) and also for elliptical structures (e.g. an inclinded disk). The obtained diameters and goodness-of-fit values ($\chi^2_r = \sum \left[(V^2 - V^2_m)/\sigma_V\right]^2 / N_V$, with V^2 the measured squared visibility, V^2_m the squared visibility computed from the model, and N_V the number of measurements) are given in Tables 6.4 and 6.5.
The χ^2_r values already indicate that the elliptical geometries are a significantly better representation of our data than the circular models. In order to illustrate this object elongation, we show the corresponding geometries in Fig. 6.7. As the detection of object elongation requires strict uniformity in the observational methodology, we did not include the single-baseline AMBER measurement because the mixture of broadband and spectrally dispersed interferometric observations might easily introduce artefacts.

Whereas the elongation is only marginally evident in the PTI NIR measurements, a significant elongation was found in the MIR data.

It is interesting to compare the elongation found in the interferometric observations with the 11.7/18.2 μm color temperature map published by Polomski et al. (2002, see Fig. 6.7*c*)). Although these color temperature maps show structures of scales of several arcseconds (e.g. on scales a hundred times larger), they reveal an orientation ($\sim$60°) and axis ratio similar to those of the structure seen in our MIDI observations.

Our combined IOTA/PTI/AMBER/MIDI dataset also allows us to study the wavelength-dependence of the apparent size. For this, we fitted the visibility measurement in each individual spectral channel with the analytic formula for Gaussian intensity profiles (the result does not depend strongly on the assumed profile). The determined diameters are shown in Fig. 6.6. The increase of the apparent size with wavelength is usually interpreted as a consequence of the radial temperature profile for the circumstellar material (i.e. material at larger distances from the star is cooler). It will be interpreted qualitatively in Sect. 6.5.1 and is also discussed in the context of our radiative transfer modeling in Sect 6.6.

Akeson et al. (2000) examined the possibility whether the measured visibilities could indicate the presence of a close companion. Since PTI has observed MWC 147 several times over a period of $\sim$ 4 yrs and found no significant variations on the NS-baseline, we consider the binary scenario as very unlikely. For example, assuming, just for the sake of argument, a total system mass of 7 $M_\odot$ and a semi-major axis of 10 AU, this would give an orbital period of $\sim$ 12 yrs and should result in significant visibility variations over the covered 4 yrs.

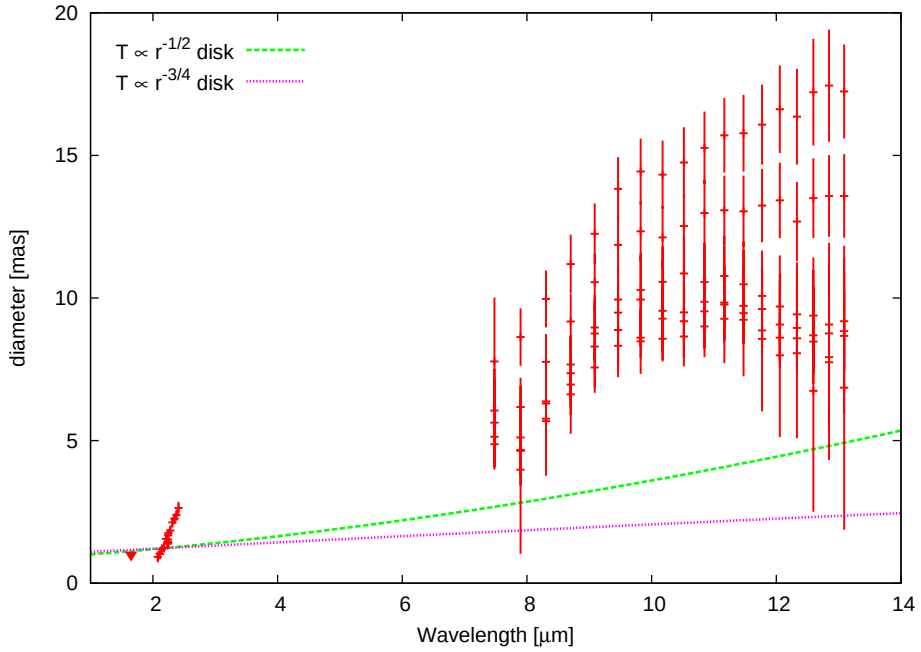

Figure 6.6: Wavelength dependence of the characteristic size over the *H*, *K* and *N*-band. Gaussian intensity profiles were assumed. The IOTA *H*-band measurement provides only an upper limit on the size.

6.5 Interpretation

6.5.1 Wavelength-dependent size and comparison with analytic disk models

While the NIR flux is dominated by thermal emission from hot ($\sim$ 1 500 K) dust in the innermost disk regions close to the dust sublimation radius, the MIR flux originates predominantly from cooler ($\sim$ 200 – 300 K) dust further out in the disk, leading to the observed increase of the apparent size with wavelength. Infrared spectro-interferometry covering a wide wavelength range therefore provides a unique insight into the radial disk structure.

The most previous interferometric studies of Herbig Be disks have focussed either on the NIR or MIR morphology. Our combined NIR + MIR dataset provides, for the first time, a much wider wavelength coverage, ranging from $\sim 2\,\mu$m to 13 μm, and allows us to test whether the disk models routinely applied for NIR or MIR interferometric observations can reproduce the wavelength-dependence of the size.

Analytical models, both of passive irradiating circumstellar disks (Friedjung 1985) as well as viscous, actively accreting disks (Lynden-Bell & Pringle 1974), predict that the radial temperature profile of YSO disks should follow a simple power-law $T(r) \propto r^{-\alpha}$. Most studies infer a power law index of $\alpha = -3/4$ (Millan-Gabet et al. 2001; Eisner et al. 2005) or $-1/2$ (e.g. Leinert et al. 2004). Using this radial temperature power law and the assumption that each disk annulus radiates as a blackbody,

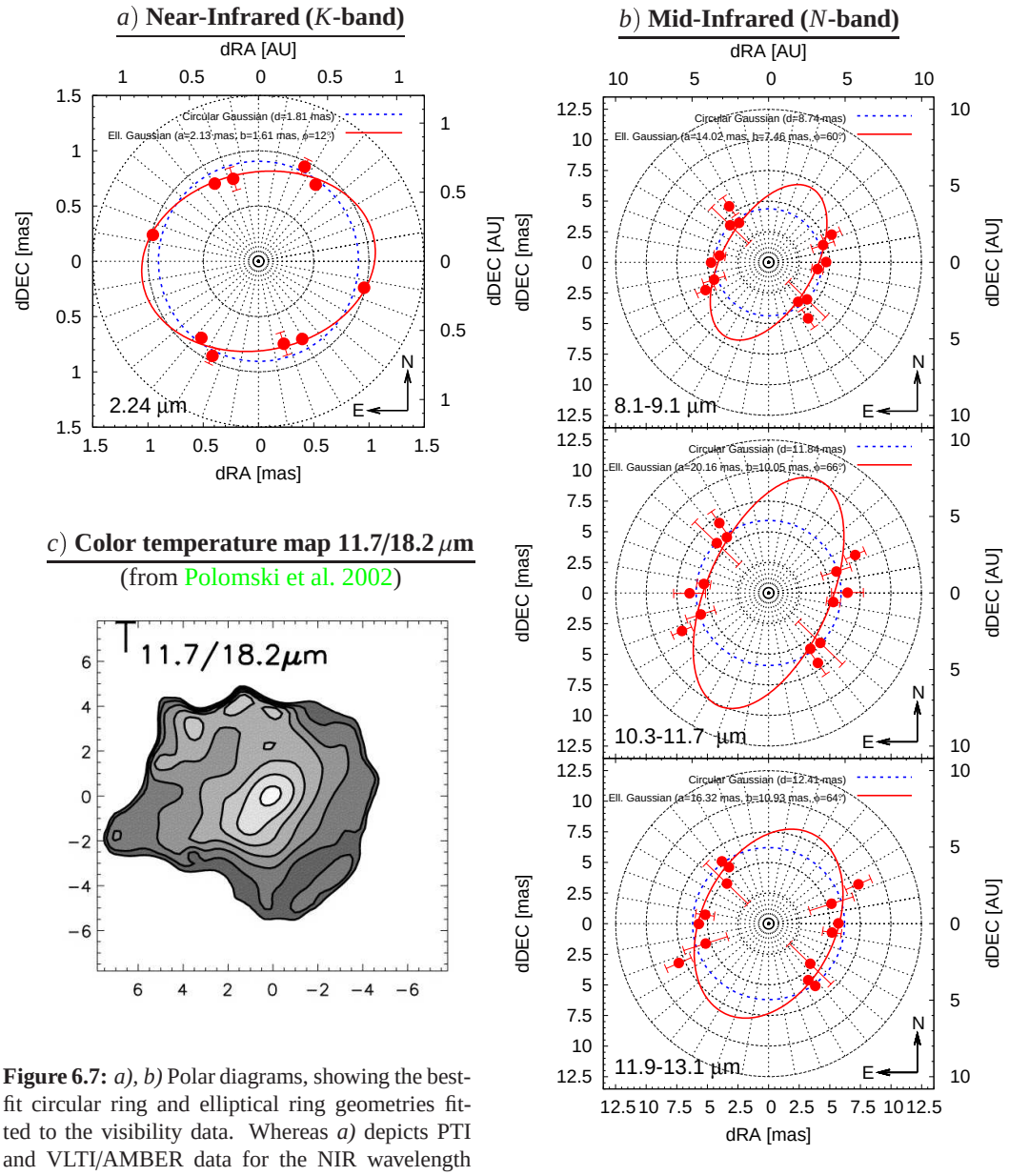

Figure 6.7: *a), b)* Polar diagrams, showing the best-fit circular ring and elliptical ring geometries fitted to the visibility data. Whereas *a)* depicts PTI and VLTI/AMBER data for the NIR wavelength 2.24 μm, the VLTI/MIDI visibilities in *b)* were averaged over certain wavelength ranges in the silicate feature (11.0 μm) and in the surrounding continuum (9.0 μm and 12.5 μm). *c)* shows the 11.7/18.2 μm color temperature map published by Polomski et al. (2002), revealing an elongated structure of similar orientation and axis ratio as our model fits to the MIR interferometric data.

Table 6.4: Model fits assuming circular geometries. For the K-band fits, we attribute 16% of the total flux to the unresolved stellar component. At a distance of 800 pc, 1 mas corresponds to 0.8 AU.

	K-band		9 μm		11 μm		12.5 μm	
	Diameter [mas]	χ^2_r	Diameter [mas]	χ^2_r	Diameter [mas]	χ^2_r	Diameter [mas]	χ^2_r
UD	2.6 ± 0.2	1.44	12.8 ± 2.0	1.38	17.3 ± 2.2	0.95	18.1 ± 2.2	0.89
Gaussian	1.6 ± 0.1	1.30	7.9 ± 1.4	1.19	10.8 ± 1.5	0.75	11.2 ± 1.5	0.90
Ring	1.8 ± 0.1	1.51	8.7 ± 1.4	1.49	11.8 ± 0.3	1.07	12.4 ± 1.3	0.90

Table 6.5: Similar as Table 6.4, but fitting inclined geometries.

	K-band				9 μm			
	Diameter [mas]	Incl. [°]	PA [°]	χ^2_r	Diameter [mas]	Incl. [°]	PA [°]	χ^2_r
Incl. UD	3.0×2.4	39	12	0.33	20.1×10.8	58	58	1.04
Incl. Gaussian	1.8×1.4	39	11	0.30	18.5×6.5	69	66	0.89
Incl. Ring	2.1×1.6	41	12	0.34	14.0×7.5	58	60	1.06

	11 μm				12.5 μm			
	Diameter [mas]	Incl. [°]	PA [°]	χ^2_r	Diameter [mas]	Incl. [°]	PA [°]	χ^2_r
Incl. UD	20.8×15.3	43	53	0.59	23.5×15.7	48	70	0.58
Incl. Gaussian	23.3×8.9	68	65	0.31	23.5×9.0	68	74	0.49
Incl. Ring	20.2×10.1	60	66	0.48	16.3×10.9	48	64	0.59

we can compute the wavelength-dependence of the disk size corresponding to a certain analytic model. To model the wavelength-dependence of the size of an accretion disk model with constant power law, we simulated disks with $T(r) = r^{-\alpha}$, where r is chosen to be in units of the disk inner radius with a temperature at the inner dust rim of $T(1) = 1\,500$ K. The outer disk radius is chosen such that the temperature drops well below 100 K. After computing the intensity profile we determine the disk size $a(\lambda)$ for these analytic disk models using the half-light radius definition by Leinert et al. (2004). Finally, we scale the half-light diameter to fit the NIR size measured on MWC 147 $a(2.1\,\mu\text{m}) = 2$ mas and show the resulting $a(\lambda)$-curve for the before-mentioned representative values for α (Fig. 6.6).

It is obvious that this analytic model underestimates the measured MIR-sizes considerably. To understand the strong increase of the apparent size with wavelength, contributions from the following effects might be of importance:

(a) Analytic disk models generally do not include the effects of scattered light, which can provide significant heating of the outer parts of the disk and thus increase the apparent disk size at MIR wavelength.

(b) It has been suggested that the disks around YSOs may not be flat but flare with increasing radius;

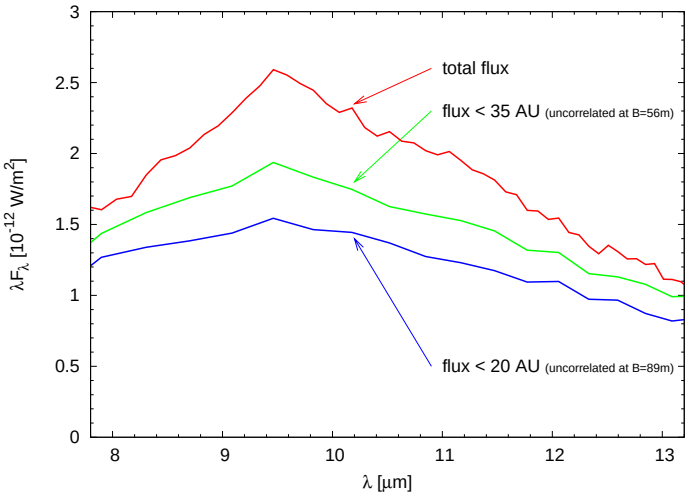

Figure 6.8: Total MIDI spectrum and the uncorrelated flux at the 56 m and 98 m baselines.

such a flaring is also expected from vertical hydrostatic equilibrium considerations (Kenyon & Hartmann 1987). As a result, the outer disk regions intercept more stellar flux, resulting in an increased luminosity and apparent size at MIR wavelengths.

(c) The flux contribution from an extended cold envelope $f_{\mathrm{env/tot}}(\lambda)$ might be non-negligible in the MIR.

(d) The NIR size might be underestimated if the amount of NIR emission originating from close to the star is inadequately estimated (e.g. due to a biased $f_{\mathrm{star/disk}}(\lambda)$ or due to additional accretion luminosity).

This enumeration illustrates that the currently routinely applied analytic disk models contain several problematic points. A more physical and consistent approach requires radiative transfer modeling. In the next section, we will present 2-D radiative transfer modeling for MWC 147.

6.5.2 The correlated spectrum – indications of grain growth

As discussed in Section 6.5.1, the visibilities measured with MIDI show significant variations along the recorded wavelength range. In particular, we detect a drop of visibility within the 10 μm silicate feature. A similar behaviour has already been observed for several HAeBe stars; e.g., in the samples of Leinert et al. (2004) and van Boekel et al. (2004a).

As the silicate emission feature is generally attributed to the presence of rather small silicate grains ($r \lesssim 0.2$ μm, REF), it is possible to probe the radial dust mineralogy by comparing the uncorrelated spectrum at various baseline lengths with the total spectrum F_{tot}. The uncorrelated spectrum F_{uncorr} corresponds to the flux integrated over the spatial area which is unresolved by the interferometer for a particular baseline length B. Therefore, for each baseline length B, the uncorrelated flux $F_{\mathrm{uncorr}}(B)$

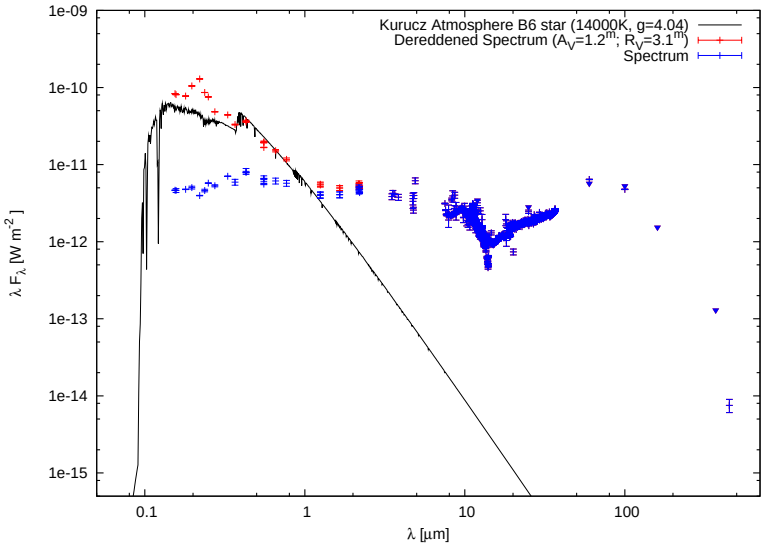

Figure 6.9: SED for MWC 147 containing the measured averaged, weighted MIDI spectrum, the archival Spitzer IRS spectrum and data from literature. We included photometric data from Thompson et al. (1978, 156.5 nm, 196.5 nm, 236.5 nm, 274.0 nm), Wesselius et al. (1982, 150 nm, 180 nm, 220 nm, 250 nm, 330 nm), Hillenbrand et al. (1992, $U, B, V, RC, IC, J, H, K, L, M, N, Q$-bands), Turon et al. (1993, V-band), Egret et al. (1992, B-band), Høg et al. (2000, VT, BT, RJ, IJ-band), Skrutskie et al. (2006, 2MASS, J, H, K_s-band), Cohen (1973, 2.2 μm, 3.5 μm, 3.65 μm, 4.8 μm, 4.9 μm, 8.4 μm, 8.6 μm, 10.8 μm, 11.0 μm, 11.3 μm, 12.8 μm, 18 μm), Polomski et al. (2002, 4.74 μm, 7.91 μm, 8.81 μm, 10.27 μm, 11.70 μm, 12.49 μm, N-band, 18.17 μm), Egan et al. (1999, MSX 2.6, 4.29 μm, 8.28 μm, 12.13 μm, 14.65 μm, 21.34 μm), Berrilli et al. (1987, 2.2 μm, 3.85 μm, 8.65 μm, 9.97 μm, 10.99 μm, 11.55 μm), Casey (1991, 160 μm, 370 μm), Mannings (1994, 450 μm).

can be computed by multiplying the total spectrum measured by MIDI in the photometry files with the visibility measured for a certain baseline. In order to probe the radial dependence of the dust minerology, measurements taken at similar PAs should be used in order to avoid contaminations by changes in the source geometry. We therefore choose the measurements from 2004-11-01 ($B = 56$ m, PA=82°) and 2004-10-30 ($B = 89$ m, PA=90°), as they have very similar PAs. The comparison of the correlated spectra for these baselines with the uncorrelated spectrum (Fig. 6.8) shows that the 10 μm silicate feature flattens out with increasing resolution. This change in the correlated spectrum might indicate spatial variations in the dust composition, with the more evolved dust grains (i.e. larger grains with their weaker silicate feature) in the innermost disk regions.

6.6 2-D Radiative Transfer Simulations

6.6.1 SED analysis

As an additional contraint for our radiative transfer modeling, we assembled the SED (Fig. 6.9) of MWC 147 by collecting photometric data from the literature. The contribution of the visual companion (Baines et al. 2006, separation $3\farcs1$) to the SED is unknown. Furthermore, the photometric data may be contaminated by the ambient reflection nebula NGC 2247 (Casey 1991). Polomski et al. (2002) studied the appearance of the circumstellar environment of MWC 147 at MIR wavelengths and found an extended structure of $\sim 12''$ diameter ($\sim$ 9 600 AU) at 10 μm.

6.6.2 Modeling procedure and simulation setup

For a physical interpretation of the measured visibilities and the SED, we employ the radiative transfer code *mcsim_mpi* (Author: K. Ohnaka), which solves the radiative transfer problem self-consistently using a Monte Carlo approach. This code was introduced in Ohnaka et al. (2006) and also applied in Hönig et al. (2006). In short, the stellar flux is treated as a finite number of photon packets, which are emitted in arbitrary directions. While propagating through the cells of the simulation grid, the photon packet can be either scattered or absorbed, where the probability of these events is given by the density and the optical properties of the dust in each particular cell. Whereas for scattering events simply the propagation direction of the photon packet changes (we assume isotropic scattering), absorption events deposit energy into the cell while the packet is isotropically re-emitted immediately. For each absorption event, the temperature of the cell is corrected using the scheme by Bjorkman & Wood (2001), resulting in a self-consistent determination of the dust temperature distribution. After tracing the propagation of a large number of photon packets through the simulation grid, the SED is computed by summing the flux from all packets. The code is parallelized using the LAM/MPI library, which allows the user to distribute the Monte Carlo computation on a large number of computers within a network.

Once the radiative transfer computation is completed, a ray-trace program is used to compute synthetic images for any wavelength of interest. For this project, we compute synthetic images for 3 wavelength bins covering the *H*-band, 3 bins for the *K*-band, and 8 bins for the *N*-band. Finally, visibilities are computed from the simulated images for the points of the *uv*-plane covered by the data. In order to treat the visibility slope in the spectro-interferometric observations properly, we compute the visibility for each spectral channel of the MIDI and AMBER observations separately, using the synthetic image computed for a wavelength as close as possible to the central wavelength of the spectral bin.

As we require particularly high spatial resolution in the inner disk region to properly resolve the structure of the inner dust rim (at scales of less than one AU) but also need to include structures with large radial extension (10 000 AU scale), we employed a spherical grid with logarithmic radial grid

spacing. The number of radial cells was chosen to be 500, while the latitudional grid resolution is 2°. We used 10^8 photon packages per simulation, which ensures sufficient statistics for Monte-Carlo radiative transfer.

As input stellar spectrum we used a Kurucz stellar atmosphere model (Kurucz 1970) for a B6-type star of solar metallicity ($T_{\rm eff} = 14\,000$ K, $\log g = +4.04$). For the optical dust properties we use a mixture of warm silicate (Ossenkopf et al. 1992) and amorphous carbon (Hanner 1988) grains. The grain size distribution follows the dependence suggested by Mathis et al. (1977, $n(a) \propto a^{-3.5}$, where $a_{\rm min} \leqslant a \leqslant a_{\rm max}$). For the outer envelope we use small grains ($a_{\rm min} = 0.005$ μm; $a_{\rm max} = 1.0$ μm), whereas for the inner disk region we mix in also larger dust grains ($a_{\rm min} = 1.0$ μm; $a_{\rm max} = 1000$ μm), which is in qualitative agreement with the indications for grain growth found in the inner disk regions (Sect. 6.5.2). The species of large and small grains are treated separately in the radiative transfer computations. A minimum dust density of 10^{-27} g cm^{-3} is assumed.

6.6.3 Iterative determination of the location and shape of the inner rim

A proper treatment of both the location and the shape of the inner rim of the dust distribution (i.e. the dust sublimation radius) is of particular importance to explain both the NIR SED and the NIR interferometric data. In the DDN01 model, the structure of the inner rim is described as a vertical wall, causing strong deviations from centro-symmetry when seen under inclination. As discussed by DDN01, this description is likely not physically reasonable. Furthermore, the strong "skew" in the NIR disk morphology predicted by a DDN01-like vertical wall also seems to contradict the recent YSO closure phase survey conducted by Monnier et al. (2006).

Thus, we added an option to our software which allows us to refine the geometry of the inner rim iteratively, taking the dust sublimation into account. For this, we first compute the temperature distribution resulting from the original density description and then check for grid cells which exhibit a temperature above the local dust sublimation temperature. For these cells, the dust density is decreased by a factor of 10^{-2} before the next iteration step. This iteration procedure is repeated until convergence is reached.

Isella & Natta (2005) have pointed out that the dust sublimation temperature $T_{\rm subl}$ depends on the gas density, which results in a higher sublimation temperature in the disk midplane than in the disk atmosphere, causing a curved shape of the inner rim. To model this effect, we compute $T_{\rm subl}(x)$ for each grid cell x separately assuming a gas-to-dust ratio of 100 and the relation by Pollack et al. (1994):

$$T_{\rm subl}(\rho) = 2\,000\ {\rm K} \cdot \rho^{\gamma} \tag{6.1}$$

with $\gamma = 1.95 \times 10^{-2}$. This iteration should improve the appearance of the disk inner rim in the synthetic images, which are then fitted to the interferometric data. We do not iterate on the vertical hydrodynamic disk structure as we consider this a second-order effect, which is out of the scope of this paper.

6.6.4 Inner gaseous accretion disk

As suggested by the rather high accretion and mass loss rates reported for MWC 147 ($\dot{M}_{\rm acc} = 10^{-5} M_{\odot}{\rm yr}^{-1}$, $\dot{M}_{\rm wind} = 2.0 \times 10^{-7} M_{\odot}{\rm yr}^{-1}$, see introduction), it might be of importance to include accretion in our model. In active accretion disks, large amounts of gas are transported inwards of the dusty inner rim. Inside the corotation radius, where the Keplerian angular velocity matches the stellar angular velocity, the matter is then accreted onto the star through magnetospheric accretion columns. While the energy of the magnetospheric accretion process is mainly radiated away in the UV continuum and in UV and optical emission lines, the infalling matter in the gaseous inner disk can also affect the infrared SED, mainly by two effects:

(a) Thermal emission from optically-thick gas in the inner gaseous disk, located between the corotation radius and the inner dust rim.

(b) Shielding of the inner dust rim by an optically thick gaseous inner disk. The gas might effectively scatter the stellar UV radiation, allowing dust to exist closer to the star.

Muzerolle et al. (2004) found that even for $\dot{M}_{\rm acc} = 10^{-6} M_{\odot}{\rm yr}^{-1}$, the gaseous inner accretion disk is typically a factor of ~ 8 times thinner than the puffed-up inner dust disk wall and is optically thick. Therefore, we consider *(a)* to be the dominant effect and include the thermal emission from the gaseous inner disk into our radiative transfer models using a similar approach as Akeson et al. (2005).

In this model, the accretion luminosity is emitted from a viscous accretion disk (Pringle 1981) which emits at each radius r as a black-body of temperature

$$T^4_{\rm gas}(r) = \left(\frac{3GM_{\star}\dot{M}}{8\pi\sigma r^3} \right) \left(1 - \sqrt{R_{\star}/r} \right)^{1/2}. \tag{6.2}$$

We run r from the magnetic truncation radius (for which we assume $5R_{\star}$) to the dust sublimation radius $R_{\rm subl}$. In our Monte Carlo radiative transfer simulation grid, the photons corresponding to the accretion luminosity are emitted isotropically from two cells around the disk midplane and then propagate through the simulation grid. The modeling of gas absorption is out of the scope of this paper, and therefore the gaseous inner disk in our simulation does not provide shielding to the dusty inner rim.

6.6.5 Simulated geometries

Besides the dust geometry iteration scheme and the inclusion of accretion luminosity, we extended the *mcsim_mpi* code by adding dust geometries, including extended envelopes (see Sect. 6.6.5.1), inner shells (Sect. 6.6.5.2), and various circumstellar disk geometries, especially flared Keplerian disks with (Sect. 6.6.5.4) and without a puffed-up inner rim (Sect. 6.6.5.3).

Before the radiative transfer simulation, the density distribution is defined using either analytic density profiles or the density distribution is computed iteratively within external software. In the later case, we

use the publically available IDL code CGplus[3] (version 2.1, Author: C.P. Dullemond) to pre-compute the radial density profile and vertical scale height for each disk radius.

In order to avoid unrealistically sharp cutoffs at outer edges in the density distribution, we used a Fermi-type function $F(r_{\rm cutoff})$ to obtain a smooth truncation of the density distribution around the radius $r_{\rm cutoff}$:

$$F(r_{\rm cutoff}) = \left[1 + \exp\left(\frac{r - r_{\rm cutoff}}{\epsilon r_{\rm cutoff}}\right)\right]^{-1}, \tag{6.3}$$

where $\epsilon = 0.05$ defines the relative width of the transition region.

6.6.5.1 Extended envelope

In the course of our modeling of the SED of MWC 147 with the before-mentioned inner geometries (spherical shell, Keplerian disk with and without an inner rim), we found that an additional component is required which contributes large amounts of the MIR to FIR flux (see SED in Fig. 6.9).

In particular, we did not succeed in modeling the pronounced change in slope in the *Spitzer*-IRS spectrum (around 15 μm, see Fig. 6.5) with a single component, but had to include an additional extended envelope component. For this envelope, we tried various geometries, in particular rotating, infalling envelopes with and without polar outflow cavities, such as those parametrized by Whitney et al. (2003). However, those geometries generally contributed too much flux around $\sim$ 20 μm and also cannot successfully reproduce the *Spitzer*-IRS spectrum. The best agreement was obtained for a simple power-law dust distribution with a rather flat slope

$$\rho_{\rm env} = \rho_0 \left(\frac{r}{r_0}\right)^{-1/2} \times F(r_{\rm cutoff}). \tag{6.4}$$

where ρ_0 is the dust density at an arbitrary characteristic radius r_0.

After fine-tuning the parameters of the envelope to match the SED above 15 μm, we fixed the geometry of the envelope and varied in the following studies (Sections 6.6.5.2 to 6.6.5.4) only the geometry of the innermost circumstellar component, being the dominant contributor to the NIR and MIR emission probed by our interferometric observations.

6.6.5.2 Model SHELL: Spherical shell geometry

Miroshnichenko et al. (1997) proposed that optically thin shells can reproduce the SED of HAeBe stars. In order to investigate whether these shell models or the disk models presented in the following sections

[3]The CGplus IDL library is available from the website http://www.mpia.de/homes/dullemon/radtrans/

provide a better fit to our simultaneous SED + visibility fits, we simulate a density distribution given by

$$\rho_{\rm Shell} = \rho_0 \left(\frac{r}{r_0}\right)^{-p} \times F(r_{\rm cutoff}) \tag{6.5}$$

with $p = 1.5$, as suggested by Miroshnichenko et al. (1997).

6.6.5.3 Model KEPLER: Flared Keplerian disk

One solution for a passive disk which is gravitationally dominated by the central star, vertically isothermal, and in vertical hydrodynamic equilibrium, is given by a flared Keplerian disk geometry (Kenyon & Hartmann 1987)

$$\rho_{\rm Kepler} = \rho_0 \left(\frac{r}{r_0}\right)^{-3/2} \exp\left[-\frac{\pi}{4}\left(\frac{z}{h_z}\right)^2\right] \times F(r_{\rm cutoff}). \tag{6.6}$$

The vertical pressure scale height h_z is coupled to the temperature at a certain radius, which results in a flaring of the disk at large radii. We use the analytic description by Chiang & Goldreich (1997), as implemented in the CGplus software, to determine h_z as a function of radius.

6.6.5.4 Model PUFFED-UP-RIM: Flared Keplerian disk with puffed-up inner rim

As the dust at the inner rim (at the dust sublimation radius) is directly exposured to the stellar radiation, the vertical scale in this region is significantly increased. Natta et al. (2001) and Dullemond et al. (2001) proposed a modification of the flared Keplerian disk geometry discussed in Sect. 6.6.5.3; namely, a "puffed-up" inner rim. To include this effect in our simulation, we compute $h_z(r)$ using the CGplus code and then apply the iterative procedure described in Sect. 6.6.3 to refine the shape of the inner rim. Again, the outer edge of the disk is truncated by applying the function $F(r_{\rm cutoff})$.

6.6.6 Modeling procedure and results

6.6.6.1 Fitting procedure

The fits were performed using the following approach: First, we fixed the geometry of the extended envelope to match the MIR to FIR SED (Sect. 6.6.5.1). Then, we tried different geometries for the inner component (Sect. 6.6.5.2 to 6.6.5.4) to obtain the best fit to the NIR and MIR SED. Finally, the agreement of the model with the interferometric observables was tested. The analytic model fits presented in Table 6.5 indicate that the disk should be notably inclined ($\sim$ 40 to 60°), therefore we fixed for the radiative transfer modeling the disk inclination to 45° (yielding for most models also the best agreement with the spectral shape of the SED). In total, about one thousand radiative transfer models have been computed to identify the best-fit models presented in the following sections.

6.6.6.2 Results for models without accretion

When neglecting the optically thick emission from an gaseous inner accretion disk (as is most often assumed for the interpretation of HAeBe NIR/MIR interferometric data) we found that especially the NIR visibilities predicted by the models were always much smaller than the measured visibilities (see Fig. 6.11 and 6.12). A similar, although less pronounced deviation was found in the MIR visibilities.

Therefore, the radiative transfer modeling confirms and quantifies the general tendency already observed in the geometric model fits; namely, that without considering accretion luminosity (or shielding of a gaseous inner disk, see discussion in Sect. 6.6.4), the measured NIR radius of $\sim$0.65 AU (see Table 6.4) is *a factor of 4 smaller than the dust sublimation radius*, as expected from the radiative transfer models. We conclude that, although passive irradiated circumstellar disk models are able to reproduce the SED of MWC 147, these models are in strong conflict with the interferometric measurements (resulting in $\chi^2_r \approx 40$ both for the KEPLER and the PUFFED-UP-RIM model; see Table 6.6 and Fig. 6.11 and 6.12). Including large grain sizes in the inner disk regions decreases the discrepancies, but we did not succeed in solving the discrepancy quantitatively solely by varying the dust chemisty.

Whereas the shell geometry can roughly reproduce the SED, it provides only a very poor fit to our interferometric observables ($\chi^2_r = 93.2$; see Fig. 6.10) and can thus be rejected.

6.6.6.3 Results for models with accretion

Including accretion luminosity from a gaseous inner disk (as described in Sect. 6.6.4) provides a much better agreement between model predictions and observed visibilities.

With a flared disk geometry (without puffed-up inner rim) and an accretion rate of $\dot{M}_{\rm acc} = 1.2 \times 10^{-5} M_{\odot}{\rm yr}^{-1}$, both the SED and the interferometric visibilities (see Fig. 6.13 and Table 6.6) are reasonably well reproduced ($\chi^2_r = 2.6$). When using disk geometries with puffed-up rim, the inner rim contributes significant NIR emission, which increases the apparent size of the disk, resulting in a poorer fit to the interferometric data ($\chi^2_r = 6.7$; see Fig. 6.14).

6.7 Conclusions

We have presented infrared long-baseline interferometric observations of MWC 147, constraining the inner circumstellar environment around a Herbig Be star over the wavelengh range from 2 to 13 μm.

The archival *Spitzer*-IRS spectra show distinct PAH line features which were not detected in the spatially filtered MIDI spectrum, indicating that the PAHs originate in the outer disk or envelope. Also, the MIDI uncorrelated spectra exhibit that the strength of the silicate feature decreases with baseline length which can be interpreted in the context of grain growth towards the inner disk regions.

The interferometric data obtained from the PTI archive and with VLTI/AMBER suggest a diameter of just $\sim$ 1.3 AU (Gaussian FWHM) for the NIR emitting region, while the MIR structure is about a factor of 7 more extended (9 AU at 11 μm). Within the *K*-band, we measured a significant increase of size with wavelength. A comparison of the wavelength-dependence of the characteristic size with the predictions from commonly used disk models with a simple temperature power-law indicate that these analytic models do significantly underestimate the size of the emitting region at MIR wavelengths. To test whether more realistic physical models of the circumstellar dust environment yield better agreement, we employed 2-D radiative transfer modeling. The radiative transfer models were constructed to fit the SED from 0.3 to 450 μm, including an extended envelope and an inner shell/dust disk geometry. Beside flared Keplerian disks without puffed-up inner rim, we also examined the case where the rim at the dust sublimation radius of this disk is puffed-up as parametrized by Dullemond et al. (2001). To refine the shape of the rim in our radiative transfer models, we have used an iterative approach, also taking the density-dependence of the dust sublimation temperature into account. While such models of passive irradiated disks are able to reproduce the SED, they are in conflict with the interferometric observables, significantly overestimating the size of both the NIR and MIR emission. Therefore, we incorporated accretion luminosity, emitted from a gaseous inner disk, in our radiative transfer models, yielding significantly better agreement both with the SED and the interferometric data. The best-fit was obtained with a flared Keplerian disk without puffed-up inner rim, which is seen under an inclination of $\sim 45^\circ$, extending out to 100 AU, and exhibiting a mass accretion rate of $1.2 \times 10^{-5}\ M_\odot \mathrm{yr}^{-1}$.

Shell geometries result in a poor fit to the interferometric data, as they cannot reproduce the asymmetry inherent in particular in the measured MIDI visibilities. Furthermore, they significantly overestimate the size of the NIR emitting region.

Our detailed study suggests that infrared long-baseline interferometry, especially if combined with spectroscopic observations, has outgrown the stage of a pure size-estimating technique and is able to provide unique constraints on the geometry and density profile of the circumstellar environment and the active accretion processes in the innermost region of YSO circumstellar disks. To obtain physically meaningful results, a proper treatment of a large variety of physical effects, e.g. dust scattering, dust sublimation, and gas accretion is required, demanding rather complex radiative transfer modeling.

Table 6.6: Parameters and fitting results for our 2-D radiative transfer models.

		SHELL (Fig. 6.10)	KEPLER (Fig. 6.11)	PUFFED-UP-RIM (Fig. 6.12)	KEPLER & Accretion (Fig. 6.13)	PUFFED-UP-RIM & Accretion (Fig. 6.14)
Outer radius	[AU]	100	100	100	100	100
Dust density at 10 AU	[g·cm^{-3}]	1.2×10^{-23}	–	–	–	–
Disk dust mass	[$M_\odot$]	–	5.0×10^{-12}	4.0×10^{-11}	8.0×10^{-11}	4.0×10^{-10}
Grain Size		Small	Small	Small	Small & Large	Small & Large
Radial power law α		1.5	1.5	1.5	1.5	1.5
Vertical power law β		–	1.175	1.175	1.175	1.175
Mass accretion rate	[$M_\odot$yr^{-1}]	–	–	–	1.2×10^{-5}	9.0×10^{-6}
Inclination		–	45°	45°	45°	45°
Best fit PA		–	50°	-50°	60°	90°
χ^2_r NIR		279.5	204.9	181.0	3.5	21.9
χ^2_r MIR		49.7	4.3	4.8	2.4	3.2
χ^2_r total		93.2	42.2	38.1	2.6	6.7

Extended Envelope – For all models we include an extended outer envelope in order to fit the MIR to FIR SED (see Sect. 6.6.5.1). The envelope is composed of small dust grains, with a density distribution $\rho \propto r^{-1/2}$ with $\rho_0 = 1.8 \times 10^{-25}$ g·cm^{-3} at $r_0 = 10$ AU (see equation 6.4). The inner radius was set to 1.8 AU, consistent with a dust sublimation temperature of 1 500 K, whereas the outer cutoff radius $r_{\rm cutoff} = 50\,000$ AU was chosen such that the dust temperature drops below 10 K.

Dust Composition – Mixture of warm silicates (Ossenkopf et al. 1992) and amorphous carbon (Hanner 1988). The size distribution follows $n(a) \propto a^{-3.5}$. For *Small Grains* we choose $a_{\rm min} = 0.005\,\mu$m and $a_{\rm max} = 1.0\,\mu$m, whereas for *Large Grains* we use $a_{\rm min} = 1.0\,\mu$m and $a_{\rm max} = 1000\,\mu$m.

Minimum Dust Density – For all models, we assume a minimum dust density of 10^{-27} g·cm^{-3}.

Inner Gaseous Accretion Disk – The inner accretion disk is modeled to be optically thick and to extend from 5 to 50 $R_\star$.

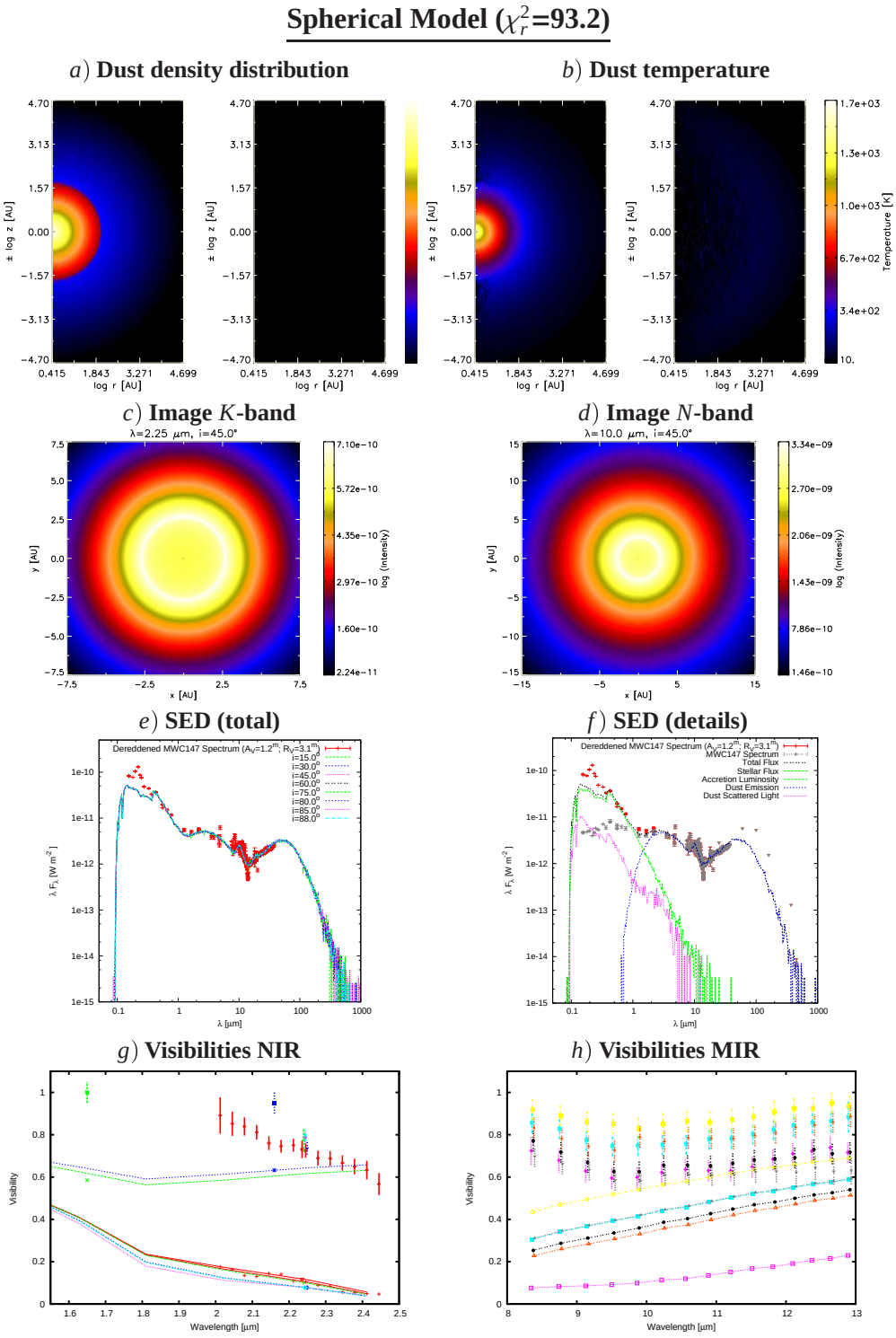

Figure 6.10: Radiative transfer model computed for MWC 147 assuming a **Spherical Shell geometry**. For the model parameters see Table 6.6. In *a*) and *b*), we show the dust density distribution and temperature for the small (left) and large (right) dust grain population. *c*) and *d*) shows the raytraced images for two representive NIR (2.25 μm) and MIR (10.0 μm) wavelengths. In order to increase the dynamic range in these images, the direct stellar flux is skipped in the raytraced images and later introduced again in the visibility computation. *e*) shows the SED for various inclination angles, whereas *f*) gives the SED for 45° and separates the flux which originates in stellar photospheric emission, thermal emission, dust irradiation, and accretion luminosity. Finally *g*) and *h*) depict the NIR and MIR visibilities computed from our radiative transfer models.

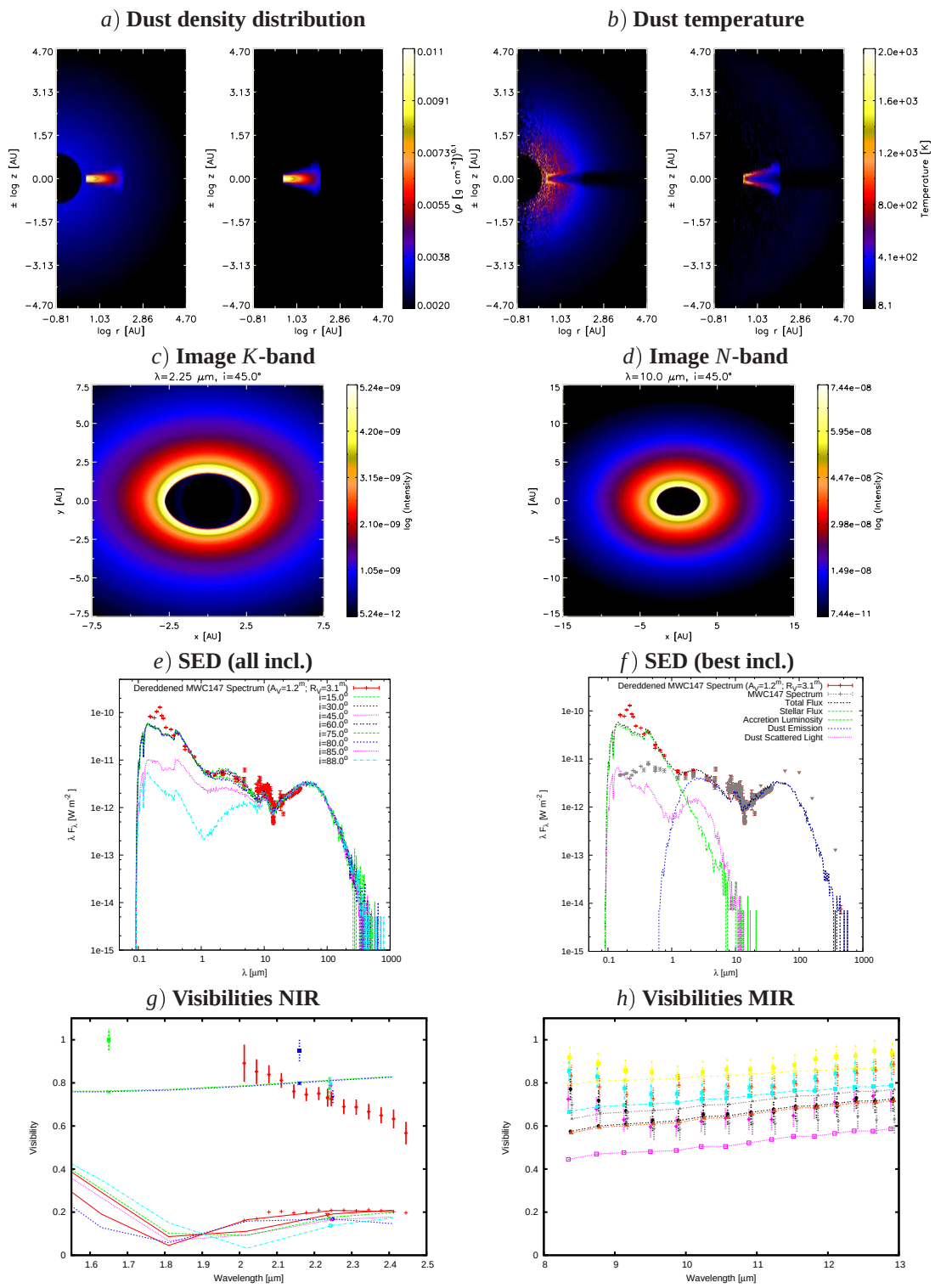

Figure 6.11: Similar as Figure 6.10, but showing the radiative transfer model for a **Flared Keplerian disk geometry without puffed-up inner rim**.

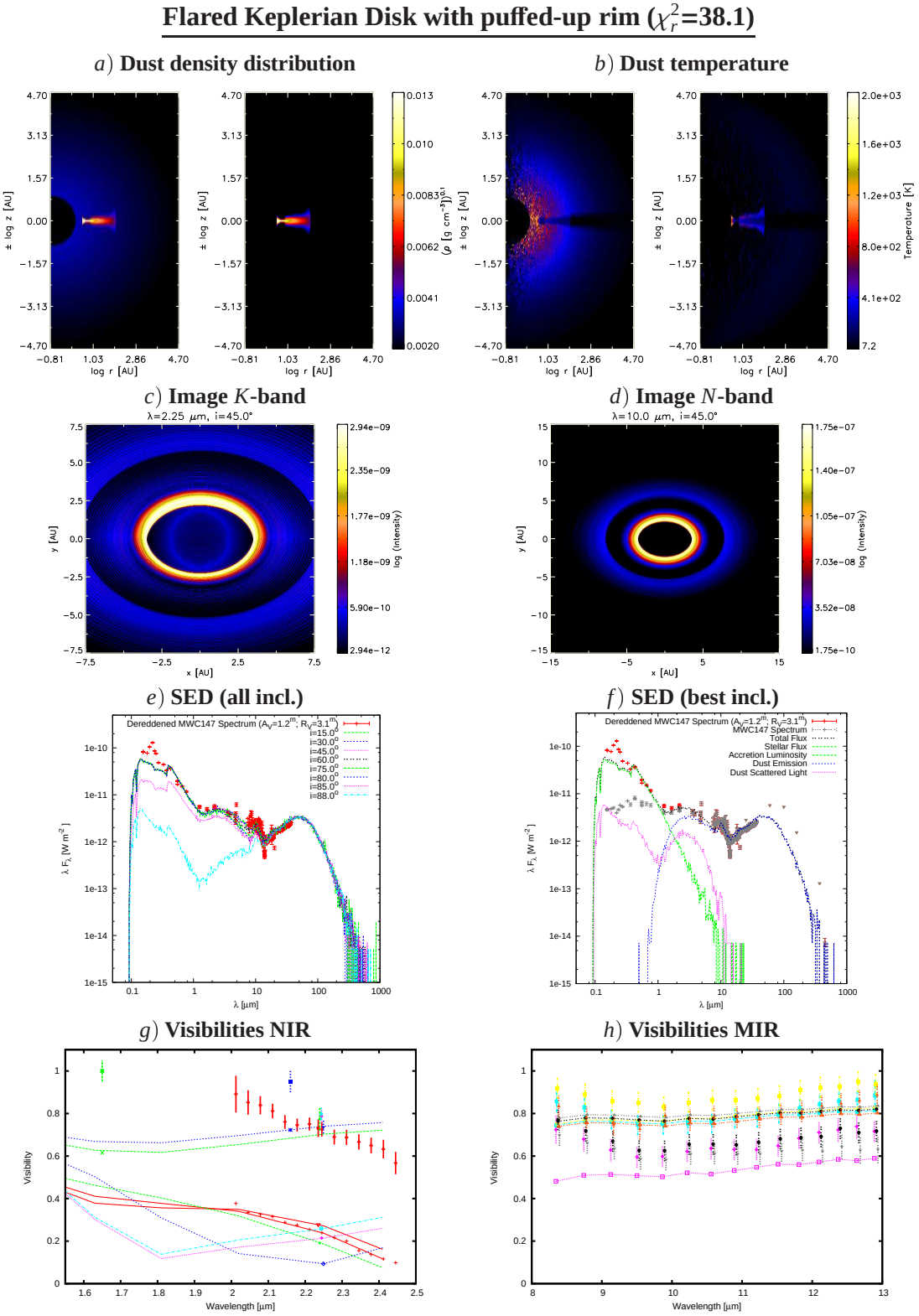

Figure 6.12: Similar as Figure 6.10, but showing the radiative transfer model for a **Flared Keplerian disk geometry with puffed-up inner rim**.

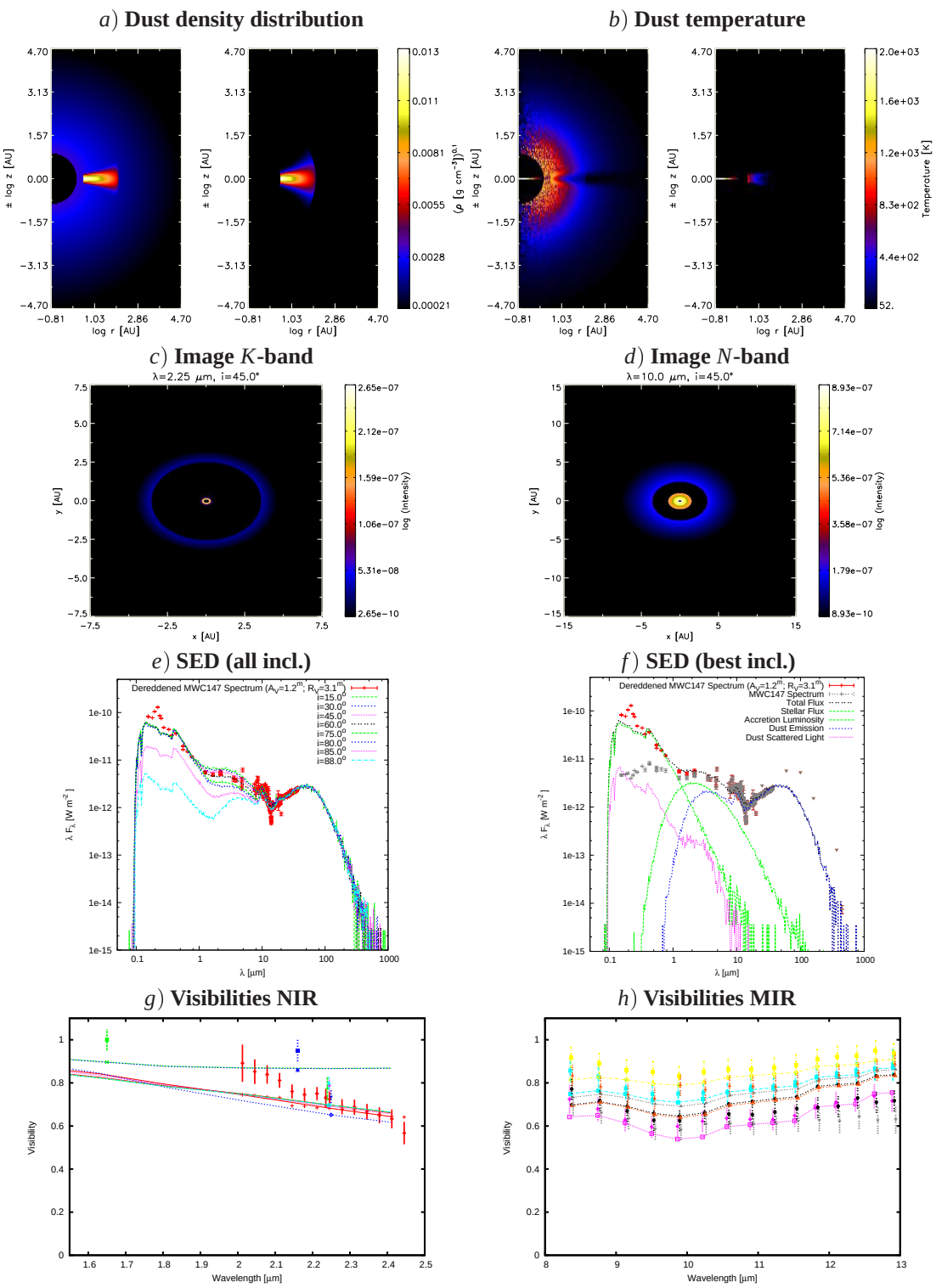

Figure 6.13: Similar as Figure 6.10, but showing the radiative transfer model for a **Flared Keplerian disk geometry without puffed-up inner rim, including accretion**.

Flared Keplerian Disk with puffed-up rim & Gaseous Accretion Disk (χ^2_r=6.7)

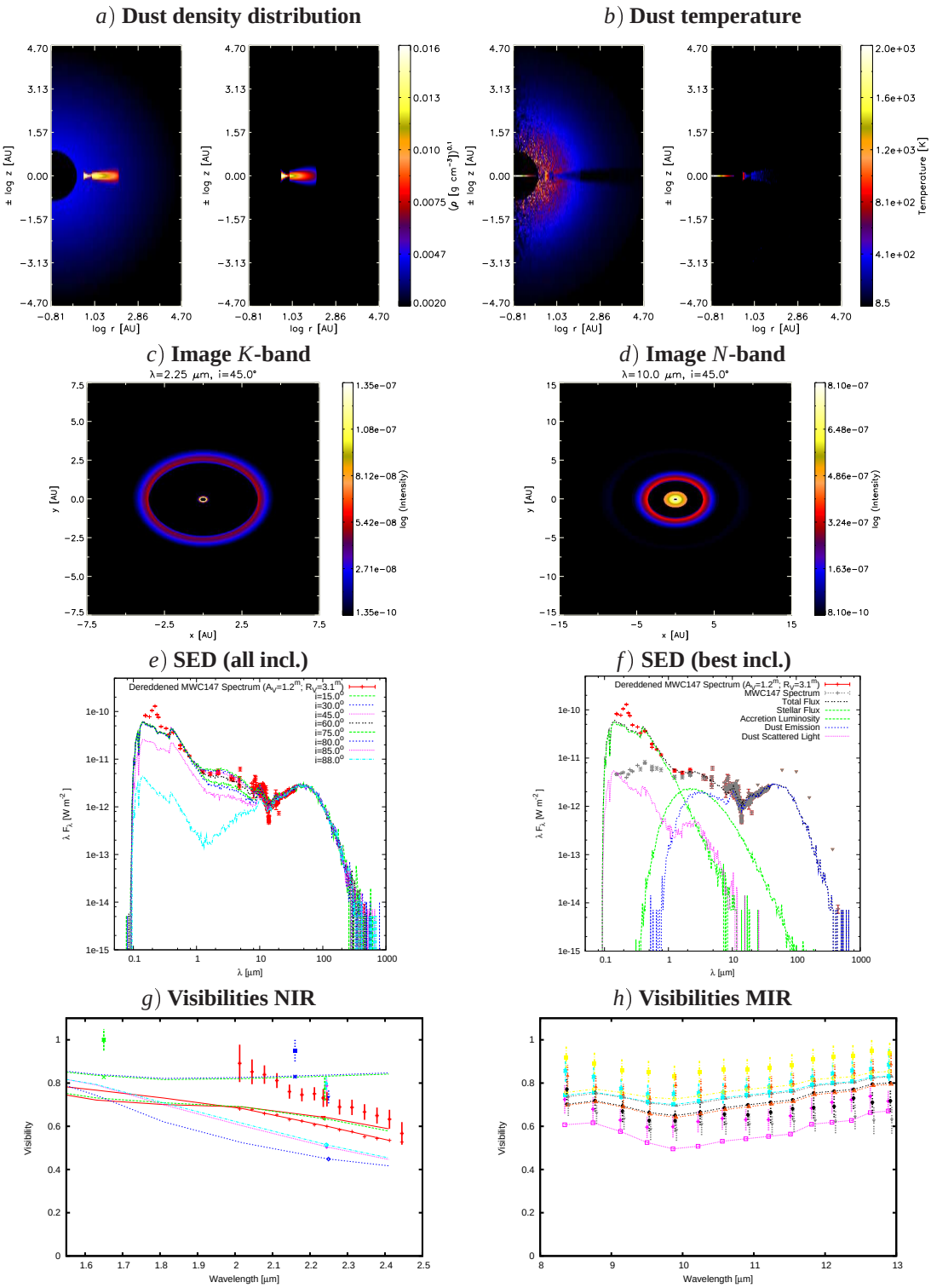

Figure 6.14: Similar as Figure 6.10, but showing the radiative transfer model for a **Flared Keplerian disk geometry with puffed-up inner rim, including accretion**.

7 Signatures of Outflow Precession from the Young High-Mass Star NGC 7538 IRS1

Based on an article which appeared in A&A:
Kraus, S., Balega, Y. Y., Elitzur, M., et al., A&A 455, 521 (2006)

7.1 Overview and Context

NGC 7538 IRS1 is a particularly young high-mass (O7-type) protostar which is still deeply embedded in its natal cloud, making the site nearly invisible at visual wavelengths. Since the discovery of a strong methanol maser feature towards IRS1 by Menten et al. (1986), the site has gained a lot of attention from the radioastronomy community. Later, VLBI observations revealed that the methanol masers are linearly aligned and might trace a Keplerian-rotating circumstellar disk (Pestalozzi et al. 2004). The relatively early evolutionary stage of NGC 7538 IRS1 (Class I) is also supported by the presence of an ultracompact H II region and a CO outflow. Surprisingly, the various associated axes are misaligned with each other.

Figure 7.1: Color composite image of the NGC 7538 star forming region (Image Credit: McCoughrean).

To investigate the NIR morphology of the source at high angular resolution and to clarify the relations among the various axes, our group performed speckle interferometric observations on NGC 7538 IRS1 at the Russian BTA 6m telescope and at the 6.5m MMT. Our high-dynamic range images show a fan-shaped outflow structure in which we detect 18 stars and several blobs of diffuse emission. Complementary IRAC images from the *Spitzer* Space Telescope Archive were used to relate the detected outflow with structures at larger scales.

We interpret the misalignment of various outflow axes in the context of a disk precession model, including numerical hydrodynamic simulations of the molecular emission. The precession period is $\sim$ 280 years and its half-opening angle is $\sim 40^\circ$. A possible triggering mechanism is non-coplanar tidal interaction of an (undiscovered) close companion with the circumbinary protostellar disk.

In addition, our observations resolve the nearby massive protostar NGC 7538 IRS2 as a close binary with separation of 195 mas. We find indications for shock interaction between the outflow activities in IRS1 and IRS2. Finally, we find prominent sites of star formation at the interface between two bubble-like structures in NGC 7538, suggestive of a triggered star-formation scenario. To date, indications of outflow precession have been discovered in a number of massive protostars, all with large precession angles ($\sim$ 20–45°). This might explain the difference between the outflow widths in low- and high-mass stars and add support to a common collimation mechanism.

The reconstruction of the bispectrum speckle images was done by Karl-Heinz Hofmann. I was responsible for the *Spitzer*-related data processing, the scientific interpretation and modeling, and the illustration and writing of major parts of the manuscript. The molecular hydrodynamics simulation and its description in Sect. 7.5.4.4 was kindly contributed by Alex Rosen. Very valuable input concerning the proper interpretation of the maser data was provided by Moshe Elitzur at discussions during his visits at the MPIfR. In this context, I would also like to note the telephone conferences of the *NGC 7538 Collaboration*, which included: Roy Booth, John Conway, James De Buizer, Moshe Elitzur, Stefan Kraus, Vincent Minier, Michele Pestalozzi, and Gerd Weigelt.

7.2 Introduction

Protostellar disks and outflows are essential constituents of the star formation process. For high-mass protostellar objects (HMPOs), direct evidence for the presence of compact circumstellar disks is still rare, whereas outflows seem to be omnipresent in the high-mass star forming regions. Outflows remove not only angular momentum from the infalling matter, but also help to overcome the radiation pressure limit to protostellar accretion by carving out optically thin cavities along which the radiation pressure can escape (Krumholz et al. 2005).

How outflows are collimated is a matter of ongoing debate and may depend on the stellar mass of the

outflow-driving source. One of the arguments in support of this conclusion is that outflows from high-mass stars appear less collimated than the outflows and jets from their low-mass counterparts (Wu et al. 2004). Therefore, it has been suggested that outflows from HMPOs might be driven by strong stellar winds, lacking a recollimation mechanism. Since HMPOs typically form in dense clusters, another possibility is confusion by the presence of multiple collimated outflows.

However, since there is evidence that the binary frequency is significantly higher for high-mass than for low-mass stars (e.g., Preibisch et al. 1999), another possibility is that outflows from HMPOs simply appear wider, assuming they undertake precession. A few cases where outflow precession have been proposed for HMPO outflows (e.g. Shepherd et al. 2000; Weigelt et al. 2002, 2006) show precession angles of $\sim$ 20 to 45°; considerably wider than the jet precession angles of typically just a few degrees observed towards low-mass stars (Terquem et al. 1999). This is in agreement with the general picture that high-mass stars form at high stellar density sites and therefore experience strong tidal interaction from close companions and stellar encounters.

The detection of precessing jet-driven outflows from HMPOs adds support to the hypothesis of a common formation mechanism for outflows from low to high-mass stars. Furthermore, jet precession carries information about the accretion properties of the driving source and, simultaneously, about the kinematics and stellar population within its closest vicinity, yielding a unique insight into the crowded places where high-mass star formation occurs.

In this study, we report another potential case of outflow precession concerning the outflow from the high-mass (30 $M_{\odot}$, Pestalozzi et al. 2004) protostellar object NGC 7538 IRS1.

We obtained bispectrum speckle interferometry of IRS1 and IRS2, which provides us with the spatial resolution to study the inner parts of the outflow, detecting filigreed fine structure within the flow. Information about even smaller scales is provided by the intriguing methanol maser feature, which was detected at the position of this infrared source and which was modeled successfully as a protostellar disk in Keplerian rotation (Pestalozzi et al. 2004). To search for outflow tracers on larger scales, we also present archival *Spitzer*/IRAC images. In addition, this allows us to relate the sources studied with bispectrum speckle interferometry with the overall star forming region and we find new hints for triggered star formation in this region.

7.2.1 Previous studies of NGC 7538

The NGC 7538 molecular cloud is located in the Cas OB2 association in the Perseus spiral arm at a distance of $\sim$ 2.8 kpc (Blitz et al. 1982). Several authors noted that NGC 7538 might present a case of triggered or induced star formation since it shows ongoing star formation at various evolutionary

stages, apparently arranged in a northwest (most developed) to southeast (youngest evolutionary stage) gradient (McCaughrean et al. 1991).

At optical wavelengths, the appearance of the region is dominated by diffuse H II emission, which extends several arcminutes from the southeast to the northwest (Lynds & O'Neil 1986). In 1974, Wynn-Williams, Becklin, & Neugebauer detected eleven infrared sources (IRS1-11) in the NGC 7538 region, wherein IRS1–3 are located on the southeast-corner of the fan-shaped H II emission in a small cluster of OB-stars. IRS1 is the brightest NIR source within this cluster and is embedded within an ultracompact (UC) H II region whose size was estimated to be $\sim 0\farcs4$ ($n_e \approx 10^5$ cm^{-3}, measured in 5 and 15 GHz CO continuum, Campbell 1984). The spectral type was estimated to be O7 (Akabane & Kuno 2005), which implies a luminosity $\sim 9.6\times10^4 L_\odot$. VLA observations with a resolution down to $0\farcs1$ (=180 AU) also revealed a double-peaked structure of ionized gas within the UC core (peaks separated by $\sim 0\farcs2$), which was interpreted as a disk collimating a north-south-oriented outflow (Campbell 1984; Gaume et al. 1995). This interpretation is also supported by the detection of elongation of the dust-emitting region at mid-infrared (MIR) wavelengths (5 μm: Hackwell et al. 1982; 11.7 μm and 18.3 μm: De Buizer & Minier 2005) and imaging studies performed in the sub-millimeter continuum (350 μm, 450 μm, 800 μm, 850 μm, 1.3 mm: Sandell & Sievers 2004, showing an elliptical source with a size of $\sim 11\farcs6\times7\farcs6$ along PA[1] $\sim -80°$) and CO line emission (Scoville et al. 1986, showing a disk-like structure extending $\sim 22''$ in the east-west direction). Also, polarization measurements of the infrared emission around IRS1 can be construed in favor of the disk interpretation (Dyck & Capps 1978; Tamura et al. 1991). Kawabe et al. (1992) carried out interferometric CS (J=2 $\rightarrow$ 1) observations and found a ring-like structure, which they interpret as a nearly face-on protostellar disk of dense molecular gas.

Further evidence for outflow activity was found by Gaume et al. (1995), who measured the profile of the H66α recombination line and derived high velocities of 250 km s^{-1}, indicating a strong stellar outflow from IRS1. CO (J=1 $\rightarrow$ 0) spectral line mapping showed a bipolar flow (Fischer et al. 1985). The mass outflow rate $\dot{M}_{\rm outflow}$ from IRS1 was estimated to be $\sim 5.4\times10^{-3}\ M_\odot$ yr^{-1} (Davis et al. 1998). Interferometric observations by Scoville et al. (1986, beam size $7''$) show that the blue and red-shifted lobes are separated by $28''$ with a position angle of $-45°$, and IRS1 is located on this axis just between the lobes of this high-velocity (-76 to -37 km s^{-1}) CO outflow. In comparing the data obtained with various beam sizes (Campbell 1984; Kameya et al. 1989), these seem to indicate a change in the position angle of the flow direction at different spatial scales, ranging from PA $\sim 0°$ at $0\farcs3$, PA $\sim -25°$ at $2''$, PA $\sim -35°$ at $7''$, to PA $-40°$ at $16''$.

Within the immediate ($\sim 0\farcs5$) vicinity of IRS1, a large variety of masers has been discovered, including OH (Dickel et al. 1982), H_2CO (formaldehyde, Rots et al. 1981; Hoffman et al. 2003), NH_3 (ammonia, Madden et al. 1986), CH_3OH (methanol, five features A, B, C, D, E were detected at 6.7 and 12.2 GHz: Menten et al. 1986; Minier et al. 1998, 2000), $^{15}NH_3$ (Johnston et al. 1989), and

[1] Following the convention, we measure the position angle (PA) from north to east.

H_2O (Kameya et al. 1990). Some of the masers show only vague signs for a systematic alignment within linear ($^{15}NH_3$, PA $\sim -60°$) or ring-like structures (H_2O, methanol-maser feature E). However, the methanol-maser feature A represents one of the most convincing cases of systematic alignment, in both linear spatial arrangement (PA $\sim -62°$) and well-defined velocity gradient, observed to date in any maser source. The qualitative interpretation of this structure as an edge-on circumstellar disk (Minier et al. 1998) was later confirmed by the detailed modeling of Pestalozzi et al. (2004), which showed that the alignment in the position–line-of-sight (LOS) velocity diagram of maser feature A can be modeled accurately assuming a protostellar disk with Keplerian rotation.

Aiming for a more complete picture, several authors (e.g. Minier et al. 1998; De Buizer & Minier 2005) also tried to incorporate the presence of methanol maser features B, C, D, and E in the circumstellar disk model for feature A and interpreted them as part of an outflow which is oriented perpedicular to feature A. Since these maser features are southwards of the putative circumstellar disk, it remains unclear why they appear blue-shifted with respect to feature A (Minier et al. 1998), whereas the southern lobe of the CO-outflow is red-shifted.

Besides the circumstellar disk interpretation for the origin of the maser feature A mentioned above, an alternative scenario was proposed by De Buizer & Minier (2005), who suggested that feature A might trace the walls of an outflow cavity.

The region was also intensively observed in the infrared. Survey images of the infrared continuum emission were presented by Campbell & Persson (1988, H, K) and Ojha et al. (2004, J, H, K_s) and showed diffuse emission, which extends from the IRS1–3 cluster in a fan-shaped structure towards the northeast and north, approximately tracing the optical H II region. The northeast border of this NIR emitting region also appears very pronounced in the continuum-subtracted H_2 2.122 μm maps by Davis et al. (1998), possibly tracing the illuminated surfaces of nearby molecular clouds or the inner walls of a vast outflow cavity. Furthermore, Davis et al. (1998) discovered two bowshock-shaped structures, centered roughly on the IRS1–3 cluster and orientated again along the northwest–southeast direction (PA $\sim -30°$) in H_2 2.122 μm. With imaging at arcsecond resolution and the use of several spectral filters (J, H, K, [Fe II] 1.65 μm, Brγ 2.165 μm, H_2 2.122 μm, and 3.29 μm), Bloomer et al. (1998) attempted to identify the source and mechanism of the outflow. Based on a cometary-shaped morphology in the [Fe II] line images and shell-like rings observed in the J, H, and K-bands, these authors propose a stellar wind bowshock model in which the motion of IRS2 relative to the molecular cloud produces the diffuse NIR emission within the vicinity of the IRS1–3 cluster.

The first K-band speckle images, taken with the 3.5 m-telescope on Calar Alto were presented by Alvarez et al. (2004) and showed substructure in the vicinity of IRS1; namely, two strong blobs (A, PA $\sim -45°$; B, PA $\sim -70°$), a diffuse emission feature (C, PA $\sim 0°$) as well as several faint point-like sources (a-f).

7.3 Observations

7.3.1 Bispectrum speckle interferometry

The first set of observations was performed on 2002-09-24 using the 6.0 m BTA (Big Telescope Alt-azimuthal) telescope of the Special Astrophysical Observatory located on Mt. Pastukhov in Russia. Additional data were gathered 2004-12-20 with the MMT (Multiple Mirror Telescope) on Mt. Hopkins in Arizona, which harbors a 6.5 m primary mirror. As detector, we used at both telescopes one 512×512 pixel quadrant of the Rockwell HAWAII array in our speckle camera. All observations were carried out using a *K*'-band filter centered on the wavelength 2.12 μm with a bandwidth of 0.21 μm. During the BTA observation run, we recorded 420 speckle interferograms on NGC 7538 IRS1 and 400 interferograms on the unresolved star BSD 19-901 in order to compensate for the atmospheric speckle transfer function. The speckle interferograms of both objects were taken with an exposure time of 360 ms per frame. For the MMT observations, the star 2MASS 23134580+6124049 was used for the calibration and 120 (200) frames were recorded on the target (calibrator) with an 800 ms exposure time. The modulus of the Fourier transform of the object (visibility) was obtained with the speckle interferometry method (Labeyrie 1970). For image reconstruction we used the bispectrum speckle interferometry method (Weigelt 1977, Weigelt & Wirnitzer 1983, Lohmann et al. 1983, Hofmann & Weigelt 1986). With pixel sizes of 27.0 mas (BTA) and 28.7 mas (MMT) on the sky, the reconstructed images possess fields of views of $13\farcs8$ (BTA) and $13\farcs1$ (MMT), respectively.

We found that the BTA data allows the highest spatial resolution (and is therefore perfectly suited for the identification of point-sources within the field), whereas the image reconstructed from the MMT data allows a high dynamic range in the diffuse emission. Therefore, we show the diffuse emission within an image of moderate resolution (reconstructed from MMT data, see Figure 7.2*a*) and perform point-source identifications within the higher resolution image reconstructed from BTA data (Figure 7.2*b*). In order to distinguish point-sources and diffuse structures reliably, we reconstructed images of various resolutions (146 mas, 97 mas, 72 mas) and carefully examined changes in the peak brightness of the detected features. Whereas for point-sources the peak brightness increases systematically, it stays constant or decreases for diffuse structures.

To perform an absolute calibration of the astrometry in our images, we measured the position of IRS1 and IRS2 in the Two Micron All Sky Survey (2MASS) K_s Atlas images and use the determined absolute positions as reference for our astrometry. We estimate that the accuracy reached in the relative astrometry is $\sim 0\farcs1$. The absolute calibration introduces further errors ($\sim 0\farcs2$).

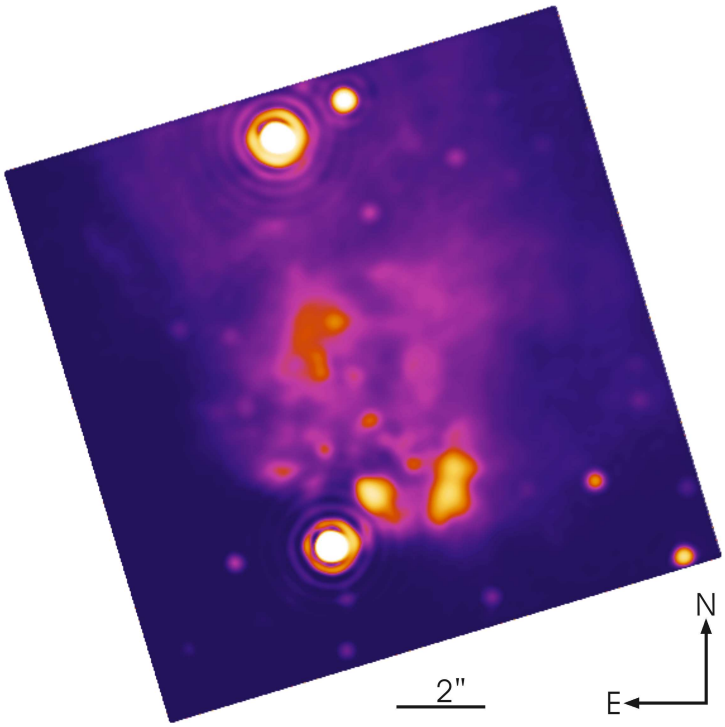

a) **MMT speckle image (334 mas resolution, 2004-12-20)**

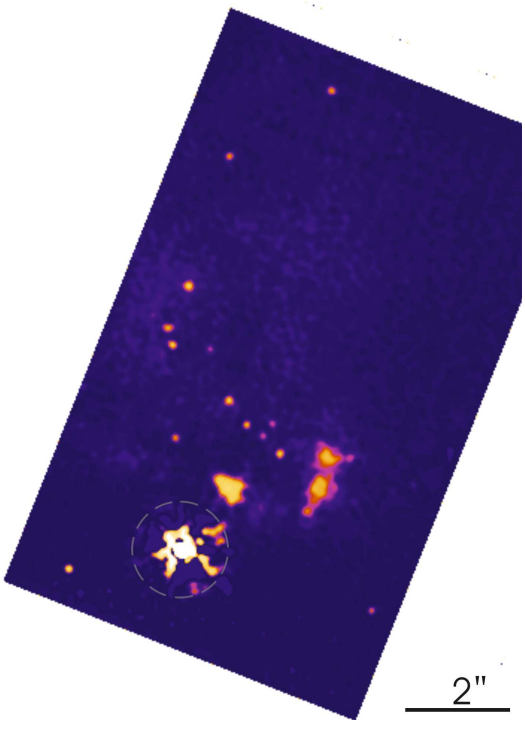

b) **BTA speckle image (146 mas resolution, 2002-09-24)**

Figure 7.2: Bispectrum speckle images (K'-band) reconstructed from data taken with *a*) the 6.5m MMT and *b*) the 6m BTA telescope. To show the weak emission features, the intensity of IRS1 was clipped to 2% of the total flux. Within the high-resolution image (*b*), speckle-noise artifacts appear around IRS1 (marked with a circle). These weak features represent small distortions of the point-spread-function (PSF) on the 1%-level and do not influence the reliability of the identification of point sources within the image. The absolute coordinates of IRS1 are $\alpha = 23^{\rm h}\,13^{\rm m}\,45\overset{\rm s}{.}35$ and $\delta = +61^{\circ}\,28'\,10\overset{''}{.}84$ (J2000, determined from 2MASS, accuracy $\sim 0\overset{''}{.}5$).

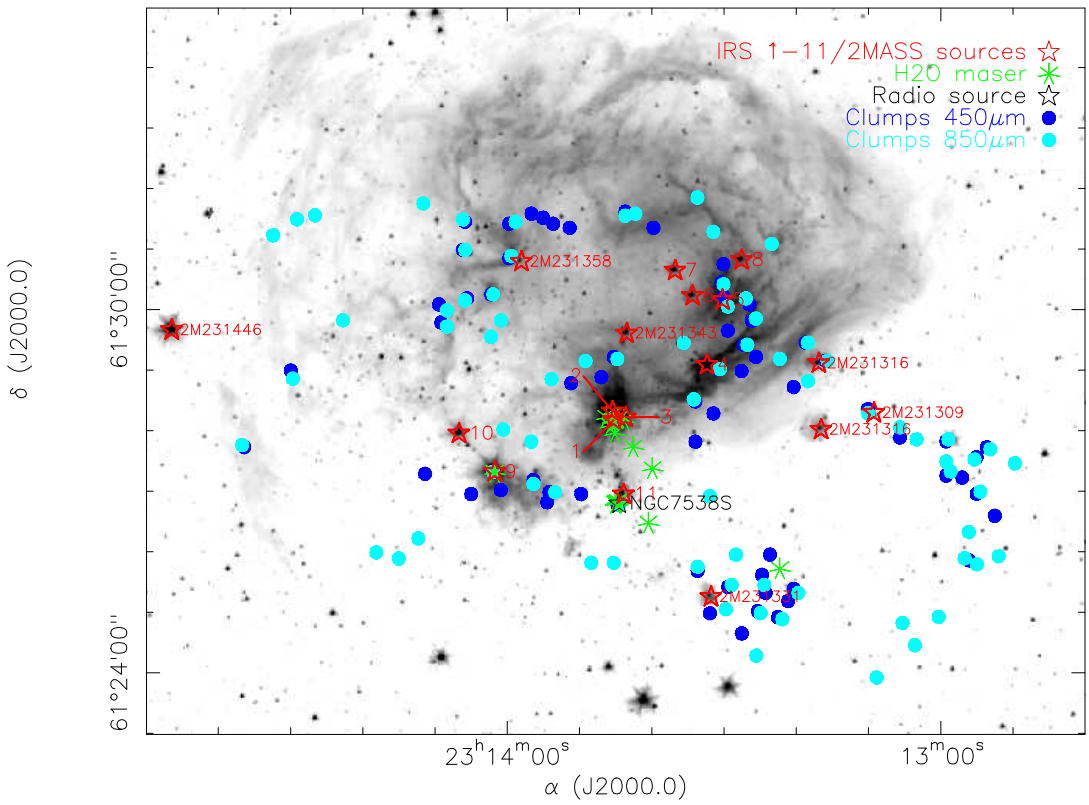

Figure 7.3: Figure *a)* shows the Spitzer/IRAC 4.5 μm image with the position of the infrared sources (IRS1 to 11 and 2MASS sources) and H_2O masers marked. Furthermore, the position of the sub-millimeter (450 μm and 850 μm) clumps reported by Reid & Wilson (2005) are shown. The position of the 2MASS sources 2MASS 23135808+6130484, 2MASS 23131660+6128017, 2MASS 23134351+6129372, 2MASS 23144651+6129397, 2MASS 23131691+6129076, 2MASS 23130929+6128184, and 2MASS 23133184+6125161 are labeled explicitly.

7.3.2 *Spitzer*/IRAC Archive data

In order to relate our high-resolution images with the morphology of the NGC 7538 molecular cloud at large scales, we examined archival 3.6, 4.5, 5.8, and 8.0 μm images (PI: G. G. Fazio), taken with the Infrared Array Camera (IRAC, Fazio et al. 2004) on the *Spitzer* Space Telescope. The four bands are recorded simultaneously using two InSb (3.6 μm, 4.5 μm) and two Si:As (5.8 μm, 8.0 μm) detectors. The central wavelengths and bandwidths of the IRAC bands (Hora et al. 2004) are 3.56 μm ($\Delta\lambda = 0.75$ μm), 4.52 μm ($\Delta\lambda = 1.01$ μm), 5.73 μm ($\Delta\lambda = 1.42$ μm), and 7.91 μm ($\Delta\lambda = 2.93$ μm). Each image consists of 256 $\times$ 256 pixels, corresponding to a $\sim 5' \times 5'$ field-of-view on the sky. The data used include 48 *Spitzer* pointings taken on 2003 December 23 in the High Dynamic Range (HDR) mode. In HDR mode, for each pointing, images are taken with two exposure times (0.6 s and 12 s) in order to

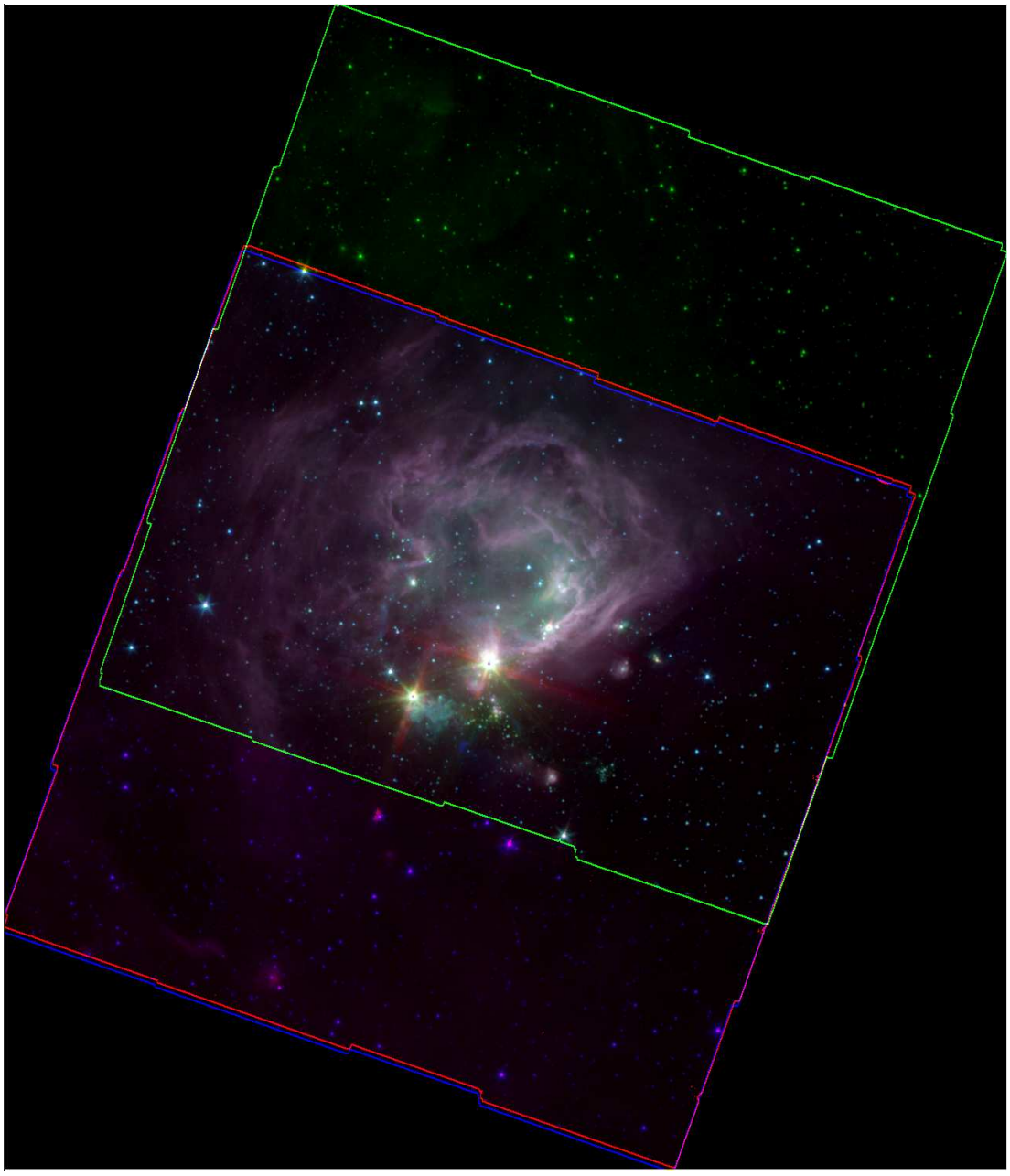

IRAC color composite: 3.6/4.5/5.8 μm

Figure 7.4: Color-composite produced from the 3.6 μm (blue), 4.5 μm (green), and 5.8 μm (red) IRAC bands. The intensity of each image was scaled logarithmically. North is up and east to the left.

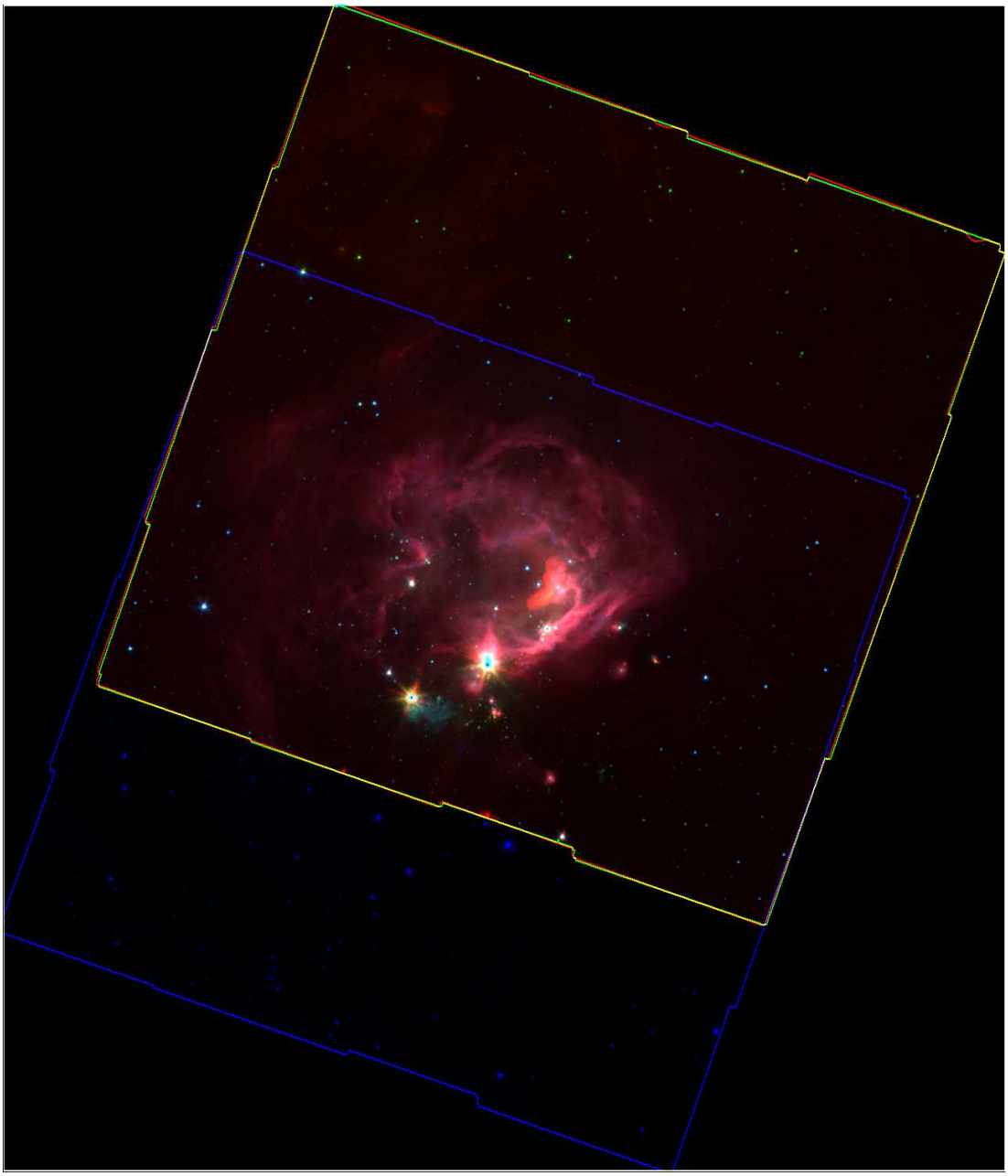

IRAC color composite: 3.6/4.5/8.0 μm

Figure 7.5: Color-composite produced from the 3.6 μm (blue), 4.5 μm (green), and 8.0 μm (red) IRAC bands. The intensity of each image was scaled logarithmically. North is up and east to the left.

record both bright and faint structures. However, the two brightest sources, IRS1 and IRS9, are saturated even within the 0.6 s exposure.

We used the *mopex* software (2005-09-05 version), released by the Spitzer Science Center (SSC), to process both the long and short exposure images. Beside the basic calibration steps applied by the Basic Calibrated Data (BCD) pipeline (S11.0.2), we performed Radhit detection, artifact masking, and pointing refinement. Finally we generated a mosaic in which the saturated pixels of the long exposure image were replaced by the corresponding pixels of the 0.6 s exposure. The optical design of IRAC induces a shift of $\sim 6\farcm8$ between the 3.6/5.8 μm and 4.5/8.0 μm pointings, leaving an overlap of $5\farcm1$ between all four bands.

In Figures 7.4 and 7.5, color composites of the 3.6/4.5/5.8 μm and 4.5/5.8/8.0 μm band images are shown.

The diffuse emission in three of the four IRAC bands is dominated by Polycyclic Aromatic Hydrocarbons (PAHs, Churchwell et al. 2004), which trace the border of regions excited by the UV photons from HMPOs particularly well. Contributions are also expected from several vibrational levels of H_2 (Smith & Rosen 2005b), atomic lines, CO vibrational bands, and thermal dust grain emission.

7.4 Results

7.4.1 Bispectrum speckle interferometry: Small-scale structures around IRS1/2

7.4.1.1 IRS1 Airy disk elongation and diffuse emission

In our speckle images, the Airy disk of IRS1 itself appears asymmetric, being more extended towards the northwest direction (PA $\sim -70°$, see Figure 7.2*b* and inset in the lower left of Figure 7.6). In the same direction (PA $\sim -60°$), we find two strong blobs (A, $B + B'$) of diffuse emission at separations of $\sim 1''$ and $2''$. These blobs and additional diffuse emission seem to form a conical (fan-shaped) region with a $90°$ opening angle extending from IRS1 towards the northwest.

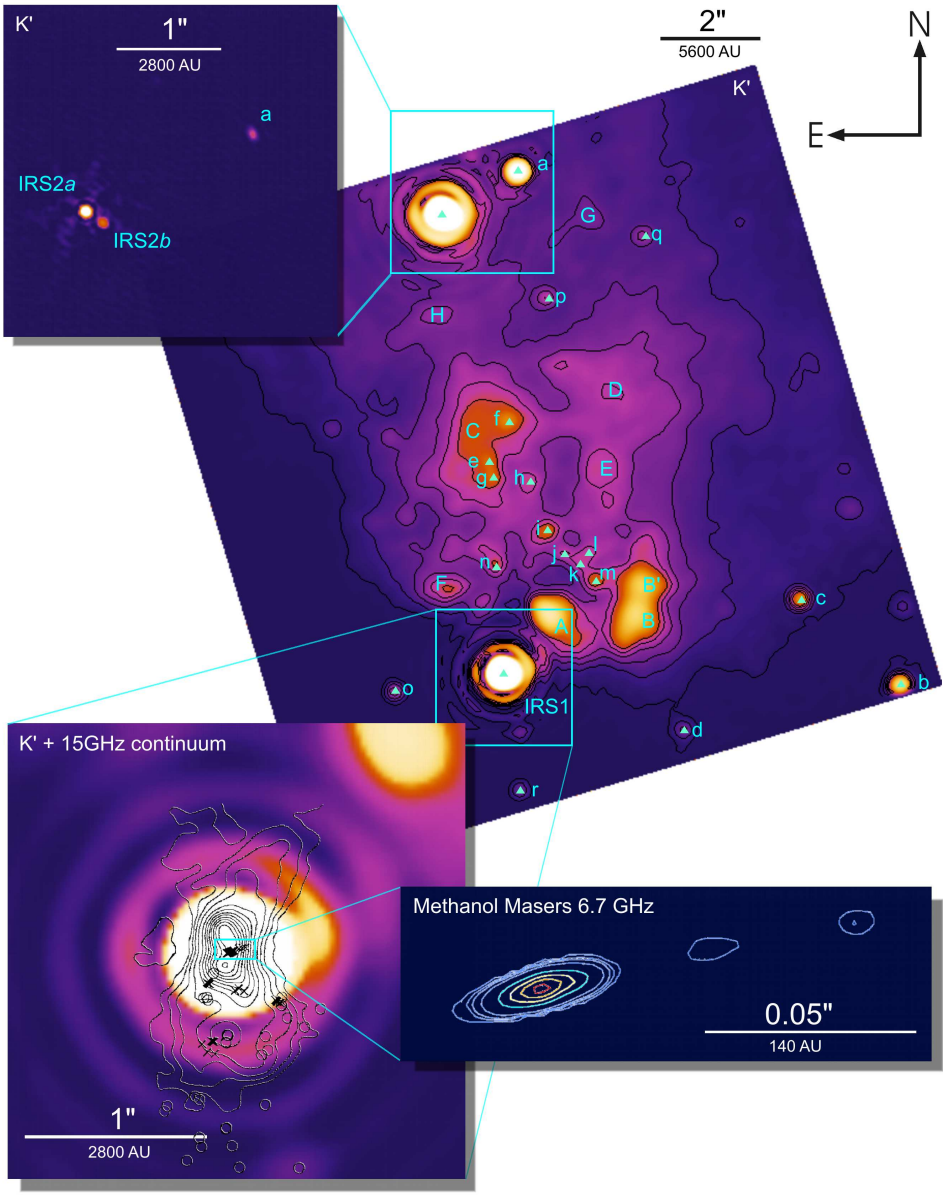

Figure 7.6: Bispectrum speckle image with identified point sources (triangles) atop marked. The astrometry for the point-sources was performed using the high-resolution BTA image, whereas the image shown was reconstructed from MMT data. The contours trace 0.25%, 0.5%, 0.75%, 1.0%, 1.25%, and 1.5% of the peak intensity. The inset on the upper left shows a reconstruction of the vicinity of IRS2 using a resolution of 80 mas (BTA data). In the lower left, IRS1 is shown using a different color table, emphasizing the elongation of the IRS1 Airy disk (MMT data) overplotted with the 15 GHz radio continuum (the contours show -1, 1, 2.5, 5, 10, 20, ..., 90% of the peak flux) and the position of the OH (circles) and methanol (crosses) masers (image from Hutawarakorn & Cohen 2003 using data from Gaume et al. 1995). In the lower right we show the integrated brightness of the methanol masers as presented by Pestalozzi et al. (2004, contour levels of 1, 3, 5, 10, 30, 50, 70, and 90% of the peak flux density are shown).

Table 7.1: NGC 7538 IRS1 outflow directions reported for various tracers.

Tracer	Structure	Beam Size [″]	Scale [″]	PA of outflow direction [°]	Dynamical Age[f] [10^3 yrs]	Ref.	Comments (Velocities in [km s^{-1}])
Methanol masers		0.03[c]		+19[a,d]	–	[8]	see Fig. 7.6
1.0 cm cont.	inner core $\lesssim$ 0.″5	0.13	0.4	+0[a]	$<$ 0.03	[9]	t_e = 0.15 yrs[e]
1.3 cm cont.	inner core $\lesssim$ 0.″4	0.11	0.4	+0[a]	$<$ 0.02	[5]	
6.0 cm cont.	inner core $\lesssim$ 0.″75	0.35	0.4	+0	$<$ 0.04	[1]	
1.0 cm cont.	outer core $\gtrsim$ 0.″5	0.13	1.0	-25[a]	$>$ 0.03	[9]	t_e = 0.3 yrs[e]
1.3 cm cont.	outer core $\gtrsim$ 0.″4	0.11	1.0	-25[a]	$>$ 0.02	[5]	
6.0 cm cont.	outer core $\gtrsim$ 0.″75	0.35	1.0	-15 ... -20	$>$ 0.04	[1]	
6.0 cm cont.	outer core $\gtrsim$ 0.″5	0.4	1.0	-25[a]	$>$ 0.03	[9]	
MIR 11.7μm	IRS1 Elongation	0.43	3	-45	0.16	[10]	see Fig. 7.10*k*
MIR 18.3μm	IRS1 Elongation	0.54	4	-45	0.16	[10]	see Fig. 7.10*l*
NIR *K*'-band	IRS1 Elongation	0.3	0.6	-78	0.03	–	see Fig. 7.6
NIR *K*'-band	feature A	0.3	1.6	-65	0.08	–	see Fig. 7.6
NIR *K*'-band	feature F	0.3	2.1	-33	0.11	–	see Fig. 7.6
NIR *K*'-band	feature B	0.3	3.0	-39	0.16	–	see Fig. 7.6
NIR *K*'-band	feature B'	0.3	3.3	-57	0.18	–	see Fig. 7.6
NIR *K*'-band	feature C	0.3	4.8	+6	0.25	–	see Fig. 7.6
NIR *K*'-band	feature E	0.3	6.2	-20	0.33	–	see Fig. 7.6
NIR *K*'-band	feature D	0.3	7.4	+10	0.39	–	see Fig. 7.6
NIR *K*'-band	eastern wall	0.3	–	+25	–	–	see Fig. 7.6
NIR *K*'-band	western wall	0.3	–	-65	–	–	see Fig. 7.6
[Fe II] 1.65 μm		1	15[a]	N-S[a]	0.8	[7]	around IRS2; see Fig. 7.10*i*
H_2	northern bow		30[a]	N-S	1.5	[6]	
H_2		1	27[a]	-25[a]	1.4	[7]	shell-like structure; see Fig. 7.10*i*
H_2	southern bow		45[a]	155[a]	2.3	[6]	see Fig. 7.10*h*

Table 7.1 – *Continued*

Tracer	Structure	Beam Size [″]	Scale [″]	PA of outflow direction [°]	Dynamical Age[f] [10^3 yrs]	Ref.	Comments (Velocities in [km s^{-1}])
CO	low velocities	7	5[a,b]	E-W	0.9	[3]	$-11 < \tilde{V}_b < -6$; $2 < \tilde{V}_r < 9$; see Fig. 7.10*g*
CO	high velocities	7	15[b]	-35	15	[3]	$-17 < \tilde{V}_b < -11$; $9 < \tilde{V}_r < 15$; see Fig. 7.10*g*
CO		34	18[b]	-50[a]	15	[2]	$-24 < \tilde{V}_b < -8$; $9 < \tilde{V}_r < 22$
CO		16	13[a,b]	-40	14	[4]	$-14 < \tilde{V}_b < -9$; $11 < \tilde{V}_r < 16$; see Fig. 7.10*f*
CO		45	12[a,b]	-50[a]	10	[3]	$-24 < \tilde{V}_b < -8$; $9 < \tilde{V}_r < 22$

Note – $\tilde{V}_r$ and $\tilde{V}_b$ are measured relative to the velocity of methanol maser feature A ($\tilde{V} = V - 56.25$ km s^{-1})

[a] Estimated from figures presented within the reference paper; therefore, with limited accuracy.

[b] The half-separation between the red- and blue-shifted CO lobe is given.

[c] For VLBI observations, we give the estimated error on the absolute position of the measured maser spots.

[d] The expected outflow direction is given; i.e., perpendicular to the measured orientation of maser feature A.

[e] Electron recombination time given in the reference paper.

[f] Assuming an outflow velocity of 250 km s^{-1}, which was measured by Gaume et al. (1995) within the H66α recombination line. For the CO emission, we also use the measured CO outflow velocity and provide the corresponding dynamical age in brackets. Since all velocities are measured along LOS, this timescale can only provide upper limits.

References: [1] Campbell (1984); [2] Fischer et al. (1985); [3] Scoville et al. (1986); [4] Kameya et al. (1989); [5] Gaume et al. (1995); [6] Davis et al. (1998); [7] Bloomer et al. (1998); [8] Minier et al. (2000); [9] Franco-Hernández & Rodríguez (2004); [10] De Buizer & Minier (2005)

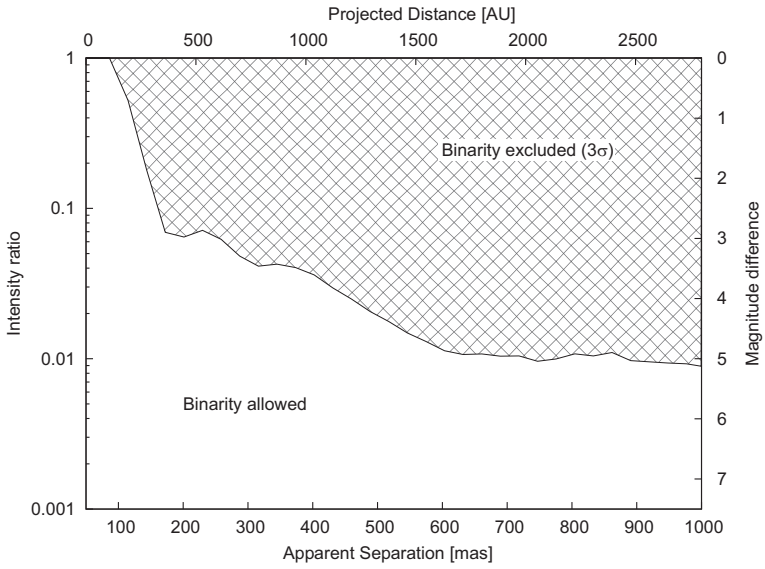

Figure 7.7: By measuring the speckle noise around the PSF of IRS1, we can rule out binarity of IRS1 on a 3σ-level as a function of apparent separation and intensity ratio.

A careful examination of the power spectrum of IRS1 has shown that the detected asymmetry of IRS1 is not caused by a companion, but seems to represent diffuse emission. Therefore, we can rule out a close binary system of similar-brightness components down to the diffraction limit of $\sim$ 70 mas. For the case of a binary system with components of significantly different brightnesses, we can put upper limits on the brightness of the hypothetical companion as a function of the projected binary separation (see Figure 7.7).

The PA of the elongation of the Airy disk is similar to the PA of *K'* blobs *A*, *B*, and B'. Another strong feature (*C*) can be seen towards PA$\sim 0°$. The blobs seem to be connected by a bridge of diffuse emission extending from feature *B* to *C*. Overall, the diffuse emission seems to form a fan-shaped region which is extending from IRS1 towards the northwest with an opening angle of nearly 90° . We identified some further features and list their position angles and separations in Table 7.1. The directions, which were reported for various outflow tracers, are also listed in this table and illustrated in Figure 7.8.

Our features *A*, $B + B'$, and *C* appear to coincide with the features *A*, *B*, and *C* identified by Alvarez et al. (2004). A comparison suggests that features $A + B + B'$, *C*, *D* correspond to the peaks 1*W*, 1*N*, and 1*NW* in Tamura et al. (1991).

7.4.1.2 Binarity of NGC 7538 IRS2

IRS2 appears resolved as a close binary system. Using an image reconstructed from BTA data with a spatial resolution of 80 mas (see inset in the upper-left corner of Figure 7.6), we determined the separation to be 195 mas and found a PA of $-123°$ for the $1\overset{m}{.}9$ fainter companion (2002-09-24). We designate the brighter component in the *K'*-band as IRS2*a* and the fainter as IRS2*b*.

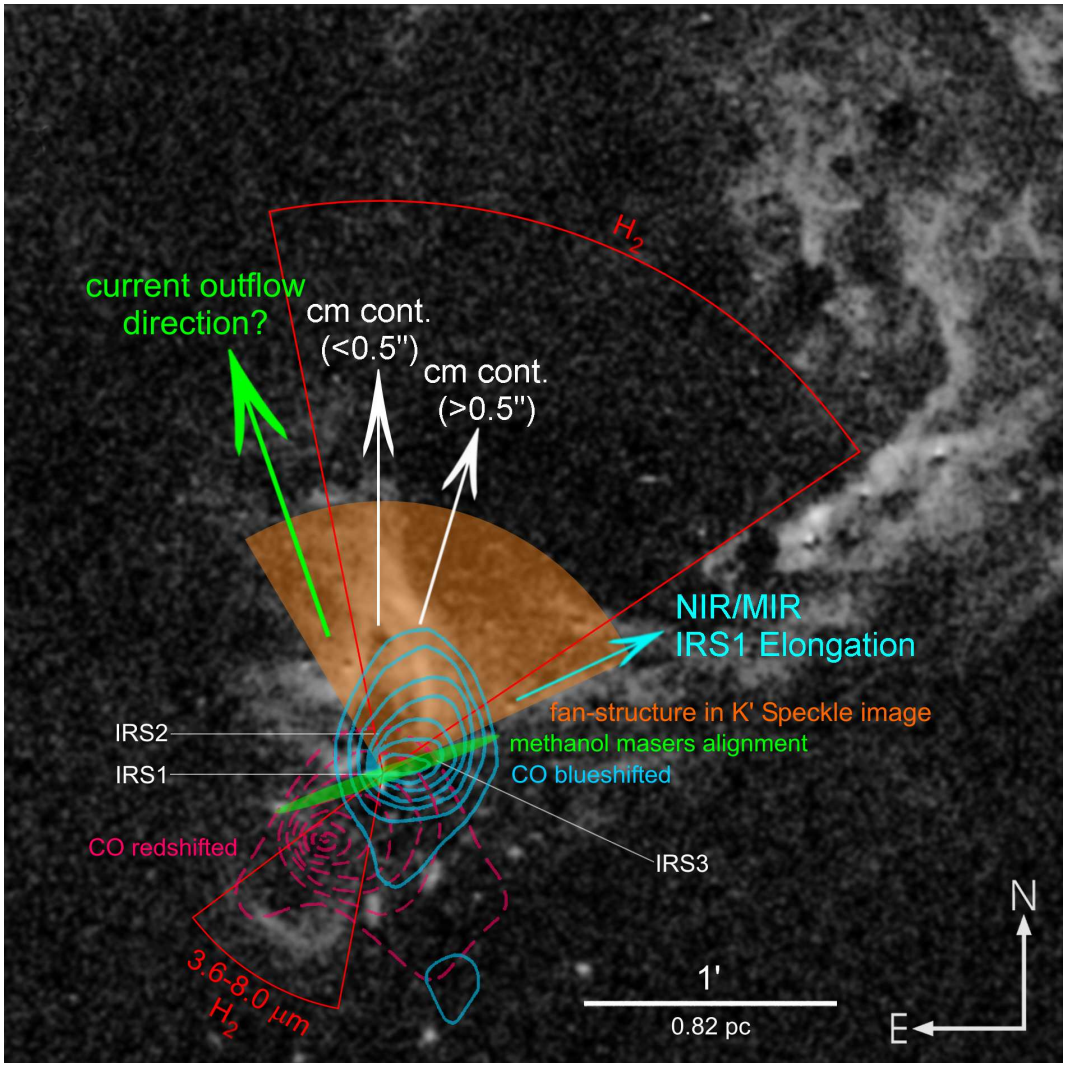

Figure 7.8: Illustration showing the outflow directions in the various tracers. The CO contours by Kameya et al. (1989, red and blue) are overlaid on the H_2 map (greyscale) by Davis et al. (1998). The orientation of the conjectural methanol maser disk (green), the fan-shaped structure detected in our *K*'-band image (orange), and the averaged direction of H_2 (red arcs) are shown schematically. The arrows indicate the direction prependicular to the alignment of the methanol masers (green), the orientation of the inner ($< 0.5''$) and outer ($> 0.5''$) core detected in the 1.0, 1.3, and 6.0 cm radio continuum (white), and the direction along which the IRS1 Airy disk was found to be elongated (MIR: De Buizer & Minier 2005; NIR: this study).

Table 7.2: Point sources identified in our speckle images. For details about IRS1 and the binary system IRS2*a*/*b*, we refer to the text. We identify components *a* to *f* with the stars already discovered in the image by Alvarez et al. (2004).

Name	RA (J2000)[a]	DEC (J2000)[a]	*K'* Magnitude[b]	Comment
a	$23^h\ 13^m\ 45\overset{s}{.}33$	$61°\ 28'\ 21\overset{''}{.}02$	$10\overset{m}{.}94$	
b	$44\overset{s}{.}81$	$10\overset{''}{.}63$	$11\overset{m}{.}29$	
c	$44\overset{s}{.}95$	$12\overset{''}{.}33$	$11\overset{m}{.}46$	
d	$45\overset{s}{.}11$	$09\overset{''}{.}69$	$11\overset{m}{.}73$	
e	$45\overset{s}{.}37$	$15\overset{''}{.}12$	$11\overset{m}{.}77$	embedded in feature *C*
f	$45\overset{s}{.}34$	$15\overset{''}{.}93$	$11\overset{m}{.}73$	embedded in feature *C*
g	$45\overset{s}{.}36$	$14\overset{''}{.}80$	$11\overset{m}{.}73$	embedded in feature *C*
h	$45\overset{s}{.}31$	$14\overset{''}{.}72$	$11\overset{m}{.}86$	
i	$45\overset{s}{.}29$	$13\overset{''}{.}74$	$11\overset{m}{.}71$	
j	$45\overset{s}{.}27$	$13\overset{''}{.}25$	$11\overset{m}{.}73$	
k	$45\overset{s}{.}25$	$13\overset{''}{.}05$	$11\overset{m}{.}81$	
l	$45\overset{s}{.}24$	$13\overset{''}{.}28$	$11\overset{m}{.}83$	
m	$45\overset{s}{.}22$	$12\overset{''}{.}71$	$11\overset{m}{.}71$	
n	$45\overset{s}{.}36$	$12\overset{''}{.}99$	$11\overset{m}{.}75$	
o	$45\overset{s}{.}50$	$10\overset{''}{.}50$	$11\overset{m}{.}60$	
p	$45\overset{s}{.}29$	$18\overset{''}{.}42$	$11\overset{m}{.}73$	
q	$45\overset{s}{.}16$	$19\overset{''}{.}69$	$11\overset{m}{.}77$	
r	$45\overset{s}{.}33$	$08\overset{''}{.}48$	$11\overset{m}{.}71$	

[a] For the astrometry, the relative errors are of the order of $0\overset{''}{.}1$. The absolute calibration using the reference position of IRS1 in 2MASS introduces further errors ($0\overset{''}{.}2$).

[b] The photometry was done relative to IRS1 with an uncertainty of $0\overset{m}{.}3$. For the conversion to absolute photometry, we assumed a IRS1 magnitude of $8\overset{m}{.}9$ (Ojha et al. 2004).

7.4.1.3 Detection of fainter cluster members

Besides IRS1 and IRS2*a*/*b*, we were able to identify 18 additional fainter point-like sources (*a*-*r*) within the BTA image, whose positions and *K'*-band magnitudes are listed in Table 7.2.

In order to test whether these sources are physically related to NGC 7538, one can compare the stellar number density for the brightness range $11\overset{m}{.}0$ to $12\overset{m}{.}0$ in our speckle image, $N_{\mathrm{Speckle}} = 18/128\,\mathrm{arcsec}^2 \approx 2.1 \times 10^6/\mathrm{deg}^2$, with the number expected from the cumulative *K*-band luminosity function (KLF) of the NGC 7538 field[2] $N_{\mathrm{field}} \approx 1.8 \times 10^3/\mathrm{deg}^2$. Although these number densities were obtained with different spatial resolution, the clear over-density of stars in our speckle image is significant and we conclude that most of the detected stars are likely members of the NGC 7538 star forming region. When using the KLF for the IRS 1-3 region instead of the whole NGC 7538 field, the stellar over-density in our speckle image becomes even more evident ($N_{\mathrm{IRS1-3\,cluster}} \approx 1.4 \times 10^3/\mathrm{deg}^2$). Since these stars are about 5 to

[2] The *K*-band luminosity function by Balog et al. (2004) for the whole NGC 7538 region, corrected with the on-cluster KLF, and cumulated for the magnitude range $11\overset{m}{.}0$ to $12\overset{m}{.}0$ was used.

6 magnitudes fainter than IRS1, they are likely to be part of the associated intermediate mass stellar population.

The arrangement of the stars within the fan-shaped nebula does not appear to be random, but follows the S-structure of the diffuse blobs (see Figure 7.6). Most remarkable, more than half of the stars seem to be aligned in a chain reaching from feature *B* to *C* (PA $\sim 45°$). Within the diffuse blobs close to IRS1 (*A*, *B*, *B*′), no stars were found, whereas embedded in blob *C*, three stars could be detected.

7.4.2 *Spitzer*/IRAC: Morphology at large spatial scales

Imaging of NGC 7538 at optical wavelengths showed that diffuse emission can mainly be found in the vicinity of IRS5 (Lynds & O'Neil 1986). At NIR wavelengths (Ojha et al. 2004), a diffuse structure can be found extending from the IRS1-3 cluster towards the northwest with the strongest emission around IRS5.

The Spitzer/IRAC images reveal a more complex, bubble-like structure (see Figures 7.4 and 7.5), whose western border is formed by a pronounced ridge-like filament connecting IRS1-3 with IRS4 and reaching up to IRS5 (see Figure 7.3). At the western border of the bubble a wide conical structure is located, with a vertex on 2MASS 23135808+6130484. Another conical structure can be detected close to the northern border of the bubble. Several other outflow structures can be found in the IRAC image; most noteworthy, the unidirectional reflection nebula around 2MASS 23144651+6129397, 2MASS 23131691+6129076, and 2MASS 23130929+6128184 (see Figure 7.3).
The sources 2MASS 23131660+6128017 and 2MASS 23133184+6125161 appear to be embedded in a shell-like cloud.

Besides the position of the strongest NIR sources, Figure 7.3 shows also the position of the submillimeter (450 μm, 850 μm) clumps reported by Reid & Wilson (2005). These clumps trace the filaments and knots of the bubble, which can be seen in the IRAC images, very well. Besides this, the submillimeter clumps suggest another bubble-like structure to the southwest of IRS4 (see also the images in Reid & Wilson 2005). This bubble seems to be invisible at near- and mid-infrared wavelengths, although several NIR sources are located on its border (2MASS 23130929+6128184, 2MASS 23133184+6125161).

As already pointed out by Reid & Wilson (2005), it is interesting to compare the position of the detected H_2O masers with the position of the centers of high-mass star formation in the region and to find agreement in many cases (IRS1–3, IRS9, NGC 7538S). However, as can be seen in Figure 7.3, for four locations of H_2O masers, no MIR counterpart can be found in the IRAC images (the detection limits for point sources in the four IRAC bands are roughly 3.6, 5.3, 31, and 34 μJy for the IRAC bands at 3.6, 4.5, 5.8, and 8 μm assuming medium sky background).

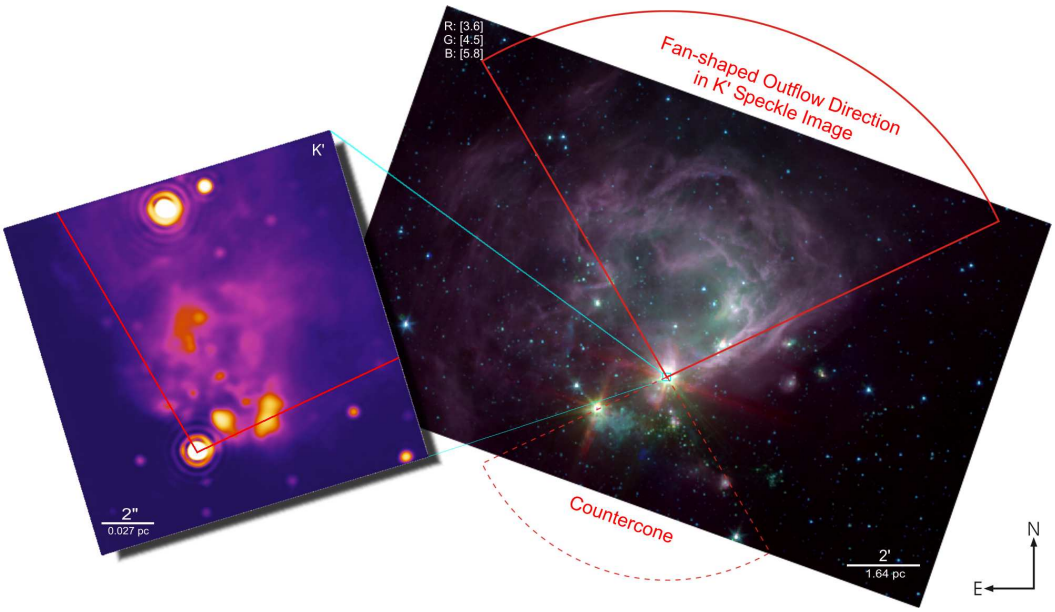

Figure 7.9: Comparison of the outflow direction imaged with Speckle interferometry with the bubble-like structure imaged with *Spitzer*-IRAC.

7.5 Discussion

7.5.1 Nature of the observed *K'*-band emission

In the wavelength range of the *K'*-band filter ($\lambda_0 = 2.12$ μm, $\Delta\lambda = 0.21$ μm), we record not only continuum radiation (e.g. scattered light, thermal dust emission, stellar continuum emission), but also line emission (e.g. H_2). However, both Bloomer et al. (1998, see Figure 7.10) and Davis et al. (1998) did not detect significant amounts of H_2 emission around IRS1. Furthermore, deep optical imaging by Elsaesser et al. (1982) and Campbell & Persson (1988) reveal a weak optical source offset 2.″2 north of the radio source IRS1. The latter authors argue that the strong extinction ($A_V = 13$) derived for IRS1 makes it highly unlikely that this optical emission is connected to IRS1 itself but that it most likely represents scattered light. The measured offset suggests that the faint optical source should be associated with blobs *A* and *B* in our images, making scattering the most likely radiation mechanism for the detected *K'*-band emission. This conclusion is also supported by polarization measurements (Dyck & Lonsdale 1979) which show a strong polarization of the 2 μm emission, tracing either scattered light or light transmitted through aligned grains. Henceforth we presume continuum to be the most important contributor to the detected emission.

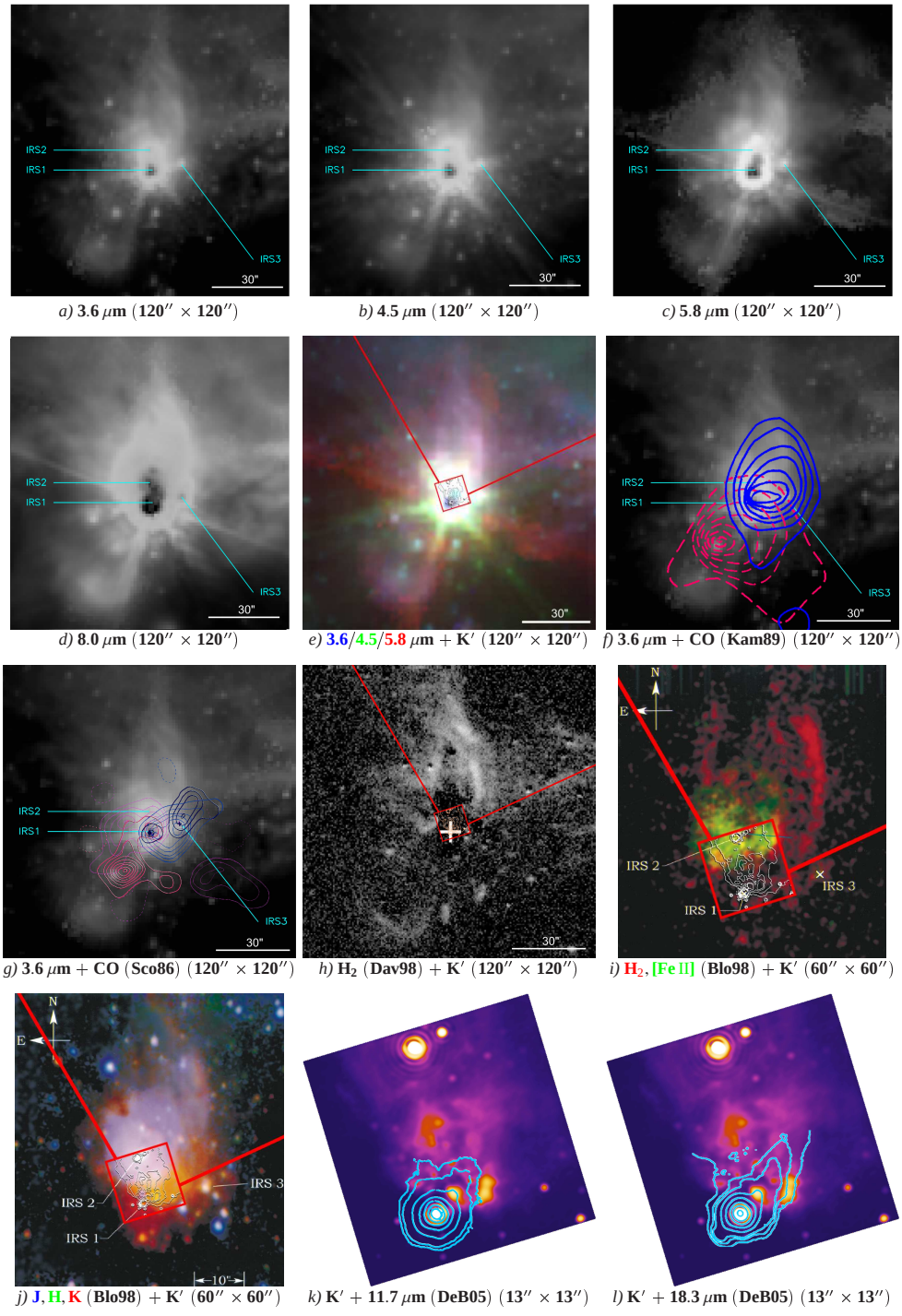

a) **3.6 μm** (**120″ × 120″**) *b)* **4.5 μm** (**120″ × 120″**) *c)* **5.8 μm** (**120″ × 120″**)

d) **8.0 μm** (**120″ × 120″**) *e)* **3.6**/**4.5**/**5.8 μm + K′** (**120″ × 120″**) *f)* **3.6 μm + CO** (**Kam89**) (**120″ × 120″**)

g) **3.6 μm + CO** (**Sco86**) (**120″ × 120″**) *h)* **H_2** (**Dav98**) **+ K′** (**120″ × 120″**) *i)* **H_2**, **[Fe II]** (**Blo98**) **+ K′** (**60″ × 60″**)

j) **J**, **H**, **K** (**Blo98**) **+ K′** (**60″ × 60″**) *k)* **K′ + 11.7 μm** (**DeB05**) (**13″ × 13″**) *l)* **K′ + 18.3 μm** (**DeB05**) (**13″ × 13″**)

Figure 7.10: Mosaic showing the IRS1–3 cluster at various wavelengths. Beside the speckle K'-band image (also marked as red box) and IRAC images, data from Scoville et al. (1986, CO), Kameya et al. (1989, CO), Bloomer et al. (1998, J, H, K, H_2, [Fe II]), Davis et al. (1998, H_2), and De Buizer & Minier (2005, 11.7 μm, 18.3 μm) was incorporated.

7.5.2 Methanol maser feature A: Protostellar disk or outflow?

We note that the 2MASS position of IRS1 (α =23$^{\rm h}$ 13$^{\rm m}$ 45$^{\rm s}$.35, δ =+61° 28′ 10″.8, J2000) and the position of the methanol maser feature A (α =23$^{\rm h}$ 13$^{\rm m}$ 45$^{\rm s}$.364, δ =+61° 28′ 10″.55, J2000) reported by Minier et al. (2000) coincide within the errors[3]. Therefore, the methanol masers and the outflow driving source are likely causually connected, however a random coincidental alignment cannot be ruled out.

Since methanol masers can trace both protostellar disks and outflows, it is not a priori clear how the linear alignment of the methanol maser feature A and the observed velocity gradient should be interpreted. For IRS1, both claims have been made (Pestalozzi et al. 2004; De Buizer & Minier 2005). However, detailed modeling has provided strong quantitative support for the disk interpretation but is still missing for the outflow interpretation. Furthermore, a study by Pestallozi et al. (in prep.) suggests that simple outflow geometries cannot explain the observed properties of feature A.

A major difference between these two scenarios is the orientation of the disk associated with the outflow driving source: Whereas in the disk scenario the methanol masers are lined up within the disk plane (PA $\sim -62°$), the outflow scenario suggests an orientation of the disk plane perpendicular to the maser alignment (PA $\sim +28°$). The observed asymmetry in our NIR speckle images, as well as the elongation of the emission observed in the 11.7 and 18.3 μm images by De Buizer & Minier (2005), can be explained within both scenarios:

Scenario A: If maser feature A traces an **outflow cavity**, the detected asymmetry might simply reflect the innermost walls of this cavity (oriented northwest), whereas the southeastern cavity of a presumably bipolar outflow might be hidden due to inclination effects.

Scenario B: Alternatively, if the masers trace an edge-on **circumstellar disk**, the asymmetry of the infrared emission could trace the western wall of an outflow cavity with a wide half-opening angle. The asymmetry cannot be attributed to the disk itself because the detection of stellar radiation scattered off the disk surface at such a large distance is highly unlikely.

For completeness, we also mention the interpretation by Kameya et al. (1989), who attributed the change between the direction observed in the UCH II region (PA 0°) and the high-velocity CO flow (PA −60°) to flow deflection, either by large-scale magnetic fields or due to density gradients.

We proceed now to discuss both scenarios within an outflow-cavity model (Sec. 7.5.3) and a precessing jet model (Sec. 7.5.4), incorporating the large amounts of evidence collected by various authors over the last three decades.

[3]The astrometric accuracy of the 2MASS catalogue was reported to be $\sim 0''.15$ (see http://ipac.caltech.edu/2mass/releases/allsky/doc/expl-sup.html).

7.5.3 Scenario A: Outflow cavity model

Since the intensity of the diffuse emission in our images seems to decrease with distance from IRS1 and the vertex of the fan-shaped region appears centered on IRS1, we cannot support the hypothesis by Bloomer et al. (1998), who identified IRS2 as the likely source of the diffuse NIR emission. Instead, the observed fan-shaped region can be interpreted as a cavity that was formed by outflow activity from IRS1. Because the walls of the fan-shaped structure are well-defined, we can measure the opening angle of the proposed outflow cavity from the eastern wall (PA 25°) to blob *A* (PA $-65°$), obtaining a wide total opening angle of 90°.

The unidirectional asymmetry of IRS1 in the NIR and MIR images (see Figure 7.10) is naturally explained in this context as scattered light from the inner (< 1500 AU) walls of the cavity. This scenario is also consistent with the southeast–northwest orientation of the CO outflow, aligned roughly parallel to the methanol masers (PA $\sim -62°$). Blobs *A*, *B*, *B′* are located within the same direction and might resemble either clumps in the cavity or recent ejecta from the outflow. The various blobs might also indicate the presence of several outflows.

In order to resolve the misalignment of the radio-continuum core with respect to the other outflow tracers, it was proposed that the radio-continuum emission might arise from a photoevaporated disk wind (Lugo et al. 2004).

However, as noted above, the methanol maser feature A lacks a quantitative modeling up to now.

7.5.4 Scenario B: Precessing jet model

7.5.4.1 Constraints from the methanol maser disk

The circumstellar-disk modeling presented by Pestalozzi et al. (2004) reproduces the observational data for maser feature A in minute detail. Assuming a central mass of $30 M_{\odot}$ and Keplerian rotation, this model confines the inner ($r_i \sim 290$ AU) and outer ($r_o \sim 750$ AU) radii of the disk (these radii scale as $(M/30M_{\odot})^{-1/3}$ with the central mass M). The model does not set strict constraints on the inclination and orientation of the disk on the sky.

An uncertainty in the disk inclination arises from the assumption that methanol is formed within a surface layer of the disk from photoevaporation of H_2O. The midplane of the disk might therefore be inclined within certain limits. A distinct inclination is suggested by the fact that the NIR/MIR continuum emission, as well as the H_2 shock tracer line emission, appears more pronounced towards the north than towards to south (see Figures 7.2 and 7.10*h*). An inclination of the northern outflow towards us is also indicated by CO outflow observations (e.g. Kameya et al. 1989), which show the blueshifted CO lobe of IRS1 towards the northwest (see Figures 7.10*f* & 7.10*g*).

The disk orientation on the sky can only be constrained by the maser observations with a limited

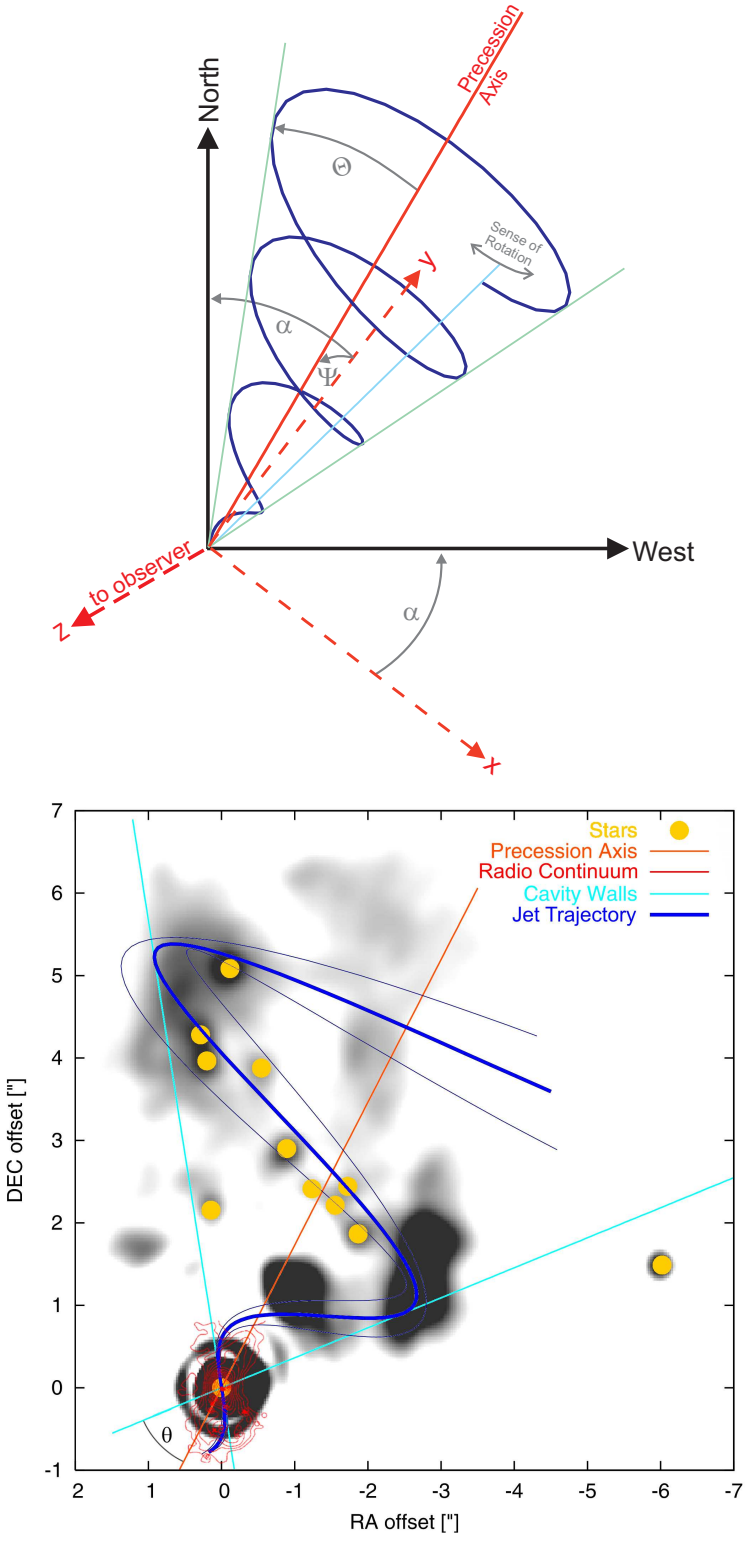

Figure 7.11: *Top:* Illustration of the analytic precession model presented in Sec. 7.5.4.3. *Bottom:* MMT speckle image overplotted with the trajectory of ejecta from a precessing outflow projected onto the plane of the sky (thick blue line) as described by the analytic precession model. For the counter-clockwise precession, the parameters $P_{\rm prec} = 280$ yrs, $\Theta = 40^\circ$, $\alpha = -30^\circ$, $\psi = 0^\circ$ (precession axis within the plane of the sky), and $\phi_0 = 0^\circ$ were used. In order to simulate a finite collimation of the flow, we varied both α and ψ by $\pm 5^\circ$, yielding the trajectory given by the thin blue lines. The red contours show the 15 GHz radio continuum map by Hutawarakorn & Cohen 2003 (using data by Gaume et al. 1995).

accuracy since the masers only trace a narrow latitudinal arc of the disk, missing potential disk warping. Nevertheless, it is still reasonable to identify the disk orientation with the linearly-aligned feature A.

7.5.4.2 Indications for disk and jet precession

Assuming that the alignment of the masers is representative of the orientation of the disk midplane (i.e. assuming disk warping is negligible[4]), it is evident that the direction perpendicular to the disk plane (PA $+19°$, the expected outflow direction) is significantly misaligned from the axes of the bipolar CO outflow and the NIR fan-shaped region (PA $\sim -20°$; illustrated within Figure 7.6). Also, the observed bending (Campbell 1984; Gaume et al. 1995) in the radio continuum could indicate a change in the outflow direction. Whereas the inner core ($\lesssim 0\farcs5$) is orientated along PA $\sim 0°$, the outer core ($0\farcs5$ – $1\farcs0$) bends slightly towards the west (PA $\sim -25°$). This might indicate that the outflow changed its direction by this amount within the times needed by the jet to propagate the appropriate projected distances (~ 25 and ~ 50 years).

The bending detectable in the UC H II region on scales of $\lesssim 1\farcs0$ seems to continue at larger scales within the morphology observed in our speckle images, suggesting an S-shaped fine-structure of the diffuse emission extending from IRS1 initially towards the northwest and further out towards north. The blobs *A*, *B*, and *B′* observed close to IRS1 (PA $\sim -60°$) might represent the most recent ejecta, whereas the weak features which appear further away in our images (*C*, *D*) might trace earlier epochs of the history of the outflow.

Based on these indications, we suggest a disk and jet precession model. The fan-shaped diffuse emission in which the S-structure is embedded can be explained as scattered light from the walls of an outflow cavity, which was cleared by the proposed wandering jet.

The western wall of this wide, carved-out outflow cavity might appear within our NIR and the MIR images as an elongation of IRS1. Since this elongation extends mainly towards the northwest, there must be an additional reason why the western wall of this cavity appears more prominent than the eastern wall. A possible explanation might be shock excitation of the western wall, which would cool through emission in shock tracer lines like H_2, which is contributing to the recorded *K'*-band.

Assuming the precession period derived in Sec. 7.5.4.3, the outflow (which currently points towards PA $\sim 19°$) would have excited the western wall of this cavity ~ 140 years ago, which corresponds roughly to the H_2 radiative cooling time.

The arrangement of the fainter cluster members embedded within the diffuse emission can be understood in this context, too: Taking into account that IRS1 is still deeply embedded in its natal circumstellar cloud, the jet would have cleared the envelope along its wandering path. The decreasing column density results in lower extinction along the jet's path, revealing the fainter stars which likely formed in the

[4] Interestingly, the converse assumption (that disk warping is non-negligible) implies disk precession as well, as the jet would be launched perpendicular to the warped surface of the inner part of the disk.

vicinity of IRS1. The fainter stars might therefore be detectable only in those regions where the precessing jet reduces the extinction sufficiently. Within the blobs closest to IRS1, stars may be undetectable because of either inclination effects or confusion with the significantly higher surface brightness of blobs IRS1 *A*, *B*, and *B*′ (limiting the sensitivity to detect point sources), or because of the high density of the outflowing material itself, providing intrinsic extinction.

The outflow tracers observed at rather large scales (CO, H_2, see Figure 7.10) are oriented roughly in the same direction as the NIR fan-shaped structure. The CO channel maps by Scoville et al. (1986, Figure 7.10*g*) suggest a change in the orientation of the CO outflow lobes for low and high velocities. Whereas the low velocity CO outflow is oriented along the east-west direction, the high velocity lobes are oriented along PA $\sim -35°$. As CO traces material swept-up by the outflow and has a relatively long cooling time (of the order of 10^4 yrs), the different orientations observed at low- and high velocities are more difficult to interpret.

Finally, we speculate that the precession model might also explain why the velocities of the methanol maser features B, C, D, and E are in the same range as the velocities of the CO outflow (De Buizer & Minier 2005), but show opposite signs for the LOS velocity with respect to feature A (maser features B, C, D, and E are blue-shifted, whereas the southern CO lobe is red-shifted). Assuming precession, the CO outflow would trace the average outflow direction around the precession axis (with the southern axis oriented away from the observer), whereas the methanol masers might trace clumps very close to the source, which were excited more recently when the southern part of the outflow was pointing towards the observer[5].

In general, precession can explain the change in the flow orientation, but potential alternative explanations include density gradients in the surroundings of IRS1, the presence of multiple outflows, and flow deflection.

7.5.4.3 Analytic precession model

In order to get a rough estimate for the precession parameters, we employ a simple analytical model with constant radial outflow speed v. On the radial motion we superpose a precession with period $P_{\rm prec}$, leading to the wave number

$$k = \frac{2\pi}{\mathrm{v} P_{\rm prec}}\,; \tag{7.1}$$

by the time that ejected material travels a distance r from the source, the direction of the jet axis changes by the angle kr.

To describe the jet propagation in three dimensions we introduce a Cartesian coordinate system centered on IRS1 whose z-axis is along the line of sight (see Figure 7.11, top). The precession axis is in the

[5] This is consistent with the precession parameters determined in Sect. 7.5.4.3, where we find that the half-opening angle of the precession Θ is larger than the inclination of the precession axis with respect to the plane of the sky ψ.

$y-z$ plane inclined by angle ψ to the plane of the sky[6], and the jet axis makes an angle Θ with it. For counter-clockwise[7] precession, the coordinates of material at distance r from the origin are

$$\begin{pmatrix} x \\ y \\ z \end{pmatrix} = r \times \begin{pmatrix} \sin\Theta\cos\phi \\ \cos\Theta\cos\psi + \sin\Theta\sin\phi\sin\psi \\ -\cos\Theta\sin\psi + \sin\Theta\sin\phi\cos\psi \end{pmatrix} \tag{7.2}$$

where $\phi = \phi_0 + kr$ is the jet's azimuthal angle from the x-axis. The initial phase ϕ_0 can be taken as 0° since the direction perpendicular to the methanol feature A seems to coincide with the eastern wall of the outflow cavity. The PA α of the y-axis can be set from the average angle of the fan-shaped region in the speckle images as $\alpha = -30^\circ$. Using $v = 250\ \mathrm{km\,s^{-1}}$, as measured by Gaume et al. (1995) within the H66α recombination line, leaves as free parameters P_{prec}, Θ, ψ, and the sense of rotation. Trying to fit the orientation of the maser disk, the orientation of the UC H II region, and the position of the NIR blobs with these parameters simultaneously, we find reasonable agreement with a precession period $P_{\mathrm{prec}} = 280 \pm 10$ yrs, a precession angle $\Theta = 40^\circ \pm 3^\circ$, a counter-clockwise sense of rotation, and small inclination $\psi = 0^\circ \pm 10^\circ$. At larger inclination angles ($\gtrsim 10^\circ$) loops start to appear, significantly degrading the agreement. In Figure 7.11, we show the projected trajectory of the proposed wandering jet with the thick line, whereas the thin lines give the path obtained with a variation of $\pm 5^\circ$ in α and ψ, resembling the finite width of the flow.

The analytic model presented in this section might suffice in order to get a rough estimate of the precession parameters, although it does not take into account the interaction of the flow with the ambient medium nor the excitation and cooling of the ambient material.

These parameters can be used to predict how the orientation of the methanol maser disk changes with time. Using the PA at the phase $\phi_0 = 0^\circ$ as reference, one expects that the PA changes only marginally (less than 1°) within 10 yrs. A much more significant change of 10° (20°) would be expected after 36 yrs (50 yrs), which would be detectable with future VLBI observations.

7.5.4.4 Numerical molecular hydrodynamic simulations

A large number of studies about the structure and evolution of precessing protostellar jets can be found in literature (e.g. Raga & Biro 1993; Völker et al. 1999; Raga et al. 2004; Rosen & Smith 2004; Smith & Rosen 2005a), although most of these studies focus on jets from low-mass stars with rather narrow precession angles. As the number of simulations carried out for wide precession angles is much more limited (e.g. Cliffe et al. 1996), we performed a new hydrodynamic simulation. Besides the general morphology, we aim for comparing the position of the newly discovered fainter stars with the column

[6] Positive values of ψ indicate an inclination out of the plane of the sky towards the observer.

[7] For the sense of rotation, we follow the convention that counter-clockwise rotation (as measured from the source along the precession axis) corresponds to a positive sign of the phase ϕ.

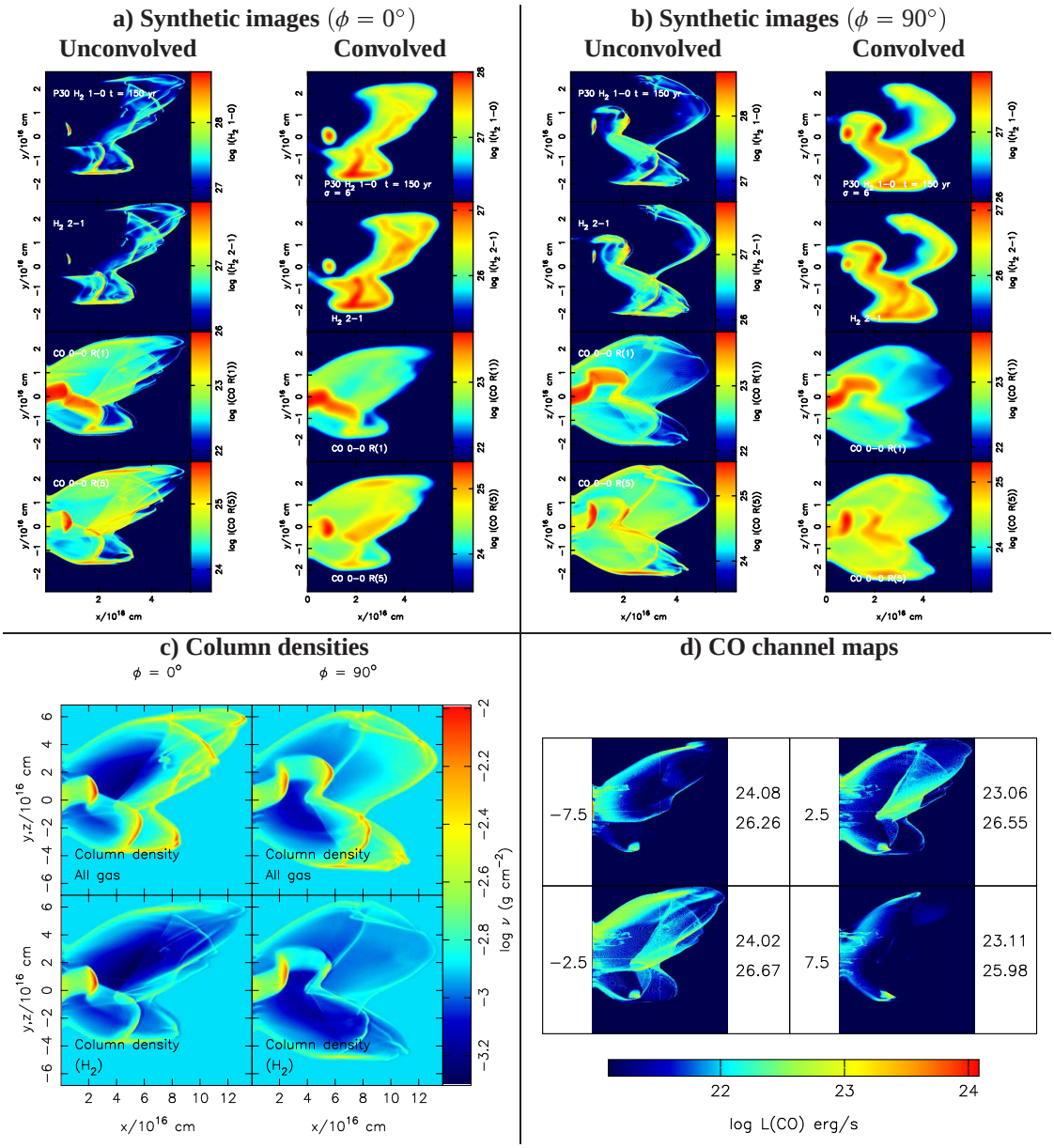

Figure 7.12: *a), b)*: Synthetic images (H_2 $1 \rightarrow 0$, $2 \rightarrow 1$; CO R(1), R(5)) from our ZEUS-3D molecular hydrodynamic simulation, shown for two different projections. In Figure *a)* the images are also shown after a convolution with a Gaussian which roughly resembles the resolution obtained in our speckle observation (Figure 7.6). Figure *c)* shows the total gas column density and the H_2 column density for the same projections. Finally, in *d)* we show channel maps of the CO outflow for four velocity bins. Each velocity bin has a width of 5 km s^{-1} and the central velocity is given by the number on the left of each image (in km s^{-1}). The two numbers on the right of each image indicate the log of the maximum integrated luminosity in any single element in the image (*Top*, in erg s^{-1}) and the log of the total integrated luminosity in the entire velocity bin (*Bottom*).
The angle ϕ gives the angle between the *z* axis and the LOS, corresponding to a rotation around the precession axis (*x* axis). Please see the text (Sec. 7.5.4.4) for a description of the complete model parameters.

density variations caused by a precessing jet, which was beyond the scope of earlier studies.

We use the version of the ZEUS-3D code as modified by Smith & Rosen (2003), which includes some molecular cooling and chemistry, as well as the ability to follow the molecular (H_2) fraction. The large precession envisioned for the flow associated with NGC 7538 IRS1 requires that the simulation be performed on a very wide computational grid. Due to computational limits, we were restrained to use for this simulation a 3D Cartesian grid of 275 zones in each direction, where each zone spans 2×10^{14} cm in each direction. This grid balances the desire for some spatial resolution of the flow with the ability to simulate a sufficiently large part of the observed flow associated with NGC 7538 IRS1. Still, the total grid size ($\sim$ 0.018 pc) is smaller than the projected distance between IRS 1 and *K*'-band feature *C*.

Owing to the rather small physical size of the grid, we have chosen a nominal speed of 150 km s^{-1}, reduced from the inferred value of 250 km s^{-1} for this source. The flow is precessed with a nearly 30° precession angle, with the amplitude of the radial components of the velocity 0.55 of that of the axial component. The precession has a period of 120 years, which leads to 1.25 cycles during a grid crossing time. The flow is also pulsed, with a 30% amplitude and a 30 year period. This short period assists in the reproduction of the multiple knots of *K*'-band emission near NGC 7538 IRS1. The jet flow also is sheared at the inlet, with the velocity at the jet radius 0.7 that of the jet center. We have chosen a jet number density of 10^5 hydrogenic nuclei cm^{-3}, while the ambient density is 10^4. The simulated jet radius is 4.0×10^{15} cm (20 zones). Thus, the time-averaged mass flux is 2.6×10^{-6} $M_\odot$ yr^{-1}, which is three orders of magnitude lower than the value as determined for the CO outflow (Davis et al. 1998). Similar calculations of the momentum flux and kinetic energy flux, or mechanical luminosity, yield values of 3.8×10^{-4} km s^{-1} $M_\odot$ yr^{-1} and 4.7 $L_\odot$, respectively.

After the convolution with a PSF resembling the resolution obtained in real observations the H_2 emission in our simulation shows a morphology which is similar to the one seen in the *K*'-band speckle image. In particular, the simulations might also explain features *D* and *E* as associated with the proposed precessing jet (compare Figure 7.12*a* with Figure 7.6). The simulations also show that the CO emission, which can be expected for a precessing jet at larger distances from the driving source, appears very smooth, which is also in accordance with the CO observations made for NGC 7538 IRS1.

We note that the fainter stars *e* to *n* reported in Sec. 7.4.1.3 are located in the region where the column density in our precessing jet simulation appears particularly low (see Figure 7.12*c*, left column), supporting the scenario proposed in Sec. 7.5.4.2.

7.5.4.5 Possible precession mechanisms

Several mechanisms have been proposed which can cause jet bending or jet precession, although most of them were established for low- and intermediate stars and can cause precession angles of only a few degrees (Fendt & Zinnecker 1998; Eislöffel & Mundt 1997). For the case of high-mass stars and larger

precession angles ($\Theta \sim 40^\circ$), Shepherd et al. (2000) summarized the three most promising concepts that could induce precession into circumstellar disks. We discuss how well these mechanisms can explain the observations of IRS1. For all cases, it is assumed that the outflow is launched close to the center of the disk and that a precession of the inner parts of the disk will translate into a precession of the collimated flow (Bate et al. 2000).

1. Radiative-induced warping: Armitage & Pringle (1997) suggested that geometrically thin, optically thick accretion disks can become unstable to warping if the incident radiation from the stellar source is strong enough. As this warping instability is expected to occur only at disk radii larger than a critical radius $R_{\rm crit}$, we can estimate whether radiative-induced disk warping is expected at the inner part of the IRS1 disk. Using a stellar mass of $M \sim 30\ M_\odot$ (Pestalozzi et al. 2004), a mass accretion rate of the order of the mass outflow rate $\dot{M}_{\rm acc} \approx \dot{M}_{\rm outflow} \approx 5.4 \times 10^{-3}\ M_\odot\ {\rm yr}^{-1}$ (Davis et al. 1998), and a luminosity $L \approx 9.6 \times 10^4\ L_\odot$ (Akabane & Kuno 2005), we use equation 5 by Armitage & Pringle (1997) and the assumptions listed in Shepherd et al. (2000) and obtain a critical radius $R_{\rm crit} \sim 200$ pc. Since this is far beyond the inner edge of the disk where the jet collimation is expected to happen, it is very unlikely that the radiation emitted by the star or due to accretion causes any noticeable warping within the disk.

2. Anisotropic accretion events: The impact/merging of (low mass) condensations can change the orientation of the disk angular momentum vector. In such a dramatic event, angular momentum can be transferred from the impactor onto the accretion disk, potentially resulting in a net torque in the rotation of the disk. To estimate the precession angle, which could result from anisotropic accretion, very detailed assumptions about the disk, the impacting condensation, and their kinematics must be made. Since no data is available to estimate these quantities, we refer to the example computed by Shepherd et al. (2000) and note that in extreme cases, such an accretion event could cause a sufficiently large precession angle in the case of NGC 7538 IRS1 as well. However, in this scenario one would expect rather sudden changes in the jet direction rather than a smooth precession.

3. Tidal interactions with a companion: Warping and precession of the disk could be caused by tidal interactions with one or more companions on non-coplanar orbits. We assume the simplest case of a binary: with stellar masses M_p (primary) and M_s (secondary), an orbit with inclination i with respect to the disk plane, and a semimajor axis a. The mass ratio shall be denoted $q = M_p/M_s$ and will be assumed as unity. Our observations place an upper limit on the separation of such a companion (see Figure 7.7). Two cases can be considered:

3a) circumprimary disk ($a > r_o$): Because tidal torques would truncate the disk at about 0.3 times the binary separation (Lubow & Ogilvie 2000), we obtain a lower limit for the binary separation (for a circular orbit), namely, $a > 2\,500$ AU. However, a binary with such a large separation would be not

suited to explain the observations since the orbital period would be $> 2 \times 10^4$ yrs ($M_p + M_s = 30\ M_\odot$), implying a disk precession rate of $> 4 \times 10^5$ yrs (Bate et al. 2000). Assuming an extreme eccentricity might yield a short precession period of the order of 10^2 yrs but implies strong, periodic interactions between the companion and the disk during each perihelion passage. As this would quickly distort and truncate the disk, we see this assumption contradicts the methanol maser structure, which suggests a smooth extension of the methanol layer from $\sim$ 290 AU to $\sim$ 750 AU.

3b) circumbinary disk ($a < r_i$): Smoothed particle hydrodynamic simulations by Larwood & Papaloizou (1997) showed that a binary on a non-coplanar orbit with large inclination i could cause strong quasi-rigid body precession of the circumbinary disk (for $q > 10$) and strong warping, especially on the inner edge of the disk ($q \sim 1$). The same authors report that the disk precession frequency $\omega_{\rm prec}$ should be lower than the orbital frequency of the binary $\omega_{\rm binary}$. To make an order-of-magnitude estimation for the orbital period that would be expected for this hypothetical IRS1 binary system, one can assume $\omega_{\rm prec} \approx \omega_{\rm binary}/20$ (Bate et al. 2000) to obtain $P_{\rm binary} \approx 14$ yrs for the binary period, corresponding to a separation of $a_{\rm binary} \approx 19$ AU ($\sim$ 7 mas). This binary separation then puts a lower limit on the radius of the inner edge of the circumstellar disk. As this scenario can trigger the fast disk precession without truncating the extended disk structure traced by the methanol masers, we consider a circumbinary disk as the most plausible explanation.

7.5.5 The IRS2 companion and flow interaction with the IRS2 UC H II region

The spectral type of IRS2 was estimated to be O4.5 (Akabane & Kuno 2005), corresponding to a luminosity of $\sim 6.4 \times 10^5 L_\odot$. Using the measured K'-band flux ratio, one can make rough estimates for the spectral type of the two components reported in Sec. 7.4.1.2. By assuming the total luminosity is attributed only to the two components, we obtain a spectral type of O5 for IRS2*a* and O9 for IRS2*b* (using the OB star luminosities from Vacca et al. 1996).

Within our images, the wide-opening angle outflow cone from IRS1 seems to extend well out to IRS2. This offers an explanation for the shock tracer line emitting region that was imaged around IRS2 (Bloomer et al. 1998, see Figure 7.10*i*). The bowshock-like morphology of the [Fe II] and H_2 emission suggests that the shock is excited from the south (which is roughly the direction towards IRS1). In the direction opposite IRS1, the [Fe II] and H_2 emission even shows a cavity-like structure, which also appears in the 6 cm-radio continuum. Bloomer et al. (1998) suggested a stellar wind bowshock scenario, in which IRS2 moves with a speed of $\sim$10 km s^{-1} towards the southwest through the ambient molecular cloud. We note that the morphology could also be explained by interaction between the IRS1 outflow and IRS2 outflows. Based on its young age, IRS2 might also launch a powerful wind itself, causing the

distinct shock zone which appears within the shock tracer emission (see Figure 7.10*i*) and which is also detectable in our *K'*-band image (arc-like morphology between features *G* and *H*).

7.5.6 Outflow structures from IRS1 at larger spatial scales

Figure 7.10*a* to *d* shows mosaics of the vicinity of IRS1 in the four IRAC bands. Although IRS1 and IRS2 appear saturated in these images (shown in logarithmic scaling) and banding (vertical and horizontal stripes produced by IRS1 and IRS9) appears especially in the 5.8 and 8.0 μm images, structures potentially related to IRS1 can be observed. About 40″ towards the southeast of IRS1, a bowshock structure can be seen, which is also present in the H_2 image by Davis et al. (1998). This bowshock points in the same direction as the redshifted lobe of the CO outflow (see Figure 7.10*f*) and just opposite to the outflow direction identified in our speckle image at small scales. Thus, it is possible that this bow traces the southeastern part of the IRS1 outflow. In our speckle image, the inner part of this southeastern outflow is not visible; likely a result of strong intervening extinction.

Furthermore, it is interesting to note that the "ridge" connecting the IRS1–3 cluster with IRS4 and IRS5 follows the western wall of the outflow direction identified in our speckle image (see top of Figure 7.10). It is possible that the total extent of the IRS1 outflow also reaches much further northwest than the structure seen in the speckle image, contributing to the excitation of the western part of the bubble seen in the IRAC bands and the shocks in the H_2 image by Davis et al. (1998, see Figure 7.10*h*).

7.6 Evidence for Triggered Star Formation in the NGC 7538 Star Forming Region

It has been proposed by many authors that star formation seems to propagate southeastwards throughout the NGC 7538 complex (Werner et al. 1979; McCaughrean et al. 1991; Ojha et al. 2004). This is indicated by the spatial arrangement of the members of this star forming region, which also seems to agree with the expected evolutionary sequence: starting about 3′ northwest of IRS1, O stars located in the H II region represent the most developed evolutionary state, followed by the IRS1–3 cluster and their associated UCH II regions, with the compact reflection nebula around IRS9 representing the youngest member of this star formation site. In agreement with this picture, Balog et al. (2004) measured the reddening of stars throughout NGC 7538 and found a gradient in reddening with the most heavily reddened sources in the southeast.

The presented IRAC images can also be interpreted in support of this scenario since the ridgelike feature connecting IRS1-3, IRS4, IRS5 seems to trace the interface between the northeastern bubble (visible at NIR/MIR wavelengths) and the submillimeter bubble, which appears in the 450 μm and 850 μm-maps

by Reid & Wilson (2005, see Figure 7.3). This suggests that in NGC 7538, star formation was triggered by the compression of gas just at the interface layer of these expanding bubbles, sequentially initiating the formation of the observed chain of infrared sources.

Ojha et al. (2004) suggested that IRS6, the most luminous source in the NGC 7538 region, might be the main exciting source responsible for the optical H II region. Inspecting the IRAC color composites, this scenario is supported by the morphology of the bright, curved structure west of IRS6. In the IRAC 8 μm band (red in Figure 7.5), this structure appears particularly prominent. As it is known that emission in this IRAC band is often associated with PAHs, this suggests that this region is illuminated by strong UV radiation from IRS6. Other features, such as the conical structure around 2MASS 23135808+6130484 and the structure northeast of IRS7, also show a symmetry towards IRS6.

7.7 Summary and Conclusions

Bispectrum speckle interferometry and archival *Spitzer*/IRAC imaging of the massive protostars NGC 7538 IRS1/2 and their vicinity are presented. We summarize our results as follows:

1. The clumpy, fan-shaped structure seen in our speckle images most likely traces recent outflow activity from IRS1, consistent with the direction of the blue-shifted lobe of the known CO outflow. A bowshock structure noticeable in the IRAC images $\sim 40''$ southeast of IRS1 suggests that the total extent of the outflow might be several parsecs. The outflow might have also contributed to shaping and exciting the bubble-like structure, which is prominent in all four IRAC bands (although contributions from several other sources, especially IRS6, are also evident).

2. A companion around the high-mass star NGC 7538 IRS2 was discovered. Furthermore, we see indications for interactions between the IRS1 flow and outflows or stellar winds from IRS2 (nebulosity surrounding IRS2).

3. A jet precession model seems suitable to describe the features observed within our NIR images, simultaneously explaining the misalignment between the putative methanol maser disk, the UCH II region, and the outflow tracers detected at larger scales (CO). A simple analytic precession model was used to extract order-of-magnitude estimates for the precession parameters. Using these we estimate tidal interaction of a close binary system with a circumbinary disk as the most plausible gyroscopic mechanism, which is triggering the precession.

4. The presented molecular hydrodynamic simulations can reproduce some of the fine-structure observed in our NIR images and indicate that the arrangement of the detected fainter stars might be explained as a column-density effect, caused by the proposed precessing jet.

5. The prominent sites of ongoing high-mass star formation in NGC 7538 seem to be located just at the interface between two bubble-like structures — one is visible in the presented IRAC images, the other traced by submillimeter observations. The gas compression caused by the expansion of these bubbles might have triggered star formation in this region.

While it is well established that the outflows of HMPOs generally appear less collimated than those of their low-mass counterparts, the recent discovery of evidence for outflow precession for an increasing number of massive YSOs might indicate a common launching mechanism for all outflow driving sources of all stellar masses. The observed widening in HMPO outflows might be due to selection effects (Shepherd 2005) and/or precession of a collimated jet. The large precession angles reported for IRAS 20126+4104 (Shepherd et al. 2000), S140 IRS1 (Weigelt et al. 2002), IRAS 23151+5912 (Weigelt et al. 2006), and now NGC 7538 IRS1 (this study) might point towards a rather dramatic precession mechanism, maybe the presence of very close, high-mass companions on non-coplanar orbits.

We strongly encourage further observations of IRS1, especially to detect potential companions either by NIR long-baseline interferometry or radial velocity measurements.

8 Visual/Infrared Interferometry of the Orion Trapezium stars θ^1Ori C and D

Based on an article which appeared in A&A:
Kraus, S., Balega, Y. Y., Berger, J.-P., et al., A&A, 466, 649-659 (2007)

8.1 Overview and Context

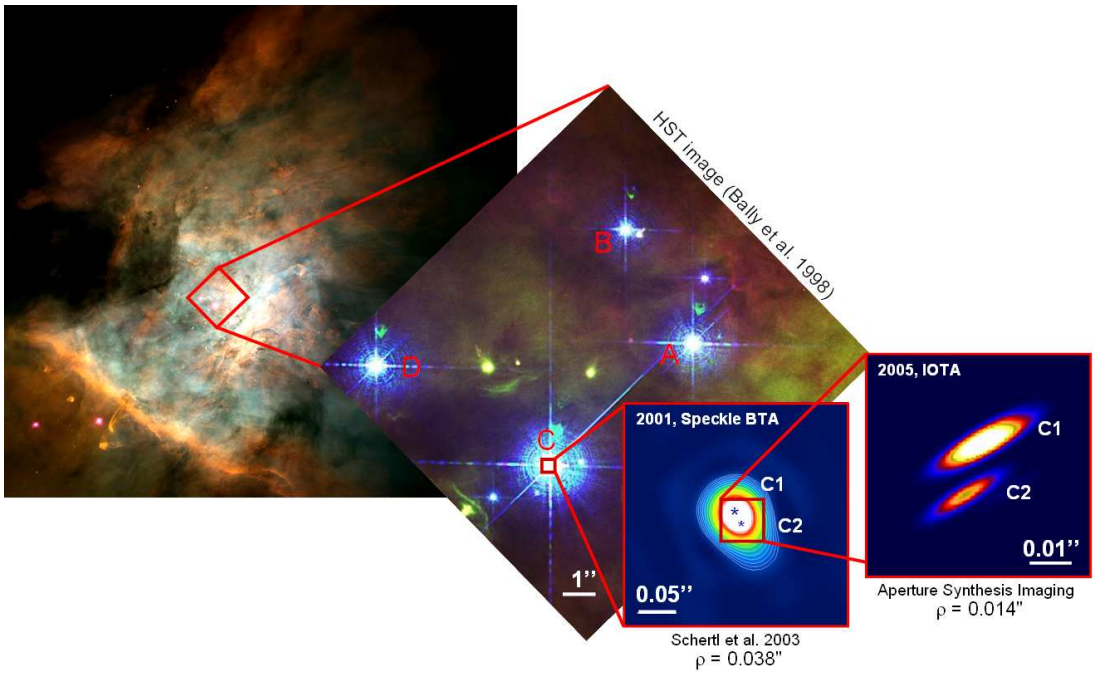

Figure 8.1: Mosaic zooming in from an HST image of the M42 H II region into the Trapezium cluster and the θ^1Ori C system, as seen with our speckle and IOTA imaging.

The Orion Nebula Cluster, at a distance of just 450 pc from earth, is the nearest high-mass star-forming region and a perfect laboratory for studying the birth of massive stars. In particular the brightest and most massive ($44 \pm 5 M_{\odot}$, Donati et al. 2002) of the Trapezium stars, Θ^1Ori C (see Figure 8.1), has been the target of numerous studies. With an age of just 200 000 yrs (Howarth & Prinja 1989), this O7V-type star is also one of the youngest O-type stars known in the sky, and its strong Lyman radiation dominates the whole Orion Nebula. Θ^1Ori C also illuminates the proplyds and shapes its environment with strong stellar winds ($\dot{M} \approx 4 \times 10^{-7}\ M_{\odot}\ \mathrm{yr}^{-1}$, Howarth & Prinja 1989).

One very unique aspect of this star was revealed by a long series of spectroscopic observations, showing strictly periodic ($P = 15.422 \pm 0.002$ d) variations both in the intensity and profile of various emission and absorption lines detected towards θ^1Ori C (Stahl et al. 1993, 1996). To explain this periodicity, in 1997 Babel & Montmerle applied the *magnetically confined wind shock* (MCWS) model to θ^1Ori C. This model, originally developed for magnetic Ap-Bp stars, describes how radiation-driven winds from both hemispheres are channeled along the magnetic field lines and collide at high velocities, forming a thin, nearly stationary shock region in the equatorial plane (Babel & Montmerle 1997; Donati et al. 2002; Gagné et al. 2005; Simón-Díaz et al. 2006). Within this disk-like structure, the plasma corotates with the field lines, cools, and is then either transferred back onto the star or expelled as asymmetric wind (Donati et al. 2002). Recently, the same period was detected in spectropolarimetric observations, tracing the strength of the magnetic field, which further confirms this interpretation (Wade et al. 2006).

Besides its amazing properties as a magnetic rotator, θ^1Ori C was found to be a particularly interesting close binary system. Since the discovery of the companion by our group in 1997 (Weigelt et al. 1999), we have detected significant orbital motion using bispectrum speckle interferometry. Tracing the orbital motion opens the prospect of determining dynamical masses of the system, yielding a characterization of the individual components and, ultimatively, also new constraints for stellar evolution models in the high-mass regime. In 1999, the largest binary separation was found to be 43 mas (Schertl et al. 2003). Since then, the separation has constantly decreased. In 2005 we found that the system was unresolved on the Russian 6 m BTA telescope with near-infrared (NIR) speckle interferometry. Thus, we performed first NIR long-baseline interferometric observations on θ^1Ori C in December 2005 using the IOTA. With baseline lengths of up to 38 m, we obtained the most precise position measurement of the binary so far.

The combined Speckle and IOTA position measurements cover the interval 1997.8 to 2005.9, from which we determined a preliminary orbital solution, which suggests a highly eccentric ($e \approx 0.91$) and short-period ($P \approx 10.9$ yrs) orbit. As the current astrometric data only allows rather weak constraints on the total dynamical mass, we present the two best-fit orbits. Of these two, the one implying a system mass of 48 $M_{\odot}$ and a distance of 434 pc to the Trapezium cluster can be favored. When also taking the measured flux ratio and the derived location in the HR-diagram into account, we find good agreement for all observables, assuming a spectral type of O5.5 for θ^1Ori C1 ($M = 34.0\ M_{\odot}$, $T_{\mathrm{eff}} = 39\,900$ K) and O9.5 for C2 ($M = 15.5\ M_{\odot}$, $T_{\mathrm{eff}} = 31\,900$ K).

We find indications that the companion C2 is massive itself, which makes it likely that its contribution to the intense UV radiation field of the Trapezium cluster is non-negligible. Furthermore, the high eccentricity of the preliminary orbit solution predicts a very small physical separation during periastron passage ($\sim$ 1.5 AU, next passage around 2007.5), suggesting strong wind-wind interaction between the two O stars.

The IOTA data on θ^1Ori C was also used to reconstruct the first NIR long-baseline aperture synthesis image of a young star. With IOTA, we also obtained first interferometric observations on θ^1Ori D, finding some evidence for a resolved structure, maybe by a faint, close companion.

All speckle observations for this project were acquired with the BTA 6.0 m telescope and recorded in the context of observing programmes by our Russian colleague Yuri Balega (measurements at visual wavelengths) or by members of the MPIfR group (measurements at NIR wavelengths). The fits to the power spectra of these observations were performed by members of the Balega group and by Dieter Schertl. The IOTA observations were performed by Keiichi Ohnaka and myself within an observing run covering 10 nights in November and December 2005. As the observed sources were significantly fainter than the sources to which the IDRS data reduction software was applied earlier, this software had to be refined and new algorithms had to be implemented both for visibility and closure phase estimation (see Sect. 3). For the IOTA data, I performed the model fits and the aperture synthesis image reconstruction using the BBM image reconstruction algorithm (Chapter 8.4). As the measurement of the dynamical masses is a major scientific objective, it is also necessary to compute orbital elements from the obtained relative position measurements, yielding the total system mass and the orbital parallax. The algorithm by Docobo (1985) is an orbit calculation method, which, for the last two decades, has also provided robust results for orbits where the observational data covers only a small fraction of the complete orbit. I implemented this and another algorithm (which scans the seven-dimensional parameter space on a grid) in order to find first preliminary orbital solutions for the θ^1Ori C orbit.

8.2 Introduction

The stellar mass is the most fundamental parameter, determining, together with the chemical composition and the angular momentum, the entire evolution of a given star. Stellar evolutionary models connect these fundamental parameters with more easily accessible, but also highly uncertain observables such as the luminosity and the stellar temperature. Particularly towards the pre-main-sequence (PMS) phase and towards the extreme stellar masses (i.e. the low- and high-mass domain), the existing stellar evolutionary models are still highly uncertain and require further empirical verification through direct and unbiased mass estimates, such as those provided by the dynamical masses accessible in binary systems. Recently, several studies were able to provide dynamical masses for low-mass PMS stars (e.g. Tamazian et al. 2002; Schaefer et al. 2003; Boden et al. 2005), while direct mass measurements for young O-type stars are still lacking.

Furthermore, in contrast to the birth of low-mass stars, the formation mechanism of high-mass stars is still poorly understood. In particular, the remarkably high binary frequency measured for young high-mass stars might indicate that the way high-mass stars are born differs significantly from the mass accretion scenario via circumstellar disks, which is well-established for low- and intermediate-mass stars. For instance, studies conducted at the nearest high-mass star-forming region, the Orion Nebular Cluster (ONC, at a distance of 450 ± 50 pc, Genzel & Stutzki 1989), revealed $\gtrsim 1.5$ companions per primary (for high-mass stars $M > 10 M_{\odot}$, Preibisch et al. 1999), which is significantly higher than the binary frequency for intermediate and low-mass stars.

In the very center of the ONC, four OB stars form the Orion Trapezium; three of which (θ^1Ori A, B, C) are known to be multiple (Weigelt et al. 1999; Schertl et al. 2003). θ^1Ori D (alias HD 37023, HR 1896, Parenago 1889) has no confirmed companion, although a preliminary analysis of the radial velocity by Vitrichenko (2002a) suggests that it might be a spectroscopic binary with a period of ~ 20 or 40 days.

A particularly intruiging young (< 1 Myr, Hillenbrand 1997) high-mass star in the Trapezium cluster is θ^1Ori C (alias 41 Ori C, HD 37022, HR 1895, Parenago 1891). θ^1Ori C is the brightest source within the ONC and also the main source of the UV radiation ionizing the proplyds and the M42 H II region. A close (33 mas) companion with a near-infrared flux ratio of ~ 0.3 between the primary (θ^1Ori C1) and the secondary (θ^1Ori C2) was discovered in 1997 using bispectrum speckle interferometry (Weigelt et al. 1999). Donati et al. (2002) estimated the mass of θ^1Ori C to be $44 \pm 5 M_{\odot}$, making it the most massive star in the cluster. The same authors give an effective temperature of $45\,000 \pm 1\,000$ K and a stellar radius of $8.2 \pm 1.1\ R_{\odot}$. Long series of optical and UV spectroscopic observations revealed that the intensity and also some line profiles vary in a strictly periodic way. With 15.422 ± 0.002 days, the shortest period was reported by Stahl et al. (1993). Several authors interpret this periodicity, which in the meantime was also detected in X-ray (Gagne et al. 1997), within an oblique magnetic rotator model, identifying 15.422 d with the rotation period of the star. Stahl et al. (1996) detected a steady increase in

radial velocity, confirmed by Donati et al. in 2002, which suggests a spectroscopic binary with an orbital period of at least 8 years. Vitrichenko (2002b) searched for long-term periodicity in the radial velocity and reported two additional periods of 66 days and 120 years, which he interpreted as the presence of, in total, three components in the system.

Given the unknown orbit of the speckle companion, it still has to be determined which one of these periods corresponds to the orbital motion of C2. Since the discovery of C2 in 1997, three measurements performed with bispectrum speckle interferometry showed that the companion indeed undertakes orbital motion (Schertl et al. 2003), reaching the largest separation of the two components in autumn 1999 with 43 ± 2 mas. In order to follow the orbital motion, we monitored the system using infrared and visual bispectrum speckle interferometry and in 2005, for the first time, also using infrared long-baseline interferometry.

An interesting aspect of the dynamical history of the ONC was presented by Tan (2004). He proposed that the Becklin-Neugebauer (BN) object, which is located 45″ to the northwest of the Trapezium stars, might be a runaway B star, ejected from the θ^1Ori C multiple system approximately 4 000 yrs ago. This scenario is based on proper motion measurements which show that BN and θ^1Ori C recoil roughly in opposite directions, and by the detection of X-ray emission potentially tracing a wind bow shock[1]. Three-body interaction is a crucial part of this interpretation, and C2 is currently the only candidate which could have been involved. Therefore, a high-precision orbit measurement of C2 might offer the unique possibility to recover the dynamical details of this recent stellar ejection. However, another study (Rodríguez et al. 2005) also aimed to identify the multiple system from which BN was ejected, and identified Source I as the likely progenitor system. Later, Gómez et al. (2005) added further evidence to this interpretation by identifying Source *n* as a potential third member of the decayed system.

8.3 Observations and Data Reduction

8.3.1 Bispectrum speckle interferometry

Speckle interferometric methods are powerful techniques for overcoming the atmospheric perturbations and for reaching the diffraction-limited resolution of ground-based telescopes, both at near-infrared and visual wavelengths. Since the discovery of θ^1Ori C2 in 1997, we have monitored the system with the *Big Telescope Alt-azimuthal* (BTA) 6.0 m telescope of the Special Astrophysical Observatory located on Mt. Pastukhov in Russia. For the speckle observations at visual wavelengths, a 1280×1024 pixel CCD with a multialkali S25 intensifier photocathode was used. The near-infrared speckle observations were carried out using one 512×512 pixel quadrant of the Rockwell HAWAII array in our speckle camera,

[1] However, the more recent detection of X-ray variability in intensity and spectrum makes it unlikely that this X-ray emission really originates in a wind bow shock, as pointed out by Grosso et al. (2005).

Table 8.1: IOTA Calibrator Stars Information

Star	V	H	Spectral Type	Adopted UD diameter [mas]
HD 14129	5.5	3.3	G8.5III	1.01 ± 0.01^a
HD 20791	5.7	3.5	G8.5III	0.89 ± 0.01^a
HD 28322	6.2	3.9	G9III	0.82 ± 0.01^a
HD 34137	7.2	4.4	K2III	0.80 ± 0.01^a
HD 36134	5.8	3.2	K1III	1.16 ± 0.02^a
HD 50281	6.6	4.3	K3V	0.77 ± 0.10^b
HD 63838	6.4	3.6	K2III	0.95 ± 0.01^a
HD 74794	5.7	3.5	K0III	1.07 ± 0.01^a

Notes – ^{a} UD diameter taken from the CHARM2 catalog (Richichi et al. 2005).
^{b} UD diameter taken from getCal tool
(http://mscweb.ipac.caltech.edu/gcWeb/gcWeb.jsp).

with pixel sizes of 13.4 mas (J-band), 20.2 mas (H-band), and 27 mas (K-band) on the sky.

For the speckle observations at infrared wavelengths, we recorded interferograms of θ^1Ori C and of the nearby unresolved star θ^1Ori D in order to compensate for the atmospheric speckle transfer function. The number of interferograms and the detector integratione times (DITs) are listed in Table 9.1.

The modulus of the Fourier transform of the object (visibility) was obtained with the speckle interferometry method (Labeyrie 1970). For image reconstruction we used the bispectrum speckle interferometry method (Weigelt 1977, Weigelt & Wirnitzer 1983, Lohmann et al. 1983, Hofmann & Weigelt 1986).

Table 8.2: Observation Log.

Target	Instrument and Configuration	Date [UT]	Filter[a]	Detector[b] and Mode[c]	No. Interferograms Target/Calibrator	Calibrators[d]
θ^1Ori C	BTA 6m/Speckle	1997.784	H	P/DIT=150 ms	519/641	θ^1Ori D
θ^1Ori C	BTA 6m/Speckle	1998.838	K'	H/DIT=120 ms	438/265	θ^1Ori D
θ^1Ori C	BTA 6m/Speckle	1999.737	J	H/DIT=100 ms	516/244	θ^1Ori D
θ^1Ori C	BTA 6m/Speckle	1999.8189	G'	S/DIT=5 ms	500/–	–
θ^1Ori C	BTA 6m/Speckle	2000.8734	V'	S/DIT=5 ms	1 000/–	–
θ^1Ori C	BTA 6m/Speckle	2001.184	J	H/DIT=80 ms	684/1 523	θ^1Ori D
θ^1Ori C	BTA 6m/Speckle	2003.8	J	H/DIT=160 ms	312/424	θ^1Ori D
θ^1Ori C	BTA 6m/Speckle	2003.9254	V'	S/DIT=2.5 ms	1 500/–	–
θ^1Ori C	BTA 6m/Speckle	2003.928	V'	S/DIT=2.5 ms	2 000/–	–
θ^1Ori C	BTA 6m/Speckle	2004.8216	V'	S/DIT=5 ms	2 000/–	–
θ^1Ori C	BTA 6m/Speckle	2006.8	V', R'	–	–	–
θ^1Ori C	IOTA A35-B15-C0	2005 Dec 04	H	1L7R, 2L7R	11 400/8 050	HD 14129, HD 36134, HD 34137, HD 50281, HD 63838
θ^1Ori C	IOTA A35-B15-C10	2005 Dec 02	H	2L7R, 4L7R	4 400/4 950	HD 34137, HD 50281, HD 63838
θ^1Ori C	IOTA A35-B15-C10	2005 Dec 03	H	2L7R	4 600/2 450	HD 28322
θ^1Ori C	IOTA A35-B15-C15	2005 Dec 01	H	2L7R, 4L7R	7 250/5 000	HD 20791, HD 34137, HD 36134
θ^1Ori C	IOTA A25-B15-C0	2005 Dec 06	H	2L7R, 4L7R	5 250/4 875	HD 28322, HD 34137, HD 36134, HD 74794
θ^1Ori D	IOTA A35-B15-C0	2005 Dec 04	H	2L7R	800/2 800	HD 14129, HD 36134, HD 34137, HD 50281, HD 63838
θ^1Ori D	IOTA A25-B15-C0	2005 Dec 06	H	2L7R, 4L7R	1 800/4 875	HD 28322, HD 34137, HD 36134, HD 74794

Notes – [a] Filter central wavelength and bandwidth, in nm ($\lambda_c/\Delta\lambda$) – V': 545/30; G': 610/20; R': 800/60; J: 1 239/138; H: 1 613/304; K': 2 115/214.

[b] P: PICNIC detector, H: HAWAII array, S: Multialkali S25 intensifier photocathode

[c] For the IOTA measurements, we used different detector read modes to adapt to the changing atmospheric conditions. The two numbers in the given 4-digit code denote the value of the *loop* and *read* parameter (Pedretti et al. 2004) of the PICNIC camera. Since data taken in different readout modes is calibrated independently, the scattering between the data sets also resembles the typical calibration errors (see Figure 8.5).

[d] The dash symbol in the calibrator column indicates speckle measurements for which no calibrator was observed.

8.3.2 IOTA long-baseline interferometry

The *Infrared Optical Telescope Array* (IOTA) is a three-telescope long-baseline interferometer located at the Fred Lawrence Whipple Observatory on Mount Hopkins, Arizona, operating at visual and near-infrared wavelengths (Traub et al. 2003). Its three 45 cm primary Cassegrain telescopes can be mounted on stations along an L-shaped track, reaching 15 m towards a southeastern and 35 m towards a northeastern direction. After passing a tip-tilt system (Schuller et al. 2004), which compensates the atmospherically induced motion of the image, and path-compensating delay lines, the three beams are fed into fibers and coupled pairwise onto the IONIC3 integrated optics beam combiner (Berger et al. 2003). The interferograms are recorded by temporal modulation around zero optical path delay (OPD). During data acquisition, a fringe tracker software (Pedretti et al. 2005) continuously compensates potential OPD drifts. This allows us to measure the three interferograms nearly simultaneously within the atmospheric coherence time, preserving the valuable closure phase (CP) information.

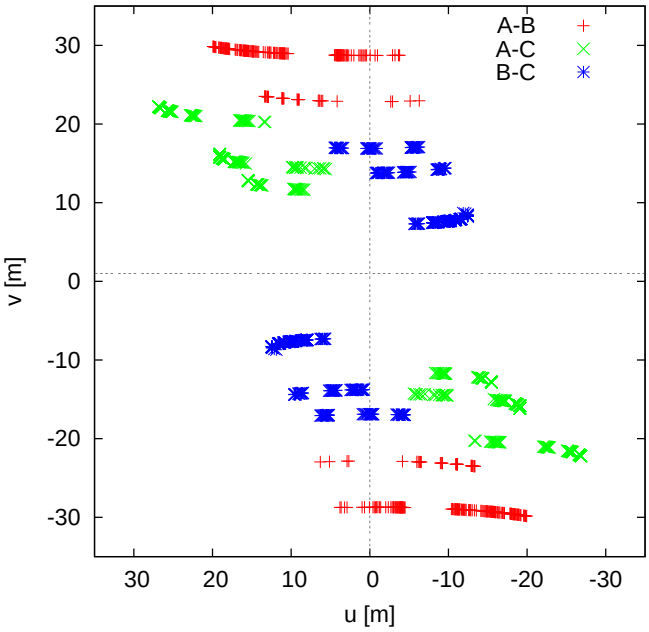

Figure 8.2: *uv*-plane coverage obtained on θ^1Ori C with the four IOTA array configurations used. The relatively strong asymmetry in the *uv*-plane coverage mainly results from the position of θ^1Ori C relatively close to the celestrial equator.

For our IOTA observations, we used four different array configurations (see Table 9.1), obtaining the *uv*-coverage shown in Figure 8.2. θ^1Ori D was observed on two different array configurations, as shown in Figure 8.3. During each night, we systematically alternated between the target star and calibrators in order to determine the transfer function of the instrument. For more details about the calibrator stars and the number of recorded Michelson interferograms, refer to Table 8.1.

In order to extract visibilities and CPs from the recorded IOTA interferograms, we used the IDRS data reduction software. Basic principles of the algorithms implemented in this software package were already presented in Kraus et al. (2005b), although several details have been refined to obtain optimal results for fainter sources as well, such as those observed in this study (see Section 3).

8.4 Aperture Synthesis Imaging

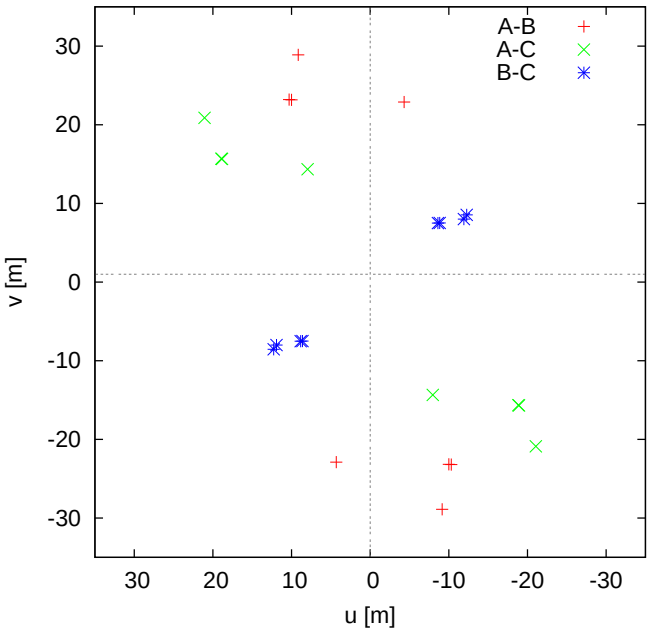

Figure 8.3: *uv*-plane coverage obtained on θ^1 Ori D with two IOTA array configurations. The meaning of the colors and symbols is the same as in Figure 8.2.

Interpreting optical long-baseline interferometric data often requires a priori knowledge about the expected source brightness distribution. This knowledge is used to choose an astrophysically motivated model whose parameters are fitted to the measured interferometric observables (as applied in Sect. 8.5).

However, the measurement of CPs allows a much more intuitive approach; namely, the direct reconstruction of an aperture synthesis image. Due to the rather small number of telescopes combined in the current generation of optical interferometric arrays, direct image reconstruction is limited to objects with a rather simple source geometry, in particular multiple systems (for images reconstructed from IOTA data, see Monnier et al. 2004; Kraus et al. 2005b).

Using our software based on the *Building Block Mapping* algorithm (Hofmann & Weigelt 1993), we reconstructed an aperture synthesis image of the θ^1 Ori C system from the data collected during our IOTA run. Starting from an initial single delta-function, this algorithm builds up the image iteratively by adding components in order to minimize the least-square distance between the measured bispectrum and the bispectrum of the reconstructed image.

The resulting image is shown in Figure 8.4 and provides a model-independent representation of our data. By combining the data collected during six nights, we make the reasonable assumption that the orbital motion over this interval is negligible.

The clean beam, which we used for convolution to obtain the final image, is rather elliptical (see inset in Figure 8.4), representing the asymmetries in the *uv*-coverage.

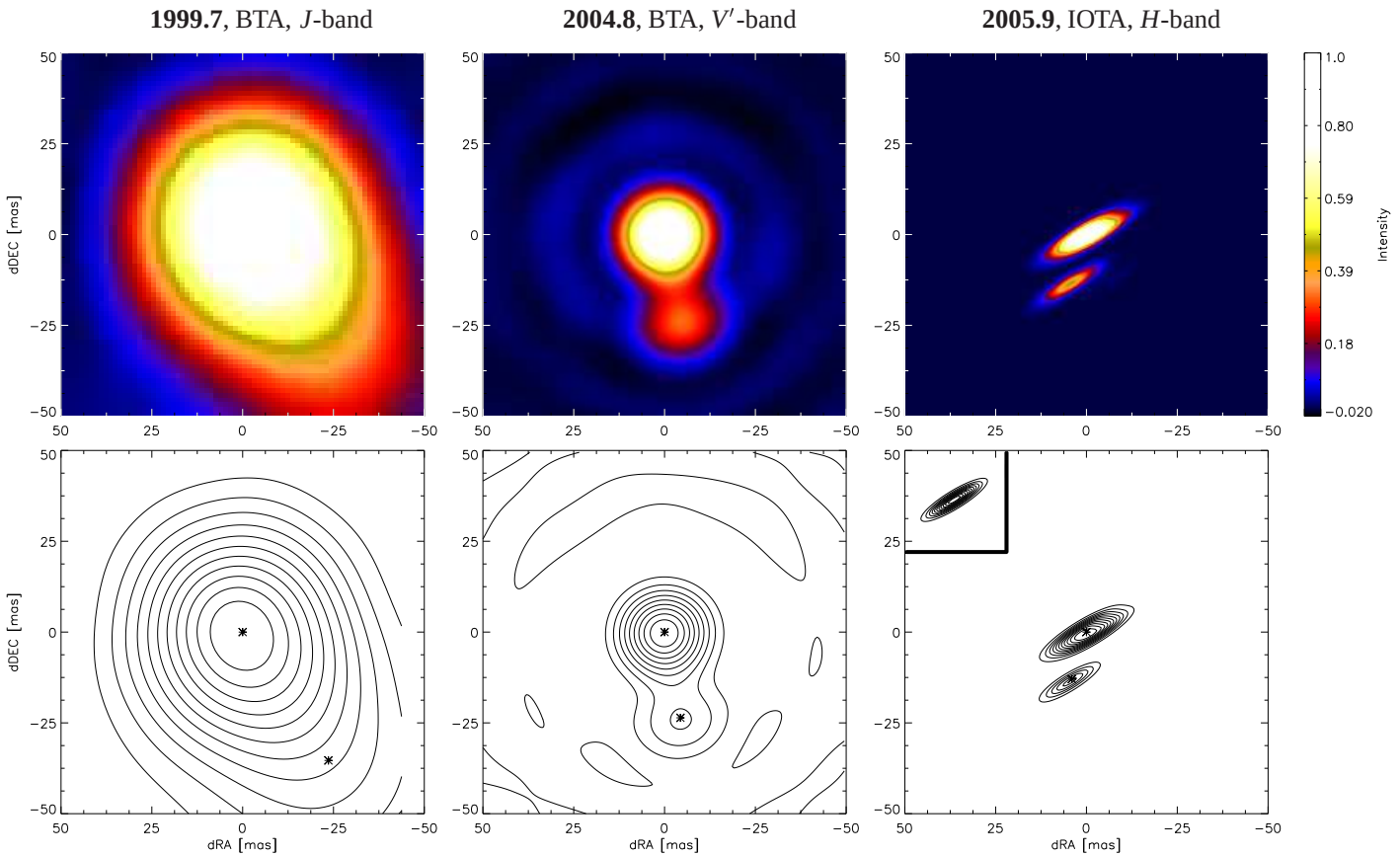

Figure 8.4: *Left, Middle:* Bispectrum speckle *J* and *V*′-band images reconstructed from BTA-data. *Right:* Aperture synthesis image of θ^1Ori C reconstructed from our IOTA *H*-band data. Besides the false-color representation in the upper row, we show the images below as contours with the best-fitted positions marked with star symbols (see Table 8.3). In the image in the lower right corner, the restoring beam for the IOTA aperture synthesis image is shown as an inset. Over the six year interval covered by the images, orbital motion is clearly conceivable (1999/2004/2005: ρ=43/24/14 mas; Θ=214°/191°/163°).

8.5 Model Fitting

8.5.1 Binary model fitting for θ^1Ori C

Although the aperture synthesis image presented in the last section might also be used to extract parameters like binary separation, orientation, and intensity ratio of the components ($I_{C2}/I_{C1} = 0.26$, $\rho = 14.1$ mas, $\Theta = 162°$), more precise values, including error estimates, can be obtained by fitting the measured visibilities and CPs to an analytical binary model.

The applied model is based on equations 7–12 presented in Kraus et al. (2005b) and uses the least-square Levenberg-Marquardt method to determine the best-fit binary separation vector and intensity ratio. In order to avoid potential local minima, we vary the initial values for the least-square fit on a grid, searching for the global minimum.

As the apparent stellar diameter of θ^1Ori C is expected to be only ~ 0.2 mas at the distance of Orion, for our fits we assume that both stellar components appear practically unresolved to the IOTA baselines. Furthermore, we assume that the relative position of the components did not change significantly over the 6 nights of observation.

Figure 8.5 shows the measured IOTA visibilities and CPs and the observables corresponding to our best-fit binary model ($\chi^2_{V^2}/\mathrm{dof} = 1.35$, $\chi^2_{CP}/\mathrm{dof} = 1.48$). The separation ρ, PA Θ, and intensity ratio of this binary model are given in Table 8.3, together with the positions derived from the speckle observations. To illustrate more clearly that the measured IOTA visibilities resemble a binary signature, in Figure 8.6 we show a projection of the sampled two-dimensional Fourier plane along the binary vector, revealing the cosine modulation corresponding to the Fourier transform of a binary brightness distribution.

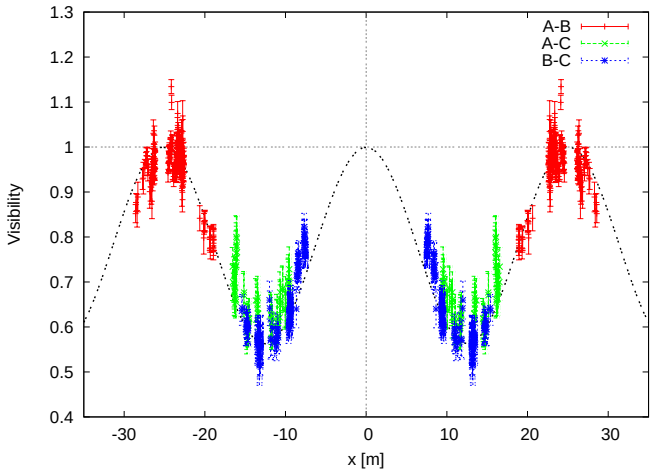

Figure 8.6: Projection of the sampled Fourier plane along the fitted binary PA of 162.74° ($x = u\cos\Theta - v\sin\Theta$), clearly revealing the binary signature. The dashed line shows the theoretical cosine visibility profile for a binary star with separation 13.55 mas and intensity ratio 0.28.

For the speckle data (providing a complete Fourier sampling up to the spatial frequency corresponding to the diameter of the telescope primary mirror), we determine the binary parameters by fitting a two-dimensional cosine function directly to the 2-D speckle interferogram power spectrum.

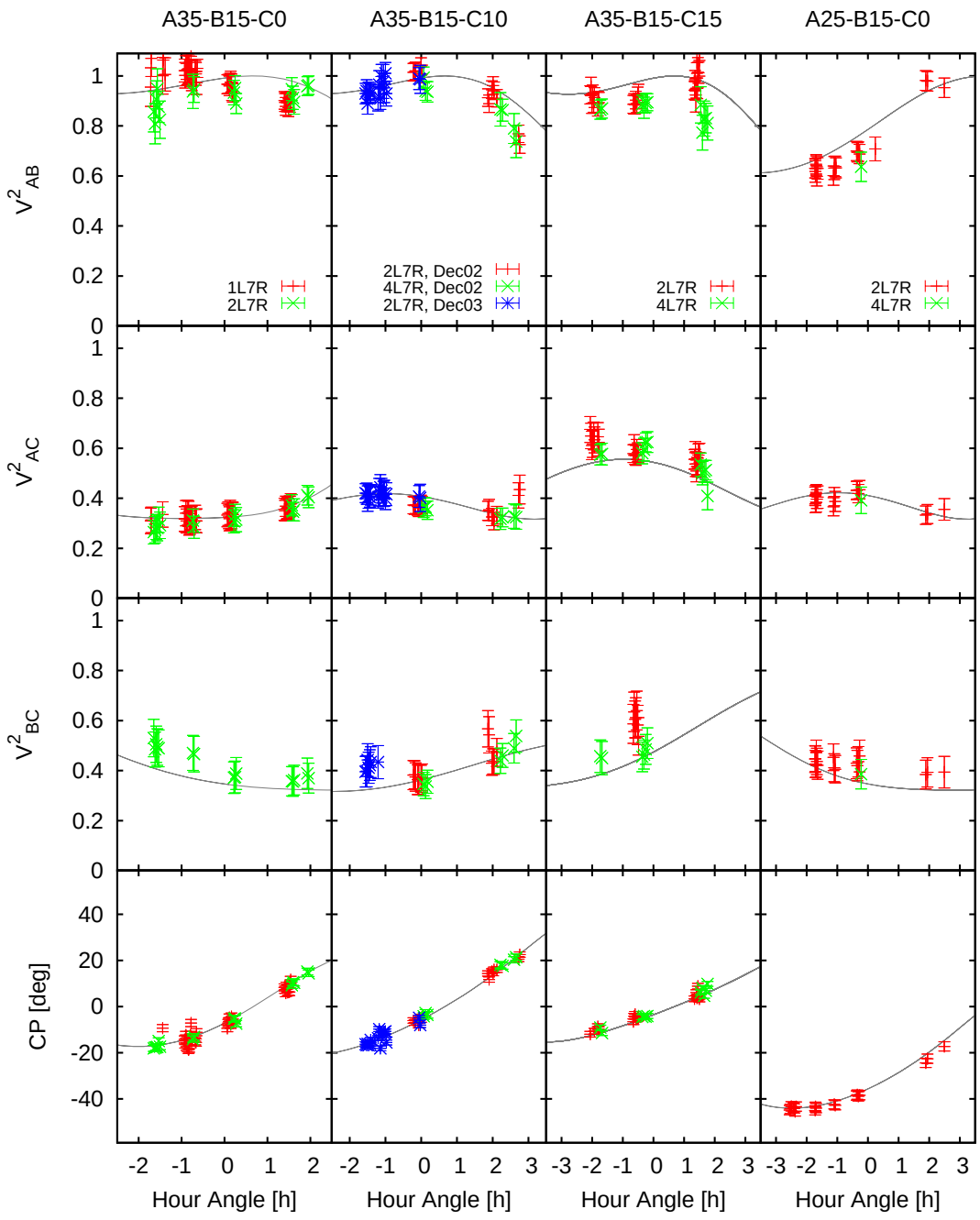

Figure 8.5: Visibilities and Closure Phases derived from the recorded IOTA interferograms for θ^1Ori C as a function of hour angle (points with error bars). The solid line shows the binary model fit, described in more detail in Section 8.5. The different symbols represent the different detector modes used (see Table 9.1). The data for each detector mode was calibrated separately, so the scattering of the data groups represents the typical calibration errors.

Table 8.3: Relative astrometry and photometry for the θ^1Ori C binary system

Telescope	Date	Filter	Flux ratio F_{C2}/F_{C1}	Θ^a [°]	ρ [mas]	Ref.	(O–C) Orbit #1 Θ [°]	(O–C) Orbit #1 ρ [mas]	(O–C) Orbit #2 Θ [°]	(O–C) Orbit #2 ρ [mas]
BTA 6m/Speckle	1997.784	H	0.26 ± 0.02	226.0 ± 3	33 ± 2	b	+3.0	+0.5	+3.0	+0.0
BTA 6m/Speckle	1998.838	K'	0.32 ± 0.03	222.0 ± 5	37 ± 4	b	+3.8	-2.5	+3.8	-2.6
BTA 6m/Speckle	1999.737	J	0.31 ± 0.02	214.0 ± 2	43 ± 1	c	-0.9	+1.5	-0.9	+1.5
BTA 6m/Speckle	1999.8189	G'	0.39 ± 0.04	213.5 ± 2	42 ± 1	–	-1.1	+0.5	-1.1	+0.5
BTA 6m/Speckle	2000.8734	V'	0.39 ± 0.03	210.0 ± 2	40 ± 1	–	-0.9	-0.8	-0.8	-0.8
BTA 6m/Speckle	2001.184	J	0.29 ± 0.02	208.0 ± 2	38 ± 1	c	-1.7	-2.1	-1.6	-2.1
BTA 6m/Speckle	2003.8	J	0.30 ± 0.02	199.3 ± 2	29 ± 2	–	+2.8	+0.5	+3.9	+0.5
BTA 6m/Speckle	2003.9254	V'	–	199.0 ± 2	29 ± 2	–	+3.4	+1.3	+3.6	+1.3
BTA 6m/Speckle	2003.928	V'	–	199.1 ± 2	29 ± 2	–	+3.6	+1.3	+3.8	+1.3
BTA 6m/Speckle	2004.8216	V'	0.38 ± 0.04	190.5 ± 4	24 ± 4	–	+4.0	+2.4	+4.2	+2.4
IOTA	2005.92055	H	0.28 ± 0.03	162.74 ± 2	13.55 ± 0.5	–	-1.0	+0.0	-0.5	+0.0
BTA 6m/Speckle	2006.8	V', R	–	–	< 15	–	–	–	–	–

Notes – a) Following the convention, we measure the position angle (PA) from north to east.
References – b) Weigelt et al. 1999, c) Schertl et al. 2003

8.5.2 Resolved structure around θ^1Ori D: Potential detection of a companion

Besides the main target of our observational programme, θ^1Ori C, during the two nights with the best seeing conditions, we also recorded four datasets on θ^1Ori D. Despite lower flux (θ^1Ori D: H=5.9, θ^1Ori C: H=4.6), the quality of the derived visibilities and CPs seems reliable, although slightly larger errors must be assumed. θ^1Ori D appears resolved in our measurements with a significant non-zero CPs signal ($\sim 10°$) on the A35-B15-C0 baseline. This CP indicates deviations from point-symmetry, as expected for a binary star. We applied the binary model fit described in Sect. 8.5.1 and found as best-fit model ($\chi^2/\mathrm{dof} = 1.36$) a binary system with an intensity ratio of 0.14, $\rho = 18.4$ mas and $\Theta = 41°$ (Figure 8.7).

However, considering the *uv*-coverage of the existing dataset, this solution is likely not unique and it can not be ruled out that other geometries, such as for inclined circumstellar disk geometries with pronounced emission from the rim at the dust sublimation radius (see e.g. Monnier et al. 2006), might also produce the asymmetry required to fit the data.

8.6 Results

8.6.1 Preliminary physical orbit and dynamical masses of the θ^1Ori C binary system

Our multi-epoch position measurements of the θ^1Ori C system can be used to derive a preliminary dynamical orbit. To find orbital solutions, we used the method described by Docobo (1985). This method generates a class of Keplerian orbits passing through three base points. From this class of possible solutions, those orbits are selected which best agree with the measured positions, where we use the error bars of the individual measurements as weight. In order to avoid over-weighting the orbit points which were sampled with several measurements at similar epochs (two measurements in 1999.7-1999.8 and three measurements in 2003.8-2003.9), we treated each of these clusters as single measurements. The dynamical mass of the total system is computed using Kepler's third law $M_{C1} + M_{C2} = a^3/P^2$ (where a is given in AU, P in years and M in solar masses).

In Table 8.4 we give the orbital elements corresponding to the two best orbital solutions found. As the χ^2/dof values of the two presented orbits are practically identical, the existing data does not allow us to distinguish between these solutions. These orbits and the corresponding O–C vectors are shown in Figure 8.8 (see Table 8.3 for a list of the O–C values). As the ephemerids in Table 8.5 and also the position predictions (dots) in Figure 8.8 show, future high-accuracy long-baseline interferometric measurements are needed to discriminate between these orbital solutions.

Potentially, additional constraints on the θ^1Ori C binary orbit could be provided by radial velocity

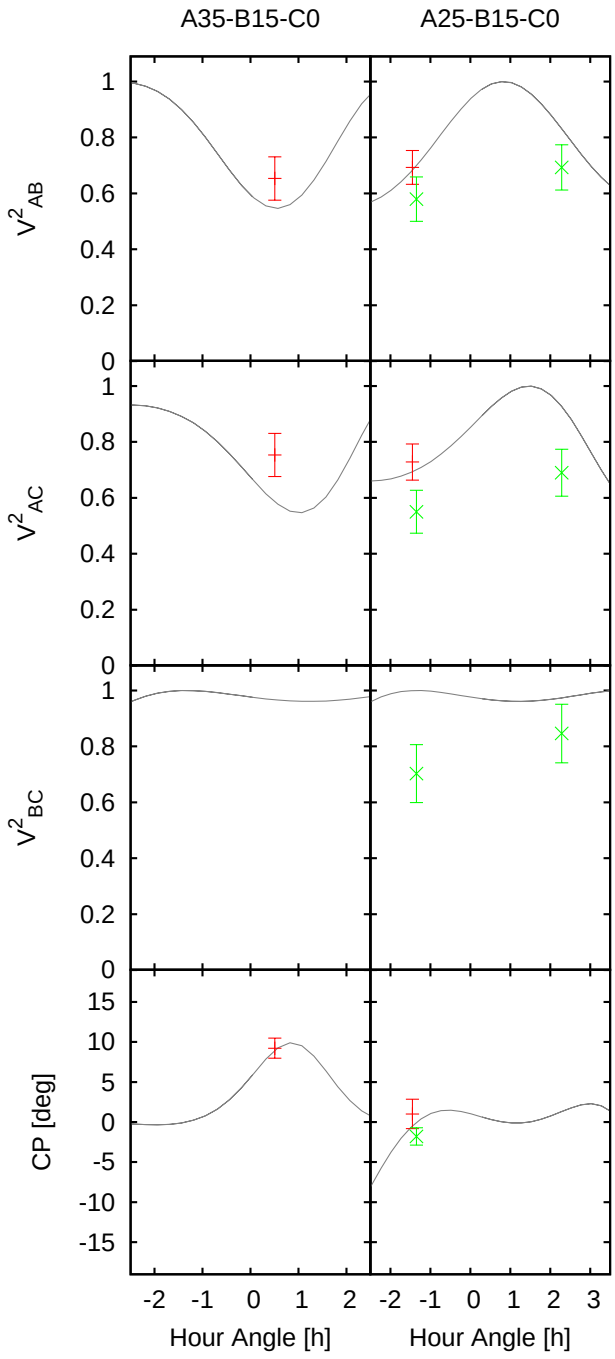

Figure 8.7: Visibilities and Closure Phases derived from the recorded IOTA interferograms for θ^1Ori D (points with error bars). The solid line shows the binary model fit, described in more detail in Section 8.5.2.

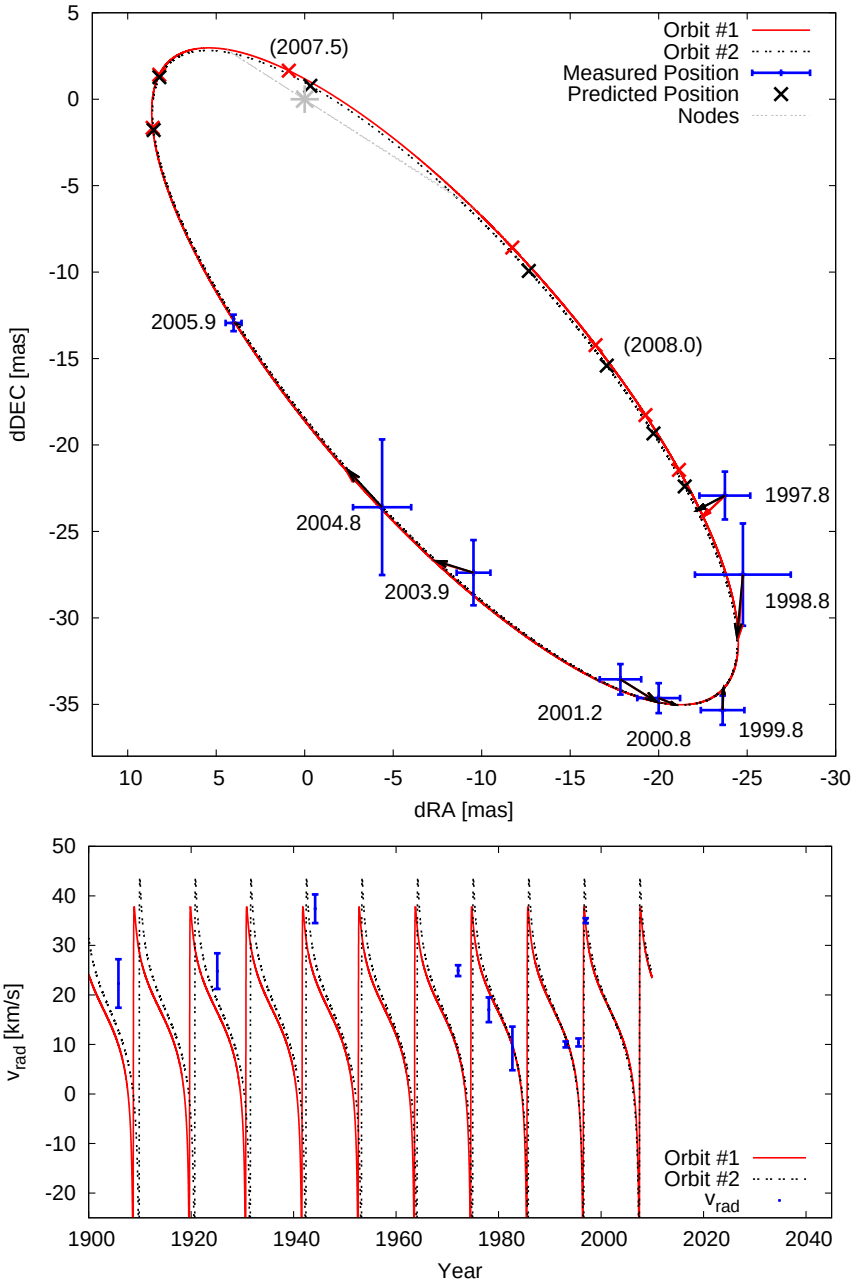

Figure 8.8: *Top:* Two best-fit apparent orbits of the θ^1Ori C binary system (solid and dashed line). Each position measurement (see Table 8.3) is connected to its predicted position with an *O–C* line. Besides our orbital solutions (see Table 8.4), the line of nodes, and the predicted positions for the interval 2007.0 to 2008.5 (step 0.25 yrs) are shown. North is up and east is to the left. *Bottom:* Radial velocity variations of both components computed for our orbital solutions using the method presented by Pourbaix (1998). For the mass ratio M_{C2}/M_{C1}, we assume 0.42, as obtained from our modeling of the flux ratio presented in Sect. 8.6.4. When computing the radial velocity curve, the (unknown) system velocity V_0 represents a free-parameter corresponding to a velocity offset, which we set to -5 km s^{-1} for this plot. The radial velocity measurements (points with errorbars) were taken from Vitrichenko (2002b).

Table 8.4: Preliminary orbital solutions for θ^1Ori C

		Orbit #1	Orbit #2
P	[yrs]	10.98	10.85
T		1996.52	1996.64
e		0.909	0.925
a	[mas]	41.3	45.0
i	[°]	105.2	103.7
Ω	[°]	56.5	56.9
ω	[°]	65.7	68.2
χ^2/dof		1.61	1.59
$\pi_{\rm dyn}{}^{a)}$	[mas]	2.304 ± 0.066	2.585 ± 0.074
$d_{\rm dyn}{}^{a)}$	[pc]	434 ± 12	387 ± 11
$(M_{\rm C1} + M_{\rm C2})^{a)}$	[$M_\odot$]	47.8 ± 4.2	44.8 ± 3.9

Notes – $^{a)}$ The errors on the dynamical parallaxes and corresponding distances were estimated by varying the measured binary flux ratio within the observational uncertainties, the assumed spectral types for the bolometric correction by one sub-class, the extinction by ± 0.2 magnitudes, and by using three different MLRs (by Baize & Romani 1946; Heintz 1978; Demircan & Kahraman 1991). However, the given errors do not reflect the uncertainties on the orbital elements a and P. Due to the presence of the multiple orbital solutions, it is currently not possible to quantify these errors reliably.

measurements, such as those published by Vitrichenko (2002b) and in the references therein. However, the complexity of the θ^1Ori C spectrum – including the line variability corresponding to the magnetically confined wind-shock region expected towards θ^1Ori C – makes both the measurement and also the interpretation of radial velocities for θ^1Ori C very challenging. Since it is unclear whether these velocities really correspond to the orbital motion of the binary system or perhaps to variations in the stellar wind from θ^1Ori C, we did not include these velocity measurements as a tough constraint in the final orbital fit, but show them in Figure 8.8 together with the radial velocities corresponding to our best-fit orbit solutions.

Both orbital solutions suggest that during periastron passage, the physical separation between the C1 and C2 decreases to $\sim$ 1.5 AU, corresponding to just $\sim$ 30 stellar radii. Besides the strong dynamical friction at work during such a close passage, strong wind-wind interaction can also be expected.

It is worth mentioning that besides the presented best-fit orbital solutions, a large number of solutions with longer orbital periods exist, which are also fairly consistent with the astrometric measurements. However, since these orbits have slightly higher χ^2/dof values than the solutions presented above and also correspond to physically unreasonable masses ($M_{C1} + M_{C2} \lesssim 20$ or $\gtrsim 140 M_\odot$), we rejected these formal solutions.

Table 8.5: Ephemerides for the θ^1Ori C orbital solutions presented in Table 8.4

Epoch	Orbit #1		Orbit #2	
	Θ [°]	ρ [mas]	Θ [°]	ρ [mas]
2007.0	100.9	8.7	101.8	8.7
2007.5	28.6	1.9	-22.4	0.8
2008.0	229.1	21.7	227.9	23.0
2008.5	224.6	30.1	223.8	31.0
2009.0	221.7	35.1	221.1	35.8
2010.0	217.5	40.2	217.0	40.5
2011.0	213.9	41.6	213.4	41.6
2012.0	210.3	40.5	209.8	40.2
2013.0	206.3	37.5	205.8	37.0
2014.0	201.4	33.0	200.8	32.3
2015.0	194.6	27.1	193.7	26.3
2016.0	183.4	20.1	181.7	19.2
2017.0	159.7	12.8	155.1	12.0

8.6.2 Dynamical masses and parallaxes

Kepler's third law relates the major axis a and the orbital period P with the product of the system mass and the cube of the parallax; i.e. $(M_{C1} + M_{C2}) \cdot \pi^3 = a^3/P^2$ (where a and π are given in mas, P in years, and M in solar masses).

In order to separate the system mass and the parallax in absence of spectroscopic orbital elements, the method by Baize & Romani (1946) can be applied. This method assumes that the component masses follow a mass-luminosity relation (MLR), which, together with a bolometric correction and extinction-corrected magnitudes, allows one to solve for the system mass $M_{C1} + M_{C2}$ and the dynamical parallax π_{dyn}. When using the MLR by Demircan & Kahraman (1991), the bolometric correction for O5.5 and O9.5 stars by Martins et al. (2005), and the extinction corrected magnitudes given in Table 8.6, we derive the dynamical masses and parallaxes given in Table 8.4. When comparing the distances corresponding to the dynamical parallaxes derived for Orbit #1 ($d_{dyn} = \pi_{dyn}^{-1} = 434$ pc) and Orbit #2 ($d_{dyn} = 387$ pc) with distance estimates from the literature (e.g. $d = 440 \pm 34$ pc from Jeffries 2007; see also references herein), orbit solution #1 appears much more likely. The dynamical system mass corresponding to Orbit #1 is 47.8 $M_\odot$, which must be scaled by a factor $(d/d_{dyn})^3$ when distances other than $d_{dyn} = 434$ pc are assumed.

8.6.3 The orbital parameters in the context of reported periodicities

Several studies have already reported the detection of periodicity in the amplitude, width, or velocity of spectral lines around θ^1Ori C. This makes it interesting to compare whether one of those periods can be attributed to the presence of companion C2:

$P \approx$ 15.422 $\pm$ 0.002 d: By far the best established periodicity towards θ^1Ori C was detected in hydrogen recombination lines and various photospheric and stellar-wind lines (Stahl et al. 1993, 1996; Walborn & Nichols 1994; Oudmaijer et al. 1997). Later, the same period was also found in the X-ray flux (Gagne et al. 1997) and even in modulations in the Stokes parameters (Wade et al. 2006). Although possible associations with a hypothetical low-mass stellar companion were initially discussed (Stahl et al. 1996), this period is, in the context of the magnetic rotator model, most often associated with the stellar rotation period. We can rule out that C2 is associated with this periodicity, as we do not see significant motion of C2 within the seven days covered by the IOTA measurements.

60 d $<$ P $<$ 2 yrs, $P \approx$ 120 yrs: Vitrichenko (2002b) fitted radial velocity variations assuming the presence of two companions and determined possible periods of $729.6/L$ days (with L an integer < 13) for the first, and $\sim$ 120 yrs for the second companion. As our orbital solutions do not match any of these periods, we consider an association of θ^1Ori C2 very unlikely.

$P \gtrsim$ 8 yrs: Stahl (1998) reported a steady increase in radial velocity. Donati et al. (2002) confirmed this trend and estimated that this increase might correspond to the orbital motion of a companion with a period between 8 yrs (for a highly eccentric orbit) and 16 yrs (for a circular orbit). With the found period of $\sim$ 11 yrs, it is indeed very tempting to associate θ^1Ori C2 with this potential spectroscopic companion. However, as noted in Sect. 8.6.1, the set of available spectroscopic radial velocity measurements seems rather inhomogeneous and fragmentary and might contain observational biases due to the superposed shorter-period spectroscopic line variations, as noted above.

8.6.4 Nature of the θ^1Ori C components

Most studies which can be found in literature attributed the whole stellar flux of θ^1Ori C to a single component and determined a wide range of spectral types including O5.5 (Gagné et al. 2005), O6 (Levato & Abt 1976; Simón-Díaz et al. 2006), O7 (van Altena et al. 1988), to O9 (Trumpler 1931). In order to resolve this uncertainty, it might be of importance to take the presence of θ^1Ori C2 into account. Besides the constraints on the dynamical masses derived in Section 8.6.1, additional information about the spectral types of θ^1Ori C1 and C2 can be derived from the flux ratio of the components in the recorded bands.

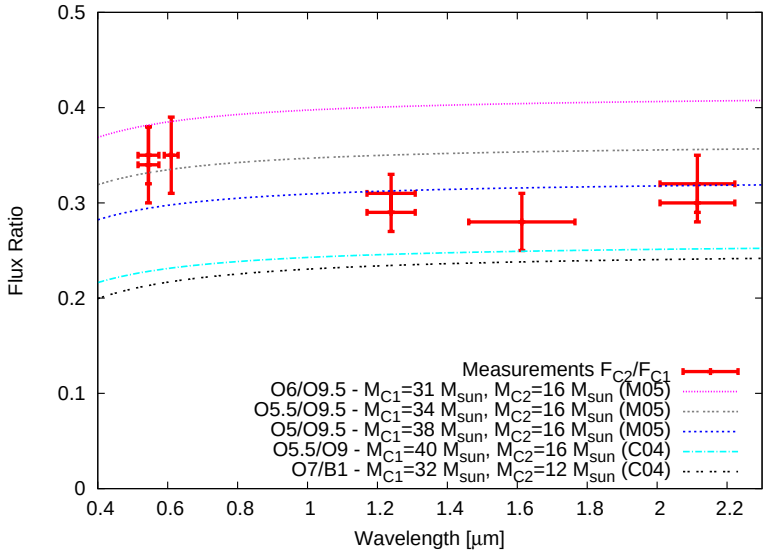

Figure 8.9: Measured intensity ratio of the θ^1Ori C components as a function of wavelength (points with errorbars). For various spectral type combinations, the curves show the expected intensity ratio, assuming the stars contribute purely photospheric emission (black-body emission with luminosities and effective temperatures as given in the stellar evolution models from Martins et al. (2005, M05) and Claret (2004, C04)).

Table 8.6: Derived dereddened magnitudes and colors for the θ^1Ori C components. For the photometry of the total system, we used data from Hillenbrand et al. (1998, J=4.63, H=4.48, K=4.41) and Hillenbrand (1997, V=5.12). An extinction of $A_V = 1.74$ (Hillenbrand 1997) was assumed (using the reddening law by Mathis 1990 and, similar to Mathis & Wallenhorst 1981, a high $R_V = 5.0$).

	V	J	H	K	V–J	V–H	V–K	J–H	J–K	H–K
θ^1Ori C1	3.70	4.35	4.38	4.49	-0.65	-0.69	-0.80	-0.04	-0.15	-0.11
θ^1Ori C2	4.87	5.65	5.81	5.73	-0.78	-0.94	-0.86	-0.15	-0.08	0.07

In contrast to our earlier studies (Weigelt et al. 1999; Schertl et al. 2003), we can now also include the V-band flux ratio measurement to constrain the spectral types of the individual components. The V-band is of particular interest, as a relative increase of the flux ratio $F_{\rm C2}/F_{\rm C1}$ from the visual to the near-infrared would indicate the presence of circumstellar material, either as near-infrared excess emission or intrinsic extinction towards C2 (assuming similar effective temperatures for both components). Our speckle measurements indicate that $F_{\rm C2}/F_{\rm C1}$ stays rather constant from the visual to the near-infrared. Therefore, in the following we assume that the major contribution of θ^1Ori C2 to the measured flux is photospheric.

In Figure 8.9 we show the measured $F_{\rm C2}/F_{\rm C1}$ as a function of wavelength and compare it to model curves corresponding to various spectral-type combinations for C1 and C2. To compute the model flux ratios, we simulate the stellar photospheric emission as black-body emission $B(T_{\rm eff})$ with effective

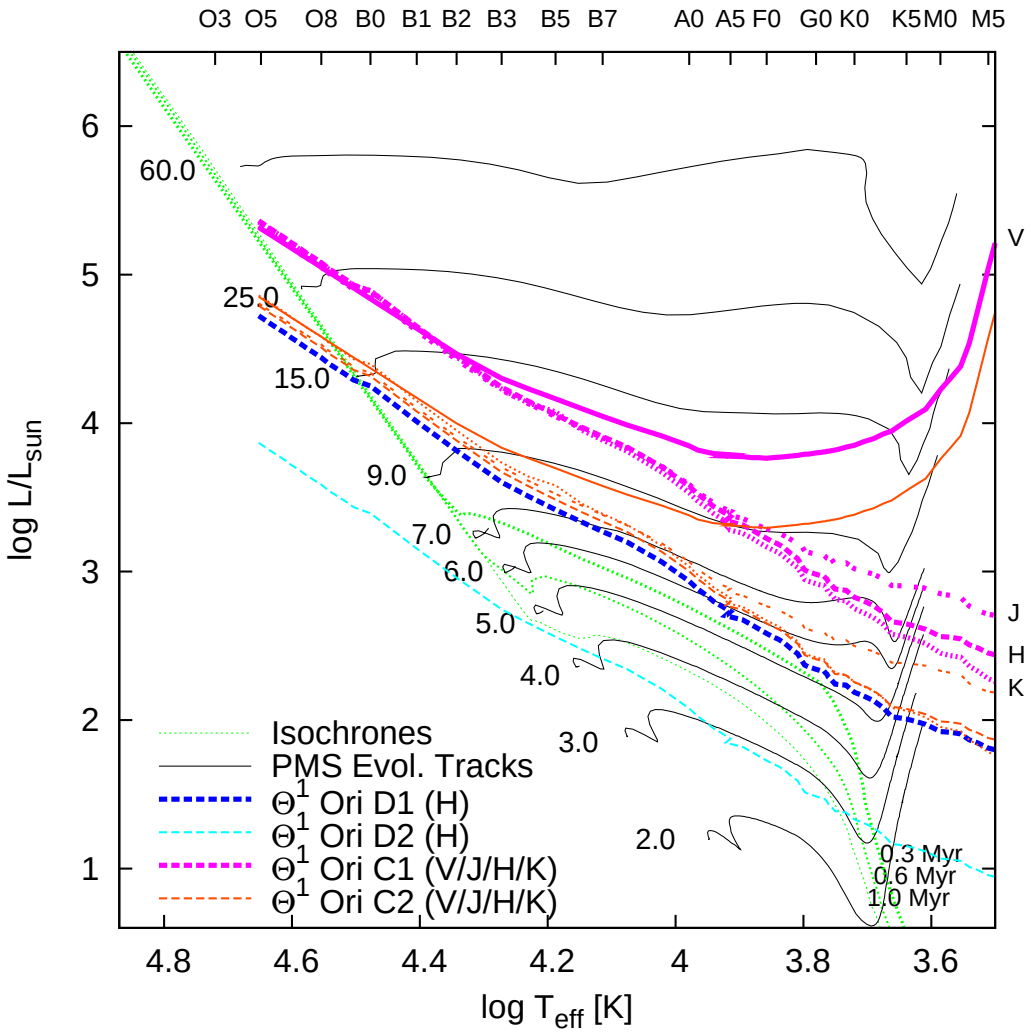

Figure 8.10: HR-diagram with PMS evolutionary tracks ($Z = 0.02$; thin solid lines with the corresponding masses labeled aside). For masses $\leqslant 7M_{\odot}$ ($\geqslant 9M_{\odot}$) the tracks from Siess et al. 2000 (Bernasconi & Maeder 1996) were used. The three dashed lines represent the isochrones for 0.3, 0.6, and 1.0 Myr (Bernasconi & Maeder 1996). Using synthetic colors and bolometric corrections from Kenyon & Hartmann (1995) and Martins et al. (2005); Martins & Plez (2006), we converted the measured photometry for θ^1Ori C1 and C2 into the corresponding allowed locations in the HR-diagram (thin red lines).

temperatures $T_{\rm eff}$ and stellar radii R, as predicted by stellar evolutionary models (Claret 2004; Martins et al. 2005):

$$\left(\frac{F_{\rm C2}}{F_{\rm C1}}\right)(\lambda) = \frac{B(T_{\rm eff}^{\rm C2})R_{\rm C2}^2}{B(T_{\rm eff}^{\rm C1})R_{\rm C1}^2} \tag{8.1}$$

Under these assumptions, the companion C2 would have to be rather massive ($M_{\rm C2}/M_{\rm C1} = 0.45 \pm 0.15$) to obtain reasonable agreement with the measured flux ratios (see Figure 8.9). Using a value for A_V from literature, the flux ratios can also be used to estimate the photometry of the individual components (Table 8.6). Then, the spectral type of C1 and C2 can be determined by comparing the location of the stars in the HR-diagram with stellar evolution models. For this, we adopt the procedure from Schertl et al. (2003) and convert the derived photometry into locations in the HR-diagram using the colors and bolometric corrections from Kenyon & Hartmann (1995, and references therein) and Martins & Plez (2006). Assuming coevality for both stars, the spectral type of the individual components can be constrained by finding the location where the curves for the various spectral bands and the isochrone intersect. As can be seen in Figure 8.10, the allowed locations for C1 intersect the Zero-Age Main Sequence[2] (ZAMS) around $T_{\rm eff} = 46\,000 \pm 4\,000$ K, $\log L/L_\odot = 5.3 \pm 0.2$ (corresponding to O5) and around $T_{\rm eff} = 33\,000 \pm 2\,000$ K, $\log L/L_\odot = 4.5 \pm 0.1$ (corresponding to O9) for C2.

We conclude that the spectral type combination, which simultaneously provides good agreement to the measured flux ratios, the HR-diagram, and the dynamical masses derived in Sect. 8.6.1, is given by the following stellar parameters (using the evolutionary models from Martins et al. 2005):
C1: O5.5 ($M = 34.0\,M_\odot$, $T_{\rm eff} = 39\,900$ K, $\log L/L_\odot = 5.41$)
C2: O9.5 ($M = 15.5\,M_\odot$, $T_{\rm eff} = 31\,900$ K, $\log L/L_\odot = 4.68$)

8.6.5 Nature of the potential θ^1Ori D companion

Although the θ^1Ori D binary parameters presented in Sect. 8.5.2 must be considered preliminary, it might be interesting to determine the spectral type of the putative components. We apply the procedure discussed in Sect. 8.6.4 to determine the photometry of the components from the measured intensity ratio (photometry for the unresolved system from Hillenbrand et al. 1998: H=5.84) and derive H_{D1}=5.98 and H_{D2}=8.12, respectively. Searching again for the intersection between the allowed locations in the HR-diagram with the isochrones applicable to the ONC (Figure 8.10) yields for D1 best agreement with $T_{\rm eff} = 31\,500 \pm 4\,000$ K, $\log L/L_\odot = 4.25 \pm 0.1$ (corresponding to O9.5). Accordingly, D2 might be either a B4 or B5 type star which has just reached the ZAMS ($T_{\rm eff} = 16\,000 \pm 4\,000$ K, $\log L/L_\odot = 2.6 \pm 0.2$) or a pre-main-sequence K0 type star ($T_{\rm eff} = 5\,000 \pm 1\,000$ K, $\log L/L_\odot = 1.3 \pm 0.2$).

Vitrichenko (2002a) examined radial velocity variations of θ^1Ori D and presented preliminary spectroscopic orbital elements for a companion with a 20.2 d period (or twice that period, P=40.5 d). As-

[2] With a dynamical age of $\sim 3 \times 10^5$ yrs, it seems justified that the Trapezium stars are real ZAMS stars (Schulz et al. 2003), although the strong magnetic activity from θ^1Ori C was also associated with a pre-main-sequence origin (Donati et al. 2002).

suming 20 $M_{\odot}$ as the system mass, these periods correspond to a major axis of 0.05 or 0.08 AU ($\sim$ 0.1 or 0.2 mas). Since this is far below the 18 mas suggested by our binary model fit, we do not associate our potential companion with the proposed spectroscopic companion.

The multiplicity rate in a young stellar population such as the Trapezium cluster is an important quantity, which might allow us to draw conclusions about the mechanisms controlling the star formation process. In particular, the significantly different binary frequencies determined for the low- and high-mass population in the ONC were interpreted as evidence that different formation mechanisms (e.g. stellar coalescence vs. accretion) might be at work in different mass regimes (Preibisch et al. 1999). The detection of a new companion around θ^1Ori D further increases the multiplicity rate for high-mass stars in the ONC, although Köhler et al. (2006) have recently also presented an upwards-correction for the rate of low-mass star binaries.

8.7 Conclusions

We have presented new bispectrum speckle interferometric and infrared long-baseline interferometric observations of the Orion Trapezium stars θ^1Ori C and D. This data was used to reconstruct diffraction-limited NIR and visual speckle images of the θ^1Ori C binary system and, to our knowledge, the first model-independent, long-baseline aperture-synthesis image of a young star at infrared wavelengths.

For θ^1Ori D, we find some indications that the system was resolved by the IOTA interferometer. Although the non-zero closure phase signal suggests asymmetries in the brightness distribution (maybe indicative of a close companion star), further observations are required to confirm this finding.

From our multi-epoch observations on θ^1Ori C (covering the interval 1997.8 to 2005.8), we derived the relative position of the companions using model-fitting techniques, clearly tracing orbital motion. We presented two preliminary orbital solutions, of which one can be favoured due to theoretical arguments. This solution implies a period of 10.98 yrs, a semi-major axis of 41.3 mas, a total system mass of $\sim 48 M_{\odot}$, and a distance of 434 pc. Furthermore, we find strong indications that θ^1Ori C2 will undergo periastron passage in mid 2007. As the binary separation at periastron is expected to be $\sim$ 1 mas, further long-baseline interferometric observations on θ^1Ori C are urgently needed to refine the orbital elements, the stellar masses, and orbital parallaxes. Through comparison with stellar evolutionary models and modeling of the measured intensity ratio, we find evidence that the companion θ^1Ori C2 is more massive ($M_{\rm C2}/M_{\rm C1} \approx 0.45 \pm 0.15$) than previously thought; likely of late O (O9/9.5) or early B-type (B0). The contribution of the companion to the total flux of θ^1Ori C and the interaction between both stars might be of special importance for a deeper understanding of this intriguing object. Therefore, we strongly encourage observers to acquire high dispersion spectra of the system in order to trace the expected radial velocity variations and the wind-wind interaction of the system.

9 Near-Infrared interferometry of η Carinae with high spatial and spectral resolution using the VLTI/AMBER instrument

Based on an article which appeared in A&A:
Weigelt, G., Kraus, S., Driebe, T., et al., A&A 464, 87-106 (2007)

9.1 Overview and Context

Although located in the active star-forming region NGC 3372 (Carina Nebula), η Carinae is already approaching the end of its stellar evolution. Of course, this is due to the comparatively short lifetime (roughly 10^6 yrs) of a star as massive as $\sim 100\ M_{\odot}$, and η Car might end its life in a supernova explosion within the next 10^5 yrs.

Due to its extreme mass and the LBV evolutionary stage, η Car is highly unstable and undergoing violent outbursts. Photometric measurements reaching back to 1500 show that the star has undergone several outbursts; the most important one in 1843 when η Car became the brightest star in the sky ($V = -1$) after Sirius (Viotti 1995). After this event, the brightness dropped to $V \approx 7$

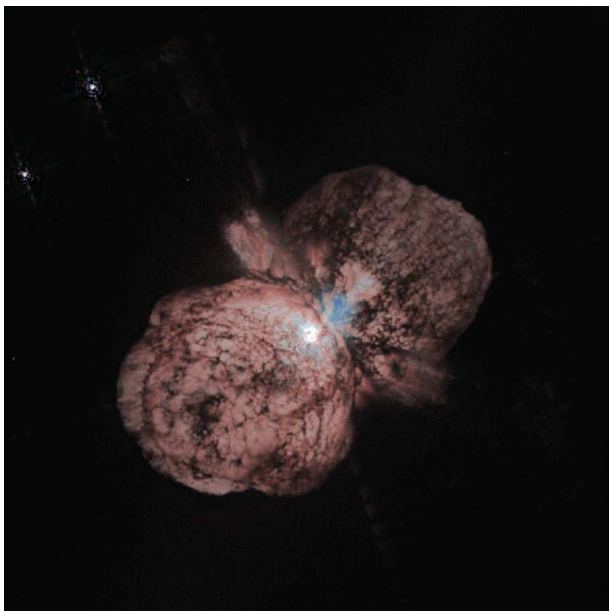

Figure 9.1: Image of the Homunculus nebula surrounding η Carinae, as seen by HST. Besides the bipolar lobes, it also reveals the equatorial disk-like feature.

within two decades, likely due to obscuration by dust ejected around that time, nowadays forming the famous *Homunculus Nebula* (see Fig. 9.1). Besides the Homunculus (extending about 8″ towards the northwest and southeast), a *Little Homunculus* is known, perhaps originating from a minor eruption event around 1890 (Ishibashi et al. 2003). However, the major source of opacity between us and the star is caused by an optically thick stellar wind, which originates from η Car. Besides continuum emission, this wind is also traced by various lines from ultraviolet to infrared wavelengths, whose intensity and profile could be reproduced by the line radiative transfer models from Hillier et al. (2001). By measuring the spectrum of the reflected light at various positions of the Homunculus, Smith et al. (2003) found indications for latitude-dependent effects in the stellar wind, suggesting an aspherical geometry with enhanced mass loss in the polar direction. This can be understood in the context of equatorial gravity darkening on a rapidly rotating star, as predicted by Zeipel (1925).

One particularly puzzling piece of evidence is the periodic spectroscopic variability, which was discovered in spectral lines in various wavelength regimes. Especially the 5.54 yr period, which has also been detected in the X-ray flux, was proposed as a strong indication for wind-wind interaction, suggestive of the presence of a hot companion star.

As the separation of the η Car components is expected to be only 8 mas, any direct detection of the proposed companion requires the high spatial resolution only achievable with optical interferometry. Besides the potential to directly image the continuum emission of the companion, the unique spectroscopic capabilities of VLTI/AMBER provide the possibility to study the proposed wind-wind interaction zone in spectral lines. One line which is believed to be a good tracer for the associated bow shock and ionization front is the He I line at 2.059 μm.

We obtained observations on this enigmatic object in the context of AMBER's GTO programme using three 8.2 m Unit Telescopes and baselines from 42 to 89 m, corresponding to a high spatial resolution of 5 mas (11 AU). The raw data are spectrally dispersed interferograms obtained with spectral resolutions of 1 500 (MR-K mode) and, for the first time, also 12 000 (HR-K mode). This allows us to investigate the *wavelength dependence* of the visibility, differential phase, and closure phase of η Car. The MR-K observations were performed in the wavelength range around both the He I 2.059 μm and the Brγ 2.166 μm emission lines; the HR-K observations only in the Brγ line region.

In this project, I was responsible for the reduction of the AMBER data (Sect. 9.3). As our group had no earlier practical experience in the processing of this kind of data, this required the development of the AMBER data reduction pipeline (described in more detail in Chapter 4). The results of the data processing were discussed in a working group, including Gerd Weigelt, Thomas Driebe, Karl-Heinz Hofmann, and Dieter Schertl. Following these meetings, I continuously improved the data reduction pipeline, implementing various methods for data selection, data averaging, and data presentation. The wavelength calibration was done in collaboration with Thomas Driebe. To yield an independent confirmation of our findings, Karl-Heinz Hofmann applied his own AMBER data reduction software to the η Car data.

Starting in summer 2005, we continued within the same team to discuss the astrophysical interpretation. Geometrical model fits to the measured visibilities within the continuum and within the line were performed by Thomas Driebe (Sect. 9.4). To yield a physically motivated model which would allow a quantitative interpretation not only of the visibilities, but also of the measured differential phases and closure phases (Sect. 9.4.5), I adopted my self-made modeling software to also compute these observables for wavelength-dependent brightness distributions. Motivated by theoretical work about stellar winds with enhanced polar mass loss, I considered an aspherical wind, whose velocity distribution is latitude-dependent, as geometry for this modeling, yielding the Brγ model presented in Sect. 9.4.6. The He I P-Cygni line data, potentially tracing the wind-wind interaction zone between the η Car primary and the proposed hot companion, was modeled using a similar procedure (Sect. 9.4.7.1). It shows that all observables can, in fact, be represented reasonably well assuming a He I-emitting region which is offset by a few mas from the continuum emitting region, such as expected by the wind-wind interaction scenario. To make statements about the direct detectability of the continuum emission from the hypothetical hot η Car companion, I adopted the software to simulate the effect of such a companion on the visibilities and closure phases. Using a statistical argument and the measured non-zero closure phase signal allowed us to put upper limits on the flux ratio of the hypothetical companion. For the manuscript, I was responsible for writing Sect. 9.3, 9.4.5, 9.4.6, 9.4.7, 9.4.7.1, and 9.4.7.2.

9.2 Introduction

The enigmatic object η Car is one of the most luminous and most massive ($M \sim 100\,M_{\odot}$) unstable Luminous Blue Variables suffering from an extremly high mass loss (Davidson & Humphreys 1997). Its distance is approximately 2300 ± 100 pc (Davidson & Humphreys 1997; Davidson et al. 2001; Smith 2006). η Car, which has been subject to a variety of studies over the last few decades, is surrounded by the expanding bipolar Homunculus nebula ejected during the Great Eruption in 1843. The inclination of the polar axis of the Homunculus nebular with the line-of-sight is $\sim 41°$, with the southern pole pointing towards us (Davidson et al. 2001; Smith 2006). The first measurements of structures in the innermost sub-arcsecond region of the Homunculus were obtained by speckle-interferometric observations (Weigelt & Ebersberger 1986; Hofmann & Weigelt 1988). These observations revealed a central object (component A) plus three compact and surprisingly bright objects (components B, C, and D) at distances ranging from approximately $0\farcs1$ to $0\farcs2$. HST observations of the inner $1''$ region (Weigelt et al. 1995) provided estimates of the proper motion of the speckle objects B, C, and D (velocity $\sim$ 50 km/s; the low velocity suggests that the speckle objects are located within the equatorial plane), and follow-up HST spectroscopy unveiled their unusual spectrum (Davidson et al. 1995). The central object (speckle object A) showed broad emission lines, while the narrow emission lines came from the speckle objects

B, C, and D. Therefore, A is certainly the central object while B,C, and D are ejecta. Recent observations of η Car by Chesneau et al. (2005) using NACO and VLTI/MIDI revealed a butterfly-shaped dust environment at 3.74 and 4.05 μm and resolved the dusty emission from the individual speckle objects with unprecedented angular resolution in the NIR. Chesneau et al. also found a large amount of corundum dust peaked $\sim 1''$ south-east of the central object.

Spectroscopic studies of the Homunculus nebula showed that the stellar wind of η Car is aspherical and latitude-dependent, and the polar axes of the wind and the Homunculus appear to be aligned (bipolar wind model; Smith et al. 2003). Using Balmer line observations obtained with HST/STIS, Smith et al. (2003) found a considerable increase of the wind velocity from the equator to the pole and that the wind density is higher in polar direction (parallel to the Homunculus; PA of the axis $\sim$132°; Davidson et al. 2001) than in equatorial direction by a factor of $\sim$2. van Boekel et al. (2003) resolved the optically thick, aspheric wind region with NIR interferometry using the VLTI/VINCI instrument. They measured a size of 5 mas (50% encircled-energy diameter), an axis ratio of 1.25 ± 0.05, and a position angle (PA) of the major axis of $134° \pm 7°$, and derived a mass-loss rate of $1.6 \times 10^{-3}\,M_{\odot}/\mathrm{yr}^{-1}$. The aspheric wind can be explained by models for line-driven winds from luminous hot stars rotating near their critical speed (e.g., Owocki et al. 1996, 1998). The models predict a higher wind speed and density along the polar axis than in the equatorial plane. In addition, van Boekel et al. showed that the *K* broad-band observations obtained with VINCI are in agreement with the predictions from the detailed spectroscopic model by Hillier et al. (2001).

The Hillier et al. (2001, 2006) model was developed to explain STIS HST spectra. The luminosity of the primary ($5 \times 10^6\,L_{\odot}$) was set by observed IR fluxes (see discussion by Davidson & Humphreys 1997) and the known distance of 2.3 kpc to η Car. Any contribution to the IR fluxes by a binary companion was neglected. Modeling of the spectra was undertaken using CMFGEN, a non-LTE line blanketed radiative transfer developed to model stars with extended outflowing atmospheres (Hillier & Miller 1998). For the modeling of η Carinae (alias η Car, HD 93308), ions of H, He, C, N, O, Na, Mg, Al, Si, S, Ca, Ti, Cr, Mn, Fe, Ni, and Co were included. The mass loss was derived from the strength of the hydrogen lines and their associated electron scattering wings. Due to a degeneracy between the mass-loss rate and the He abundance, the H/He helium abundance ratio could not be derived, but was set at 5:1 (by number), which is similar to that found by Davidson et al. (1986) from nebula studies. CNO abundances were found to be consistent with those expected for full CNO processing. With the exception of Na (which was found to be enhanced by at least a factor of 2), the adoption of solar abundances for other metal species was found to yield satisfactory fits to the STIS spectra. A more recent discussion of the basic model, with particular reference to the UV and outer wind, is given by Hillier et al. (2006).

Because the wind is optically thick, the models are fairly insensitive to the radius adopted for the hydrostatic core (i.e., the radius at which the velocity becomes subsonic). One exception was the He I lines, which decreased in strength as the radius increased and, in general, were very sensitive to model

details. Additional HST STIS observations show that the He I lines are strongly variable and blue-shifted throughout most of the 5.54-year variability period. These observations cannot be explained in the context of a spherical wind model. It now appears likely that a large fraction of the He I line emission originates in the bow shock and an ionization zone, associated with the wind-wind interaction zone in a binary system (Davidson et al. 1999; Davidson 2001; Hillier et al. 2006; Nielsen et al. 2006). Consequently, the hydrostatic radius derived by Hillier et al. (2001) is likely to be a factor of 2 to 4 too small. Because the wind is so thick, a change in radius will not affect the Brγ formation region, and it will only have a minor influence on the Brγ continuum emitting region. If this model is correct, the He I emission will be strongly asymmetrical and offset from the primary star.

A variety of observations suggest that the central source of η Car is a binary. Damineli (1996) first noticed the 5.5-year periodicity in the spectroscopic changes of this object (see Damineli et al. 1997, 2000; Duncan et al. 1999; Ishibashi et al. 1999; Davidson et al. 1999, 2000; van Genderen et al. 2003; Steiner & Damineli 2004; Whitelock et al. 2004; Corcoran 2005; Weis et al. 2005). On the other hand, to date, the binary nature of the central object in η Car and its orbital parameters are still a matter of debate (see, e.g., Zanella et al. 1984; Davidson 1999, 2001; Davidson et al. 1999, 2000, 2005; Ishibashi et al. 1999; Smith et al. 2000; Feast et al. 2001; Ishibashi 2001; Pittard & Corcoran 2002; Smith et al. 2003; Martin et al. 2006).

The 1997.9 X-ray peak with the subsequent rapid drop to a few-month-long minimum was detected by RXTE (see Corcoran 2005). Then the first spectra with HST/STIS were obtained at 1998.0, demonstrating changes in both the central star and the aforementioned speckle objects (Davidson et al. 1999; Gull et al. 1999). Pittard & Corcoran (2002) demonstrated that the CHANDRA X-ray spectrum can be explained by the wind-wind collisions of the primary star ($\dot{M} = 2 \times 10^{-4}\,M_{\odot}/\mathrm{yr}^{-1}$ at 500 km/s) and a hot companion ($\dot{M} = 10^{-5}\,M_{\odot}/\mathrm{yr}^{-1}$ at 3 000 km/s). Verner et al. (2005) used models calculated with the CLOUDY code to demonstrate that during the spectroscopic minimum, the excitation of the speckle objects is supported by the primary stellar flux, but that the UV flux of a hot companion consistent with an O7.5V, O9I, or early WN star was probably necessary to excite the speckle objects during the broad spectroscopic maximum.

In this paper we present the first spectro-interferometric K-band observations of η Car obtained with the VLTI beam-combiner instrument AMBER with medium and high spectral resolution and in the projected baseline range from 28 to 89 m.

The paper is organized as follows: In Sect. 2 we give an overview of the AMBER observations of η Car and describe the data reduction procedure in detail, and in Sect. 3, the analyses of the continuum data and the measurements within the Brγ and He I lines are discussed individually.

Table 9.1: Summary of the AMBER η Car observations using the UT2, UT3, and UT4 telescopes.

Date [UT]	Time [UT] Start	End	Orbital phase[e]	spectral mode	line within spectral range	DIT[d] [ms]	$N^{f}_{\eta\ Car}$	Calibrator	$N^{g}_{calib.}$	Calibrator uniform disk diameter [mas]
2004 Dec. 26	07:52	08:16	0.267	MR-K	Brγ	40	7 500	HD 93030	5 000	0.39[a]
	08:19	08:32	0.267	MR-K	He I 2.059 μm	40	5 000	HD 93030	5 000	0.39[a]
2005 Feb. 25	04:33	04:43	0.298	MR-K	Brγ	50	5 000	HD 89682	2 500	3.08[b]
	04:55	05:05	0.298	MR-K	He I 2.059 μm	50	5 000	HD 89682	2 500	3.08[b]
2005 Feb. 26	08:16	08:57	0.299	HR-K	Brγ	82	7 500	L Car	2 500	2.70[c]

Notes – [a] Uniform disk (UD) diameter estimated using the method described by Dyck et al. (1996).
[b] UD diameter taken from the CHARM2 catalog (Richichi et al. 2005).
[c] UD diameter of L Car at the time of the AMBER high-resolution observations derived from the limb-darkened diameter $d_{\rm LD} = 2.80$ mas at the L Car pulsation phase ϕ=0.0 (Kervella et al. 2004b, 2006) and $d_{\rm UD}/d_{\rm LD} = 0.966$ (Kervella et al. 2004a).
[d] Detector integration time per interferogram.
[e] The orbital phase was computed assuming a zero point at JD 2 450 800.0 and a period of 2024 days (Corcoran 2005).
[f] Number of η Car interferograms.
[g] Number of calibrator interferograms.

9.3 AMBER Observations and Data Processing

η Car was observed with AMBER on 2004 December 26, 2005 February 25, and 2005 February 26 with the three 8.2 m *Unit Telescopes* UT2, UT3, and UT4. With projected baseline lengths up to 89 m, an angular resolution of $\sim$5 mas was achieved in the *K*-band. As listed in Table 9.1, the MR-K observations were performed in the wavelength range around both the He I 2.059 μm and the Brγ 2.166 μm emission lines. The HR-K observations were only performed in a wavelength range around the Brγ line. The widths of the wavelength windows of the obtained MR-K and HR-K observations are approximately 0.05 μm and 0.02 μm, respectively.

Figure 9.2 shows two AMBER raw interferograms taken in the wavelength range around the Brγ line in HR (top) and MR (bottom) mode. In the MR data sets, the Doppler-broadened Brγ line covers $\sim$ 8 spectral channels, whereas in HR mode, the line is resolved by $\sim$ 50 spectral channels.

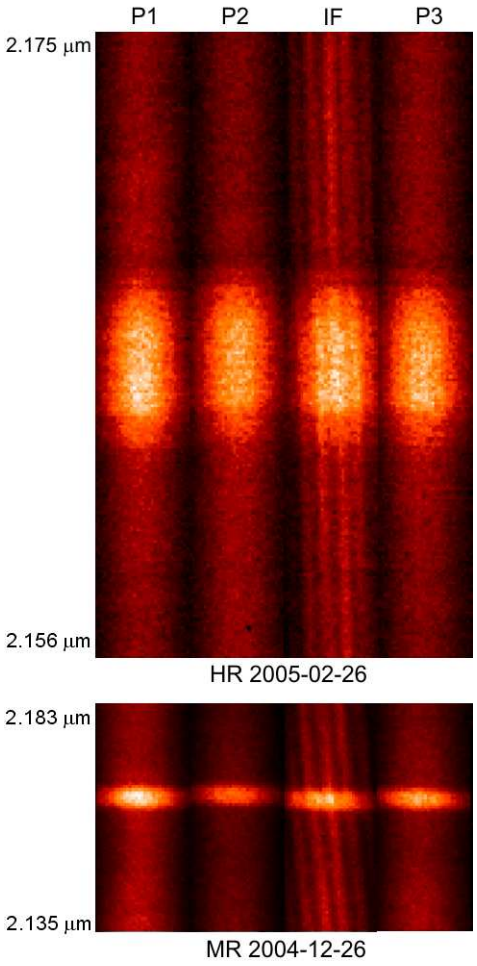

Figure 9.2: Spectrally dispersed VLTI/AMBER Michelson interferograms of η Car. The two panels show the spectrally dispersed fringe signal (IF) as well as the photometric calibration signals from the three telescopes (P1-P3) in high (HR, upper panel) and medium spectral resolution mode (MR, lower panel). In both panels, the bright regions are associated with the Doppler-broadened Brγ emission line.

For the reduction of the AMBER data, we used version 2.4 of the *amdlib* software package. This software uses the P2VM (*pixel-to-visibilities matrix*) algorithm (Tatulli et al. 2006) in order to extract complex visibilities for each baseline and each spectral channel of an AMBER interferogram. From these three complex visibilities, the amplitude and the closure phase are derived. While the closure phase is self-calibrating, the visibilities have to be corrected for atmospheric and instrumental effects. This is done by dividing the η Car visibility through the visibility of a calibrator star measured on the same night. In order to take the finite size of the calibrator star into account, the calibrator visibility is corrected beforehand through division by the expected calibrator star visibility (see Table 9.1). In the case of the MR measurement performed on

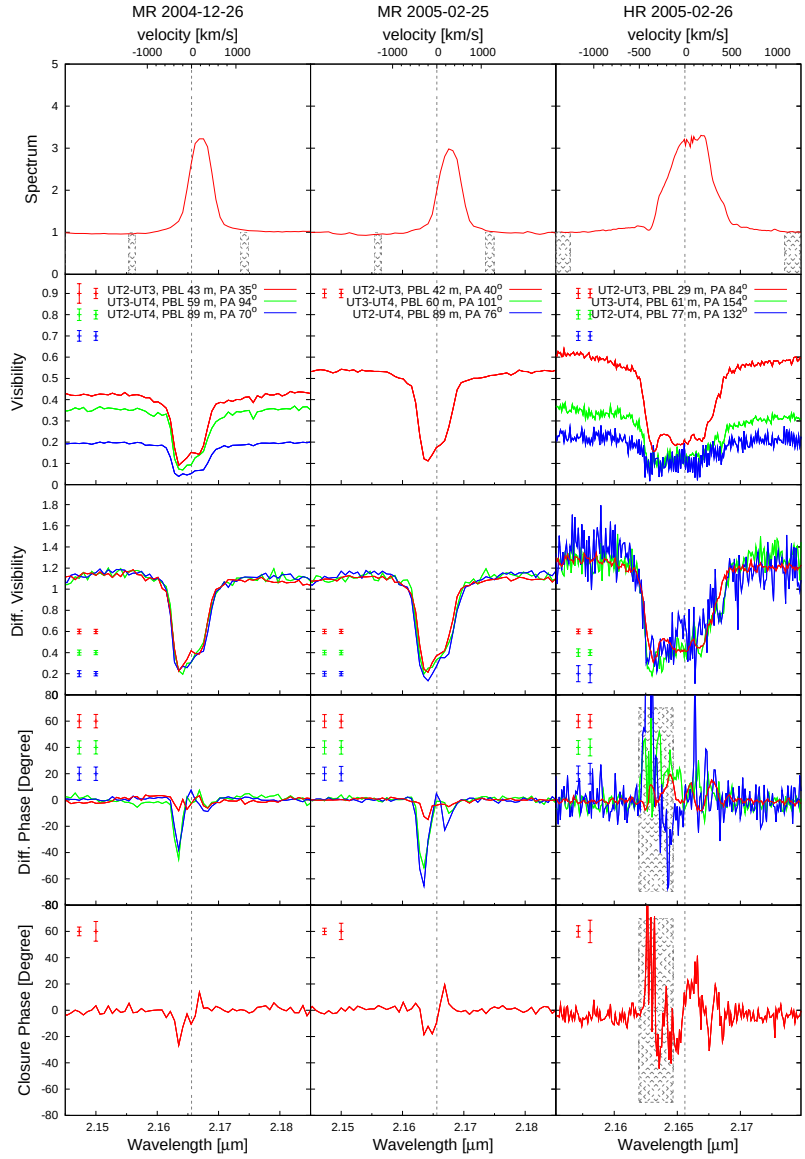

Figure 9.3: AMBER observables derived from our η Car data around the Brγ line for three independent measurements (*Left:* MR, 2004 December 26, *Middle:* MR, 2005 February 25, *Right:* HR, 2005 February 26). The first row shows the continuum-normalized spectra as extracted from the interferometric channels, followed by the derived calibrated visibilities and the differential visibilities. In the fourth and fifth row, the differential phase and the closure phase are presented. In the spectra we mark the wavelength regimes, which we defined as continuum for our analysis (shaded regions). The vertical grey line marks the rest-wavelength of Brγ ($\lambda_{\rm vac} = 2.1661\,\mu$m; the small correction due to the system velocity of -8 km/s (Smith 2004) has been neglected). We show different error bars within each panel: The left error bars correspond to the total (including statistical and systematic) error estimated for the continuum wavelength range, and the error bar towards the right visualizes the total error for the wavelength range within the line. For the HR 2005-02-26 measurement, data splitting showed that for a small wavelength range (hatched areas in the two lower right panels), the differential phase for the longest and middle baseline as well as the closure phase become very noisy and are therefore not reliable. Furthermore, the HR differential phase of the longest baseline is noisy at all wavelengths. See Sect. 9.3 for further details.

2005-02-25, the interferograms recorded on the calibrator contain only fringes corresponding to the shortest baseline (UT2-UT3). Thus, the η Car visibility for this night could only be calibrated for this shortest baseline.

Besides the calibrated visibility and the closure phase, the spectral dispersion of AMBER also allows us to compute differential observables; namely the differential visibility and the differential phase (Petrov et al. 2003a, 2006a,b; Millour et al. 2006). These quantities are particularly valuable, as they provide a measure of the spatial extent and spatial offset of the line-emitting region with respect to the continuum emission. Since the measured complex visibilities are affected by wavelength-dependent atmospheric piston (optical path difference), the piston has to be estimated and subtracted. This was done using the *ammyorick* tool (version 0.56).

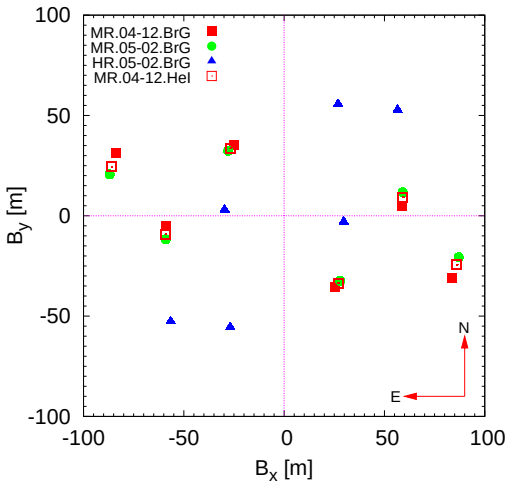

Figure 9.4: *uv*-coverage of the AMBER η Car observations. The data obtained with medium spectral resolution in Dec. 2004 and Feb. 2005 are indicated by red squares and green bullets, respectively, while the high-resolution measurements are shown as blue triangles. Filled symbols denote observations around the Brγ line, and open symbols denote observations around the He I line.

Since a large fraction of the interferograms is of low contrast (probably due to vibration; see Malbet et al. 2006b), we removed a measurement from the data sets if *(a)* the intensity ratio of two of the photometric channel signals is larger than 4 (a large ratio means that the interferograms are very noisy since the signal is very weak in one channel) or *(b)* it belongs to the 70 percent of the interferograms with the lowest fringe contrast SNR (with the SNR defined as in Tatulli et al. 2006). In order to optimize the selection for each baseline of the telescope triplet, both of these criteria are applied for each telescope pair individually. Furthermore, the first 10 frames in each new sequence of recorded interferograms are removed since they are degraded by electronic noise.

Figures 9.3 and 9.5 show the spectra as well as the wavelength dependence of the visibilities, differential visibilities, differential phases, and closure phases derived from the AMBER interferograms for the observations around the Brγ and He I emission lines. The *uv*-coverage of the observations is displayed in Fig. 9.4.

The η Car spectra were corrected for instrumental effects and atmospheric absorption through division by the calibrator spectrum. For the HR 2005-02-26 measurement, we found that the calibrator itself (L Car) shows prominent Brγ line absorption (see Fig. 9.14). Therefore, we had to remove this stellar

line by linear interpolation before the spectrum could be used for the calibration. The wavelength calibration was done using atmospheric features, as described in more detail in Appendix 9.6.

In order to test the reliability of our results, we split each of the raw data sets into 5 subsets, each containing the same number of interferograms. The results obtained with these individual subsets allowed us to test that the major features detected in the visibility, differential visibility, differential phase, and closure phase are stable, even without any frame selection applied. As an exception, we found that for a small wavelength range of the HR 2005-02-26 data set (hatched areas in the two lower right panels of Figure 9.3), the differential phase corresponding to the middle and longest baselines and the closure phase vary strongly within the subsets and are, therefore, unreliable. This is likely due to the very low visibility value on these two baselines, resulting in a low fringe SNR within this wavelength range. Furthermore, with this method we found that the differential visibility, differential phase, and closure phase extracted from the MR 2005-02-25 He I data set are very noisy and not reliable. Therefore, these differential quantities and closure phases were dropped from our further analysis.

The subsets were also used to compute statistical errors. We estimated the variance for each spectral channel and derived formal statistical errors for both the continuum and line wavelength ranges. In each panel of Figures 9.3 and 9.5, we show two types of error bars corresponding to these regions, which not only take these statistical errors but also a systematic error (e.g. resulting from an imperfect calibration) into account.

9.4 Observational Results and Interpretation

9.4.1 Comparison of the observed wavelength dependence of the visibility with the NLTE radiative transfer model of Hillier et al. (2001)

For the analysis presented in this chapter, we used the AMBER data sets from 2004 Dec. 26 and 2005 Feb. 25 and 26, presented in Figs. 9.3 and 9.5, and compared the AMBER visibilities and spectra with the NLTE radiative transfer model of Hillier et al. (2001). To directly compare the AMBER measurements with this model, we derived monochromatic model visibilities for all wavelengths between 2.03 and 2.18 μm (with $\Delta\lambda = 10^{-4}\,\mu$m) from the model intensity profiles, assuming a distance of 2.3 kpc for η Car. The comparison is visualized in Fig. 9.6 for the individual AMBER HR and MR measurements. The first row displays the AMBER and model spectra, while all other panels show the AMBER and model visibilities for the different projected baselines. We note that for the comparison shown in Fig. 9.6, we used the original model of Hillier et al. (2001) without any additional size scaling or addition of a background component.

As the figure reveals, the NLTE model of Hillier et al. (2001) can approximately reproduce the AMBER *continuum* observations for all wavelengths (i.e. 2.03–2.18 μm) and all baselines. Moreover, the

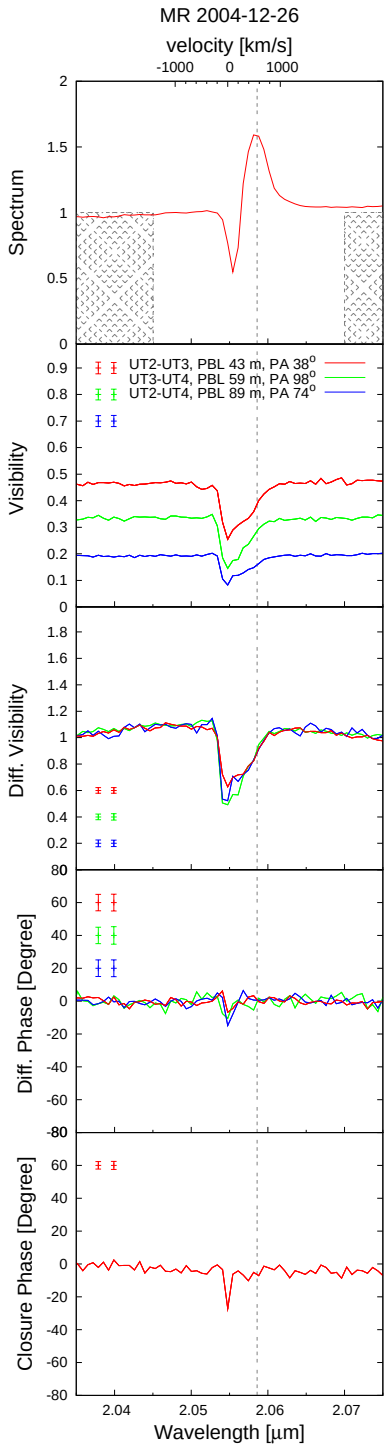

Figure 9.5: Similar to Fig. 9.3, but showing the MR measurement from 2004 December 26 covering the region around the He I line. The vertical grey line marks the He I rest-wavelength ($\lambda_{\rm vac} = 2.0586\,\mu$m).

wavelength dependence of the model visibilities inside the Brγ line is also similar to the AMBER data. There is a slight tendency for the model visibilities in the Brγ line to be systematically lower, which can be attributed to the overestimated model flux in the line. On the other hand, there is an obvious difference in the wavelength dependence of the visibility across the He I line between the observations and the model predictions. This difference probably indicates that the primary wind model does not completely describe the physical origin and, hence, the spatial scale of the He I line-forming region. The discrepancy is possibly caused by additional He I emission from the *wind-wind interaction zone* between the binary components and by the *primary's ionized wind zone* caused by the secondary's UV light illuminating the primary's wind (e.g., Davidson et al. 1999; Davidson 2001; Pittard & Corcoran 2002; Steiner & Damineli 2004; Hillier et al. 2006; Nielsen et al. 2006; Martin et al. 2006), as discussed in Sects. 9.2, 9.4.4.2, and 9.4.7.2 in more detail.

Figure 9.7 shows the AMBER and model visibilities as a function of spatial frequency and the corresponding model center-to-limb intensity variations (CLVs) for seven selected wavelengths (2 continuum wavelengths; center, blue-shifted, and red-shifted wings of Brγ emission; center of both He I emission and absorption). As Fig. 9.7 reveals, at several wavelengths we find a very good agreement between the visibilities measured with AMBER and the visibilities predicted by the model of Hillier et al. (2001). This is especially true for the continuum data (upper two panels).

From the model CLVs, FWHM model continuum diameters of 2.24 mas and 2.33 mas can be derived for $\lambda = 2.040$ and $2.174\,\mu$m, respectively. If we allow for a moderate rescaling of the size of the model, we find that the best χ^2 fit at both continuum wavelengths can be obtained with scaling factors of 1.015 and 1.00, respectively. This means that the model size has to be increased by only 1.5% at $\lambda = 2.040\,\mu$m and that the best fit at $2.174\,\mu$m is indeed obtained with the original Hillier model with a scaling factor of 1.0. Thus, taking the slight rescaling for the best χ^2 fit into account, we can conclude that, based on the NLTE model from Hillier et al. (2001, 2006) and the AMBER measurements, the apparent FWHM diameters of η Car in the K-band continuum at $\lambda = 2.040\,\mu$m and $2.174\,\mu$m are 2.27 mas and 2.33 mas, respectively (see Table 2), corresponding to a physical size of approximately 5 AU.

Since the deviations between the model and the measurements are larger in the case of the Brγ and He I line data (lower 5 panels in Fig. 9.7), the scaling factors corresponding to the best χ^2 fit in the lines show stronger deviations from unity. For the Brγ emission line, we find scaling factors of 0.74, 0.76, and 0.78 for $\lambda = 2.1661, 2.1635$, and $2.1669\,\mu$m, corresponding to FWHM diameters of 1.83, 9.52 and 2.02 mas (see Table 2).

For the He I emission line, rescaled models with scaling factors of 1.24 and 1.11 provide the best χ^2 fit for the peaks of the emission and absorption within the He I line ($\lambda = 2.058$ and $2.056\,\mu$m), resulting in FWHM diameters of 4.24 and 4.19 mas, respectively.

In addition to the inner CLV core, at several wavelengths, the CLVs show a very extended wing corresponding to the extended Brγ and He I line emission regions. Since the intensity in the wing

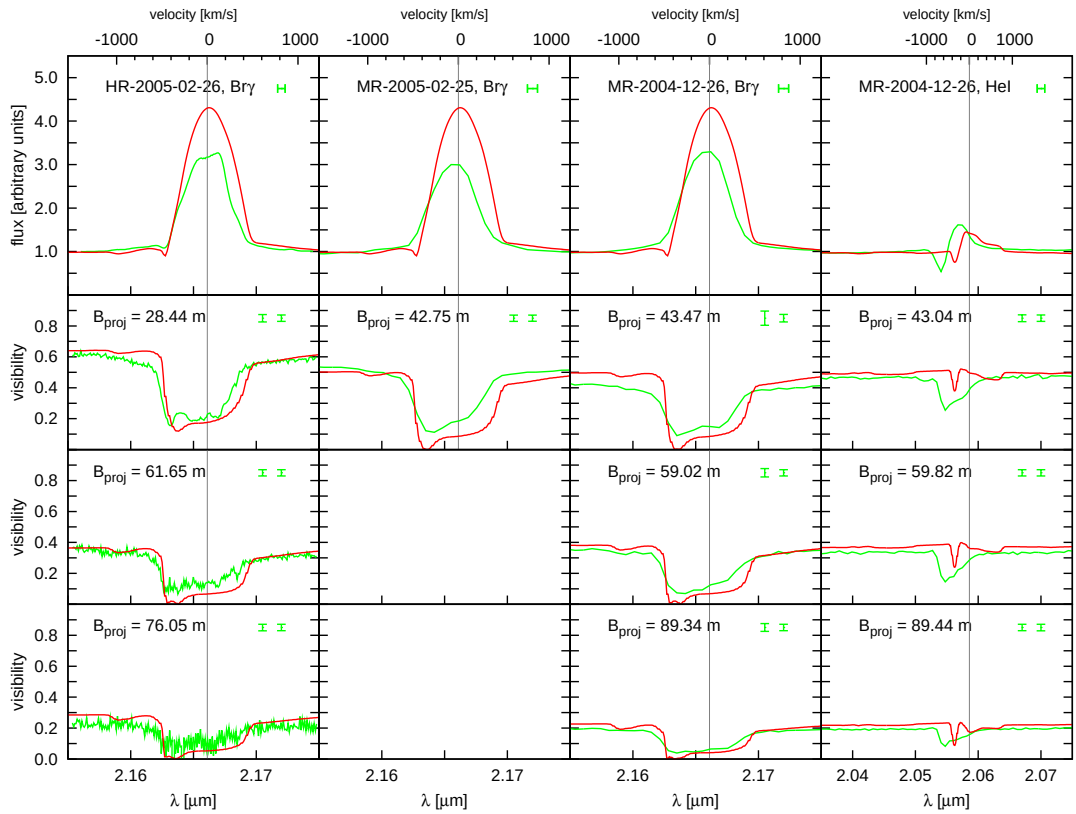

Figure 9.6: Comparison of the AMBER spectra and visibilities with the NLTE model predictions of Hillier et al. (2001). The figure displays the spectra (upper row) and visibilities (lower three rows, see labels for projected baselines) of the four AMBER measurements (green lines) and the corresponding data of the Hillier et al. NLTE model (red lines). The errors of the AMBER continuum and line visibility measurements are indicated by the two vertical error bars (see Figs. 9.3 and 9.5; the left bar is the continuum error bar), and the uncertainty of the AMBER wavelength calibration is indicated by the horizontal error bar. As the figure shows, we find good agreement between the AMBER data and the model predictions for the continuum visibilities as well as the shape and depth of the visibility inside the Brγ line. In the case of the He I line, the wavelength dependence of the model visibility inside the line differs considerably from the AMBER measurements, indicating a *different physical process involved in the line formation* (see Sect. 9.4.1). The He I wavelength shift can be attributed to a combination of both Doppler shift (e.g. Nielsen et al. 2006; Hillier et al. 2006) and uncertainties in the wavelength calibration of the AMBER data. Note that no additional scaling has been applied to the Hillier et al. model. The model spectra and visibilities have a spectral resolution ($\lambda/\Delta\lambda \sim 20\,000$) comparable to the HR measurements.

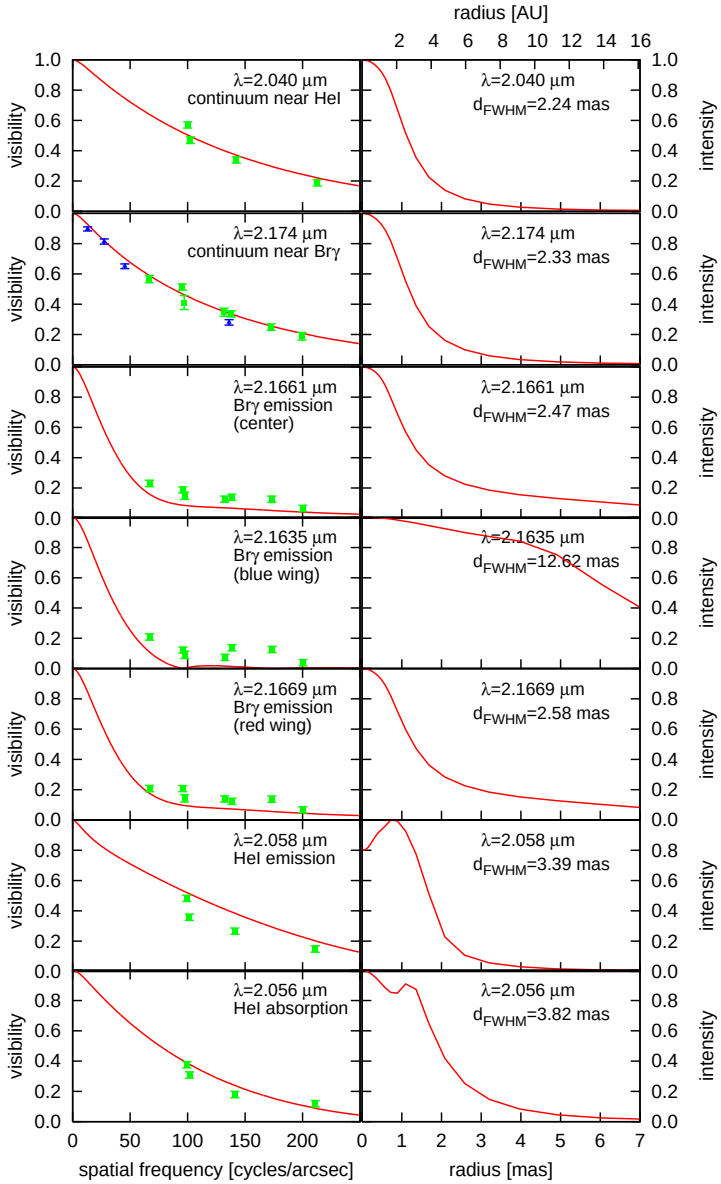

Figure 9.7: *Left*: Comparison of the AMBER visibilities (filled green squares; baseline range 28–89 m) as a function of spatial frequency with the NLTE model predictions of Hillier et al. (2001) (solid red lines) for two continuum wavelengths (upper two panels; see labels for the exact wavelengths), the central wavelength of the Brγ emission line (third), wavelengths in the blue and red wing of the Brγ emission line (fourth and fifth row; at these wavelengths, the AMBER data show the strongest differential and closure phase signals), and the central wavelengths of the He I emission and P Cygni absorption (lower two panels). The blue triangles are the background-corrected VINCI *K*-band measurements from van Boekel et al. (2003). *Right*: Center-to-limb variation (CLV; i.e. intensity as a function of angular radius) of the monochromatic Hillier et al. (2001) NLTE models for the wavelengths indicated by the labels. As the figures show, the typical FWHM diameter of the models is of the order of $\sim$2–4 mas for an assumed distance of 2.3 kpc for η Car. See text for details.

is much lower than 50% of the peak intensity, the FWHM diameter is not very sensitive to this part of the CLV. In other words, in the case of CLVs with multiple or very extended components, a FWHM diameter can be quite misleading. In such a case, it seems to be more appropriate to use, for instance, the diameter measured at 10% of the peak intensity ($d_{10\%}$) or the *50% encircled-energy diameter* ($d_{50\%\,\mathrm{EED}}$). For example, at $\lambda = 2.1661\,\mu$m we obtain $d_{10\%} = 9.39$ mas and $d_{50\%\,\mathrm{EED}} = 9.58$ mas, while for the continuum at $2.174\,\mu$m we find $d_{10\%} = 5.15$ mas and $d_{50\%\,\mathrm{EED}} = 4.23$ mas. Thus, based on $d_{50\%\,\mathrm{EED}}$, η Car appears ~ 2.2 times larger at $\lambda = 2.1661\,\mu$m compared to the continuum at $\lambda = 2.174\,\mu$m. The best-fit model diameters at the other wavelengths are listed in Table 2. The errors of the diameter measurements are $\pm$4% for the two continuum diameters and $\pm$10% for the line diameters, derived from the visibility errors and the uncertainty of the fitting procedure.

Table 9.2: Diameters obtained by fitting Hillier et al. (2001) model visibilities to the measured AMBER visibilities. Errors are $\pm$4% for the diameters in the continuum and $\pm$10% in the lines (see text).

Spectral region	Wavelength [μm]	d_{FWHM} [mas]	$d_{10\%}$ [mas]	$d_{50\%\,\mathrm{EED}}$ [mas]
continuum	2.0400	2.27	4.85	3.74
continuum	2.1740	2.33	5.15	4.23
Brγ (center)	2.1661	1.83	9.39	9.58
Brγ (blue wing)	2.1635	9.52	16.46	9.60
Brγ (red wing)	2.1669	2.02	9.61	9.78
He I (absorption)	2.0560	4.24	8.22	5.36
He I (emission)	2.0580	4.19	4.30	6.53

d_{FWHM} = FWHM diameter,
$d_{10\%}$ = diameter measured at 10% peak intensity,
$d_{50\%\,\mathrm{EED}}$ = 50% encircled-energy diameter.

9.4.2 Continuum visibilities

9.4.2.1 Comparison of the continuum visibilities with the Hillier et al. (2001) model predictions

The comparison of the AMBER *continuum* visibilities with the NLTE model from Hillier et al. (2001, 2006) is shown in the two upper left panels of Fig. 9.7 for the continuum near the He I 2.059 μm and Brγ 2.166 μm emission lines (the exact wavelengths are described in Fig. 6). Taking a slight rescaling into account, we concluded in the previous section that, based on the NLTE model from Hillier et al. (2001) and the AMBER measurements, the apparent 50% encircled-energy diameters $d_{50\%\,\mathrm{EED}}$ of η Car in the K-band continuum at $\lambda = 2.040\,\mu$m and $2.174\,\mu$m are 3.74 mas and 4.23 mas, respectively (see Table 2). These diameters are in good agreement with the 50% encircled-energy K-band diameter of 5 mas

reported by van Boekel et al. (2003).

For comparison, we also fitted the AMBER visibilities with simple analytical models such as Gaussian profiles, as described in more detail in Sect. 9.7 in the Appendix. From a Gaussian fit of the AMBER visibilities, we obtain a FWHM diameter of $d_{\rm Gauss} \sim 4.0 \pm 0.2$ mas in the K-band continuum. As outlined in Sect. 9.7, the diameter value strongly depends on the range of projected baselines used for the fit, since a Gaussian without an additional background component is not a good representation of the visibility measured with AMBER. As discussed in Appendix 9.7, using a Gaussian fit with a fully resolved background component as a free parameter results in a best fit with a 30% background flux contribution (see also Petrov et al. 2006a).

9.4.2.2 Comparison of the VINCI and AMBER continuum visibilities

In Fig. 9.7 (left, second row) displaying the averaged Brγ continuum data, the visibilities of η Car obtained with VLTI/VINCI are shown in addition to the AMBER data. These VINCI measurements were carried out in 2002 and 2003 using the 35 cm test siderostats at the VLTI with baselines ranging from 8 to 62 m (for details, see van Boekel et al. 2003). Like AMBER, VINCI is a single-mode fiber instrument. Therefore, its field-of-view is approximately equal to the Airy disk of the telescope aperture on the sky, which is $\sim 1\farcs4$ in the case of the siderostats. From the VINCI measurements and using only the 24 m baseline data, van Boekel et al. (2003) derived a FWHM Gaussian diameter of $d_{\rm Gauss} \sim 7$ mas for the wind region of η Car. At first glance, this diameter measurement seems to contradict the $d_{\rm Gauss} \sim 4.0$ mas FWHM diameter derived from the AMBER data. This is not the case, however, since the diameter fit is very sensitive to the baseline (or spatial frequency) fit range, because a Gaussian is not a good representation of the visibility curve at all, as can be seen in Fig. 9.15. If only the VINCI data points are fitted, which have spatial frequencies < 60 cycles/arcsec (corresponding to projected baselines < 28 m), $d_{\rm Gauss} \sim 7$ mas provides the best fit. On the other hand, if the data point at 136 cycles/arcsec (corresponding to a projected baseline of ~ 62 m) is included in the fit, we obtain $d_{\rm Gauss} \sim 4.3$ mas (see also the discussion Sect. 9.7). Thus, when using comparable baseline ranges for the Gaussian fits, there is good agreement between the AMBER and VINCI measurements.

To account for the background contamination of the VINCI data caused by nebulosity within VINCI's large $1\farcs4$ field-of-view (in which, for instance, all speckle objects B, C, and D are located), van Boekel et al. introduced a background component (derived from NACO data) providing 55% of the total flux. Adding this background component to the model of Hillier et al. (2001), they found a good match between the model and the observations. Since our AMBER observations were carried out with the 8.2 m Unit Telescopes of the VLTI, the field-of-view of the AMBER observations was only $\sim$60 mas. Thus, the background contamination of the AMBER data can be expected to be much weaker, if not negligible, compared to the VINCI measurements. To check this, we first performed a fit of the Hillier et al. (2001)

model, which not only contains the size scaling as a free parameter, but also a fully resolved background component. As we expected, we found the best fit (smallest χ^2) with no background contamination. [1] Therefore, when we finally compared the AMBER observations with the model from Hillier et al. (2001), we did not introduce a background component. In Fig. 9.7 (second row, left) we plot both the AMBER visibilities (no background correction required) plus the background-corrected VINCI data (assuming a 55% background contribution; blue triangles). As can be seen from the figure, these VINCI points nicely match the AMBER data and the corresponding fit of the NLTE model from Hillier et al. (2001). Therefore, from the analysis of the continuum data, we can conclude that the background contamination in the AMBER measurements is negligible and that the AMBER measurements are in good agreement with both the previous VINCI measurements and the model predictions from Hillier et al. (2001).

9.4.3 Elongated shape of the continuum intensity distribution

To look for detectable elongations of the continuum intensity distribution, we fitted an elliptically stretched 2-D version of the radiative transfer model visibilities from Hillier et al. (2001) to the measured visibilities. Our best χ^2 fit reveals a projected axis ratio of $\xi = 1.18 \pm 0.10$ and PA $= 120 \pm 15°$. Comparison with the results found by van Boekel et al. (2003) shows that the projected axis ratio ξ derived from the AMBER data is in basic agreement with the K-broad-band values of $\xi = 1.25 \pm 0.05$ and PA $= 138 \pm 7°$ from van Boekel et al. (2003).

We also studied the elongation inside the Brγ emission line at $\lambda = 2.166\,\mu$m, following the same procedure as in the continuum; i.e., we fitted an elliptically stretched 2-D version of the Hillier et al. model shown in Fig. 9.7 to the AMBER data. However, since the global shape of the model function at $\lambda = 2.166\,\mu$m shows stronger deviations from the measurements than in the continuum, the elongation determination suffers from larger uncertainties, resulting in large error bars of the fit parameters. For instance, for $\lambda = 2.166\,\mu$m we obtained $\xi = 1.66 \pm 0.60$ and PA=$81 \pm 40°$ from the best ellipse fit.

The 2-D ellipse fitting was also performed for the continuum near the He I emission line and in the center of the He I line ($\lambda = 2.057\,\mu$m), where our model fits give an axis ratio of $\xi = 1.35 \pm 0.30$ and a PA of the major axis of $98 \pm 40°$ in the continuum, and $\xi = 1.74 \pm 0.60$ and PA = $159 \pm 40°$ in the center of the He I emission line. It should be noted that for the He I line region, only four visibility points are available, covering the small PA range of only 60°. Because of this limited number of data points and the small PA coverage, we conclude that the He I elongation measurements in the continuum as well as the line region are not reliable and abandoned in the further elongation analysis of the He I data.

[1] An additional argument in favor of only a very faint background contribution in the AMBER UT observation can be found in the shape of the high spectral resolution line: the light from the speckle objects B, C, and D is produced in areas with velocities smaller than 50 km/s. Therefore, it produces a narrow emission line which should appear in the center of the broad Brγ line. Just looking at the shape of the line, it can be concluded that such an effect is negligible.

From the *K*-band VINCI data, van Boekel et al. (2003) derived a PA of $138 \pm 7^\circ$ for the major axis, very well aligned with the Homunculus (132°, Davidson et al. 2001) and in agreement with our results (PA $= 120 \pm 15^\circ$). Van Boekel's and our continuum elongation measurements favor the physical model according to which η Car exhibits an enhanced mass loss in polar direction as proposed, for instance, by Owocki et al. (1996, 1998) or Maeder & Desjacques (2001) for stars rotating close to their critical rotation speed. Axis ratios of the order of 1.2 appear reasonable in the context of such polar-wind models. Suppose, for example, that the wind's polar/equatorial density ratio is 2 at any given radius r, as reported by Smith et al. (2003) to explain latitude-dependent changes in the Balmer line profiles. Relevant absorption and scattering coefficients have radial dependencies between $n_e \sim r^{-2}$ (Thomson scattering) and $n_e^2 \sim r^{-4}$ (most forms of thermal absorption and emission). A meridional map of projected optical thickness through the wind would show cross-sections of prolate spheroids, correlated with the appearance of the configuration. With the radial dependencies and polar/equatorial density ratio mentioned above, these spheroids have axial ratios between about 1.2 and 1.4; i.e., appreciably less than 2. Viewed from an inclination angle $i \approx 45^\circ$(Davidson et al. 2001), the apparent (projected) axis ratios are between 1.1 and 1.2. This is merely one example, and we have omitted many details, but it illustrates that the polar/equatorial density ratio is around 2, in agreement with Smith et al. (2003).

Finally, Smith et al. (2003) suggested that the stellar wind should become basically spherical during an event at periastron. This prediction can be tested if VLTI/AMBER data are obtained at the next periastron passage.

9.4.4 Continuum-corrected visibilities

9.4.4.1 Continuum-corrected visibility in the Brγ emission line

To investigate the brightness distribution in the Brγ line in more detail, we tried to disentangle the continuum and pure line emission from both the AMBER data as well as the model data to derive the size of the pure Brγ line-emitting region. Since the visibility measured inside an emission or absorption line is the composite of a pure line component and an underlying continuum, the measured line visibility, $V_{\rm tot}$ (see Fig. 9.8 top), has to be corrected for the continuum contribution to obtain the visibility $V_{\rm line}$ of the line emitting (absorbing) region. As discussed in Malbet et al. (2006b), $V_{\rm line}$ can be calculated if the continuum level within the line is known. If the continuum within the line is equal to the continuum level outside the line for an optically thin environment, as assumed in Fig. 9.8, we obtain:

$$V_{\rm line} = \frac{V_{\rm tot} \cdot F_{\rm tot} - V_{\rm cont} \cdot F_{\rm cont}}{F_{\rm line}} \tag{9.1}$$

with $F_{\rm tot} = F_{\rm cont} + F_{\rm line}$ being the total measured flux and $V_{\rm tot}$ being the measured visibility (also see Fig. 9.8 top for illustration). As outlined in the Appendix, taking a non-zero differential phase Φ' into

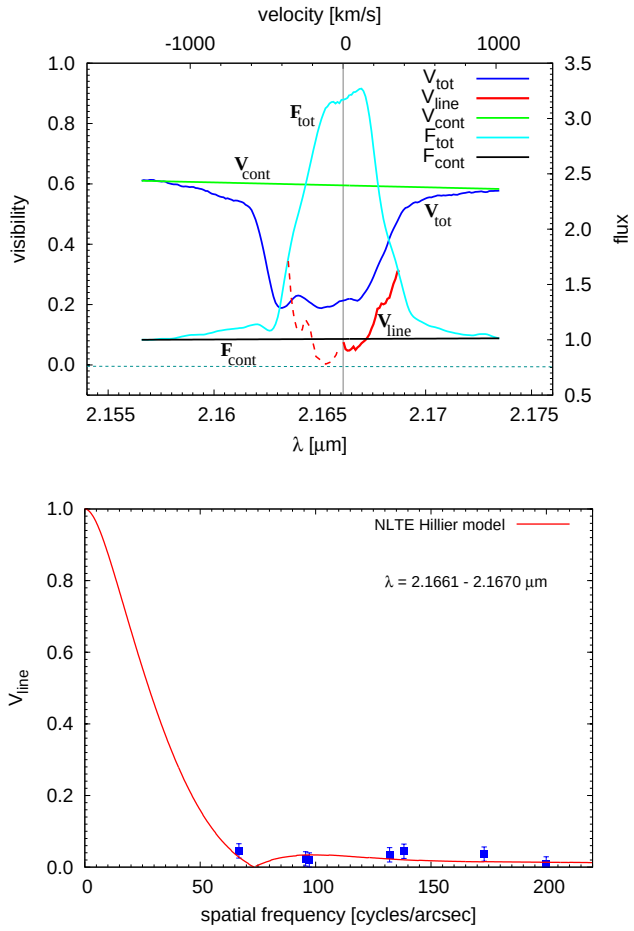

Figure 9.8: *Left, top*: The solid and dashed red lines show the continuum-corrected visibility inside the Brγ line of the HR measurement with the shortest projected baseline (29 m). The continuum correction follows Eq. (9.2). Except for the phase, all quantities entering Eq. (9.2) are indicated in the figure. We assume $F_{\rm tot} = F_{\rm cont} + F_{\rm line}$ and that $F_{\rm cont}$ inside the line is approximately equal to the level outside the line. The continuum-corrected visibility in the blue-shifted region of the emission line is shown with a dashed line since it is highly uncertain due to the presence of the P Cygni-like absorption component (see text for details). *Left, bottom*: Continuum-corrected AMBER visibilities (filled blue squares) in the red region of the Brγ line as a function of spatial frequency. To derive the visibilities according to Eq. (9.2), the data in the wavelength range 2.1661–2.1670 μm (red-shifted line region) were averaged before the continuum correction. The solid red line shows the continuum-corrected model visibility. Obviously, observations at shorter baselines are needed to further test the model predictions.

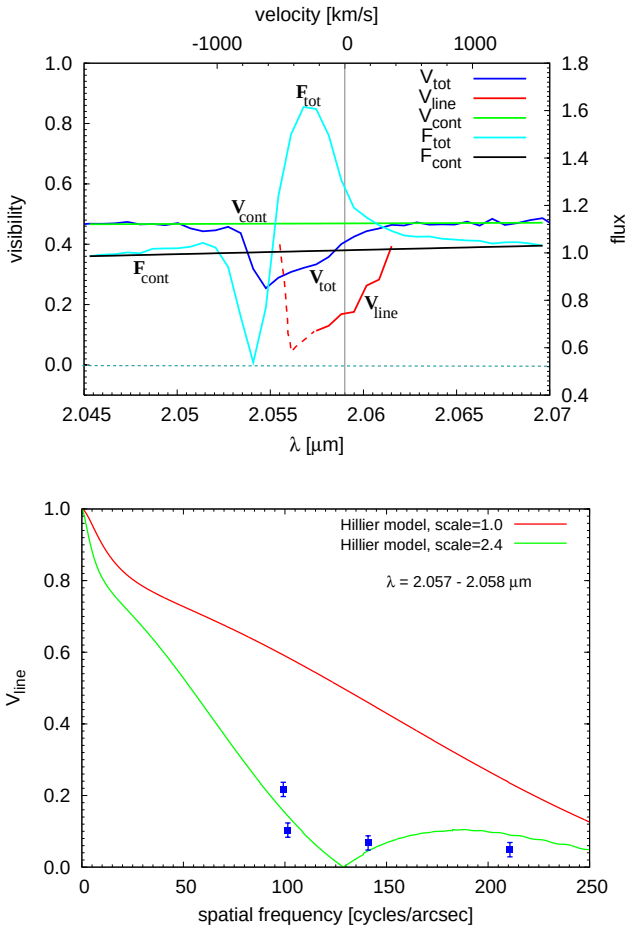

Figure 9.9: Visibility in the He I line. *Right, top*: The figure is similar to Fig. 9.8 (top) but displays the MR-2004-12-26 data with the shortest projected baseline (43m). As in the case of the Brγ emission, the figure reveals that the region dominated by line emission is fully resolved by the AMBER measurements. As in Fig. 9.8 (top), the continuum-corrected visibility is shown with a dashed line in the blue-shifted region of the emission line to indicate that in this region, the line visibility is highly uncertain due to the presence of the P Cygni absorption. *Right, bottom*: Continuum-corrected AMBER visibilities (filled blue squares) in the red region of the He I emission line as a function of spatial frequency and continuum-corrected visibility curve (solid red line) according to the NLTE model of Hillier et al. (2001). To derive the visibilities according to Eq. (9.2), the data in the wavelength range 2.057–2.058 μm were averaged before the continuum correction. The model curve predicts much larger visibility values in the line, which indicates that the size of the line-emitting region in the model is probably underestimated by the model. A rescaling of the size of the model by a factor of $\sim$2.3 (green line) reveals better agreement with the AMBER measurements.

account introduces an additional term in Eq. (9.1), leading to

$$V_{\rm line} = \frac{\sqrt{|V_{\rm tot}F_{\rm tot}|^2 + |V_{\rm cont}F_{\rm cont}|^2 - 2V_{\rm tot}F_{\rm tot}V_{\rm cont}F_{\rm cont} \cdot \cos\Phi'}}{F_{\rm line}} \tag{9.2}$$

We applied Eq. (9.2) to the line-dominated AMBER data in the 2.155-2.175 μm Brγ wavelength range to derive the continuum-corrected visibility of the region emitting the Brγ line radiation. One *big uncertainty* in this correction is the unknown continuum flux within the line. Due to intrinsic absorption, the continuum flux might be considerably lower within the line than measured at wavelengths outside the line. Especially the blue-shifted wing of the Brγ emission line might be affected by the P Cygni-like absorption, as discussed below. In case such an absorption component is present, our continuum-correction would overestimate the size of the line-emitting region. The influence of this effect on the red-shifted wing of the line is likely to be much smaller, as P Cygni-like absorption mainly affects the blue-shifted emission.

The visibility across the Brγ line is shown in Fig. 9.8 (top) for the HR data corresponding to the shortest projected baseline. The results for the other data sets are similar. From Fig. 9.8 (top), one can see that after the subtraction of a continuum contribution equal to the continuum outside the line, the visibility reaches very small values in the center of the emission line. This means that the pure line-emitting region is much larger than the region providing the continuum flux.

Fig. 9.8 (top) shows a strong *asymmetry* between the blue- and red-shifted part of the visibility in the line with respect to the spectrum. While the visibility ($V_{\rm tot}$ as well as $V_{\rm line}$) rises concomitantly with the drop of the line flux on the red side, the situation is very different on the blue side line center. In agreement with the model predictions from Hillier et al. (2001), this indicates the existence of a P Cygni-like absorption component in this wavelength region. In fact, at $\lambda = 2.1625\,\mu$m, we see a small dip in the Brγ spectrum in both the model spectrum from Hillier et al. (2001) and the HR AMBER observations. If such an absorption component is present, it can explain the asymmetric behaviour of the line visibility with respect to the spectrum. The P Cygni absorption in the blue wing of the Brγ line makes the continuum correction of the visibility uncertain for wavelengths shorter than the central wavelength $\lambda_{\rm c}$ of the emission line. Because of this uncertainty, in Fig. 9.8 (top) the continuum corrected visibility is shown with a dashed line for $\lambda < \lambda_{\rm c}$, and the following discussion is restricted to the red-shifted region of the Brγ line emission.

The continuum-corrected AMBER visibilities in the red-shifted region of the Brγ line are displayed in Fig. 9.8 (bottom) for all data sets. To derive the visibilities in the red region, the data in the wavelength range 2.1661–2.1670 μm were averaged before the continuum correction. To now compare the continuum-corrected AMBER visibilities with the model predictions (2.1661–2.1670 μm), we constructed a model intensity profile of the pure Brγ emission line region by subtracting the Hillier et al. intensity profile of the nearby continuum from the combined line + continuum profile.

As Fig. 9.8 illustrates, the model prediction is in agreement with the low visibilities found for spatial frequencies beyond 60 cycles/arcsec. On the other hand, the figure also clearly indicates that measurements at smaller projected baselines are needed to further constrain the Hillier et al. model in the line-emitting region. With the baseline coverage provided by the current AMBER measurements, we obtain a FWHM diameter of $\gtrsim$ 15.4 mas (lower limit) for the (continuum-corrected) line-emitting region in the red line wing.

9.4.4.2 Continuum-corrected visibility in the He I emission line

As can be seen in Fig. 9.5, the AMBER spectrum of the He I line shows a P Cygni-like profile with a prominent absorption and emission component. This is in agreement with earlier findings by Smith (2002) from long-slit spectroscopy using OSIRIS on the CTIO 4m telescope.

To estimate the spatial scale of the region emitting the He I emission line, we followed the same approach as outlined in the previous section for the Brγ line; i.e., we first applied Eq. (9.2) and then compared the continuum-corrected visibility with the continuum-corrected radiative transfer model of Hillier et al. (2001). Figure 9.9 (top) shows the measured flux and visibility for the MR-2004-12-26 measurement with the shortest projected baseline (43m) as well as the continuum-corrected visibility across the He I emission component (solid red line). Because of the P Cygni-like absorption component, the continuum subtraction is highly uncertain in the blue region of the emission line (dashed red line in Fig. 9.9), as already discussed in the context of the Brγ line in Sect. 9.4.4.1.

In Fig. 9.9 (bottom), the continuum-corrected visibility of all AMBER data in the red region of the He I emission line (averaged over the wavelength range 2.057–2.058 μm) is shown as a function of spatial frequency. As the figure reveals, similar to the Brγ emission, the visibilities inside the He I emission line region reach rather low values. As the comparison shows, the line visibilities predicted by the model are much higher than the line visibilities measured with AMBER, indicating that the size of the line-emitting region in the model is too small. Rescaling of the model size by a factor of 2.4 results in a much better agreement between the model and observations (green curve in Fig. 9.9, bottom) and a FWHM diameter of $\gtrsim$ 8.2 mas, which is 3.6 times larger than the FWHM diameter of 2.3 mas in the continuum. Due to the lack of interferometric data at small projected baselines, this value can only give a rough lower limit of the size.

The results for the visibility inside the He I line can possibly be explained in a qualitative way in the framework of the binary model for the central object in η Car (e.g. Davidson et al. 1999; Davidson 2001; Pittard & Corcoran 2002; Hillier et al. 2006; Nielsen et al. 2006). In a model of this type, He I emission should arise near the wind-wind interaction zone between the binary components. The hot secondary star is expected to ionize helium in a zone in the dense primary wind, adjoining the wind-

wind interaction region. Such a region can produce He I recombination emission.[2] The wind-wind shocked gas, by contrast, is too hot for this purpose, while the density of the fast secondary wind is too low. Since the AMBER measurements (Dec. 2004 and Feb. 2005, at orbital phases $\phi = 0.268$ and $\phi = 0.299$, see Table 9.1) were obtained at an intermediate phase between periastron in July 2003 and apoastron in April 2006, the extension of the He I emission zone is expected to be rather diffuse and larger than the continuum size. In other words, the He I emission zone should be fairly extended and larger than the Hillier et al. model prediction, which is in agreement with the AMBER data.

9.4.5 Differential Phases and Closure Phases

The measurement of phase information is essential for the reconstruction of images from interferometric data, but such an image reconstruction is only possible with an appropriate coverage of the *uv*-plane. Nevertheless, even single phase measurements, in particular of the closure phase and differential phase, provide important information.

The closure phase (CP) is an excellent measure for asymmetries in the object brightness distribution. In our AMBER measurements, as illustrated in Figs. 9.3 and 9.5, we find that the CP in the *continuum* is zero within the errors for all the various projected baselines of the UT2-UT3-UT4 baseline triplet, indicating a point-symmetric continuum object. However, in the line emission, we detect a non-zero CP signal in all data sets. In both MR measurements covering the Brγ line, we find the strongest CP signal in the blue wing of the emission line at $\lambda = 2.164\,\mu$m (-34° and -20°) and a slightly weaker CP signal in the red wing of the emission line at $\lambda = 2.167\,\mu$m (+12° and +18°). We also detected non-zero CP signals in the HR measurement around Brγ taken at a different epoch. In the case of the He I line, a non-zero CP could only be detected at $\lambda = 2.055\,\mu$m, just in the middle between the emission and absorption part of the P Cygni line profile.

The differential phase (DP) at a certain wavelength bin is measured relative to the phase at all wavelength bins. Therefore, the DP measured within a wavelength bin containing line emission yields approximately the Fourier phase of the combined object (continuum plus line emission) measured relative to the continuum. This Fourier phase might contain contributions from both the object phase of the combined object and a shift phase, which corresponds to the shift of the photocenter of the combined object relative to the photocenter of the continuum object. Significant non-zero DPs were detected in the Doppler-broadened line wings of the Brγ line. Particularly within the blue-shifted wings, we found a strong signal (up to $\sim -60°$), whereas the signals are much weaker within the red-shifted line wings. These DPs might correspond to small photocenter shifts, possibly arising if the outer Brγ wind region consists of many clumps which are distributed asymmetrically. The small differential phases of up to

[2] For a qualitative sketch of the geometry, see "zone 4" in Figure 8 of Martin et al. (2006), even though this figure was drawn to represent He^{++} in a different context. For reasonable densities, the predicted He^{+} zone has a quasi-paraboloidal morphology. In addition, some extremely dense cooled gas, labeled "zone 6" in the same figure, may also produce He I emission.

$\sim -15°$ for the different baselines of the blue-shifted light in the He I line can perhaps also be explained by the above-mentioned asymmetries or within the framework of the binary model discussed in previous sections. In the binary model, a large fraction of the He I is possibly emitted from the wind-wind collision zone, which is located between the primary and the secondary (Davidson et al. 1999; Davidson 2001; Pittard & Corcoran 2002; Hillier et al. 2006; Nielsen et al. 2006).

9.4.6 Modeling with an inclined aspherical wind geometry

The goal of the modeling presented in this section is to find a model which is able to explain several remarkable features in our data; in particular, *(a)* the asymmetry in the Brγ line profile (showing less emission in the blue-shifted wing than in the red-shifted wing) and the P Cygni-like absorption dip in the blue-shifted Brγ wing, *(b)* the strong DP in the blue-shifted wing and a weaker DP signal in the red-shifted wing, and *(c)* the structure of the CP, showing a change in the sign between the blue- and red-shifted line wing. We aimed for a geometrical but physically motivated model which would reproduce these features at all wavelength channels simultaneously. For this, we concentrate on the Brγ line, as this line shows a stronger phase signal than the He I line and was measured with a better *uv*-coverage.

As Smith et al. (2003) convincingly showed, the stellar wind from η Car seems to be strongly latitude-dependent, with the highest mass flux and velocities at the poles. This anisotropy can be understood in the context of theoretical models (see, e.g., Maeder & Desjacques 2001), which take the higher temperatures at the poles ($g_{\rm eff}$-effect) and the equatorial gravity darkening on a rapidly rotating star into account (*von Zeipel* effect, Zeipel 1925). As these models are quite successful in explaining the bipolar structure of the Homunculus nebula, we investigated whether such bipolar geometries with a latitude-dependent velocity distribution might also be suited to explain our interferometric data.

Due to its success in reproducing both the spectrum and the measured visibilities, we based our wind model on the spherical Hillier et al. (2001) model and superposed a weak aspherical stellar wind geometry, which is inclined with respect to the line-of-sight. Our model includes three components (see Fig. 9.10); namely,

(1) a continuum component (using the Hillier et al. continuum CLV, see Fig. 9.7 top) with a blue-shifted absorption component,

(2) a spherical stellar wind (using the Hillier et al. continuum-subtracted Brγ CLV), and

(3) an aspherical wind geometry, represented by a $41°$ inclined ellipsoid.

The relative contribution of these different constituents to the total flux is given by the input spectra shown in the upper row of Fig. 9.11. For the spherical and aspherical wind component, we assume Gaussian-shaped spectra. The original Hillier et al. CLVs slightly underestimate the size of the observed

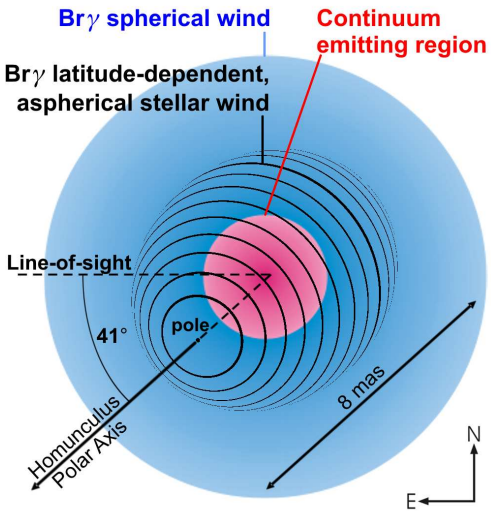

Figure 9.10: *Left:* Illustration of the components of our geometric model for an optically thick, latitude-dependent wind (see text for details). For the weak aspherical wind component, we draw the lines of latitudes to illustrate the 3D-orientation of the ellipsoid. *Below (a, b):* The upper row shows the brightness distribution of the modeled aspherical wind component (item (3) in the text) for two representative wavelengths. The figures below show the total brightness distribution after adding the contributions from the two spherical consituents of our model.

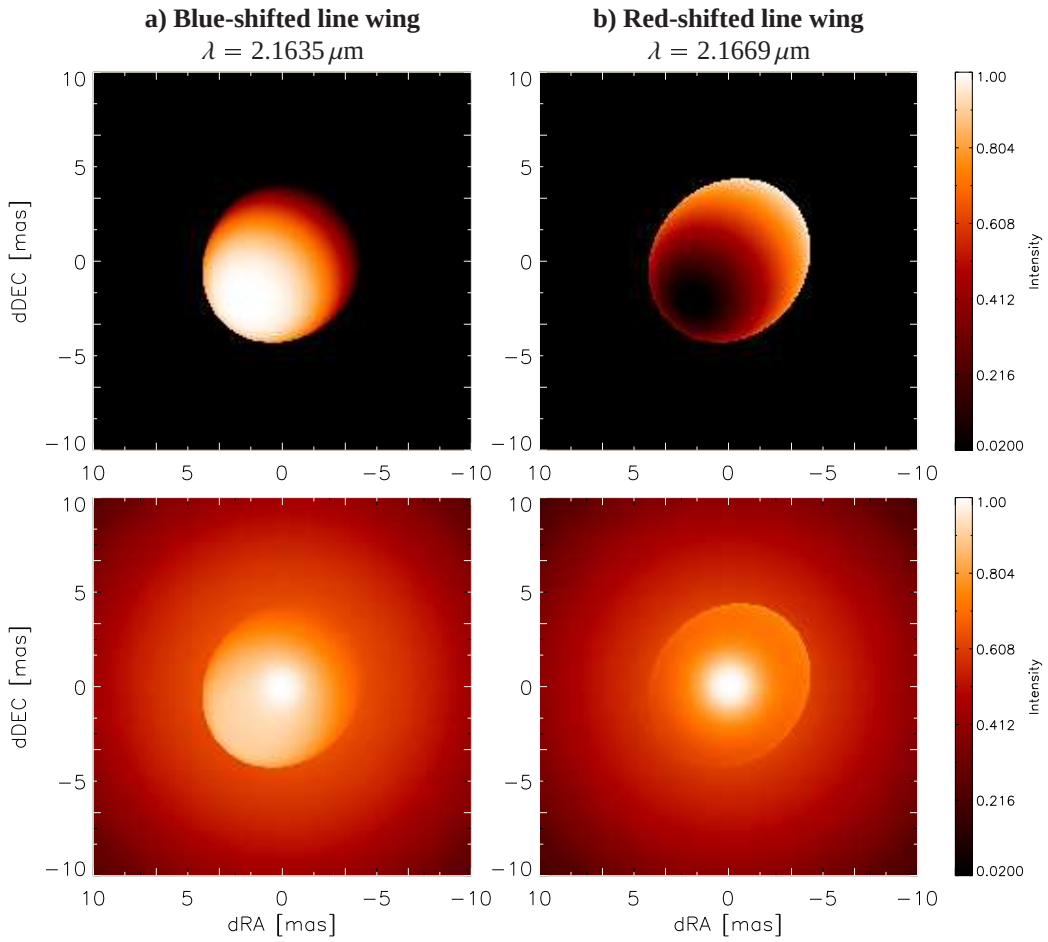

structures (see Fig. 9.6). Therefore, we rescaled them by 10% to obtain a better agreement for the visibilities at continuum wavelengths.

The aspherical wind of η Car is simulated as an ellipsoid with an inclination similar to the inclination angle of the Homunculus (41°, Smith 2006). While the south-eastern pole (which is inclined towards the observer) is in sight, the north-western pole is obscured. The latitude-dependent velocity distribution expected for the η Car wind was included in our model by coupling the latitude-dependent brightness distribution of the ellipsoid to the wind velocity. At the highest *blue-shifted* velocities, mainly the *south-eastern polar region* contributes to the emission (see Fig. 9.10a). In the *red-shifted* line wing, mainly the (obscured) *north-western pole* radiates (see Fig. 9.10b). The axis of the ellipsoid was assumed to be oriented along the Homunculus polar axis (PA 132°, Smith 2006) and its axis ratio was fixed to 1.5.

As our simulations show, such an asymmetric geometry can already explain the measured DPs and CPs with a rather small contribution of the asymmetric structure to the total flux (see black line in Fig. 9.11, upper row). Although the large number of free parameters prevented us from scanning the whole parameter space, we found reasonable agreement with a size of the ellipsoid major axis of 8 mas. Fig. 9.11 shows the spectrum, visibilities, DPs, and CPs computed from the model.

As our model was inspired by physical models, but does not take the complicated radiation transport and hydrodynamics involved in reality into account, we would like to note that our model allows us to check for consistency between the considered geometry and the AMBER spectro-interferometric data, but can neither constrain the precise parameters of a possible aspherical latitude-dependent stellar wind around η Car, nor can it rule out other geometries. We summarize some qualitative properties of our wind model as follows:

- The strong underlying spherical component mainly accounts for the very low visibilities measured within the line.

- The aspherical wind component introduces the asymmetry required to roughly explain the measured phase signals. In particular, it reproduces the larger DPs and CPs within the blue-shifted line wing compared to the red-shifted wing, as the red-shifted emission region is considerably obscured. It also accounts for the flip in the CP sign, as the photocenter of the line emission shifts its location between the blue- and red-shifted wing relative to the continuum photocenter.

- The absorption component which we introduced in the blue-shifted wing of the Brγ line allows us to reproduce the asymmetry measured in the shape of the Brγ emission line profile (showing an increase of flux towards red-shifted wavelengths) and the weak dip observed at far-blue-shifted wavelengths. Furthermore, with the decrease of the continuum contribution, the absorption component helps to lower the visibilities in the blue-shifted line wing, simultaneously increasing the asymmetry in the brightness distribution (increasing the phase signals). Finally, with the interplay

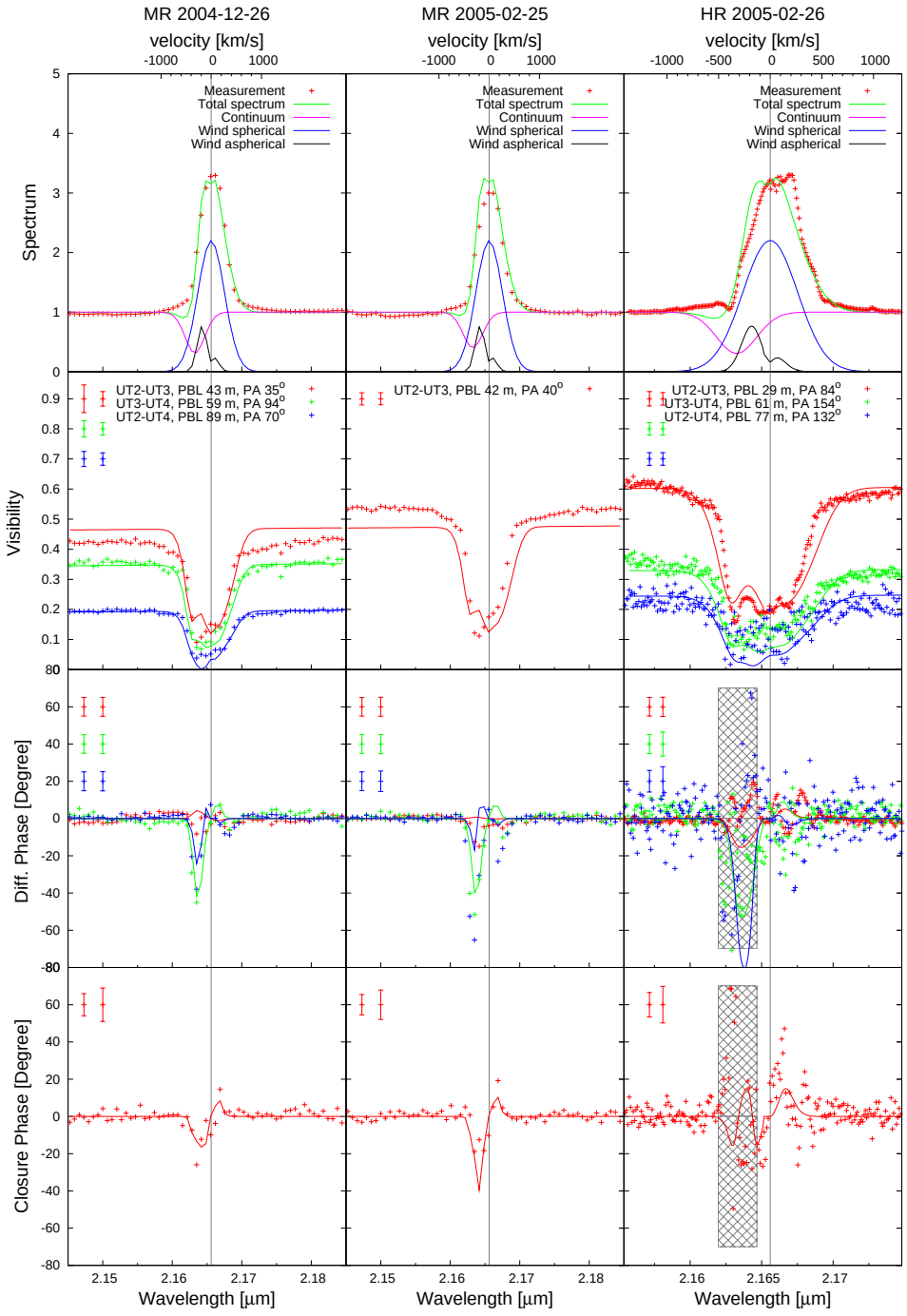

Figure 9.11: Observables computed from our optically thick, latitude-dependent wind model (see Fig. 9.10 for a model illustration). The points (crosses) represent the measurements (as also shown in Fig. 9.3), and the solid lines give the observables computed from our model. The upper row shows the contributions from the various model components to the total flux. Besides the continuum emission (purple line), we introduced a spherical (blue line) and an aspherical (black line) wind component.

between the absorption and emission component, our simulation reproduced a b̈umpïn the visibility similar to the one observed on the shortest baseline of our HR measurement ($\lambda \approx 2.163\mu$m).

9.4.7 Feasibility of the detection of the hypothetical hot companion and the wind-wind interaction zone

One of the most intriguing questions regarding η Car is whether or not its central object is a binary, as suggested to explain cycle (e.g., Damineli 1996).

9.4.7.1 A simple binary continuum model

To investigate whether the AMBER measurements presented here can shed more light on the binarity hypothesis, we used the following approach: We constructed a *simple binary model* consisting of a primary wind component with a CLV according to the continuum model of Hillier et al. (2006; FWHM diameter $\sim$ 2.3 mas; see upper panels in Fig. 9.7) and an unresolved binary companion represented by a point-like source (uniform disk with $\sim$ 0.1 mas FWHM diameter). The secondary component is predicted to be approximately located at PA –36° with a separation of 8 mas from the primary for the time of the AMBER observations (Nielsen et al. 2006). The continuum flux ratio q was treated as a free parameter. We would like to note that in our model, we assumed that all K-band light from the secondary is reaching us unprocessed; i.e. we ignored a possible dilution or re-distribution of the secondary's radiation.

We calculated the 2D visibility function (see Fig. 9.12c) of this model intensity distribution for different values of q, as well as the closure phases for the baselines and PAs corresponding to our AMBER measurements (Fig. 9.12d). Finally, we compared the results with those obtained from a single component model where only the primary wind is present (Fig. 9.12b). The differences of the visibilities and closure phases between the single star and the binary model (at the baselines and PAs corresponding to our AMBER measurements) are displayed in Fig. 9.12d as a function of the K-band flux ratio of the binary components.

Fig. 9.12d shows two interesting results: First, the closure phase is more sensitive to the binary signature than the visibilities and, thus, a more suitable observable to constrain the binary hypothesis. And second, given the accuracies of our first AMBER visibility and closure phase measurements (indicated by the horizontal dashed-dotted lines), we can conclude, for the particular model shown in Fig. 9.12, that the AMBER closure phases put an intensity ratio limit $q_{\rm min} \approx 110$ on the binary K-band flux ratio. This limit is in line with the estimate $q \approx 200$ given by Hillier et al. (2006). Thus, based on the model shown in Fig. 9.12, the AMBER measurements are not in conflict with recent model predictions for the binary.

To investigate whether we can put similar constraints on the minimum K-band flux ratio $q_{\rm min}$ for arbitrary separations and PAs, we calculated a larger grid of binary models and compared the residuals of visibilities and closure phases analogue to the example shown in Fig. 9.12.

For these grid calculations, we used values in the range from 4 to 14 mas for the binary separation with increments of 1 mas, and PAs of the secondary in the whole range from 0° to 360° in steps of 10°. The K-band flux ratio q of the binary components was varied in the range from 1 to 250 with $\Delta q = 4$. As a result of the grid calculation, we obtained the minimum K-band flux ratio $q_{\rm min}$ as a function of binary separation and orientation.

Whereas the study with a fixed companion position presented above allowed us to put rather stringent constraints on $q_{\rm min}$ (see Fig. 9.12), this systematic study revealed that due to the rather poor *uv*-coverage, a few very specific binary parameter sets exist where we are only sensitive to $q_{\rm min} \approx 10$. Nevertheless, for the above-mentioned separation interval (4 to 14 mas), we found that we are able to detect companions up to $q_{\rm min} = 50$ at more than 90% of all PAs. In order to push this sensitivity limit in future observations, a better *uv*-coverage will be required. Together with the expected higher closure phase accuracy, AMBER will be sensitive up to $q > 200$ and, therefore, have the potential to probe the currently favored binary models.

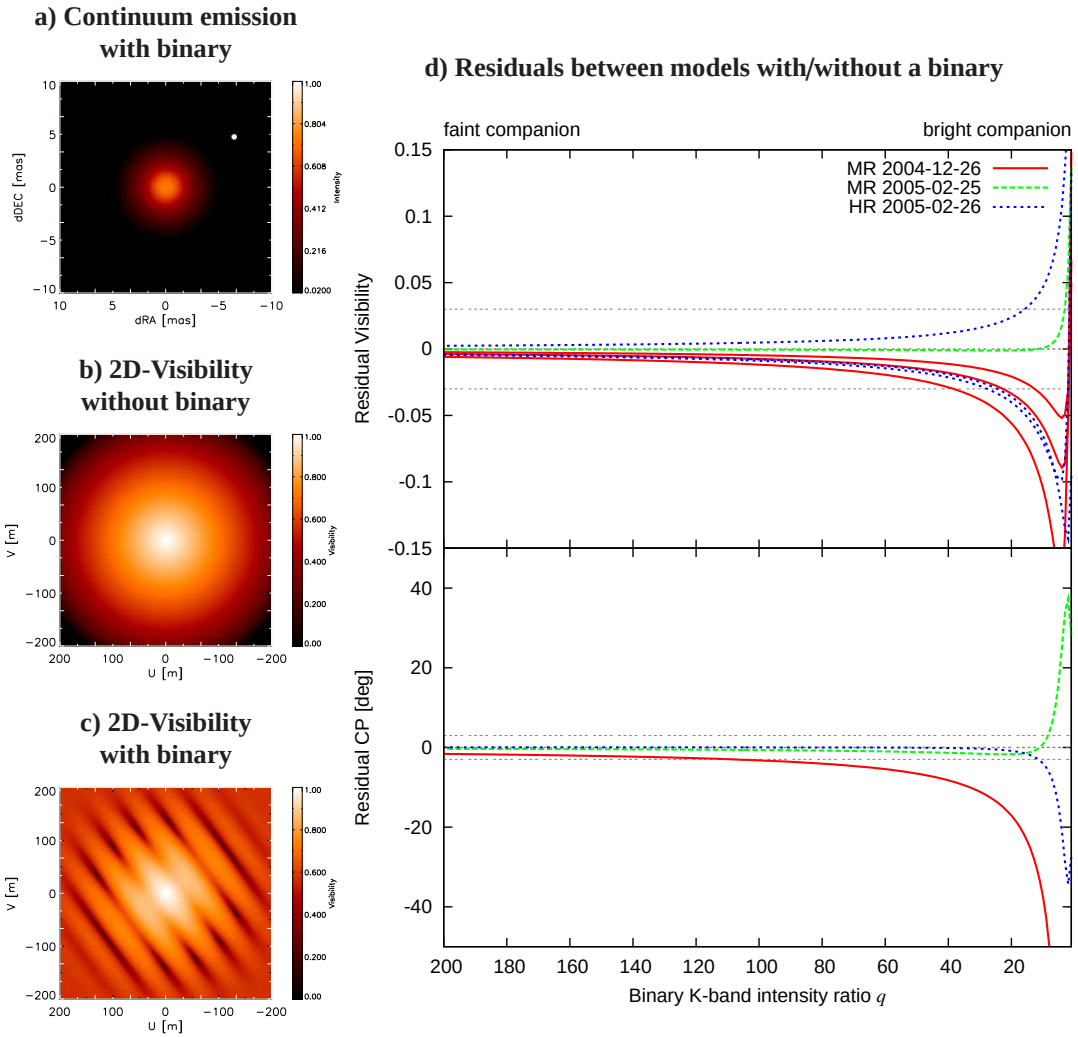

Figure 9.12: Simulation illustrating the signatures of a binary companion at the predicted position (for the orbital phase at the time of our continuum observations around the Brγ line; separation $\sim$ 8 mas, $PA \sim -36^{\circ}$; see Nielsen et al. 2006). For the primary component, we assume a continuum emission CLV from Hillier et al. (2006), to which we add a uniform disk of 0.1 mas diameter to account for the binary companion (see **a**). Figure **b** shows the 2D-visibility function of a single component model containing only the continuum-emitting object with Hillier-type CLV. Figure **c** shows the 2D-visibility corresponding to the binary model shown in panel **a** for a small K-band flux ratio $q = 10$ between the continuum emitting region (Hillier-type CLV) and the companion. In **d** the residuals of the visibilities (upper panel) and closure phases (lower panel) between the models with and without a companion are shown as a function of flux ratio q for baselines and PAs corresponding to the seven AMBER measurements. The dashed horizontal lines indicate the uncertainty of the measurements. Given these uncertainties, the figure illustrates that a companion signature should be visibile from the AMBER closure phase measurements, if the binary is less than $\sim$ 110 times fainter compared to the primary. See text for details.

9.4.7.2 Can AMBER detect a He I wind-wind interaction zone shifted a few mas from the primary wind?

In the context of the binary hypothesis, it is also important to discuss the implications for the interpretation of the AMBER He I measurements. According to the binary model, a large fraction of the He I line emission should arise from the wind-wind collision zone expected between the primary and the secondary (Davidson et al. 1999; Davidson 2001; Hillier et al. 2006; Nielsen et al. 2006). The exact intensity ratio of primary He I wind and He I emission from the wind-wind interaction zone is not known. Figure 9.6 suggests that during the AMBER observations, the total He I flux was roughly two times larger than the model prediction of Hillier et al. (2001) for the primary He I wind.

At the orbital phases of the AMBER measurements, the wind-wind collision zone should be at resolvable distances from η Car's primary (resolution $\sim$ 5 mas; companion separation $\sim$ 8 mas, PA $\sim$–36°, Nielsen et al. 2006). Looking at the AMBER He I data, we see that the differential as well as the closure phases are zero everywhere except for the transition region between the absorption and emission part of the He I line, where we find differential phases of $\sim$ 10–20° and a closure phase of $\sim$–30°; i.e., the phases measured across the He I line are significantly weaker compared to the Brγ line. The question is now, why AMBER measured weaker phase signals within the He I line and if this result is in line with the predictions of the wind-wind collision model.

One possible explanation for the small measured phases could be the orientation of the binary orbit. If the orbit's major axis is nearly aligned with the line-of-sight, the photocenter shift inside the He I line will be very small. In addition, the deviations from point symmetry would be rather small. Therefore, in the case of this special geometry, both differential phases and the closure phase would be small, in qualitative agreement with the AMBER data. Another explanation could be that the contribution of the wind-wind collision zone to the He I line emission is much weaker than that of the primary wind. However, this is not very likely (see Hillier et al. 2006).

A different explanation for the weak phases can be found from a modeling approach similar to the one for the Brγ line region outlined in Sect. 9.4.6. Based on the results presented in Sects. 9.4.1 and 9.4.4.2, we constructed a simple He I model consisting of a spherical primary wind component with a Hillier-type CLV (2.5 mas FWHM diameter) and an extended spherical He I line-emitting region with Gaussian CLV and a 7 mas FWHM diameter (i.e., for simplicity, we assumed that all He I flux is emitted from the wind-wind interaction region; however, some fraction of He I is also emitted from the primary wind; see Hillier et al. 2006 and Fig. 9.6 of the present paper). The center of the line-emitting component of this model is located 3 mas away from the primary wind component towards PA 132°; i.e., in the direction of the Homunculus axis. The spectra of the continuum and line-emitting components were chosen in such a way that the combined spectrum resembles the observed He I line spectrum.

The modeling results show that this simple model is approximately able to simultaneously reproduce

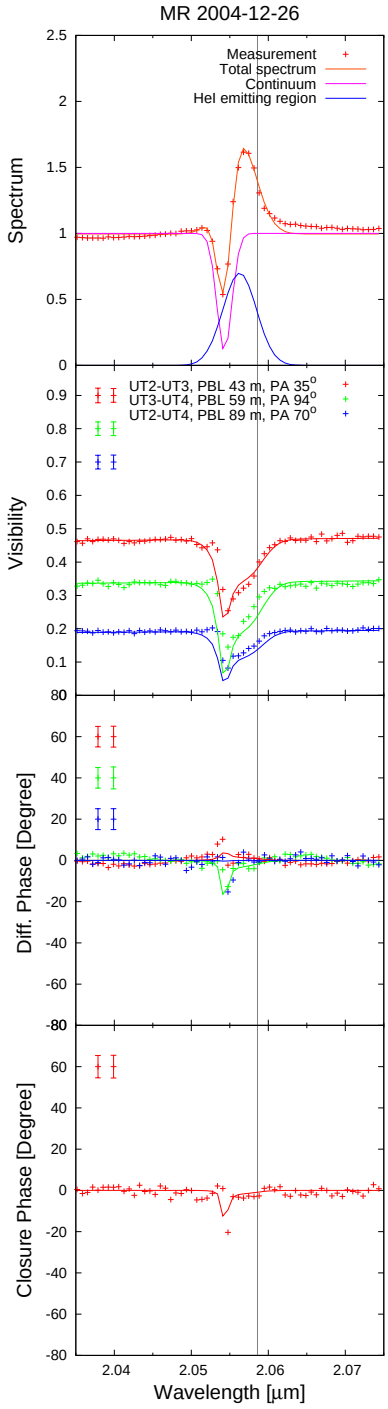

Figure 9.13: Observables computed for our He I line model. For this model we assume beside a Hillier-type CLV for the continuum emission a He I emitting region with Gaussian profile, offset by 3 mas along the Homunculus axis (PA 132°).

the observed spectrum and the wavelength dependence of visibilities, differential phases (10–20°), and closure phases ($\sim$ –30°). Thus, our simple model example illustrates that the AMBER measurements can be understood in the context of a binary model for η Car and the predicted He I wind-wind collision scenario (e.g. Davidson et al. 1999; Davidson 2001; Hillier et al. 2006; Nielsen et al. 2006). We note that the model parameter values given above are of preliminary nature. A more detailed, quantitative modeling is in preparation and will be subject of a forthcoming paper. Furthermore, we would like to emphasize, as already discussed in previous sections, that there are likely to be *three* sources of He I emission - the primary wind, a wind-wind interaction zone (bow shock), and the ionized wind zone caused by the ionization of the secondary. For both the bow shock and the ionized wind zone, the ionizing UV radiation field of the secondary is of crucial importance. On the basis of the observed blue-shift and the weakness of the He I during the event, we believe that the primary wind contribution is small. It is not yet possible to decide on the relative contributions of the bow shock and the ionized wind region.

9.5 Conclusions

In this paper we present the first near-infrared spectro-interferometry of the enigmatic Luminous Blue Variable η Car obtained with AMBER, the 3-telescope beam combiner of ESO's VLTI. In total, three measurements with spectral resolutions of $R = 1\,500$ and $R = 12\,000$ were carried out in Dec. 2004 ($\phi = 0.268$) and Feb. 2005 ($\phi = 0.299$), covering two spectral windows around the He I and Brγ emission lines at $\lambda = 2.059$ and $2.166\,\mu$m, respectively. From the measurements, we obtained spectra, visibilities, differential visibilities, differential phases, and closure phases. From the analysis of the data, we derived the following conclusions:

- In the K-band continuum, we resolved η Car's optically thick wind. From a Gaussian fit of the K-band continuum visibilities in the projected baseline range from 28–89 m, we obtained a FWHM diameter of 4.0 ± 0.2 mas. Taking the different fields-of-view into account, we found good agreement between the AMBER measurements and previous VLTI/VINCI observations of η Car presented by van Boekel et al. (2003).

- When comparing the AMBER *continuum* visibilities with the NLTE radiative transfer model from Hillier et al. (2001), we find very good agreement between the model and observations. The best fit was obtained with a slightly rescaled version of the original Hillier et al. model (rescaling by 1–2%), corresponding to FWHM diameters of 2.27 mas at $\lambda = 2.040\,\mu$m and 2.33 mas at $\lambda = 2.174\,\mu$m.

- If we fit Hillier et al. (2001) model visibilities to the observed AMBER visibilities, we obtain, for

example, 50% encircled-energy diameters of 4.2, 6.5, and 9.6 mas in the 2.17 μm continuum, the He I, and the Brγ emission lines, respectively.

- In the continuum around the Brγ line, we found an asymmetry towards position angle PA=120° $\pm$ 15° with a projected axis ratio of $\xi = 1.18 \pm 0.10$. This result confirms the earlier finding of van Boekel et al. (2003) using VLTI/VINCI and supports theoretical studies which predict an enhanced mass loss in polar direction for massive stars rotating close to their critical rotation rate (e.g. Owocki et al. 1996, 1998).

- For both the Brγ and the He I emission lines, we measured non-zero differential phases and non-zero closure phases within the emission lines, indicating a complex, asymmetric object structure.

- We presented a physically motivated model which shows that the asymmetries (DPs and CPs) measured within the wings of the *Brγ line* are consistent with the geometry expected for an aspherical, latitude-dependent stellar wind. Additional VLTI/AMBER measurements and radiative transfer modeling will be required to determine the precise parameters of such an inclined aspherical wind.

- Using a simple binary model, we finally looked for a possible binary signature in the AMBER closures phases. For separations in the range from 4 to 14 mas and arbitrary PAs, our simple model reveals a minimum *K*-band flux ratio of $\sim$50 with a 90% likelihood.

Our observations demonstrate the potential of VLTI/AMBER observations to unveil new structures of η Car on the scales of milliarcseconds. Repeated observations will allow us to trace changes in observed morphology over η Car's spectroscopic 5.5 yr period, possibly revealing the motion of the wind-wind collision zone as predicted by the η Car binary model. Furthermore, future AMBER observations with higher accuracy might be sensitive enough to directly detect the hypothetical hot companion.

9.6 APPENDIX: Wavelength Calibration

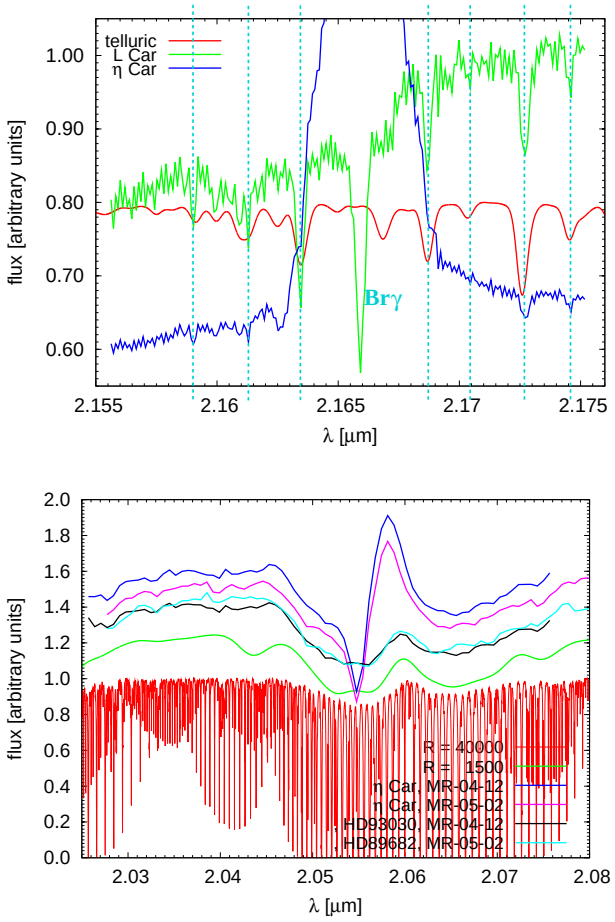

Figure 9.14: *Left, top*: Spectral calibration of the AMBER observations. The figure shows the spectrum of η Car (blue) and the calibrator star L Car (green) around the Brγ line obtained from the HR measurements in Feb. 2005. In addition, a telluric spectrum from the Kitt Peak Observatory is shown in red. The original telluric spectrum with a spectral resolution of $R = 40\,000$ was spectrally convolved to match the resolution of the AMBER measurements. For the flux calibration of the η Car spectrum, the Brγ line in the L Car spectrum was interpolated before the division. See text for further details. *Left, bottom*: Same as top panel, but for both MR measurements around the He I emission line. Together with the η Car spectra, the spectra of the calibrators HD 93030 and HD 89682 are displayed. In addition, the telluric spectrum obtained at Kitt Peak with $R = 40\,000$ and a spectrally convolved telluric spectrum is shown, which matches the spectral resolution of the MR measurements ($R = 1\,500$). The figure illustrates that the forest of telluric lines forms a quasi-continuum which modulates the AMBER spectra.

To obtain both an accurate wavelength calibration of the AMBER raw data and properly calibrated spectra of η Car, we compared the AMBER raw spectra of η Car as well as the calibrator stars L Car, HD 93030, and HD 89682 with a K-band telluric spectrum recorded at the Kitt Peak Observatory with a spectral resolution of 40 000. For the comparison with the AMBER spectrum, this telluric spectrum was spectrally convolved to match the spectral resolution of the AMBER measurements with high ($R \sim 12\,000$) and medium ($R \sim 1\,500$) spectral resolution.

The result of the comparison is shown in Fig. 9.14. In the upper panel, the high spectral resolution AMBER spectra of η Car and the calibrator L Car are shown together with the telluric spectrum with $R = 10\,000$. From the comparison with the telluric spectrum, we identified 7 prominent telluric absorption features in the L Car spectrum, which are indicated by the dashed vertical lines. The strongest absorption line seen in the L Car spectrum is not telluric, but can be identified as intrinsic Brγ absorption in L Car.

Therefore, to properly calibrate the η Car spectrum with the L Car spectrum, we had to interpolate the Brγ line region in the L Car spectrum before dividing the two spectra. From the spectral calibration shown in Fig. 9.14, we estimated a wavelength calibration error of the AMBER data $\Delta\lambda = 3 \times 10^{-4}\,\mu$m

The lower panel in Fig. 9.14 shows the wavelength calibration of the medium spectral resolution data in the wavelength region around the He I line. The figure contains the two η Car MR spectra and the spectra of the two corresponding calibrator stars, HD 93030 and HD 89682, as well as the telluric spectra with spectral resolutions of $R = 40\,000$ and $R = 1\,500$. As the telluric spectra reveal, there is a forest of telluric lines in the spectral region around the He I line. As can be seen in Fig. 9.5, the modulation of the continuum flux introduced by the telluric quasi-continuum cancels out completely when the η Car spectra are divided by the corresponding calibrator spectra, which show no prominent intrinsic line features. Since there are no sharp spectral features in the 2.03–2.08 μm region of either the calibrator or telluric spectras which could be used for the spectral calibration, we estimated a wavelength calibration error $\Delta\lambda = 6 \times 10^{-4}\,\mu$m for the MR He I data. On the other hand, for the MR data around the Brγ line, we found $\Delta\lambda = 4 \times 10^{-4}\,\mu$m.

9.7 APPENDIX: Continuum Uniform Disk and Gauss Diameter Fits

For each spectral channel as well as for an averaged continuum, we performed 1-D fits to the visibility data using simple uniform disk (UD) and Gaussian models. In this step of the analysis, possible asymmetries were ignored and all visibility points at a given wavelength were fitted together, regardless of the position angle of the observations. The results of these 1-D fits are illustrated in the two upper panels of Fig. 9.15 for the averaged continuum data in the wavelength ranges 2.03–2.08 μm and 2.155–2.175 μm, respectively. As the figure reveals, neither a uniform disk nor a single Gaussian provides a good fit to the continuum data. At least, this is true as long as no contamination by a fully resolved background component is taken into account.

The wavelength dependence of the apparent size obtained from the UD and GAUSS model fits for the individual spectral channels is shown in the lower left panel of Fig. 9.15. This panel illustrates that the equivalent UD and GAUSS K-band diameters of η Car derived from the AMBER data are $\sim$4 and $\sim$6.5 mas, respectively.

It should be added here that a good fit of the AMBER data using, for instance, a Gaussian can indeed be obtained when a certain amount of contamination due to a fully resolved background component is taken into account (see also Petrov et al. 2006a). To illustrate that, we performed Gaussian fits to the AMBER data, where we introduced such a fully resolved component as a free fitting parameter. We found that the best Gaussian fit is obtained with a FWHM diameter $d_{\rm Gauss} = 3.01$ mas and a $\sim$ 29%

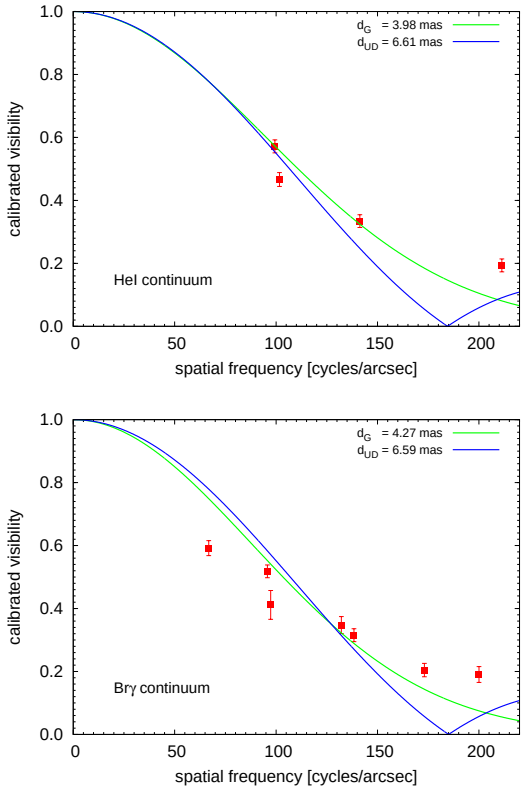

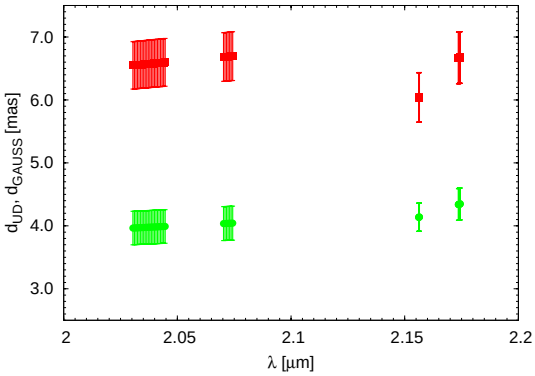

Figure 9.15: 1-D visiblity fits of the AMBER continuum measurements. The two panels to the left show uniform-disk and Gaussian fits for the averaged continuum around the He I and Brγ lines, respectively. As both panels illustrate, neither a uniform disk nor a Gaussian is a good representation of the AMBER measurements. The panel to the top summarizes the fitting attempt for all continuum wavelength channels by displaying the fitted diameters of the UD and GAUSS models as a function of wavelength.

Figure 9.16: Dependence of the Gaussian FWHM diameter on the fit range. The figure shows the background-corrected visibilities obtained with VLTI/VINCI (see van Boekel et al. 2003) as well as Gaussian fits of (a) all four data points (long-dashed green line), (b) only the point with $q = 45$ cycles/arcsec (short-dashed blue), (c) only the point corresponding to the longest baseline (dotted purple), and (d) only the point corresponding to the shortest baseline (dashed-dotted light blue). See the labels for the Gaussian FWHM diameters resulting from the different fits. The figure illustrates that the fitted diameter strongly depends on the spatial frequency range which is used to fit the data. The strong diameter variation (in this case, the diameter changes by a factor of ~ 3) occurs since a Gaussian is not a good representation of the measured visibility function. See text for further discussion.

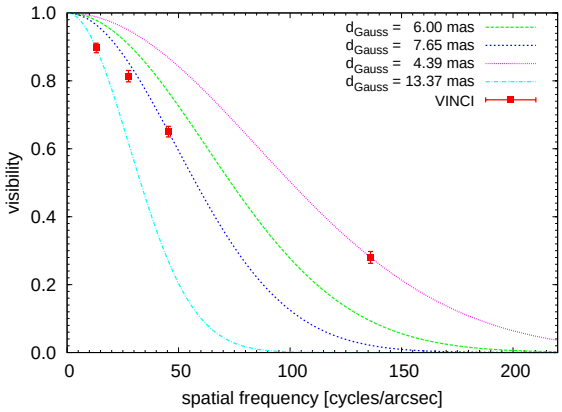

background contamination for the He I continuum region and $d_{\rm Gauss} = 3.32$ mas and a $\sim$ 30% background contamination for the Brγ continuum region. Thus, from this fit we would derive a background contamination which is only $\sim$ 50% smaller than in the VINCI data. We think that such a large amount of background contamination is not very likely given the small AMBER fiber aperture (60 mas) of the 8.2 m telescopes. We think that the large amount of background contamination needed to find a reasonable Gauss fit just reflects the fact that a Gaussian is not appropriate to describe the observations. This is confirmed by the fact that for the fit of the radiative transfer model of Hillier et al. (2001), no background component has to be taken into account to reproduce the AMBER measurements.

We would like to note here that the Gaussian FWHM diameters of typically $\sim$ 4 mas found from the AMBER measurements are not in contrast to the value $d_{\rm Gauss} \sim 7$ mas found by van Boekel et al. (2003) from VLTI/VINCI observations for the following reason: Since a Gaussian is not a good representation of both the VINCI and the AMBER visibilities, the diameter resulting from a Gaussian fit strongly depends on the fit range. This is illustrated in Fig. 9.16 for the four VINCI measurements given in Fig. 1 of van Boekel et al. (2003). As the figure shows, from a Gaussian fit of all four data points, $d_{\rm Gauss} = 6.0$ mas is obtained. If only the data point with $q = 45$ cycles/arcsec is fitted (corresponding to a projected baseline length of $\sim$ 24 m), we get $d_{\rm Gauss} = 7.65$ mas. This is in agreement with the values given in van Boekel et al. (2003) for the elliptical Gaussian fit of the large number of VINCI measurements with a projected baseline of 24 m (see their Fig. 2). On the other hand, if we fit only the VINCI data point corresponding to the longest projected baseline ($q = 136$ cycles/arcsec), a Gaussian fit provides $d_{\rm Gauss} = 4.39$ mas (see Fig. 9.16), which is very close to the diameter we obtain from the AMBER measurements for $\lambda \sim 2.174\,\mu$m ($d_{\rm Gauss} = 4.35$ mas). This is not surprising since the spatial frequency of this VINCI data point agrees with the average spatial frequency of our AMBER observations ($q \sim$50–200 cycles/arcsec). Thus, it can be concluded that good agreement between the Gaussian FWHM diameters derived from the AMBER and VINCI measurements is found if a comparable spatial frequency range is used for the fit.

9.8 APPENDIX: Visibility and Differential Phase of an Emission Line Object

We assume that the target's intensity distribution can be described by two components: the continuum spectrum $o_{\rm cont}(x,y;\lambda)$ and the emission line spectrum $o_{\rm line}(x,y;\lambda)$. In the part of the spectrum containing the emission line, both $o_{\rm cont}$ and $o_{\rm line}$ contribute to the total intensity distribution $o_{\rm tot}$. According to the van-Zittert-Zernike theorem, the Fourier transforms $O_{\rm cont}(B/\lambda)$ and $O_{\rm line}(B/\lambda)$ of $o_{\rm cont}(x,y;\lambda)$ and $o_{\rm line}(x,y;\lambda)$ are measured with an optical long baseline interferometer at wavelength λ and projected baseline vector B. In the following, we assume that all Fourier spectra are normalized to 1 at frequency zero. The complex Fourier spectrum $O_{\rm tot}(B/\lambda)$ of the intensity distribution $o_{\rm tot}$ measured at the emission line $\lambda_{\rm line}$ is given by

$$O_{\rm tot} = \frac{1}{F_{\rm cont} + F_{\rm line}} (F_{\rm cont} \cdot O_{\rm cont} + F_{\rm line} \cdot O_{\rm line}), \tag{9.3}$$

where $F_{\rm cont}$ and $F_{\rm line}$ are the fluxes of the continuum component $o_{\rm cont}$ and the line component $o_{\rm line}$, respectively. In the emission line, the total flux measured is $F_{\rm tot} := F_{\rm cont} + F_{\rm line}$.

From the spectrally dispersed interferometric data, we can derive the differential phase, which is the difference of the Fourier phases of the continuum component $o_{\rm cont}$ and the total intensity $o_{\rm tot}$ in the emission line. The differential phase $\Phi'(B/\lambda_{\rm line})$ in the emission line at $\lambda_{\rm line}$ is given by

$$O_{\rm cont} \cdot O_{\rm tot}^{*} = V_{\rm cont} \cdot V_{\rm tot} \cdot e^{i\Phi'}, \tag{9.4}$$

where $\Phi'(B/\lambda_{\rm line}) := \Phi_{\rm cont}(B/\lambda_{\rm line}) - \Phi_{\rm tot}(B/\lambda_{\rm line})$. $\Phi_{\rm cont}(B/\lambda_{\rm line})$ is the Fourier phase of the continuum component, and $\Phi_{\rm tot}(B/\lambda_{\rm line})$ denotes the Fourier phase of $o_{\rm tot}$ at the position of the emission line $\lambda_{\rm line}$. The asterisk * in this equation denotes conjugate complex operation. $V_{\rm cont}(B/\lambda_{\rm line})$ describes the visibility of the continuum component at the position of the emission line $\lambda_{\rm line}$, and $V_{\rm tot}(B/\lambda_{\rm line})$ is the visibility measured at the position of the emission line $\lambda_{\rm line}$. Inserting Eq. (9.3) into Eq. (9.4) yields

$$V_{\rm cont} \cdot V_{\rm tot} \cdot e^{i\Phi'}$$

$$= \frac{V_{\rm cont}}{F_{\rm cont} + F_{\rm line}} \cdot (F_{\rm cont} V_{\rm cont} + F_{\rm line} V_{\rm line} e^{i\Delta\Phi}), \tag{9.5}$$

where $\Delta\Phi(B/\lambda_{\rm line})$ denotes the difference of the Fourier phases of the continuum and line components; i.e., $\Delta\Phi(B/\lambda_{\rm line}) := \Phi_{\rm cont}(B/\lambda_{\rm line}) - \Phi_{\rm line}(B/\lambda_{\rm line})$. $\Phi_{\rm cont}(B/\lambda_{\rm line})$ and $\Phi_{\rm line}(B/\lambda_{\rm line})$ are the Fourier phases of the continuum and line components, respectively.

In the vector representation of complex numbers, the three quantities $F_{\rm cont}V_{\rm cont}$, $F_{\rm line}V_{\rm line}$, and $F_{\rm tot}V_{\rm tot}$ form a triangle with one corner placed at the center of the coordinate system. According to the law of

cosines, the correlated flux of the line component is given by Eq. (9.2) (see Sect. 9.4.4.1):

$$\begin{aligned} |F_{\rm line}V_{\rm line}|^2 &= |F_{\rm tot}V_{\rm tot}|^2 + |F_{\rm cont}V_{\rm cont}|^2 - \\ &\quad -2\cdot F_{\rm tot}V_{\rm tot}\cdot F_{\rm cont}V_{\rm cont}\cdot\cos(\Phi'). \end{aligned} \tag{9.6}$$

Since the flux $F_{\rm line}$ can be calculated from the measured fluxes $F_{\rm cont}$ and $F_{\rm tot}$, the visibility $V_{\rm line}$ of the line component can be derived using Eq. (9.6).

Applying the law of sines to this triangle in the complex plane yields the differential phase $\Delta\Phi(B/\lambda_{\rm line})$, which is the difference between the Fourier phase $\Phi_{\rm cont}(B/\lambda_{\rm line})$ of the continuum component and the Fourier phase $\Phi_{\rm line}(B/\lambda_{\rm line})$ of the line component:

$$\sin(\Delta\Phi) = \sin(\Phi')\cdot\frac{|F_{\rm tot}V_{\rm tot}|}{|F_{\rm line}V_{\rm line}|}, \tag{9.7}$$

where $\Phi'(B/\lambda_{\rm line})$ is the differential phase measured at the position of the emission line $\lambda_{\rm line}$.

10 Summary and Outlook

As part of my PhD thesis, I have used state-of-the-art infrared interferometric techniques to investigate a selection of massive stars and their circumstellar environment with unprecedented angular resolution. For these studies, the VLTI (AMBER and MIDI) and the IOTA interferometer as well as bispectrum speckle interferometry on 6 m-class telescopes were used. My work included the development of...

- a comprehensive IOTA data reduction software package (Chapter 3).
- an AMBER data processing pipeline which pre-processes AMBER raw data files, reduces them using the *amdlib* consortium software, and post-processes and presents the observables (Chapter 4).

For the astrophysical modeling and interpretation of the obtained data, I have worked on...

- radiative transfer modeling of circumstellar disk and envelope geometries (see Chapter 6). For this purpose, the Monte Carlo radiative transfer code by Keiichi Ohnaka (Ohnaka et al. 2006) was extended to perform an iterative refinement of the dust geometry. Furthermore, the software was embedded in a framework, which allowed us to scan with hundreds of models a wide range of the parameter-space, varying both the complex dust geometry and the dust chemistry.
- the modeling and least-square fitting of spectro-interferometric data, using either radiative transfer images (such as applied for MWC 147, see Chapter 6, and HR 5999, see Preibisch et al. 2006) or geometric, wavelength-dependent models (such as applied for θ^1Ori C, see Chapter 8, and η Car, see Chapter 9).
- the implementation, refinement, and testing of aperture synthesis image reconstruction algorithms (Chapter 5), in particular of the Building Block mapping algorithm developed by Karl-Heinz Hofmann.
- the implementation of sophisticated orbit fitting algorithms, in particular by Docobo (1985, see Section 8.6.1).

In the following, I review the astrophysical results of my PhD work and give an outlook of potential future interferometric investigations on these targets.

10.1 Radiative Transfer Modeling of the Active Accretion Disk around MWC 147

Summary: Herbig AeBe stars provide excellent targets for studying the structure of circumstellar disks and the accretion process. With MWC 147 (spectral type B6), we chose a star in the upper mass range of the Herbig Be class ($M \sim 7\ M_{\odot}$). We obtained VLTI/AMBER and VLTI/MIDI long-baseline interferometric data which was complemented by archival PTI data, resolving the circumstellar environment around MWC 147 on the AU-scale. To also optimally constrain the SED, we used archival high-resolution mid-infrared *Spitzer*/IRS spectroscopy. When applying sophisticated 2-D radiative transfer modeling, we found that the commonly favoured irradiated disk models can easily reproduce the SED of MWC 147, but are in strong conflict with the interferometric data. As this discrepancy could not be resolved by modifying the disk geometry (e.g. including a puffed-up inner rim) nor by varying the disk chemistry, we modified the radiative transfer code to include an actively accreting inner gaseous disk. Using a flared Keplerian disk geometry with an outer radius of 100 AU, an outer envelope, and an inner accretion disk with an mass accretion rate of $1.2 \times 10^{-5} M_{\odot}\mathrm{yr}^{-1}$ resulted in a good fit both to the SED and the NIR and MIR visibilities. Combining this surprising result (obtained from our detailed, physical modeling of the SED and the NIR+MIR interferometric data) with the general trend found by Monnier (2003) in the size-luminosity relation for Herbig AeBe stars might suggest that with increasing mass and stellar luminosity, the NIR emission gets dominated by accretion luminosity originating from an optically thick gaseous disk close to the star.

Outlook: The best-fit geometry which we found with our radiative transfer modeling (including an inner accretion disk and an outer irradiated disk) predicts a distinct visibility profile, especially for higher spatial frequencies. Besides the continuum visibility profile, new observations using VLTI/AMBER (and the VLTI fringe tracker) could separate the accretion and dust emission using spectro-interferometric observation on accretion diagnostic hydrogen recombination (e.g., Brγ) or atomic lines (e.g., Na I, O I, or Ca II).

10.2 Signatures of Outflow Precession from the Young High-Mass Star NGC 7538 IRS1

Summary: Likely at a similar evolutionary stage as MWC 147, but with a spectral type of O7 far more massive ($M \sim 30\ M_{\odot}$), we searched for indications of accretion and outflows around NGC 7538 IRS1 using bispectrum speckle interferometry. Earlier radio VLBI observations had detected a Class II methanol maser feature, which was interpreted as a Keplerian-rotating circumstellar disk, providing indirect evidence for an accretion-based high-mass star formation scenario. However, as an alternative

explanation (and in better agreement with the direction defined by the CO outflow), it has been suggested that the linear alignment and systematic velocity-gradient of the maser feature could trace an outflow cavity. In order to clarify this issue and to resolve the misalignment found between various outflow axes, we imaged the NIR emission with unprecedented resolution, finding a fan-shaped cavity and several blobs of diffuse emission, likely indicating outflow activity from IRS1. Using archival high-sensitivity *Spitzer*-IRAC images, we can trace the same outflow out to large scales, ceasing in a bow-shock-like structure. Although we cannot rule out that the potentially systematic arrangement of the discovered blobs results from the presence of multiple outflows, we employed an analytic flow precession model, as well as a full hydrodynamic simulation, and found that this NIR morphology could also be caused by a precessing outflow originating from a compact disk. As the likely mechanism triggering the potential short period ($\sim$ 280 yrs), wide-angle ($\sim 40^\circ$) precession, we identified tidal interaction with a close (yet undiscovered) companion. Indeed, for the nearby, even more massive protostar NGC 7538 IRS2 (O4.5 type), we discovered a close (195 mas) companion in our speckle images.

Outlook: To achieve further progress on IRS1, higher sensitivity and higher angular resolution imaging (i.e. speckle or AO imaging) of the outflow structures are required. On the scale of several decades, the precession should also become detectable using VLBI imaging of the methanol maser feature. Ultimatively, infrared long-baseline interferometry should also be able to directly detect the putative IRS1 companion star causing the precession, although currently no long-baseline interferometer on the northern hemisphere complies with the technical requirements for such observations.

10.3 Visual/Infrared Interferometry of the Orion Trapezium Stars θ^1Ori C and D

Summary: For the intruiging high-mass star θ^1Ori C, a very close ($\sim$ 30 mas) companion was already discovered in 1997 using speckle interferometry. In order to track its orbital motion, we have monitored the system over the past eight years using speckle interferometry at infrared and visual wavelengths. As the separation of the components already diminished far below the theoretical diffraction-limit of single-dish telescopes, we obtained first long-baseline interferometric observations using the IOTA array. The obtained high-accuracy position measurement allowed us to derive a preliminary orbit solution, from which we identify 53 $M_\odot$ as the most likely value for the dynamical mass of the system. By modeling the wavelength-dependence of the flux ratio between the components (and examining their position in the HR-diagram), we estimate that – in contrast to earlier expectations – the companion is rather massive itself ($M_{C2}/M_{C1} = 0.45 \pm 0.15$). Especially during periastron passage, which we predict will take place in the near future (mid 2007), this might result in strong wind-wind interaction between the two O-stars (O5 and O9.5).

Outlook: Over the last few months, several VLTI/AMBER observations on θ^1Ori C have been obtained, which should allow us to verify the preliminary orbit solution presented in Section 8.6.1. The refined orbit should also result in more precise dynamic masses, which can be used to contrain stellar evolutionary models. Ultimately, AMBER's MR mode might also allow a direct imaging of the geometry of the putative wind-wind interaction region in emission lines.

10.4 Near-Infrared Interferometry of η Carinae using VLTI/AMBER

Summary: η Carinae ($M \sim 100\ M_{\odot}$) is also proposed to be a binary system with a strong wind-wind interaction zone, although this hot-companion scenario is still strongly debated. Using AMBER's medium ($R = 1\,500$) and high spectral resolution mode ($R = 12\,000$), our study on η Car provides a first glimpse into the bright future of NIR spectro-interferometry on spectrally resolved, Doppler-broadened lines. We find (in agreement with earlier studies) that the K-band continuum emission from η Car is dominated by an optically thick wind, resulting in an emission region with 2.3 mas FWHM diameter and a radial intensity profile which follows the predictions from the 1-D line radiative transfer model by Hillier et al. (2001) very well. For the Brγ hydrogen recombination line, we also find remarkable agreement for the line profile as well as for the wavelength-dependence of the measured visibilities. In the wings of the Brγ line, we measure non-zero differential phases and closure phases. As this points towards asymmetries in the brightness distribution and is, therefore, beyond the 1-D approach of the Hillier et al. model, we successfully employ a geometric model of an inclined, aspherical, latitude-dependent stellar wind to reproduce the measured phases. This result strengthens models with enhanced mass loss at the polar regions around rapidly rotating stars, as predicted by Owocki et al. (1996). For the He I line, we find significant deviations between the Hillier et al. predictions and the measured line profiles and visibilities. This, and our modelling of the measured non-zero phase signals, might indicate that the He I line forms in a wind-wind interaction zone, as expected in the context of the hot-companion scenario.

Outlook: As demonstrated with the simulations presented in Section 9.4.7.2, VLTI/AMBER currently seems to be the most powerful instrument to directly detect the proposed hot companion using the continuum closure phase. For this purpose, and to trace temporal variations over the 5.54 yrs period, we have obtained several new VLTI/AMBER observations on η Car within the last year, maybe resulting in a new insight in the process causing the variability. Furthermore, η Car will be a prime target for aperture-synthesis imaging of the putative bow-shaped wind-wind interaction zone or its aspherical stellar wind, yielding mas-resolution NIR images in hundreds of fine-sampled velocity bins; somewhat similar to the well-established *channel maps* in radio astronomy.

10.5 Future Perspectives

From our pioneering studies on a number of key objects (covering a broad range of stellar masses, as well as evolutionary states), I conclude that studies on massive stars might benefit to a dramatical extent, and maybe more than any other field of stellar astrophysics, from the recent advent of infrared interferometry. This is due to the essential need of high angular resolution to study these distant objects and their compact (AU-scale) circumstellar environments, often located in the heart of dense, compact clusters. In addition, during their most enigmatic evolutionary phases (namely the pre- and post-main-sequence phase), these objects are deeply obscured by ambient material, making the infrared the optimal wavelength range for detailed studies. The intriguing phenomena, which can now be studied on massive stars using infrared long-baseline interferometry, include mass accretion processes (e.g. the structure of circumstellar accretion disks), mass ejection and outflow collimation processes (e.g. to reveal the origin and collimation processes of YSO jets), stellar winds (their geometry and kinematics), the geometry of wind-wind interaction regions, and likely many other applications yet to be identified.

As also demonstrated in the framework of this thesis, aperture synthesis imaging is coming into reach for optical interferometric arrays. However, we expect that the number of studies applying imaging techniques will remain limited with the current generation of interferometric arrays, due to the substantial amount of observing time required for the imaging of complex structures. Therefore, this requires new initiatives for next-generation instruments (like VLTI/MATISSE and VLTI/VSI), and international collaborations to realize future arrays that will combine a larger number of apertures.

Inspite of this limitation of the imaging capabilities of the current generation of instruments, it is important to point out the tremendous scientific potential of the spectro-interferometric capabilities of the latest generation of instruments, allowing one to physically characterize the detected structures and to study their kinematics. Once the imaging and spectroscopic capabilities can be combined and made accessible to the broad astronomical community, optical interferometry will deploy its full potential; likely revolutionizing galactic and maybe also extra-galactic observational astronomy.

List of Publications

Refereed Articles (with direct contributions):

Kraus, S., Preibisch, Th., Ohnaka, K.: *Spectro-interferometry and radiative transfer modeling of the accretion disk around MWC 147*, **ApJ**, submitted

Kraus, S., Balega, Y. Y., Berger, J.-P., Hofmann, K.-H., Millan-Gabet, R., Monnier, J. D., Ohnaka, K., Pedretti, E., Preibisch, Th., Schertl, D., Schloerb, F. P., Traub, W. A., Weigelt, G.: *Visual/infrared interferometry of Orion Trapezium stars: Preliminary dynamical orbit and aperture synthesis imaging of the θ^1 Orionis C system*, **A&A**, 466, 649-659 (2007)

Weigelt, G., **Kraus, S.**, Driebe, T., Petrov, R.G., Hofmann, K.-H., Millour, F., Chesneau, O., Schertl, D., Malbet, F., Hillier, J.D., Gull, T., Davidson, K., Domiciano de Souza, A., AMBER consortium: *Near-infrared interferometry of η Carinae with spectral resolutions of 1 500 and 12 000 using AMBER/VLTI*, **A&A**, 464, 87-106 (2007)

Preibisch, Th., **Kraus, S.**, Driebe, T., van Boekel, R., Weigelt, G.: *A compact dusty disk around the Herbig Ae star HR 5999 resolved with VLTI/MIDI*, **A&A**, 458, 235-243 (2006)

Kraus, S., Balega, Y., Elitzur, M., Hofmann, K.-H., Preibisch, Th., Rosen, A., Schertl, D., Weigelt, G., Young, E.T.: *Outflows from the high-mass protostars NGC 7538 IRS1/2 observed with bispectrum speckle interferometry – Signatures of flow precession*, **A&A**, 455, 521-537 (2006)

Malbet, F., Benisty, M., De Wit, W.J., **Kraus, S.**, Meilland, A., Millour, F., Tatulli, E., Berger, J.-P., Chesneau, O., Hofmann, K.-H., Isella, A., Natta, A., Petrov, R., Preibisch, Th., Stee, P., Testi, L., Weigelt, G., AMBER consortium: *Disk and wind interaction in the young stellar object MWC 297 spatially resolved with VLTI/AMBER*, **A&A**, 464, 43-53 (2007)

Domiciano de Souza, A., Driebe, T., Chesneau, O., Hofmann, K.-H., **Kraus, S.**, Miroshnichenko, A.S., Ohnaka, K., Petrov, R.G., Preibisch, Th., Stee, P., Weigelt, G.: *VLTI/AMBER and VLTI/MIDI spectro-interferometric observations of the B[e] supergiant CPD*$-57^\circ 2874$, **A&A**, 464, 81-86 (2007)

Kraus, S., Schloerb, F. P., Traub, W. A., Carleton, N. P., Lacasse, M., Pearlman, M., Monnier, J. D., Millan-Gabet, R., Berger, J.-P., Haguenauer, P., Perraut, K., Kern, P., Malbet, F., and Labeye, P.: *Infrared Imaging of Capella with the IOTA Closure Phase Interferometer*, **AJ**, 130, 246-255 (2005)

Monnier, J. D., Traub, W. A, Schloerb, F. P., Millan-Gabet, R., Berger, J.-P., Pedretti, E., Carleton, N. P, **Kraus, S.**, Lacasse, M. G., Brewer, M., Ragland, S., Ahearn, A., Coldwell, C., Haguenauer, P., Kern, P., Labeye, P., Lagny, L., Malbet, F., Malin, D., Maymounkov, P., Morel, S., Papaliolios, C., Perraut, K., Pearlman, M., Porro, I. L., Schanen, I., Souccar, K., Torres, G., Wallace, G.: *First Results with the IOTA3 Imaging Interferometer: The Spectroscopic Binaries λ Virginis and WR 140*, **ApJ**, L57, (2004)

Refereed Articles (with indirect contributions):

Petrov, P. G., Malbet, F., Weigelt, G., AMBER consortium: *AMBER, the near-infrared spectro-interferometric three telescopes VLTI instrument*, **A&A**, 464, 1-12 (2007)

Robbe-Dubois, S., Lagarde, S., Petrov, R. G., AMBER consortium: *Optical configuration and analysis of the AMBER/VLTI instrument*, **A&A**, 464, 13-27 (2007)

Tatulli, E., Millour, F., Chelli, A., AMBER consortium: *Interferometric data reduction with AMBER/VLTI.Principle,estimators and illustration*, **A&A**, 464, 29-42 (2007)

Tatulli, E., Isella, A., Natta, A., AMBER consortium: *Constraining the wind launching region in Herbig Ae stars: AMBER/VLTI spectroscopy of HD104237*, **A&A**, 464, 55-58 (2007)

Meilland, A., Millour, F., Stee, P., AMBER consortium: *An asymmetry detected in the disk of K CMa with the VLTI/AMBER*, **A&A**, 464, 73-79

Millour, F., Petrov, R., Chesneau, O., AMBER consortium: *Direct constraint on the distance of γ2 Velorum from AMBER/VLTI observations*, **A&A**, 464, 107-118 (2007)

Conference Proceedings

Kraus, S., Preibisch, Th., Ohnaka, K., *The inner gaseous accretion disk around a Herbig Be star revealed by NIR/MIR spectro-interferometry*, **Proceedings for IAU Symposium 243 "Star-Disk Interaction"**, to be published by Cambridge University Press (2007)

Hofmann, K.-H., **Kraus, S.**, Lopez, B., Weigelt, G., Wolf, S.: *Aperture synthesis image reconstruction study for the mid-infrared VLTI imager MATISSE*, **Proceedings of SPIE**: Vol. 6268, p. 112, Danchi, W., Monnier, J., Schöller, M., eds. (2006)

Weigelt, G., Petrov, R., Chesneau, O., Davidson, K., Domiciano de Souza, A., Driebe, T., Foy, R., Fraix-Burnet, D., Gull, T., Hillier, J., Hofmann, K.-H., **Kraus, S.**, Malbet, F., Marconi, A., Mathias, P., Monin, J.-L., Millour, F., Ohnaka, K., Rantakyr, F., Richichi, A., Schertl, D., Schller, M., Stee, P., Testi, L., and Wittkowski, M.: *VLTI-AMBER observations of Eta Carinae with high spatial resolution and spectral resolutions of 1,500 and 10,000*, **Proceedings of SPIE**: Vol. 6268, p. 88, Danchi, W., Monnier,

J., Schöller, M., eds. (2006)

Lopez, B., Wolf, S., Lagarde, S., Abraham, P., Antonelli, P., Augereau, J. C., Beckman, U., Behrend, J., Berruyer, N., Bresson, Y., Chesneau, O., Clausse, J. M., Connot, C., Demyk, K., Danchi, W. C., Dugué, M., Flament, S., Glazenborg, A., Graser, U., Henning, T., Hofmann, K.-H., Heininger, M., Hugues, Y., Jaffe, W., Jankov, S., **Kraus, S.**, Laun, W., Leinert, Ch., Linz, H., Mathias, Ph., Meisenheimer, K., Matter, A., Menut, J. L., Millour, F., Neumann, U., Nussbaum, E., Niedzielski, A., Mosonic, L., Petrov, R., Ratzka, T., Robbe-Dubois, S., Roussel, A., Schertl, D., Schmider, F.-X., Stecklum, B., Thiebaut, E., Vakili, F., Wagner, K., Waters, L. B. F. M., Weigelt, G.: *MATISSE: perspective of imaging in the mid-infrared at the VLTI*, **Proceedings of SPIE**: Vol. 6268, p. 31, Danchi, W., Monnier, J., Schöller, M., eds. (2006)

Domiciano de Souza, A., Driebe, T., Chesneau, O., Hofmann, K.-H., **Kraus, S.**, Miroshnichenko, A.S., Ohnaka, K., Petrov, R.G., Preibisch, Th., Stee, P., Weigelt, G.: *The vicinity of the galactic supergiant B[e] star CPD*−57°2874 *from near- and mid-IR long baseline spectro-interferometry with the VLTI (AMBER and MIDI)*. **Workshop Proceedings** on "Stars with the B[e] phenomenon" from July 10-16, 2005 in Vlieland, the Netherlands. ASP Conference Series, Vol. 355, p. 155 (2006)

Lagarde, S., Lopez, B., Antonelli, P., Beckman, U., Behrend, J., Bresson, Y., Chesneau, O., Dugu, M., Glazenborg, A., Graser, U., Hofmann, K.-H., Jaffe, W., Leinert, Ch., Millour, F., Menut, J.L., Petrov, R.G., Ratzka, T., Weigelt, G., Wolf, S., Abraham, P., Connot, C., Henning, T., Heininger, M., Hugues, Y., **Kraus, S.**, Laun, W., Matter, A., Neumann, U., Nussbaum, E., Niedzielski, A., Mosoni, L., Robbe-Dubois, S., Roussel, A., Schertl, D., Vakili, F., Wagner, K., and Waters, L. B. F. M.: *MATISSE: a four beams combiner in the mid-infrared for the VLTI*, **Proceedings of SPIE**: Vol. 6268, p. 115, Danchi, W., Monnier, J., Schöller, M. eds. (2006)

Lawson, P. R., Cotton, W., Hummel, C.A., Baron, F., Young, J. S., Meimon, S. C., Le Besnerais, G., Mugnier, L. M., Ireland, M. J., Monnier, J. D., Thiebaut, E. M., Zavala, R. T., **Kraus, S.**, Hofmann, K.-H., Weigelt, G., Pott, J., Sridharan, R., Hope, D. A.: *Interferometry imaging beauty contest*, **Proceedings of SPIE**: Vol. 6268, p. 59, Danchi, W., Monnier, J., Schöller, M. eds. (2006)

Malbet, F., Benisty, M., de Wit, W. J., **Kraus, S.**, Meilland, A., Millour, F., Tatulli, E., Berger, J.-P., Chesneau, O., Hofmann, K.-H., Isella, A., Petrov, R., Preibisch, Th., Stee, P., Testi, L., Weigelt, G., and the AMBER consortium (invited paper): *Disentangling the wind and the disk in the close surrounding of the young stellar object MWC297 with AMBER/VLTI*, ESO Workshop: "The power of optical/IR interferometry: recent scientific results and 2nd generation VLTI instrumentation", April 4-8, 2005 in Garching, Germany; F. Paresce, A. Richichi, A. Chelli & F. Delplancke (eds.), Springer-Verlag series "ESO Astrophysics Symposia", in press (2006)

Petrov, R. G., Millour, F., Chesneau, O., Weigelt, G., Bonneau, D., Stee, Ph., **Kraus, S.**, Mourard, D., Meilland, A., Vannier, M., Malbet, F., Lisi, F., Antonelli, P., and Kern, P., Beckmann, U., Lagarde, S., Perraut, K., Gennari, S., Lecoarer, T., Driebe, Th., Accardo, M., Robbe-Dubois, S., Ohnaka, K., Busoni, S., Roussel, A., Zins, G., Behrend, J., Ferruzi, D., Bresson, Y., Duvert, G., Nussbaum, E., Marconi, A., Feautrier, Ph., Dugu, M., Chelli, A., Tatulli, E., Heininger, M., Delboulbe, A, Bonhomme, S., Schertl, D., Testi, L., Mathias, Ph., Monin, J.-L., Gluck, L., Hofmann, K.-H., Salinari, P., Puget, P., Clausse, J.-M., Fraix-Burnet, D., Foy, R., and Isella, A.: *First AMBER/VLTI observations of hot massive stars*,

ESO Workshop: ”The power of optical/IR interferometry: recent scientific results and 2nd generation VLTI instrumentation”, April 4-8, 2005 in Garching, Germany; F. Paresce, A. Richichi, A. Chelli & F. Delplancke (eds.), Springer-Verlag series “ESO Astrophysics Symposia”, in press (2006)

Preibisch, Th., Driebe, T., **Kraus, S.**, Lachaume, R., van Boekel, R., Weigelt, G.: *VLTI MIDI observations of the Herbig Ae star HR 5999*, ESO Workshop: ”The power of optical/IR interferometry: recent scientific results and 2nd generation VLTI instrumentation”, April 4-8, 2005 in Garching, Germany; F. Paresce, A. Richichi, A. Chelli & F. Delplancke (eds.), Springer-Verlag series “ESO Astrophysics Symposia”, in press (2006)

Benistry, M., Berger, J.-P., Cheasneau, O., Isella, A., **Kraus, S.**, Malbet, F., Meilland, A., Petrov, R., Stee, P., Tatulli, E., Testi, L., Weigelt, G. + AMBER consortium, + ESO AMBER astronomers, *VLTI/AMBER resolves disk-outflow interaction region of the B1.5V star MWC297*, **IAU Symposium 227** - ”Massive Star Birth: A Crossroads of Astrophysics”, May 16-20, 2005 in Acireale, Italy.

Kraus, S., Schloerb, F. P., 2004, *Infrared imaging of Capella with the IOTA interferometer*, **Proceedings of SPIE**: Vol. 5491, 56, Traub, W.A., Monnier, J.D., Schöller, M., eds. (2004)

Curriculum Vitae

Name:	Stefan Kraus

Education:

1985–1991	Grund/Volksschule, Hösbach, Germany
1991–1995	Staatliche Realschule, Hösbach, Germany
1995	Mittlere Reife
1995–1998	Bachgau Oberstufengymnasium, Babenhausen, Germany
1998	Abitur
1998–1999	Civil Service, Lebenshilfe Werkstätten e.V., Schmerlenbach
1999–2002	Undergraduate Studies, Faculty for Physics and Astronomy, Ruprecht-Karls-Universität, Heidelberg
2001	Vordiplom, Physics, Ruprecht-Karls-Universität, Heidelberg
2002–2003	Graduate Studies and Research Assistant, Department of Astronomy, University of Massachusetts, Amherst, USA
2003	Master of Science, University of Massachusetts, Amherst
since 2004	PhD research, Max-Planck-Institut für Radioastronomy Rheinische Friedrich-Wilhelms Universität, Bonn

Research Experience:

Research Project, 2002:	Landessternwarte, Heidelberg, Germany Topic: *FORS2 spectroscopy of the HH34/HH222 complex* Advisor: Immo Appenzeller
Observations, 2002:	Observations on Be stars with the HEROS spectrograph at the 2 m telescope at Ondrejov, Czechoslovakia
Observations, 2002/03:	Observations of close binaries with the IOTA, Whipple Observatory, Mt. Hopkins, Arizona
Master Thesis, 2003:	University of Massachusetts, Amherst, USA Topic: *Aperture Synthesis Imaging of Close Binary Stars in the Infrared with the IOTA* Advisor: F. Peter Schloerb

PhD research, 2004–2007:	Max-Planck-Institut für Radioastronomie, Bonn, Germany Topic: *Infrared Spectro-Interferometry of the Massive Stars: Disks, Winds, Outflows, and Stellar Multiplicity* Advisor: Gerd Weigelt
Observations, 2004:	Speckle observations of young outflow sources with the MPIfR visitor instrument at the MMT, Whipple Observatory, Mt. Hopkins, Arizona
Observations, 2005:	IOTA/IONIC3 Observations on Orion Trapezium stars and YSOs, Whipple Observatory, Mt. Hopkins, Arizona
Observations, 2006:	VLTI/AMBER-AT Commissioning Run Cerro Paranal, Chile
Observations, 2007:	VLTI/AMBER-UT Visitor Mode, OT observations VLTI/AMBER-AT Visitor Mode, GTO observations Cerro Paranal, Chile

Acknowledgements

Foremost, I would like to express my gratitude to my PhD supervisor, Prof. Dr. Gerd Weigelt, for the great opportunity to work in his group at the MPIfR on this innovative branch of astronomy. Besides his continuous encouragement, I thank him for the financial support, which allowed me to attend numerous conferences as well as observation runs at the MMT and IOTA.

I am indebted to my advisor on young star topics, Dr. Thomas Preibisch, not only for the chance to work on the MWC 147 data, but also for his advice in many other projects. I hope his focused way to do science will be guidance to me in the future.

Special thanks go to Prof. Dr. Ulrich Klein, who consented to be an examiner on my PhD thesis. I am also very grateful to Prof. Dr. Norbert Wermes and Prof. Dr. Christoph Strelen, who agreed to join the examination committee.

To Dr. Keichii Ohnaka and Dr. Karl-Heinz Hofmann, I am very grateful for the productive collaboration concerning Radiative Transfer Modeling and Image Reconstruction, respectively. I sincerely appreciate the teamwork with Dr. Alexander Rosen. I also want to thank all collaborators from the AMBER and MATISSE consortia, and the IOTA/IONIC3 group.

The friendly atmosphere I experienced in the group is also due to my colleagues Dr. Thomas Driebe, Dr. Dieter Schertl, Dr. Karl-Heinz Hofmann, our secretary Michelle Fekety, and all other colleagues from the group and the technical department. I want to thank Thomas and Michelle for reading parts of the thesis draft.

The International Max-Planck Research School of the Max-Planck-Institute for Radioastronomy (IMPRS) has funded my PhD research and has also financially supported me in attending the PPV conference. My thanks to Prof. Dr. Anton Zensus, the IMPRS coordinator Dr. Eduardo Ros and the IMPRS secretary Gabi Breuer for making IMPRS the great institution it has become. I acknowledge a grant from the organizers of Protostars & Planets V, which allowed me to attend the PPV meeting.

For the pleasant chats at coffee time over the last three years, I thank Sebastian, Bérengère, Alina, Nicolas, Kester, Curtis, Corinna, Regis, and all other attendants of the coffee club. It has also been very enjoyable to join the social activities with the other IMPRS students, like the IMPRS retreat and the movie nights.

Last but not least, I want to thank my parents for the freedom to chose this profession and for their invaluable and perpetual support in this endeavour. Finally, I want to express my deep thanks to Silke, for support, encouragement, help with the proof-reading of the manuscript, and for her understanding and patience while I was working on this project, sometimes far away from home.

Specific to the project on MWC 147:

I thank the VLTI astronomers who performed the service mode observations, and the ESO staff, engineers, and software engineers, who make this incredible instrument work.

This project is based in part on archival data obtained with the Spitzer Space Telescope, which is operated by the Jet Propulsion Laboratory, California Institute of Technology under a contract with NASA.

Specific to the project on NGC 7538:

I am very grateful to Prof. Dr. Moshe Elitzur for the highly motivative discussions and correspondance concerning this project. Furthermore, I thank all the participants of the *NGC 7538 collaboration*, which consisted of Roy Booth, John Conway, James De Buizer, Moshe Elitzur, Stefan Kraus, Vincent Minier, Michele Pestalozzi, and Gerd Weigelt. I also acknowledge the support of the BTA and MMT staff during the observations, as well as D. Apai and I. Pascucci for their assistance at the MMT. The numerical hydrodynamic simulations were executed on the Armagh SGI Origin 2000 computer (FORGE), acquired through the Particle Physics and Astronomy Research Council (PPARC) JREI initiative with SGI participation. This project is based in part on archival data obtained with the Spitzer Space Telescope, which is operated by the Jet Propulsion Laboratory, California Institute of Technology under a contract with NASA.

Specific to the project on θ^1 Ori C/D:

I would like to express my appreciation to the IOTA and IONIC3 team, who after the highly instructive and formative experience of my Master thesis work with Prof. Dr. Peter Schloerb, provided me again with the opportunity to work with this outstanding instrument. Dr. Keichii Ohnaka joined the IOTA observing run in November/December 2005, and I thank him for the highly motivated attitude, with which he supported the observations. For sharing some overlap time and refreshing our knowledge about IOTA operation, I express my gratitude to Dr. Jean-Phillipe Berger and Myriam Benisty.
I am also obliged to the IOTA technical staff, especially Marc Lacasse, for support during the observations. I thank Dr. John Monnier for very helpful discussions concerning the photometric correction of IOTA/IONIC3 data.

Specific to the project on η Carinae:

This work is based on observations made with the European Southern Observatory telescopes. This research has also made use of the ASPRO observation preparation tool from the *Jean-Marie Mariotti Center* in France, the SIMBAD database at CDS, Strasbourg (France), and the Smithsonian/NASA Astrophysics Data System (ADS). We thank the referees N. Smith and A. Damineli for very valuable comments and suggestions, which helped to considerably improve the manuscript. The NSO/Kitt Peak FTS data used here to identify the telluric lines in the AMBER data were produced by NSF/NOAO. This project has benefitted from funding from the French Centre National de la Recherche Scientifique (CNRS) through the Institut National des Sciences de l'Univers (INSU) and its Programmes Nationaux (ASHRA, PNPS). The authors from the French laboratories would like to thank the successive directors of the INSU/CNRS directors. C. Gil's work was partially supported by the Fundação para a Ciência e a Tecnologia through project POCTI/CTE-AST/55691/2004 from POCTI, with funds from the European program FEDER. K. Weis is supported by the state of North-Rhine-Westphalia (Lise-Meitner fellowship).

This work makes use of data products from the Two Micron All Sky Survey, which is a joint project of the University of Massachusetts and the Infrared Processing and Analysis Center/California Institute of Technology, funded by the National Aeronautics and Space Administration and the National Science Foundation.

Bibliography

Ábrahám, P., Mosoni, L., Henning, T., et al. 2006, A&A, 449, L13 [ADS] 6.2

Acke, B. & van den Ancker, M. E. 2004, A&A, 426, 151 [ADS] 6.4.1

Akabane, K. & Kuno, N. 2005, A&A, 431, 183 [ADS] 7.2.1, 7.5.4.5, 7.5.5

Akeson, R. L., Ciardi, D. R., van Belle, G. T., Creech-Eakman, M. J., & Lada, E. A. 2000, ApJ, 543, 313 [ADS] 6.2, 6.2, 6.3.1, 6.3, 6.4.2, 6.4.2.1

Akeson, R. L., Walker, C. H., Wood, K., et al. 2005, ApJ, 622, 440 [ADS] 6.6.4

Allamandola, L. J., Tielens, A. G. G. M., & Barker, J. R. 1985, ApJ, 290, L25 [ADS] 6.4.1

Alvarez, C., Hoare, M., Glindemann, A., & Richichi, A. 2004, A&A, 427, 505 [ADS] 7.2.1, 7.4.1.1, 7.2

Armitage, P. J. & Pringle, J. E. 1997, ApJ, 488, L47+ [ADS] 7.5.4.5

Babel, J. & Montmerle, T. 1997, ApJ, 485, L29+ [ADS] 8.1

Baines, D., Oudmaijer, R. D., Porter, J. M., & Pozzo, M. 2006, MNRAS, 367, 737 [ADS] 6.2, 6.6.1

Baize, P. & Romani, L. 1946, Annales d'Astrophysique, 9, 13 8.4, 8.6.2

Baldwin, J. E., Beckett, M. G., Boysen, R. C., et al. 1996, A&A, 306, L13+ [ADS] 1.3.3

Balog, Z., Kenyon, S. J., Lada, E. A., et al. 2004, AJ, 128, 2942 [ADS] 2, 7.6

Bate, M. R., Bonnell, I. A., Clarke, C. J., et al. 2000, MNRAS, 317, 773 [ADS] 7.5.4.5

Berger, J.-P., Haguenauer, P., Kern, P. Y., et al. 2003, in Interferometry for Optical Astronomy II. Edited by Wesley A. Traub . Proceedings of the SPIE, Volume 4838, pp. 1099-1106 (2003)., ed. W. A. Traub, 1099–1106 [ADS] 3.2, 8.3.2

Bergmann & Schaefer. 1993, Lehrbuch der Experimentalphysik, Band 3, OPTIK (Berlin: Walter de Gruyter) 2.1

Bernasconi, P. A. & Maeder, A. 1996, A&A, 307, 829 [ADS] 1.1, 1.2, 8.10

Berrilli, F., Lorenzetti, D., Saraceno, P., & Strafella, F. 1987, MNRAS, 228, 833 [ADS] 6.9

Bertout, C., Robichon, N., & Arenou, F. 1999, A&A, 352, 574 [ADS] 6.2

Bik, A. & Thi, W. F. 2004, A&A, 427, L13 [ADS] 1.2

Bjorkman, J. E. & Wood, K. 2001, ApJ, 554, 615 [ADS] 6.6.2

Blitz, L., Fich, M., & Stark, A. A. 1982, ApJS, 49, 183 [ADS] 7.2.1

Bloomer, J. D., Watson, D. M., Pipher, J. L., et al. 1998, ApJ, 506, 727 [ADS] 7.2.1, 7.4.1.1, 7.5.1, 7.10, 7.5.3, 7.5.5

Boden, A. F., Sargent, A. I., Akeson, R. L., et al. 2005, ApJ, 635, 442 [ADS] 8.2

Boehm, T. & Catala, C. 1995, A&A, 301, 155 [ADS] 6.2

Bonnell, I. A., Bate, M. R., & Zinnecker, H. 1998, MNRAS, 298, 93 [ADS] 1.2

Bouret, J.-C., Martin, C., Deleuil, M., Simon, T., & Catala, C. 2003, A&A, 410, 175 [ADS] 6.2

Buscher, D. 1988, MNRAS, 235, 1203 [ADS] 1.3.1

Buscher, D. F., Baldwin, J. E., Warner, P. J., & Haniff, C. A. 1990, MNRAS, 245, 7P [ADS] 1.3.3

Campbell, B. 1984, ApJ, 282, L27 [ADS] 7.2.1, 7.4.1.1, 7.5.4.2

Campbell, B. & Persson, S. E. 1988, AJ, 95, 1185 [ADS] 7.2.1, 7.5.1

Casey, S. C. 1991, ApJ, 371, 183 [ADS] 6.9, 6.6.1

Cesaroni, R., Neri, R., Olmi, L., et al. 2005, A&A, 434, 1039 [ADS] 1.2

Chesneau, O., Min, M., Herbst, T., et al. 2005, A&A, 435, 1043 [ADS] 9.2

Chiang, E. I. & Goldreich, P. 1997, ApJ, 490, 368 [ADS] 6.1, 6.6.5.3

Chini, R., Hoffmeister, V. H., Nielbock, M., et al. 2006, ApJ, 645, L61 [ADS] 1.2

Churchwell, E., Whitney, B. A., Babler, B. L., et al. 2004, ApJS, 154, 322 [ADS] 7.3.2

Claret, A. 2004, A&A, 424, 919 [ADS] 8.9, 8.6.4

Cliffe, J. A., Frank, A., & Jones, T. W. 1996, MNRAS, 282, 1114 [ADS] 7.5.4.4

Cohen, M. 1973, MNRAS, 161, 105 [ADS] 6.9

Colavita, M. M. 1999, PASP, 111, 111 [ADS] 4.2

Colavita, M. M., Wallace, J. K., Hines, B. E., et al. 1999, ApJ, 510, 505 [ADS] 6.3.1

Conti, P. S. 1984, in IAU Symp. 105: Observational Tests of the Stellar Evolution Theory, ed. A. Maeder & A. Renzini, 233–+ [ADS] 1.2

Corcoran, M. F. 2005, AJ, 129, 2018 [ADS] 9.2, 9.1

Cornwell, T. J. & Wilkinson, P. N. 1981, MNRAS, 196, 1067 [ADS] 5.1

Corporon, P. & Lagrange, A.-M. 1999, A&AS, 136, 429 [ADS] 6.2

Coude Du Foresto, V., Ridgway, S., & Mariotti, J.-M. 1997, A&AS, 121, 379 [ADS] 3.2, 3.3

Damineli, A. 1996, ApJ, 460, L49 [ADS] 9.2, 9.4.7

Damineli, A., Conti, P. S., & Lopes, D. F. 1997, New Astronomy, 2, 107 [ADS] 9.2

Damineli, A., Kaufer, A., Wolf, B., et al. 2000, ApJ, 528, L101 [ADS] 9.2

Davidson, K. 1999, in ASP Conf. Ser. 179: Eta Carinae at The Millennium, ed. J. A. Morse, R. M. Humphreys, & A. Damineli, 304 [ADS] 9.2

Davidson, K. 2001, in ASP Conf. Ser. 242: Eta Carinae and Other Mysterious Stars: The Hidden Opportunities of Emission Spectroscopy, ed. T. R. Gull, S. Johannson, & K. Davidson, 3 [ADS] 9.2, 9.4.1, 9.4.4.2, 9.4.5, 9.4.7.2, 9.4.7.2

Davidson, K., Dufour, R. J., Walborn, N. R., & Gull, T. R. 1986, ApJ, 305, 867 [ADS] 9.2

Davidson, K., Ebbets, D., Weigelt, G., et al. 1995, AJ, 109, 1784 [ADS] 9.2

Davidson, K. & Humphreys, R. M. 1997, ARA&A, 35, 1 [ADS] 9.2

Davidson, K., Ishibashi, K., Gull, T. R., & Humphreys, R. M. 1999, in ASP Conf. Ser. 179: Eta Carinae at The Millennium, ed. J. A. Morse, R. M. Humphreys, & A. Damineli, 227 [ADS] 9.2, 9.4.1, 9.4.4.2, 9.4.5, 9.4.7.2, 9.4.7.2

Davidson, K., Ishibashi, K., Gull, T. R., Humphreys, R. M., & Smith, N. 2000, ApJ, 530, L107 [ADS] 9.2

Davidson, K., Martin, J., Humphreys, R. M., et al. 2005, AJ, 129, 900 [ADS] 9.2

Davidson, K., Smith, N., Gull, T. R., Ishibashi, K., & Hillier, D. J. 2001, AJ, 121, 1569 [ADS] 9.2, 9.4.3

Davis, C. J., Moriarty-Schieven, G., Eislöffel, J., Hoare, M. G., & Ray, T. P. 1998, AJ, 115, 1118 [ADS] 7.2.1, 7.4.1.1, 7.8, 7.5.1, 7.10, 7.5.4.4, 7.5.4.5, 7.5.6

De Buizer, J. M. 2003, MNRAS, 341, 277 [ADS] 1.2

De Buizer, J. M. & Minier, V. 2005, ApJ, 628, L151 [ADS] 7.2.1, 7.4.1.1, 7.8, 7.10, 7.5.2, 7.5.4.2

Delplancke, F., Derie, F., Paresce, F., et al. 2003, Ap&SS, 286, 99 [ADS] 2.2.2

Demircan, O. & Kahraman, G. 1991, Ap&SS, 181, 313 8.4, 8.6.2

Dickel, H. R., Rots, A. H., Goss, W. M., & Forster, J. R. 1982, MNRAS, 198, 265 [ADS] 7.2.1

Docobo, J. A. 1985, Celestial Mechanics, 36, 143 [ADS] 8.1, 8.6.1, 10

Dodson, R., Ojha, R., & Ellingsen, S. P. 2004, MNRAS, 351, 779 [ADS] 1.2

Donati, J.-F., Babel, J., Harries, T. J., et al. 2002, MNRAS, 333, 55 [ADS] 8.1, 8.2, 8.6.3, 2

Dullemond, C. P., Dominik, C., & Natta, A. 2001, ApJ, 560, 957 [ADS] 6.1, 6.2, 6.6.5.4, 6.7

Duncan, R. A., White, S. M., Reynolds, J. E., & Lim, J. 1999, in ASP Conf. Ser. 179: Eta Carinae at The Millennium, ed. J. A. Morse, R. M. Humphreys, & A. Damineli, 54 [ADS] 9.2

Dyck, H. M., Benson, J. A., van Belle, G. T., & Ridgway, S. T. 1996, AJ, 111, 1705 [ADS] 9.1

Dyck, H. M. & Capps, R. W. 1978, ApJ, 220, L49 [ADS] 7.2.1

Dyck, H. M. & Lonsdale, C. J. 1979, AJ, 84, 1339 [ADS] 7.5.1

Egan, M. P., Price, S. D., Shipman, R. F., et al. 1999, in ASP Conf. Ser. 177: Astrophysics with Infrared Surveys: A Prelude to SIRTF, ed. M. D. Bicay, R. M. Cutri, & B. F. Madore, 404–+ [ADS] 6.9

Egret, D., Didelon, P., McLean, B. J., Russell, J. L., & Turon, C. 1992, A&A, 258, 217 [ADS] 6.9

Eislöffel, J. & Mundt, R. 1997, AJ, 114, 280 [ADS] 7.5.4.5

Eisner, J. A., Hillenbrand, L. A., White, R. J., Akeson, R. L., & Sargent, A. I. 2005, ApJ, 623, 952 [ADS] 6.5.1

Eisner, J. A., Lane, B. F., Hillenbrand, L. A., Akeson, R. L., & Sargent, A. I. 2004, ApJ, 613, 1049 [ADS] 6.2

Ellingsen, S. P. 2006, ApJ, 638, 241 [ADS] 1.2

Elsaesser, H., Birkle, K., Eiroa, C., & Lenzen, R. 1982, A&A, 108, 274 [ADS] 7.5.1

Fazio, G. G., Hora, J. L., Allen, L. E., et al. 2004, ApJS, 154, 10 [ADS] 7.3.2

Feast, M., Whitelock, P., & Marang, F. 2001, MNRAS, 322, 741 [ADS] 9.2

Fendt, C. & Zinnecker, H. 1998, A&A, 334, 750 [ADS] 7.5.4.5

Fischer, J., Sanders, D. B., Simon, M., & Solomon, P. M. 1985, ApJ, 293, 508 [ADS] 7.2.1, 7.4.1.1

Franco-Hernández, R. & Rodríguez, L. F. 2004, ApJ, 604, L105 [ADS] 7.4.1.1

Friedjung, M. 1985, A&A, 146, 366 [ADS] 6.5.1

Gagne, M., Caillault, J.-P., Stauffer, J. R., & Linsky, J. L. 1997, ApJ, 478, L87+ [ADS] 8.2, 8.6.3

Gagné, M., Oksala, M. E., Cohen, D. H., et al. 2005, ApJ, 628, 986 [ADS] 8.1, 8.6.4

Gai, M., Menardi, S., Cesare, S., et al. 2004, in New Frontiers in Stellar Interferometry, Proceedings of SPIE Volume 5491. Edited by Wesley A. Traub. Bellingham, WA: The International Society for Optical Engineering, 2004., p.528, ed. W. A. Traub, 528–+ [ADS] 4.1.1

Gaume, R. A., Goss, W. M., Dickel, H. R., Wilson, T. L., & Johnston, K. J. 1995, ApJ, 438, 776 [ADS] 7.2.1, 7.6, 7.4.1.1, 7.11, 7.5.4.2, 7.5.4.3

Genzel, R. & Stutzki, J. 1989, ARA&A, 27, 41 [ADS] 8.2

Gitton, P. B., Leveque, S. A., Avila, G., & Phan Duc, T. 2004, in New Frontiers in Stellar Interferometry, Proceedings of SPIE Volume 5491. Edited by Wesley A. Traub. Bellingham, WA: The International Society for Optical Engineering, 2004., p.944, ed. W. A. Traub, 944–+ [ADS] 4.1.1

Glindemann, A., Algomedo, J., Amestica, R., et al. 2003, in Interferometry for Optical Astronomy II. Edited by Wesley A. Traub. Proceedings of the SPIE, Volume 4838, pp. 89-100 (2003)., ed. W. A. Traub, 89–100 [ADS] 4.2

Gómez, L., Rodríguez, L. F., Loinard, L., et al. 2005, ApJ, 635, 1166 [ADS] 8.2

Grosso, N., Feigelson, E. D., Getman, K. V., et al. 2005, ApJS, 160, 530 [ADS] 1

Gull, T. R., Ishibashi, K., Davidson, K., & The Cycle 7 STIS Go Team. 1999, in ASP Conf. Ser. 179: Eta Carinae at The Millennium, ed. J. A. Morse, R. M. Humphreys, & A. Damineli, 144 [ADS] 9.2

Habart, E., Natta, A., & Krügel, E. 2004, A&A, 427, 179 [ADS] 6.4.1

Habart, E., Natta, A., Testi, L., & Carbillet, M. 2006, A&A, 449, 1067 [ADS] 6.4.1

Hackwell, J. A., Grasdalen, G. L., & Gehrz, R. D. 1982, ApJ, 252, 250 [ADS] 7.2.1

Hanner, M. 1988, Grain optical properties, Tech. rep. [ADS] 6.6.2, 6.6

Hartmann, L., Kenyon, S. J., & Calvet, N. 1993, ApJ, 407, 219 [ADS] 6.1

Heintz, W. D. 1978, Geophysics and Astrophysics Monographs, 15 8.4

Hernández, J., Calvet, N., Briceño, C., Hartmann, L., & Berlind, P. 2004, AJ, 127, 1682 [ADS] 6.1, 6.2

Higdon, S. J. U., Devost, D., Higdon, J. L., et al. 2004, PASP, 116, 975 [ADS] 6.3.4

Hillenbrand, L. A. 1997, AJ, 113, 1733 [ADS] 8.2, 8.6

Hillenbrand, L. A., Strom, S. E., Calvet, N., et al. 1998, AJ, 116, 1816 [ADS] 8.6, 8.6.5

Hillenbrand, L. A., Strom, S. E., Vrba, F. J., & Keene, J. 1992, ApJ, 397, 613 [ADS] 6.1, 6.2, 6.2, 6.9

Hillier, D. J., Davidson, K., Ishibashi, K., & Gull, T. 2001, ApJ, 553, 837 [ADS] 9.1, 9.2, 9.4.1, 9.4.1, 9.6, 9.7, 9.2, 9.4.2.1, 9.4.2.2, 9.4.3, 9.9, 9.4.4.1, 9.4.4.2, 9.4.7.2, 9.5, 9.7, 10.4

Hillier, D. J., Gull, T., Nielsen, K., et al. 2006, ApJ, 642, 1098 [ADS] 9.2, 9.4.1, 9.4.1, 9.6, 9.4.2.1, 9.4.4.2, 9.4.5, 9.4.7.1, 9.12, 9.4.7.2, 9.4.7.2

Hillier, D. J. & Miller, D. L. 1998, ApJ, 496, 407 [ADS] 9.2

Hoare, M. G. 2005, Ap&SS, 295, 203 [ADS] 1.2

Hoffman, I. M., Goss, W. M., Palmer, P., & Richards, A. M. S. 2003, ApJ, 598, 1061 [ADS] 7.2.1

Hofmann, K.-H. & Weigelt, G. 1986, A&A, 167, L15+ [ADS] 1.3.2, 7.3.1, 8.3.1

Hofmann, K.-H. & Weigelt, G. 1988, A&A, 203, L21 [ADS] 9.2

Hofmann, K.-H. & Weigelt, G. 1993, A&A, 278, 328 [ADS] 3.3.2, 5.1, 8.4

Høg, E., Fabricius, C., Makarov, V. V., et al. 2000, A&A, 355, L27 [ADS] 6.9

Högbom, J. A. 1974, A&AS, 15, 417 [ADS] 5.1

Hönig, S. F., Beckert, T., Ohnaka, K., & Weigelt, G. 2006, A&A, 452, 459 [ADS] 6.6.2

Hora, J. L., Fazio, G. G., Allen, L. E., et al. 2004, in Microwave and Terahertz Photonics. Edited by Stohr, Andreas; Jager, Dieter; Iezekiel, Stavros. Proceedings of the SPIE, Volume 5487, pp. 77-92 (2004)., ed. J. C. Mather, 77–92 [ADS] 7.3.2

Houck, J. R., Roellig, T. L., van Cleve, J., et al. 2004, ApJS, 154, 18 [ADS] 6.3.4

Howarth, I. D. & Prinja, R. K. 1989, ApJS, 69, 527 [ADS] 8.1

Hummel, C. A., Armstrong, J. T., Quirrenbach, A., et al. 1994, AJ, 107, 1859 [ADS] 5.2

Hutawarakorn, B. & Cohen, R. J. 2003, MNRAS, 345, 175 [ADS] 7.6, 7.11

Isella, A. & Natta, A. 2005, A&A, 438, 899 [ADS] 6.1, 6.6.3

Ishibashi, K. 2001, in ASP Conf. Ser. 242: Eta Carinae and Other Mysterious Stars: The Hidden Opportunities of Emission Spectroscopy, ed. T. R. Gull, S. Johannson, & K. Davidson, 53 [ADS] 9.2

Ishibashi, K., Corcoran, M. F., Davidson, K., et al. 1999, ApJ, 524, 983 [ADS] 9.2

Ishibashi, K., Gull, T. R., Davidson, K., et al. 2003, AJ, 125, 3222 [ADS] 9.1

Ivanescu, L., Arsenault, R., Fedrigo, E., et al. 2004, in Advancements in Adaptive Optics. Edited by Domenico B. Calia, Brent L. Ellerbroek, and Roberto Ragazzoni. Proceedings of the SPIE, Volume 5490, pp. 1534-1545 (2004)., ed. D. Bonaccini Calia, B. L. Ellerbroek, & R. Ragazzoni, 1534–1545 [ADS] 4.1.1

Jain, S. K., Bhatt, H. C., & Sagar, R. 1990, A&AS, 83, 237 [ADS] 6.2

Jeffries, R. D. 2007, ArXiv Astrophysics e-prints 8.6.2

Jennison, R. C. 1958, MNRAS, 118, 276 [ADS] 2.2.2

Johnston, K. J., Stolovy, S. R., Wilson, T. L., Henkel, C., & Mauersberger, R. 1989, ApJ, 343, L41 [ADS] 7.2.1

Kameya, O., Hasegawa, T. I., Hirano, N., Takakubo, K., & Seki, M. 1989, ApJ, 339, 222 [ADS] 7.2.1, 7.4.1.1, 7.8, 7.10, 7.5.2, 7.5.4.1

Kameya, O., Morita, K.-I., Kawabe, R., & Ishiguro, M. 1990, ApJ, 355, 562 [ADS] 7.2.1

Kawabe, R., Suzuki, M., Hirano, N., et al. 1992, PASJ, 44, 435 [ADS] 7.2.1

Kenyon, S. J. & Hartmann, L. 1987, ApJ, 323, 714 [ADS] 6.5.1, 6.6.5.3

Kenyon, S. J. & Hartmann, L. 1995, ApJS, 101, 117 [ADS] 8.10, 8.6.4

Kervella, P., Fouqué, P., Storm, J., et al. 2004a, ApJ, 604, L113 [ADS] 9.1

Kervella, P., Mérand, A., Perrin, G., & Coudé de Foresto, V. 2006, A&A, 448, 623 [ADS] 9.1

Kervella, P., Nardetto, N., Bersier, D., Mourard, D., & Coudé du Foresto, V. 2004b, A&A, 416, 941 [ADS] 9.1

Kervella, P., Ségransan, D., & Coudé du Foresto, V. 2004c, A&A, 425, 1161 [ADS] 3.3.1, 3.3.1

Knox, K. T. & Thompson, B. J. 1974, ApJ, 193, L45 [ADS] 1.3.2

Köhler, R., Petr-Gotzens, M. G., McCaughrean, M. J., et al. 2006, A&A, 458, 461 [ADS] 1.2, 8.6.5

Kraus, S. 2003, Master's thesis, University of Massachusetts, Amherst, USA 2.5.1, 3.1, 3.2, 3.3.1, 3.3.1, 3.3.2, 5.2

Kraus, S., Heiniger, M., & Weigelt, G. 2005a, Investigating the dependence of AMBER results on the Bad Pixel Mask, AMBER Memo, 2005-10-19, Max-Planck-Institute for Radioastronomy 4.6

Kraus, S., Schloerb, F. P., Traub, W. A., et al. 2005b, AJ, 130, 246 [ADS] 3.3.1, 3.3.1, 3.3.2, 5.2, 6.4.2.1, 8.3.2, 8.4, 8.5.1

Kroupa, P. 2002, Science, 295, 82 [ADS] 1.1

Krumholz, M. R., McKee, C. F., & Klein, R. I. 2005, ApJ, 618, L33 [ADS] 1.2, 7.2

Kurucz, R. L. 1970, SAO Special Report, 309 [ADS] 6.6.2

Labeyrie, A. 1970, A&A, 6, 85 [ADS] 1.3.2, 7.3.1, 8.3.1

Lagarde, S., Lopez, B., Antonelli, P., et al. 2006, in Advances in Stellar Interferometry. Edited by Monnier, John D.; Schöller, Markus; Danchi, William C.. Proceedings of the SPIE, Volume 6268, pp. (2006). [ADS] 5.3

Laques, P. & Vidal, J. L. 1979, A&A, 73, 97 [ADS] 1.2

Larwood, J. D. & Papaloizou, J. C. B. 1997, MNRAS, 285, 288 [ADS] 7.5.4.5

Lawson, P. R., Cotton, W. D., Hummel, C. A., et al. 2006, in Advances in Stellar Interferometry. Edited by Monnier, John D.; Schöller, Markus; Danchi, William C.. Proceedings of the SPIE, Volume 6268, pp. (2006). [ADS] 5.4, 5.6

Lawson, P. R., Cotton, W. D., Hummel, C. A., et al. 2004, in New Frontiers in Stellar Interferometry, Proceedings of SPIE Volume 5491. Edited by Wesley A. Traub. Bellingham, WA: The International Society for Optical Engineering, 2004., p.886, ed. W. A. Traub, 886–+ [ADS] 5.4

Leinert, C., van Boekel, R., Waters, L. B. F. M., et al. 2004, A&A, 423, 537 [ADS] 6.2, 6.3.3, 6.5.1, 6.5.2

Levato, H. & Abt, H. A. 1976, PASP, 88, 712 [ADS] 8.6.4

Lohmann, A. W., Weigelt, G., & Wirnitzer, B. 1983, Appl. Opt., 22, 4028 [ADS] 1.3.2, 2.2.2, 7.3.1, 8.3.1

Lopez, B., Wolf, S., Lagarde, S., et al. 2006, in Advances in Stellar Interferometry. Edited by Monnier, John D.; Schöller, Markus; Danchi, William C.. Proceedings of the SPIE, Volume 6268, pp. (2006). [ADS] 5.3

Lubow, S. H. & Ogilvie, G. I. 2000, ApJ, 538, 326 [ADS] 7.5.4.5

Lugo, J., Lizano, S., & Garay, G. 2004, ApJ, 614, 807 [ADS] 7.5.3

Lynden-Bell, D. & Pringle, J. E. 1974, MNRAS, 168, 603 [ADS] 1.2, 6.1, 6.5.1

Lynds, B. T. & O'Neil, E. J. 1986, ApJ, 306, 532 [ADS] 7.2.1, 7.4.2

Madden, S. C., Irvine, W. M., Matthews, H. E., Brown, R. D., & Godfrey, P. D. 1986, ApJ, 300, L79 [ADS] 7.2.1

Maeder, A. & Desjacques, V. 2001, A&A, 372, L9 [ADS] 9.4.3, 9.4.6

Malbet, F., Benisty, M., De Wit, W. J., et al. 2006a, A&A accepted 6.2

Malbet, F., Benisty, M., De Wit, W. J., et al. 2006b, A&A accepted 9.3, 9.4.4.1

Malbet, F., Berger, J.-P., Colavita, M. M., et al. 1998, ApJ, 507, L149 [ADS] 6.2

Malbet, F., Kern, P., Schanen-Duport, I., et al. 1999, A&AS, 138, 135 [ADS] 2.4

Mannings, V. 1994, MNRAS, 271, 587 [ADS] 6.2, 6.9

Martin, J. C., Davidson, K., Humphreys, R. M., Hillier, D. J., & Ishibashi, K. 2006, ApJ, 640, 474 [ADS] 9.2, 9.4.1, 2

Martins, F. & Plez, B. 2006, A&A, 457, 637 [ADS] 8.10, 8.6.4

Martins, F., Schaerer, D., & Hillier, D. J. 2005, A&A, 436, 1049 [ADS] 8.6.2, 8.9, 8.10, 8.6.4, 8.6.4

Mathis, J. S. 1990, ARA&A, 28, 37 [ADS] 8.6

Mathis, J. S., Rumpl, W., & Nordsieck, K. H. 1977, ApJ, 217, 425 [ADS] 6.6.2

Mathis, J. S. & Wallenhorst, S. G. 1981, ApJ, 244, 483 [ADS] 8.6

McCaughrean, M., Rayner, J., & Zinnecker, H. 1991, Memorie della Societa Astronomica Italiana, 62, 715 [ADS] 7.2.1, 7.6

Meeus, G., Waters, L. B. F. M., Bouwman, J., et al. 2001, A&A, 365, 476 [ADS] 6.4.1

Men'shchikov, A. B. & Henning, T. 1997, A&A, 318, 879 [ADS] 6.1

Menten, K. M., Pillai, T., & Wyrowski, F. 2005, in IAU Symposium, ed. R. Cesaroni, M. Felli, E. Churchwell, & M. Walmsley, 23–34 [ADS] 1.2

Menten, K. M., Walmsley, C. M., Henkel, C., et al. 1986, A&A, 169, 271 [ADS] 7.1, 7.2.1

Michelson, A. A. 1891, PASP, 3, 274 [ADS] 1.3.3

Michelson, A. A. & Pease, F. G. 1921, ApJ, 53, 249 [ADS] 1.3.3

Millan-Gabet, R., Malbet, F., Akeson, R., et al. 2007, in Protostars and Planets V, ed. B. Reipurth, D. Jewitt, & K. Keil, 539–554 6.1

Millan-Gabet, R., Schloerb, F. P., & Traub, W. A. 2001, ApJ, 546, 358 [ADS] 2.5.1, 6.1, 6.2, 6.3, 6.4.2, 6.4.2.1, 6.5.1

Millour, F., Vannier, M., Petrov, R. G., et al. 2006, in EAS Publications Series, Vol. in press 4.2, 9.3

Minier, V., Booth, R. S., & Conway, J. E. 1998, A&A, 336, L5 [ADS] 7.2.1

Minier, V., Booth, R. S., & Conway, J. E. 2000, A&A, 362, 1093 [ADS] 1.2, 7.2.1, 7.4.1.1, 7.5.2

Miroshnichenko, A., Ivezić , Ž., Vinković , D., & Elitzur, M. 1999, ApJ, 520, L115 [ADS] 6.2

Miroshnichenko, A., Ivezic, Z., & Elitzur, M. 1997, ApJ, 475, L41+ [ADS] 6.1, 6.2, 6.6.5.2, 6.6.5.2

Monnier, J. D. 2001, PASP, 113, 639 [ADS] 3.3

Monnier, J. D. 2003, Reports of Progress in Physics, 66, 789 [ADS] 10.1

Monnier, J. D., Berger, J.-P., Millan-Gabet, R., et al. 2006, ApJ, 647, 444 [ADS] 6.3.1, 6.6.3, 8.5.2

Monnier, J. D. & Millan-Gabet, R. 2002, ApJ, 579, 694 [ADS] 6.1, 6.2, 6.4.2

Monnier, J. D., Millan-Gabet, R., Billmeier, R., et al. 2005, ApJ, 624, 832 [ADS] 6.4.2.1

Monnier, J. D., Traub, W. A., Schloerb, F. P., et al. 2004, ApJ, 602, L57 [ADS] 8.4

Muzerolle, J., D'Alessio, P., Calvet, N., & Hartmann, L. 2004, ApJ, 617, 406 [ADS] 6.6.4

Natta, A. & Kruegel, E. 1995, A&A, 302, 849 [ADS] 6.2

Natta, A., Prusti, T., Neri, R., et al. 2001, A&A, 371, 186 [ADS] 6.1, 6.2, 6.6.5.4

Nielsen, K. E., Corcoran, M. F., Gull, T. R., et al. 2006, ApJ submitted 9.2, 9.4.1, 9.6, 9.4.4.2, 9.4.5, 9.4.7.1, 9.12, 9.4.7.2, 9.4.7.2

Nisini, B., Milillo, A., Saraceno, P., & Vitali, F. 1995, A&A, 302, 169 [ADS] 6.2

Norris, R. P., Byleveld, S. E., Diamond, P. J., et al. 1998, ApJ, 508, 275 [ADS] 1.2

O'dell, C. R. 1998, AJ, 115, 263 [ADS] 1.2

Ohnaka, K., Driebe, T., Hofmann, K.-H., et al. 2006, A&A, 445, 1015 [ADS] 6.6.2, 10

Ojha, D. K., Tamura, M., Nakajima, Y., et al. 2004, ApJ, 616, 1042 [ADS] 7.2.1, 7.2, 7.4.2, 7.6

Ossenkopf, V., Henning, T., & Mathis, J. S. 1992, A&A, 261, 567 [ADS] 6.6.2, 6.6

Oudmaijer, R. D., Drew, J. E., Barlow, M. J., Crawford, I. A., & Proga, D. 1997, MNRAS, 291, 110 [ADS] 8.6.3

Owocki, S. P., Cranmer, S. R., & Gayley, K. G. 1996, ApJ, 472, L115 [ADS] 9.2, 9.4.3, 9.5, 10.4

Owocki, S. P., Cranmer, S. R., & Gayley, K. G. 1998, Ap&SS, 260, 149 [ADS] 9.2, 9.4.3, 9.5

Pasinetti Fracassini, L. E., Pastori, L., Covino, S., & Pozzi, A. 2001, A&A, 367, 521 [ADS] 6.2

Pearson, T. J. & Readhead, A. C. S. 1984, ARA&A, 22, 97 [ADS] 5.1

Pearson, T. J., Shepherd, M. C., Taylor, G. B., & Myers, S. T. 1994, in Bulletin of the American Astronomical Society, 1318–+ [ADS] 5.1

Pedretti, E., Millan-Gabet, R., Monnier, J. D., et al. 2004, PASP, 116, 377 [ADS] 3.2, 8.2

Pedretti, E., Traub, W. A., Monnier, J. D., et al. 2005, Appl. Opt., 44, 5173 [ADS] 8.3.2

Pestalozzi, M. R., Elitzur, M., Conway, J. E., & Booth, R. S. 2004, ApJ, 603, L113 [ADS] 1.2, 7.1, 7.2, 7.2.1, 7.6, 7.5.2, 7.5.4.1, 7.5.4.5

Pestalozzi, M. R., Minier, V., & Booth, R. S. 2005, A&A, 432, 737 [ADS] 1.2

Petrov, R. G., Malbet, F., Antonelli, P., et al. 2006a, A&A submitted 4.1.1, 6.3.2, 9.3, 9.4.2.1, 9.7

Petrov, R. G., Malbet, F., Antonelli, P., et al. 2006b, A&A submitted 4.1.1, 9.3

Petrov, R. G., Malbet, F., Weigelt, G., et al. 2003a, in Interferometry for Optical Astronomy II. Edited by Wesley A. Traub . Proceedings of the SPIE, Volume 4838, pp. 924-933 (2003)., ed. W. A. Traub, 924–933 [ADS] 4.1.1, 9.3

Petrov, R. G., Malbet, F., Weigelt, G., et al. 2003b, in Interferometry for Optical Astronomy II. Edited by Wesley A. Traub . Proceedings of the SPIE, Volume 4838, pp. 924-933 (2003)., ed. W. A. Traub, 924–933 [ADS] 6.3.2

Pittard, J. M. & Corcoran, M. F. 2002, A&A, 383, 636 [ADS] 9.2, 9.4.1, 9.4.4.2, 9.4.5

Pollack, J. B., Hollenbach, D., Beckwith, S., et al. 1994, ApJ, 421, 615 [ADS] 6.6.3

Polomski, E. F., Telesco, C. M., Piña, R., & Schulz, B. 2002, AJ, 124, 2207 [ADS] 6.2, 6.4.2.1, 6.4.2.1, 6.7, 6.9, 6.6.1

Pourbaix, D. 1998, A&AS, 131, 377 [ADS] 8.8

Preibisch, T., Balega, Y., Hofmann, K.-H., Weigelt, G., & Zinnecker, H. 1999, New Astronomy, 4, 531 [ADS] 1.2, 7.2, 8.2, 8.6.5

Preibisch, T., Kraus, S., Driebe, T., van Boekel, R., & Weigelt, G. 2006, ArXiv Astrophysics e-prints [ADS] 6.2, 10

Pringle, J. E. 1981, ARA&A, 19, 137 [ADS] 6.6.4

Przygodda, F., Chesneau, O., Graser, U., Leinert, C., & Morel, S. 2003, Ap&SS, 286, 85 [ADS] 6.3.3

Quanz, S. P., Henning, T., Bouwman, J., Ratzka, T., & Leinert, C. 2006, ApJ, 648, 472 [ADS] 6.2

Raga, A. C. & Biro, S. 1993, MNRAS, 264, 758 [ADS] 7.5.4.4

Raga, A. C., Riera, A., Masciadri, E., et al. 2004, AJ, 127, 1081 [ADS] 7.5.4.4

Rathborne, J. M., Jackson, J. M., & Simon, R. 2006, ApJ, 641, 389 [ADS] 1.2

Readhead, A. C. S., Nakajima, T. S., Pearson, T. J., et al. 1988, AJ, 95, 1278 [ADS] 2.2.2

Reid, M. A. & Wilson, C. D. 2005, ApJ, 625, 891 [ADS] 7.3, 7.4.2, 7.6

Rho, J., Reach, W. T., Lefloch, B., & Fazio, G. G. 2006, ApJ, 643, 965 [ADS] 6.4.1

Richichi, A. & Percheron, I. 2002, A&A, 386, 492 [ADS] 6.2

Richichi, A., Percheron, I., & Khristoforova, M. 2005, A&A, 431, 773 [ADS] 6.2, 8.1, 9.1

Rodríguez, L. F., Poveda, A., Lizano, S., & Allen, C. 2005, ApJ, 627, L65 [ADS] 8.2

Rogers, A. E. E., Hinteregger, H. F., Whitney, A. R., et al. 1974, ApJ, 193, 293 [ADS] 1.3.3, 2.2.2

Rosen, A. & Smith, M. D. 2004, MNRAS, 347, 1097 [ADS] 7.5.4.4

Rots, A. H., Dickel, H. R., Forster, J. R., & Goss, W. M. 1981, ApJ, 245, L15 [ADS] 7.2.1

Ryle, M. & Hewish, A. 1960, MNRAS, 120, 220 [ADS] 1.3.3

Sandell, G. & Sievers, A. 2004, ApJ, 600, 269 [ADS] 7.2.1

Sarazin, M. & Roddier, F. 1990, A&A, 227, 294 [ADS] 1.3.1

Schaefer, G. H., Simon, M., Nelan, E., & Holfeltz, S. T. 2003, AJ, 126, 1971 [ADS] 8.2

Schertl, D., Balega, Y. Y., Preibisch, T., & Weigelt, G. 2003, A&A, 402, 267 [ADS] 8.1, 8.2, 8.3, 8.6.4, 8.6.4

Schöller, M., Wilhelm, R., & Koehler, B. 2000, A&AS, 144, 541 [ADS] 2.4

Schuller, P. A., Lacasse, M. G., Lydon, D. S., et al. 2004, in New Frontiers in Stellar Interferometry, Proceedings of SPIE Volume 5491. Edited by Wesley A. Traub. Bellingham, WA: The International Society for Optical Engineering, 2004., p.1137, ed. W. A. Traub, 1137–+ [ADS] 8.3.2

Schulz, N. S., Canizares, C., Huenemoerder, D., & Tibbets, K. 2003, ApJ, 595, 365 [ADS] 2

Scoville, N. Z., Sargent, A. I., Sanders, D. B., et al. 1986, ApJ, 303, 416 [ADS] 7.2.1, 7.4.1.1, 7.10, 7.5.4.2

Ségransan, D., Kervella, P., Forveille, T., & Queloz, D. 2003, A&A, 397, L5 [ADS] 3.3.1

Shepherd, D. 2005, in IAU Symposium, 237–246 [ADS] 7.7

Shepherd, D. S., Yu, K. C., Bally, J., & Testi, L. 2000, ApJ, 535, 833 [ADS] 7.2, 7.5.4.5, 7.7

Siess, L., Dufour, E., & Forestini, M. 2000, A&A, 358, 593 [ADS] 8.10

Simón-Díaz, S., Herrero, A., Esteban, C., & Najarro, F. 2006, A&A, 448, 351 [ADS] 8.1, 8.6.4

Skinner, S. L., Brown, A., & Stewart, R. T. 1993, ApJS, 87, 217 [ADS] 6.2

Skrutskie, M. F., Cutri, R. M., Stiening, R., et al. 2006, AJ, 131, 1163 [ADS] 6.9

Smith, M. D. & Rosen, A. 2003, MNRAS, 339, 133 [ADS] 7.5.4.4

Smith, M. D. & Rosen, A. 2005a, MNRAS, 357, 579 [ADS] 7.5.4.4

Smith, M. D. & Rosen, A. 2005b, MNRAS, 357, 1370 [ADS] 7.3.2

Smith, N. 2002, MNRAS, 337, 1252 [ADS] 9.4.4.2

Smith, N. 2004, MNRAS, 351, L15 [ADS] 9.3

Smith, N. 2006, ApJ, 644, 1151 [ADS] 9.2, 9.4.6

Smith, N., Davidson, K., Gull, T. R., Ishibashi, K., & Hillier, D. J. 2003, ApJ, 586, 432 [ADS] 9.1, 9.2, 9.4.3, 9.4.6

Smith, N., Morse, J. A., Davidson, K., & Humphreys, R. M. 2000, AJ, 120, 920 [ADS] 9.2

Stahl, O. 1998, in Cyclical Variability in Stellar Winds, ed. L. Kaper & A. W. Fullerton, 246–+ [ADS] 8.6.3

Stahl, O., Kaufer, A., Rivinius, T., et al. 1996, A&A, 312, 539 [ADS] 8.1, 8.2, 8.6.3

Stahl, O., Wolf, B., Gang, T., et al. 1993, A&A, 274, L29+ [ADS] 8.1, 8.2, 8.6.3

Steiner, J. E. & Damineli, A. 2004, ApJ, 612, L133 [ADS] 9.2, 9.4.1

Tamazian, V. S., Docobo, J. A., White, R. J., & Woitas, J. 2002, ApJ, 578, 925 [ADS] 8.2

Tamura, M., Gatley, I., Joyce, R. R., et al. 1991, ApJ, 378, 611 [ADS] 7.2.1, 7.4.1.1

Tan, J. C. 2004, ApJ, 607, L47 [ADS] 8.2

Tatulli, E., Millour, F., Chelli, A., et al. 2006, A&A accepted 4.3, 4.2, 4.4.2, 4.5, 6.3.2, 9.3, 9.3

Terquem, C., Eislöffel, J., Papaloizou, J. C. B., & Nelson, R. P. 1999, ApJ, 512, L131 [ADS] 7.2

Thompson, A. R., Moran, J. M., & Swenson, G. W. 1986, Interferometry and synthesis in radio astronomy (New York, Wiley-Interscience, 1986, 554 p.) [ADS] 2.5

Thompson, G. I., Nandy, K., Jamar, C., et al. 1978, Catalogue of stellar ultraviolet fluxes. A compilation of absolute stellar fluxes measured by the Sky Survey Telescope (S2/68) aboard the ESRO satellite TD-1 (Unknown) [ADS] 6.9

Torrence, C. & Compo, G. P. 1998, Bulletin of the American Meteorological Society, vol. 79, Issue 1, pp.61-78, 79, 61 [ADS] 3.3.1

Traub, W. A., Ahearn, A., Carleton, N. P., et al. 2003, in Interferometry for Optical Astronomy II. Edited by Wesley A. Traub. Proceedings of the SPIE, Volume 4838, pp. 45-52 (2003)., ed. W. A. Traub, 45–52 [ADS] 3.2, 8.3.2

Trumpler, R. J. 1931, PASP, 43, 255 [ADS] 8.6.4

Turon, C., Creze, M., Egret, D., et al. 1993, Bulletin d'Information du Centre de Donnees Stellaires, 43, 5 [ADS] 6.9

Vacca, W. D., Garmany, C. D., & Shull, J. M. 1996, ApJ, 460, 914 [ADS] 7.5.5

van Altena, W. F., Lee, J. T., Lee, J.-F., Lu, P. K., & Upgren, A. R. 1988, AJ, 95, 1744 [ADS] 8.6.4

van Boekel, R., Kervella, P., Schöller, M., et al. 2003, A&A, 410, L37 [ADS] 9.2, 9.7, 9.4.2.1, 9.4.2.2, 9.4.3, 9.5, 9.16, 9.7

van Boekel, R., Min, M., Leinert, C., et al. 2004a, Nature, 432, 479 [ADS] 6.5.2

van Boekel, R., Waters, L. B. F. M., Dominik, C., et al. 2004b, A&A, 418, 177 [ADS] 6.4.1

van den Ancker, M. E., de Winter, D., & Tjin A Djie, H. R. E. 1998, A&A, 330, 145 [ADS] 6.2

van Dishoeck, E. F. 2004, ARA&A, 42, 119 [ADS] 6.4.1

van Genderen, A. M., Sterken, C., Allen, W. H., & Liller, W. 2003, A&A, 412, L25 [ADS] 9.2

Verner, E., Bruhweiler, F., & Gull, T. 2005, ApJ, 624, 973 [ADS] 9.2

Vieira, S. L. A. & Cunha, N. C. S. 1994, Informational Bulletin on Variable Stars, 4090, 1 [ADS] 6.2

Vinković, D., Ivezić, Ž., Jurkić, T., & Elitzur, M. 2006, ApJ, 636, 348 [ADS] 6.1, 6.2

Viotti, R. 1995, in Revista Mexicana de Astronomia y Astrofisica Conference Series, ed. V. Niemela, N. Morrell, & A. Feinstein, 1–+ [ADS] 9.1

Vitrichenko, É. A. 2002a, Astronomy Letters, 28, 843 [ADS] 8.2, 8.6.5

Vitrichenko, É. A. 2002b, Astronomy Letters, 28, 324 [ADS] 8.2, 8.8, 8.6.1, 8.6.3

Völker, R., Smith, M. D., Suttner, G., & Yorke, H. W. 1999, A&A, 343, 953 [ADS] 7.5.4.4

Wade, G. A., Fullerton, A. W., Donati, J.-F., et al. 2006, A&A, 451, 195 [ADS] 8.1, 8.6.3

Walborn, N. R. & Nichols, J. S. 1994, ApJ, 425, L29 [ADS] 8.6.3

Walsh, A. J., Burton, M. G., Hyland, A. R., & Robinson, G. 1998, MNRAS, 301, 640 [ADS] 1.2

Weigelt, G., Albrecht, R., Barbieri, C., et al. 1995, in Revista Mexicana de Astronomia y Astrofisica Conference Series, ed. V. Niemela, N. Morrell, & A. Feinstein, 11 [ADS] 9.2

Weigelt, G., Balega, Y., Preibisch, T., et al. 1999, A&A, 347, L15 [ADS] 8.1, 8.2, 8.3, 8.6.4

Weigelt, G., Balega, Y. Y., Preibisch, T., Schertl, D., & Smith, M. D. 2002, A&A, 381, 905 [ADS] 7.2, 7.7

Weigelt, G., Beuther, H., Hofmann, K.-H., et al. 2006, A&A, 447, 655 [ADS] 7.2, 7.7

Weigelt, G. & Ebersberger, J. 1986, A&A, 163, L5 [ADS] 9.2

Weigelt, G. & Wirnitzer, B. 1983, Optics Letters, 8, 389 [ADS] 1.3.2, 7.3.1, 8.3.1

Weigelt, G. P. 1977, Optics Communications, 21, 55 [ADS] 1.3.2, 7.3.1, 8.3.1

Weis, K., Stahl, O., Bomans, D. J., et al. 2005, AJ, 129, 1694 [ADS] 9.2

Werner, M. W., Becklin, E. E., Gatley, I., et al. 1979, MNRAS, 188, 463 [ADS] 7.6

Wesselius, P. R., van Duinen, R. J., de Jonge, A. R. W., et al. 1982, A&AS, 49, 427 [ADS] 6.9

Whitelock, P. A., Feast, M. W., Marang, F., & Breedt, E. 2004, MNRAS, 352, 447 [ADS] 9.2

Whitney, B. A., Wood, K., Bjorkman, J. E., & Wolff, M. J. 2003, ApJ, 591, 1049 [ADS] 6.6.5.1

Wilkin, F. P. & Akeson, R. L. 2003, Ap&SS, 286, 145 [ADS] 6.3.1, 6.3, 6.4.2

Wolf, S. 2003, Computer Physics Communications, 150, 99 [ADS] 5.3

Wu, Y., Wei, Y., Zhao, M., et al. 2004, A&A, 426, 503 [ADS] 7.2

Wynn-Williams, C. G., Becklin, E. E., & Neugebauer, G. 1974, ApJ, 187, 473 [ADS] 7.2.1

Yorke, H. W. & Sonnhalter, C. 2002, ApJ, 569, 846 [ADS] 1.2

Zanella, R., Wolf, B., & Stahl, O. 1984, A&A, 137, 79 [ADS] 9.2

Zeipel, H. V. 1925, MNRAS, 85, 678 [ADS] 9.1, 9.4.6

Zinnecker, H. 2004, in ASP Conf. Ser. 322: The Formation and Evolution of Massive Young Star Clusters, ed. H. J. G. L. M. Lamers, L. J. Smith, & A. Nota, 349–+ [ADS] 1.2